Lifetime prediction for rocks - a numerical concept based on linear elastic fracture mechanics, subcritical crack growth, and elasto-plastic stress redistributions

Von der Fakultät für Geowissenschaften, Geotechnik und Bergbau
der Technischen Universität Bergakademie Freiberg
genehmigte

DISSERTATION

zur Erlangung des akademischen Grades

Doktor-Ingenieur
Dr.-Ing.

vorgelegt

von Dipl.-Ing. Xiang, Li
geboren am 07.12.1983 in Zhengzhou, China

Gutachter: Prof. Dr.-Ing. habil. Heinz Konietzky, Freiberg
Prof. Dr. mont. Wulf Schubert, Graz (Österreich)
Prof. Dr.-Ing. Guijun Wang, Tianjing (China)

Tag der Verleihung: Freiberg, den 30.09.2013

Acknowledgements

I would like to first thank the China Scholarship Council for providing the financial support for this study, which makes the 4-year doctoral research work in Germany possible.

This study was accomplished under the supervision of Prof. Dr. habil. Heinz Konietzky, Head of the Geotechnical Institute (IfGT), TU Bergakademie Freiberg. I feel grateful to have had the chance to be instructed by such a perfect professor. During my stay in Germany, he has provided me not only academic instructions concerning the technical field, but also various support in other aspects of my study life. His patience, diligence and academic competence has greatly inspired and influenced me. What I have learned from him has been and will be my motive power of advance. Here I would like to express my deepest and sincerest gratitude to him.

I also would like to express my thankfulness to the colleagues in Geotechnical Institute for creating such a pleasant research environment. Thank Mrs. Angela Griebsch for the very kind and heart warming help whenever I need. Thank Ms. Anett Wagner for the very useful mathematical help in this study. Special thanks to Dr. Martin Herbst for the important mathematical support and valuable programming advices. Thank Dr. Axel Hausdorf for the valuable advices. Thank you all for the kindness and patience.

Special thanks to Prof. Ove Stephansson from Helmholtz Center Potsdam, GFZ German Rersearch Center for Geosciences for providing me very valuable academic advices.

Thank my whole family for the understanding and support of my study abroad. Special thanks to my mother, who has given me her whole hearted care and support.

Abstract

A lifetime prediction scheme is proposed based on the assumption that the lifetime (time to failure) of rocks under load is governed by the growth of microstructual defects (microcracks). The numerical approach is based on linear elastic fracture mechanics. The numerical calculation scheme is implemented as a cellular automat, where each cell contains a microcrack with length and orientation following certain distributions. The propagation of the microcrack is controlled by the Charles equation, based on subcritical crack growth. The zone inside the numerical model fails if the microcrack has reached the zone dimension or the stress intensity factor of the crack reached the fracture toughness. Macroscopic fractures are formed by these coalesced propagating microcracks, and finally lead to failure of the model. In the numerical approaches, elasto-plastic stress redistributions take place during the forming of the macroscopic fractures. Distinct microcrack propagation types have been programmed and applied to the proposed numerical models. These numerical models are studied under different loading conditions. Numerical results with excellent agreement with the analytical solutions are obtained with respective to predicted lifetime, important parameters for the microcracks, fracture pattern and damage evolution. Potential applications of the proposed numerical model schemes are investigated in some preliminary studies and simulation results are discussed. Finally, conclusions are drawn and possible improvements to the numerical approaches and extensions of the research work are given.

Abstract (in Chinese)

摘要

本文认为微结构缺陷（微裂纹）的扩展决定了受力岩石的寿命（破坏时间）。基于此假设，提出了岩石寿命预测方法。利用线弹性断裂力学理论，通过 FLAC 进行了数值模拟。数值模型中每个单元定义一条初始裂纹，其长度与方向服从特定分布。基于亚临界裂纹扩展理论，由 Charles 方程决定微裂纹的扩展（速度）。如微裂纹发展至单元边界，或应力强度系数到达断裂韧度，则单元破坏。宏观裂纹由微裂纹所联合形成，并最终贯穿模型导致破坏。在形成宏观裂纹的过程中，发生弹塑性应力重分布。在数值模型中，编制了不同类型的微裂纹扩展方式，并在不同的受力条件下加以分析。数值模型的岩石寿命，裂纹形状，破坏方式以及一些重要的参数的数值模拟结果与解析解有较好的一致性。对本文所提出的数值模型的初步实际应用进行了分析，并讨论了计算结果。最后讨论了本文所提出的岩石寿命预测方法的可能改良与发展，并对进一步的研究工作给出建议。

Table of contents

Acknowledgements I
Abstract III
Abstract (in Chinese) IV
Table of contents V
List of figures VII
List of tables XIX
Abbreviations XXI
Symbols XXIII
1 Introduction 1
2 State of the art 3
3 Theoretical concepts 7
3.1 Griffith energy balance theory and the energy criterion 7
3.2 Crack opening modes 9
3.3 Crack-tip field and stress intensity factor 10
3.4 Fracture criterion based on the stress intensity factor 12
3.5 Stress intensity factor and Griffith's energy release rate 14
3.6 Subcritical crack growth 15
3.7 Charles equation 18
3.8 Lab and field results 19
3.9 Life time prediction idea 21
4 Numerical cellular automate for lifetime prediction 23
4.1 Basic model 23
4.1.1 Model idea 23
4.1.2 Application 25
4.2 Time-dependent studies 28
4.2.1 The lifetime prediction scheme and results (single zone) 28
4.2.2 Time step study on multi-zone models 31
4.2.3 Calculation scheme with changeable time steps 38
4.2.4 Conclusions 49
4.3 New modeling strategies 49
4.4 Fixed orientation model 52
4.4.1 Initial microcracks 52
4.4.2 The lifetime prediction scheme for fixed orientation model (single zone) 52
4.4.3 Study on the multi-zone models 64
4.4.4 Conclusions 80
4.5 Wing crack model 80
4.5.1 Crack initiation (Kink model) 81
4.5.2 Crack propagation model (Wing crack model) 83
4.5.3 Stress intensity factor calculation 84
4.5.4 K value verification for wing crack model 89
4.5.5 Life time prediction for wing crack model (single zone) 90
4.5.6 Study on the multi-zone wing crack model 104
4.5.7 Conclusions 114
4.6 Combined ubiquitous-joint model 115
4.6.1 Modeling scheme 115
4.6.2 Fixed orientation combined ubiquitous-joint model 117
4.6.3 Wing crack combined ubiquitous-joint model 119
4.6.4 Conclusions 122
4.7 Comparison between different model concepts 123

5 Application of the numerical models 125
5.1 Existing weak plane problems 125
5.1.1 Single weak plane simulation 125
5.1.2 Two weak planes simulation 128
5.1.3 Conclusions 133
5.2 Underground opening problems 133
5.2.1 Numerical implementation and initial simulation results 134
5.2.2 Simulation of underground openings with different shape 139
5.2.3 Conclusions 157
5.3 Underground pillar problems 158
5.3.1 Numerical simulation 158
5.3.2 Conclusions 165
5.4 Comparison between numerical results and observations in situ 165
6 Summaries and conclusions 171
7 Major contributions of this thesis 175
References 177

List of figures

Figure 3-1 An infinitely wide plate subjected to a remote tensile stress 7
Figure 3-2 Three crack opening modes with corresponding stress conditions (Gross 2006).....9
Figure 3-3 Crack under mixed-mode loadings (modified from Li 1988).....10
Figure 3-4 Stresses near the crack tip in a two-dimensional problem (modified from Anderson 1995).....11
Figure 3-5 K_I-determined field near the crack tip (Gross 2006).....14
Figure 3-6 Schematic stress intensity factor/crack velocity diagram for tensile crack growth (Atkinson 1987) 17
Figure 3-7 General relation between life time and load for brittle solids (Konietzky et al. 2009) 19
Figure 3-8 Spatial acoustic emission (AE) locations and experimental failure of red sandstone at a confining pressure of 35 MPa (Yang et al. 2012) 20
Figure 3-9 Three-point bending test on semi-circular rock specimen (a) experimental set-up; (b) fracture pattern of Johnstone in the three point bending test (Ayatollahi and Aliha 2007).....20
Figure 3-10 Acoustic emission (AE) locations and final macroscopic fracture pattern in the three-point bending test (a) Berea sandstone; (b) Sioux quartzite; (c) Charcoal granite; (d) Rockville granite (Zietlow and Labuz 1998).....20
Figure 4-1 Flow chart for one calculation cycle in a zone.....24
Figure 4-2 The macroscopic fracturing process (zones in gray: failed zones) 25
Figure 4-3 Initial crack length distributions of the models.....27
Figure 4-4 Uniaxial tensile test of model A, B and C under tensile load of 12 MPa (Initial crack lengths: normal distribution, mean = 0.013 m, standard deviation = 0.0001 m) (Konietzky et al. 2009).....27
Figure 4-5 Uniaxial compressive test of model A, B and C under compressive load of 12 MPa (Initial crack lengths: normal distribution, mean = 0.013 m, standard deviation = 0.0001 m) (Konietzky et al. 2009) 28
Figure 4-6 Geometry of model A.....31
Figure 4-7 Uniaxial tensile tests (6 MPa) with different time steps (Zones in green: tensile failure; zones in gray: failed in the past) 34
Figure 4-8 First zone failure time results with different constant time steps.....35
Figure 4-9 Uniaxial compressive tests (12 MPa) with different time steps (zones in green: tensile failure; zones in red: shear failure; zones in gray: failed in the past).....38
Figure 4-10 Uniaxial tensile test (6 MPa applied on model A) with changeable time steps (Zones in green: tensile failure).....40
Figure 4-11 Life time predictions with different Min. time steps.....41

Figure 4-12 Uniaxial compressive tests (12 MPa) with different minimum time steps (zones in green: tensile failure; zones in red: shear failure; zones in gray: failed in the past) 47
Figure 4-13 Life time predictions with different min. time steps 48
Figure 4-14 Different new model schemes 50
Figure 4-15 Zone of the model with initial crack 52
Figure 4-16 Cases of the critical crack length in single zone models 54
Figure 4-17 Crack condition at failure under uniaxial loads 56
Figure 4-18 Crack condition at failure under biaxial loads (Initial crack length: 0.013 m) 58
Figure 4-19 Natural logarithm of lifetimes (seconds) with different constant loads 63
Figure 4-20 Natural logarithm of lifetimes (seconds) with different initial crack lengths 64
Figure 4-21 Natural logarithm of lifetimes (seconds) with different crack orientations 64
Figure 4-22 Lognormal distribution of initial crack lengths (model D) 65
Figure 4-23 Uniform distribution of crack orientation 65
Figure 4-24 Normal distribution of crack orientation (Mean value: 10º; standard deviation: 1º) 65
Figure 4-25 5Initial crack conditions of fixed orientation model (Initial crack lengths (realization: model A): normal distribution, mean = 0.013 m, STD = 0.0001 m; initial crack orientation: uniform distribution) 66
Figure 4-26 Initial crack conditions of fixed orientation model (Initial crack lengths (realization: model A): normal distribution, mean = 0.013 m, STD = 0.0001 m; initial crack orientation: normal distribution, mean = 10º, STD = 1º) 66
Figure 4-27 Uniaxial tensile tests (12 MPa) of model A (zones in green: tensile failure; zones in red: shear failure; zones in gray: failed in past) 67
Figure 4-28 Uniaxial tensile tests (12 MPa) of model B (zones in green: tensile failure; zones in red: shear failure; zones in gray: failed in the past) 67
Figure 4-29 Uniaxial tensile tests (12 MPa) of model C (zones in green: tensile failure; zones in red: shear failure; zones in gray: failed in the past) 68
Figure 4-30 Uniaxial tensile tests (12 MPa) of model D (zones in green: tensile failure; zones in red: shear failure; zones in gray: failed in the past) 68
Figure 4-31 Crack condition of model A at failure (zones in green: tensile failure; zones in red: shear failure; zones in gray: failed in the past; initial crack lengths: normal distribution, mean = 0.013 m, STD = 0.0001 m; initial crack orientation: uniform distribution) 70

Figure 4-32 Crack condition of model A at failure (zones in green: tensile failure; initial crack lengths: normal distribution, mean = 0.013 m, STD = 0.0001 m; initial crack orientation: normal distribution, mean = 10º, STD = 1º).....70
Figure 4-33 Natural logarithm of lifetime (seconds) in uniaxial tensile test (tensile load of 12 MPa) with different mean crack orientations 71
Figure 4-34 Uniaxial compressive tests (18 MPa) of model A (zones in green: tensile failure; zones in red: shear failure; zones in gray: failed in the past).....72
Figure 4-35 Uniaxial compressive tests (18 MPa) of model B (zones in green: tensile failure; zones in red: shear failure; zones in gray: failed in the past).....73
Figure 4-36 Uniaxial compressive tests (18 MPa) of model C (zones in green: tensile failure; zones in red: shear failure; zones in gray: failed in the past).....74
Figure 4-37 Uniaxial compressive tests (18 MPa) of model D (zones in green: tensile failure; zones in red: shear failure; zones in gray: failed in the past).....75
Figure 4-38 Crack condition of model A at failure (zones in green: tensile failure; zones in red: shear failure; zones in gray: failed in the past; initial crack lengths: normal distribution, mean = 0.013 m, STD = 0.0001 m; initial crack orientation: uniform distribution).....78
Figure 4-39 Fracture pattern of model A at failure (zones in green: tensile failure; zones in red: shear failure; zones in gray: failed in the past; initial crack lengths: normal distribution, mean = 0.013 m, STD = 0.0001 m; initial crack orientation: normal distribution, mean = 45º, STD = 1º) 78
Figure 4-40 Natural logarithm of lifetime (seconds) in uniaxial compressive test with different mean crack orientation 79
Figure 4-41 Initiation of the crack under mixed-mode loading 81
Figure 4-42 Replacement of the real wing crack with a straight one (Baud et al. 1996) 83
Figure 4-43 Simplified propagation scheme for wing crack.....84
Figure 4-44 Superposition method for K value under biaxial compressions (Baud et al. 1996) 85
Figure 4-45 The superposition method for K value with tensile normal stress on the main crack 88
Figure 4-46 Comparison of normalized K values between numerical model and results from Baud et al. (1996) (l: wing crack length; a: half initial crack length).....89
Figure 4-47 Normalized K values with different l_{eq} schemes compared to exact solution (Horii and Nemat-Nasser 1985).....90
Figure 4-48 Cases of the critical wing crack length in single zone models (The major principal stress: σ_V; the minor principal stress: σ_H; β = 45º) 92
Figure 4-49 Crack condition at failure under uniaxial loads (initial crack orientation: 45º).....96

Figure 4-50 Crack pattern at failure for the biaxial test (initial crack orientation: 45º) 99
Figure 4-51 Natural logarithm of lifetimes (seconds) with different constant loads 103
Figure 4-52 Natural logarithm of lifetimes (seconds) with different initial crack lengths 103
Figure 4-53 Natural logarithm of lifetime (seconds) with different initial crack orientations 103
Figure 4-54 Uniaxial tensile test of the wing crack model (zones in green: tensile failure; zones in gray: failed in the past) 105
Figure 4-55 Crack characteristics after 23 days in the uniaxial tensile test (zones in green: tensile failure; zones in gray: failed in the past; initial crack lengths: normal distribution, mean = 0.035 m, STD = 0.0001 m; initial crack orientation: uniform distribution) 106
Figure 4-56 Crack characteristics at failure in the uniaxial tensile test (zones in green: tensile failure; initial crack lengths: normal distribution, mean = 0.035 m, STD = 0.0001 m; initial crack orientation: normal distribution, mean = 45º, STD = 1º) 106
Figure 4-57 Natural logarithm of lifetime (seconds) in tensile test (tensile load of 5.5 MPa) with different mean initial crack orientations (initial crack lengths: normal distribution, mean = 0.035 m, STD = 0.0001 m) 108
Figure 4-58 Uniaxial compressive test of the wing crack model (zones in green: tensile failure; zones in red: shear failure; zones in gray: failed in the past) 109
Figure 4-59 Crack characteristics at failure in the uniaxial compressive test (zones in green: tensile failure; zones in red: shear failure; zones in gray: failed in the past; initial crack lengths: normal distribution, mean = 0.035 m, STD = 0.0001 m; initial crack orientation: uniform distribution) 110
Figure 4-60 Crack characteristics at failure in the uniaxial compressive test (zones in green: tensile failure; zones in red: shear failure; zones in gray: failed in the past; initial crack lengths: normal distribution, mean = 0.035 m, STD = 0.0001 m; initial crack orientation: normal distribution, mean = 45º, STD = 1º) 110
Figure 4-61 Natural logarithm of lifetime (seconds) in compressive test (compressive load of 22 MPa) with different mean initial crack orientations (initial crack lengths: normal distribution, mean = 0.035 m, STD = 0.0001 m; initial crack orientation: normal distribution, mean = 45º, STD = 1º) 111
Figure 4-62 Biaxial compressive test of the wing crack model (major compressive load of 22 MPa applied vertically; minor compressive load of 0.5 MPa applied horizontally; zones in green: tensile failure; zones in red: shear failure; zones in gray: failed in the past) 113
Figure 4-63 Crack characteristics at failure in the biaxial compressive test (major compressive load of 22 MPa applied vertically; minor compressive load of

0.5 MPa applied horizontally; zones in green: tensile failure; zones in red: shear failure; zones in gray: failed in the past; initial crack lengths: normal distribution, mean = 0.035 m, STD = 0.0001 m; initial crack orientation: uniform distribution) .113
Figure 4-64 Crack characteristics at failure in the biaxial compressive test (major compressive load of 22 MPa applied vertically; minor compressive load of 0.5 MPa applied horizontally; zones in green: tensile failure; zones in red: shear failure; zones in gray: failed in the past; initial crack lengths: normal distribution, mean = 0.035 m, STD = 0.0001 m; initial crack orientation: normal distribution, mean = 45º, STD = 1º) 114
Figure 4-65 Model scheme for fixed orientation combined ubiquitous-joint model (the solid line in the zone is the actual crack) 116
Figure 4-66 Model scheme for wing crack combined ubiquitous-joint model (the solid line in the zone is the actual crack) 117
Figure 4-67 Uniaxial tensile test of model A (zones in red: slip along ubiquitous joint; zones in green: tensile failure on ubiquitous joint; zones in yellow: zone failed in tension; zones in black: failed in past (elastic); zones in gray: ubiquitous joint failed in the past) 118
Figure 4-68 Uniaxial compressive test of model A (zones in red: slip along ubiquitous joint; zones in green: tensile failure on ubiquitous joint; zones in yellow: zone failed in tension; zones in black: failed in past (elastic); zones in gray: ubiquitous joint failed in the past) 119
Figure 4-69 Uniaxial tensile test of the wing crack combined ubiquitous-joint model (zones in red: slip along ubiquitous joint; zones in green: tensile failure on ubiquitous joint; zones in yellow: zone failed in tension; zones in black: failed in past (elastic); zones in gray: ubiquitous joint failed in the past).....120
Figure 4-70 Uniaxial compressive test of the wing crack combined ubiquitous-joint model (zones in red: slip along ubiquitous joint; zones in green: tensile failure on ubiquitous joint; zones in yellow: zone failed in tension; zones in black: failed in past (elastic); zones in gray: ubiquitous joint failed in the past) 121
Figure 4-71 Biaxial compressive test of the wing crack combined ubiquitous-joint model (major compressive load of 22 MPa applied vertically; minor compressive load of 0.5 MPa applied horizontally; zones in red: slip along ubiquitous joint; zones in green: tensile failure on ubiquitous joint; zones in yellow: zone failed in tension; zones in gray: ubiquitous joint failed in the past) 122
Figure 5-1 Weak plane inside the model (Zones in red: failed zones forming the weak plane with inclination of 45º to the horizontal direction).....126
Figure 5-2 Failure of the model with different modeling schemes under compressive load of 12 MPa (initial crack lengths: normal distribution, mean = 0.02 m, STD = 0.005 m) (Zones in red: shear failure of the zone/slip along ubiquitous joint; zones in green: tensile failure of the zone/tensile failure on

ubiquitous joint; zones in gray: zone failed in the past/ubiquitous joint failed in the past) 128
Figure 5-3 Weak planes inside the model (Inclination: 45º) 129
Figure 5-4 Failure of basic model under compressive load of 12 MPa (Zones in red: shear failure of the zone; zones in green: tensile failure of the zone; zones in gray: zone failed in the past) 129
Figure 5-5 Failure of fixed orientation model under compressive load of 12 MPa (Zones in red: shear failure of the zone; zones in green: tensile failure of the zone; zones in gray: zone failed in the past) 130
Figure 5-6 Failure of fixed orientation combined ubiquitous-joint model under compressive load of 12 MPa (Zones in red: slip along ubiquitous joint; zones in green: tensile failure on ubiquitous joint; zones in yellow: zone failed in tension; zones in gray: ubiquitous joint failed in the past) 131
Figure 5-7 Failure of wing crack model under compressive load of 12 MPa (Zones in red: shear failure of the zone; zones in green: tensile failure of the zone; zones in gray: zone failed in the past) 132
Figure 5-8 Failure of wing crack combined ubiquitous-joint model under compressive load of 12 MPa (zones in red: slip along ubiquitous joint; zones in green: tensile failure on ubiquitous joint; zones in yellow: zone failed in tension; zones in black: failed in past (elastic); zones in gray: ubiquitous joint failed in the past) 132
Figure 5-9 Geometry of numerical models for underground opening problems (Model size: 2×2 m^2; opening size: 0.4×0.4 m^2) 134
Figure 5-10 Initial principal stress vectors of the numerical model (red vector: tensile stress; blue vector: compressive stress) 135
Figure 5-11 Failure of the numerical models under biaxial loading conditions (compressive load: 8 MPa (vertical), 2 MPa (horizontal); zones in red: shear failure of the zone/slip along ubiquitous joint; zones in green: tensile failure of the zone/tensile failure on ubiquitous joint; zones in gray: zone failed in the past/ubiquitous joint failed in the past) 137
Figure 5-12 A zoomed in area in fixed orientation model at failure (corresponding to Fig. 5-11 (b); zones in red: shear failure of the zone; zones in green: tensile failure of the zone; zones in gray: zone failed in the past) 138
Figure 5-13 A zoomed in area in fixed orientation combined ubiquitous-joint model at failure (corresponding to Fig. 5-11 (c); zones in red: slip along ubiquitous joint; zones in gray: ubiquitous joint failed in the past) 138
Figure 5-14 A zoomed in area in wing crack model at failure (corresponding to Fig. 5-11 (d); zones in red: shear failure of the zone; zones in green: tensile failure of the zone; zones in gray: zone failed in the past) 139

Figure 5-15 A zoomed in area in wing crack combined ubiquitous-joint model at failure (corresponding to Fig. 5-11 (e); zones in red: slip along ubiquitous joint; zones in gray: ubiquitous joint failed in the past) 139
Figure 5-16 Geometry of the numerical models 140
Figure 5-17 Stress condition at the periphery of the square opening (compressive load: 8 MPa (vertical), 2 MPa (horizontal); red vector: tensile stress; blue vector: compressive stress, unit: Pa) 141
Figure 5-18 Stress condition at the periphery of the arched opening (compressive load: 8 MPa (vertical), 2 MPa (horizontal); red vector: tensile stress; blue vector: compressive stress, unit: Pa) 141
Figure 5-19 Stress condition at the periphery of the circular opening (compressive load: 8 MPa (vertical), 2 MPa (horizontal); red vector: tensile stress; blue vector: compressive stress, unit: Pa) 142
Figure 5-20 Failure process of the basic models (compressive load: 8 MPa (vertical), 2 MPa (horizontal); initial crack lengths: normal distribution, mean = 0.02 m, STD = 0.005 m; initial crack orientation: normal distribution, mean = 45º, STD = 1º) 143
Figure 5-21 Failing process of the fixed orientation models (compressive load: 8 MPa (vertical), 2 MPa (horizontal); initial crack lengths: normal distribution, mean = 0.02 m, STD = 0.005 m; initial crack orientation: normal distribution, mean = 45º, STD = 1º; zones in red: shear failure of the zone; zones in green: tensile failure of the zone; zones in gray: zone failed in the past) 144
Figure 5-22 Final fracture pattern for fixed orientation models at failure (compressive load: 8 MPa (vertical), 2 MPa (horizontal); initial crack lengths: normal distribution, mean = 0.02 m, STD = 0.005 m; initial crack orientation: normal distribution, mean = 45º, STD = 1º) 145
Figure 5-23 Microcracks around the up right corner of the square opening at failure (corresponding to Fig. 5-21 (a); initial crack lengths: normal distribution, mean = 0.02 m, STD = 0.005 m; initial crack orientation: normal distribution, mean = 45º, STD = 1º; zones in red: shear failure of the zone; zones in green: tensile failure of the zone; zones in gray: zone failed in the past) 145
Figure 5-24 Microcracks around the right side of the arched opening at failure (corresponding to Fig. 5-21 (b); initial crack lengths: normal distribution, mean = 0.02 m, STD = 0.005 m; initial crack orientation: normal distribution, mean = 45º, STD = 1º; zones in red: shear failure of the zone; zones in green: tensile failure of the zone; zones in gray: zone failed in the past) 146
Figure 5-25 Microcracks around the right side of the circular opening at failure (corresponding to Fig. 5-21 (c); initial crack lengths: normal distribution, mean = 0.02 m, STD = 0.005 m; initial crack orientation: normal distribution,

mean = 45º, STD = 1º; zones in red: shear failure of the zone; zones in green: tensile failure of the zone; zones in gray: zone failed in the past) 146
Figure 5-26 Failure process of the fixed orientation combined ubiquitous-joint models (compressive load: 8 MPa (vertical), 2 MPa (horizontal); initial crack lengths: normal distribution, mean = 0.02 m, STD = 0.005 m; initial crack orientation: normal distribution, mean = 45º, STD = 1º; zones in red: slip along ubiquitous joint; zones in green: tensile failure on ubiquitous joint; zones in gray: ubiquitous joint failed in the past) 148
Figure 5-27 Final fracture pattern for fixed orientation combined ubiquitous-joint models (compressive load: 8 MPa (vertical), 2 MPa (horizontal); initial crack lengths: normal distribution, mean = 0.02 m, STD = 0.005 m; initial crack orientation: normal distribution, mean = 45º, STD = 1º) 148
Figure 5-28 Microcracks around the up left corner of the square opening at failure (corresponding to Fig. 5-26 (a); initial crack lengths: normal distribution, mean = 0.02 m, STD = 0.005 m; initial crack orientation: normal distribution, mean = 45º, STD = 1º; zones in red: slip along ubiquitous joint; zones in green: tensile failure on ubiquitous joint/zone failed in tension; zones in gray: ubiquitous joint failed in the past) 149
Figure 5-29 Microcracks around the left side of the arched opening at failure (corresponding to Fig. 5-26 (b); initial crack lengths: normal distribution, mean = 0.02 m, STD = 0.005 m; initial crack orientation: normal distribution, mean = 45º, STD = 1º; zones in red: slip along ubiquitous joint; zones in green: tensile failure on ubiquitous joint/zone failed in tension; zones in gray: ubiquitous joint failed in the past) 149
Figure 5-30 Microcracks around the left side of the circular opening at failure (corresponding to Fig. 5-26 (c); initial crack lengths: normal distribution, mean = 0.02 m, STD = 0.005 m; initial crack orientation: normal distribution, mean = 45º, STD = 1º; zones in red: slip along ubiquitous joint; zones in green: tensile failure on ubiquitous joint/zone failed in tension; zones in gray: ubiquitous joint failed in the past) 150
Figure 5-31 Failure process of the wing crack models (compressive load: 8 MPa (vertical), 2 MPa (horizontal); initial crack lengths: normal distribution, mean = 0.02 m, STD = 0.005 m; initial crack orientation: normal distribution, mean = 45º, STD = 1º; zones in red: shear failure of the zone; zones in green: tensile failure of the zone; zones in gray: zone failed in the past) 151
Figure 5-32 Final fracture pattern for the wing crack models (compressive load: 8 MPa (vertical), 2 MPa (horizontal); initial crack lengths: normal distribution, mean = 0.02 m, STD = 0.005 m; initial crack orientation: normal distribution, mean = 45º, STD = 1º) 152

Figure 5-33 Microcracks around the lower right corner of the square opening at failure (corresponding to Fig. 5-31 (a); initial crack lengths: normal distribution, mean = 0.02 m, STD = 0.005 m; initial crack orientation: normal distribution, mean = 45º, STD = 1º; zones in red: shear failure of the zone; zones in green: tensile failure of the zone; zones in gray: zone failed in the past) 152
Figure 5-34 Microcracks around the floor of the arched opening at failure (corresponding to Fig. 5-31 (b); initial crack lengths: normal distribution, mean = 0.02 m, STD = 0.005 m; initial crack orientation: normal distribution, mean = 45º, STD = 1º; zones in red: shear failure of the zone; zones in green: tensile failure of the zone; zones in gray: zone failed in the past) 153
Figure 5-35 Microcracks around the up right side of the circular opening at failure (corresponding to Fig. 5-31 (c); initial crack lengths: normal distribution, mean = 0.02 m, STD = 0.005 m; initial crack orientation: normal distribution, mean = 45º, STD = 1º; zones in red: shear failure of the zone; zones in green: tensile failure of the zone; zones in gray: zone failed in the past) 153
Figure 5-36 Failure process of the wing crack combined ubiquitous-joint models (compressive load: 8 MPa (vertical), 2 MPa (horizontal); initial crack lengths: normal distribution, mean = 0.02, STD = 0.005; initial crack orientation: normal distribution, mean = 45º, STD = 1º; zones in red: slip along ubiquitous joint; zones in green: tensile failure on ubiquitous joint; zones in gray: ubiquitous joint failed in the past) 155
Figure 5-37 Final failure pattern of the wing crack combined ubiquitous-joint models at failure (compressive load: 8 MPa (vertical), 2 MPa (horizontal); initial crack lengths: normal distribution, mean = 0.02, STD = 0.005; initial crack orientation: normal distribution, mean = 45º, STD = 1º) 155
Figure 5-38 Microcracks around the up right corner of the square opening at failure (corresponding to Fig. 5-36 (a); initial crack lengths: normal distribution, mean = 0.02 m, STD = 0.005 m; initial crack orientation: normal distribution, mean = 45º, STD = 1º; zones in red: slip along ubiquitous joint; zones in green: tensile failure on ubiquitous joint; zones in yellow: zone failed in tension; zones in gray: ubiquitous joint failed in the past) 156
Figure 5-39 Microcracks around the up right side of the arched opening at failure (corresponding to Fig. 5-36 (b); initial crack lengths: normal distribution, mean = 0.02 m, STD = 0.005 m; initial crack orientation: normal distribution, mean = 45º, STD = 1º; zones in red: slip along ubiquitous joint; zones in green: tensile failure on ubiquitous joint; zones in black: failed in past (elastic); zones in gray: ubiquitous joint failed in the past) 156
Figure 5-40 Microcracks around the up right side of the circular opening at failure (corresponding to Fig. 5-36 (c); initial crack lengths: normal distribution, mean = 0.02 m, STD = 0.005 m; initial crack orientation: normal distribution,

mean = 45º, STD = 1º; zones in red: slip along ubiquitous joint; zones in green: tensile failure on ubiquitous joint; zones in yellow: zone failed in tension; zones in gray: ubiquitous joint failed in the past) 157
Figure 5-41 Geometry of numerical models for underground pillar (Model height: 12 m; pillar height 5 m; zone size: 0.04 × 0.04 m^2).....158
Figure 5-42 Initial principal stress vectors at the joint of the pillar top and the ceiling (under uniaxial compressive load of 8 MPa) 159
Figure 5-43 Failure process of the basic model (zones in red: shear failure of the zone; zones in green: tensile failure of the zone; zones in gray: zone failed in the past).....160
Figure 5-44 Failure process of the fixed orientation model (zones in red: shear failure of the zone; zones in green: tensile failure of the zone; zones in gray: zone failed in the past) (Initial crack lengths: normal distribution, mean = 0.02 m, STD = 0.005 m) 161
Figure 5-45 Failure process of the fixed orientation combined ubiquitous-joint model (zones in red: slip along ubiquitous joint; zones in green: tensile failure on ubiquitous joint; zones in gray: ubiquitous joint failed in the past; initial crack lengths: normal distribution, mean = 0.02 m, STD = 0.005 m).....162
Figure 5-46 Failure process of the wing crack model (zones in red: shear failure of the zone; zones in green: tensile failure of the zone; zones in gray: zone failed in the past; initial crack lengths: normal distribution, mean = 0.02 m, STD = 0.005 m) 163
Figure 5-47 Failure process of the wing crack combined ubiquitous-joint model (zones in red: slip along ubiquitous joint; zones in green: tensile failure on ubiquitous joint; zones in yellow: zone failed in tension; zones in black: failed in past (elastic); zones in gray: ubiquitous joint failed in the past; initial crack lengths: normal distribution, mean = 0.02 m, STD = 0.005 m) 164
Figure 5-48 The excavation disturbed zone around a tunnel (a) the fracture features around the sidewalls in wing crack combined ubiquitous-joint model with initial crack orientation following normal distribution; (b) at an intersection of two tunnels at Mont Terri (Blümling and Konietzky 2003, photo B. Niederberger) 166
Figure 5-49 Damage zones around underground cavities on different scales (a) macroscopic fracture in wing crack model, σ1 = 8 MPa, σ2 = 2 MPa (b) slim horizontal borehole (c) Gas path through host rock and along seal sections/ HG-A microtunnel (d) overbreak in the EZ-A tunnel of the Mont Terri Underground Research Laboratory, σ1 = 6.5 MPa, σ1 / σ2 = 1.5 ~ 2 (Marschall et al. 2008) (dashed line: (a) mean initial crack orientation; (b), (c) and (d): bedding direction) 167
Figure 5-50 Tip of the V-shaped notch of the underground opening (a) macroscopic fracture pattern at the sidewalls at the early stage of the damage process of the opening in wing crack combined ubiquitous-joint model with initial

crack orientation following normal distribution (b) V-shaped notch tip of a Mine-by Experiment Tunnel at the Underground Research Laboratory in Canada (Chandler 2004) 167
Figure 5-51 Macroscopic fracture pattern of underground opening (a), (d) fixed orientation model, α = 45º - φ/2 = 30º, φ = 30º (b), (c), (e) classical fracture pattern of underground opening ((b): sidewalls are not stable; (c) sidewalls are stable; (e) pressure arch is not formed naturally) (modified from Xu 1993) (P: initial vertical pressure on the rock, dashed line: presumable ground, red line: sliding face).....168
Figure 5-52 Spalling at the rib of the pillar (a) fracture pattern of pillar in fixed orientation model (b) fracture pattern of pillar in wing crack model (c) hourglass formation of a pillar because of spalling (Esterhuizen et al. 2011) 169

List of tables

Table 4-1 Material parameters (Konietzky et al. 2009) 26
Table 4-2 Calculation results for uniaxial tests (initial crack length: 0.013 m) 30
Table 4-3 Calculated life times with different constant time steps (corresponding to Fig. 4-7) (analytical 1st failure time: 4,801,063,122 seconds) 34
Table 4-4 Calculated life times with different constant time steps (corresponding to Fig. 4-9) (analytical 1st failure time: 4.8011e9 seconds) 38
Table 4-5 Comparison between life time results.....39
Table 4-6 Predicted life time results with changeable time steps 40
Table 4-7 Comparison between predicted life times.....41
Table 4-8 Predicted life times with changeable time steps (corresponding to Fig. 4-12).....48
Table 4-9 Distinct characteristics of numerical models 51
Table 4-10 Calculation results under uniaxial loads (corresponding to Fig. 4-17).....55
Table 4-11 Calculation results under biaxial loads (corresponding to Fig. 4-18).....59
Table 4-12 Uniaxial tests under different constant loads (corresponding to Fig. 4-19) 61
Table 4-13 Uniaxial tests with different initial crack lengths (corresponding to Fig. 4-20).....62
Table 4-14 Uniaxial tests with different crack orientations (corresponding to Fig. 4-21).....62
Table 4-15 Lifetime results of models in uniaxial tensile tests (12 MPa).....69
Table 4-16 Lifetime of model A with different mean orientations under tensile load of 12 MPa (initial crack orientation following normal distribution) 71
Table 4-17 Lifetime results of models under compressive load of 18 MPa 77
Table 4-18 Lifetime of model A with different mean orientations under compressive load of 18 MPa (initial crack orientation follow normal distribution)....79
Table 4-19 Calculation results under uniaxial loads (corresponding to Fig. 4-49).....96
Table 4-20 Calculation results for the biaxial tests (corresponding to Fig. 4-50).....99
Table 4-21 Uniaxial tests with different constant loads (corresponding to Fig. 4-51) 100
Table 4-22 Uniaxial tests with different initial crack lengths (corresponding to Fig. 4-52).....101
Table 4-23 Uniaxial tests with different initial crack orientations (corresponding to Fig. 4-53) 102
Table 4-24 Lifetime results of uniaxial tensile test 105
Table 4-25 Lifetime results of unaxial tensile test (tensile load of 5.5 MPa) with different mean initial crack orientations 107
Table 4-26 Lifetime results of uniaxial compressive test 109

Table 4-27 Lifetime results of unaxial compressive test (compressive load of 22 MPa) with different mean orientations 111
Table 4-28 Lifetime results of biaxial compressive test 112

Abbreviations

2D	two deminsional
AE	acoustic emission
d	day(s)
DIT	damage initiation threshold
EDZ	excavation damaged zone
FLAC	Fast lagrangian analysis of continua
h	hour(s)
LEFM	linear elastic fracture mechanical theory
m	meter(s)
Max.	maximum
mean	mean value
min.	minute(s)
Min.	minimum
MPa	megapascal
PFC	Particle flow code
s	second(s)
STD	standard deviation
t	time
y	year(s)

Symbols

a	half initial crack length
A	crack area
a_c	critical (half) crack length
a_o	initial crack length
C	fracture growth constant
E	total energy/ Young's modulus
G	energy release rate
G_c	critical energy release rate
G_I	energy release rate (Mode I)
G_{II}	energy release rate (Mode II)
G_{III}	energy release rate (Mode III)
$k_{1\theta}$	stress intensity factor for the kink
K	stress intensity factor
K_I	stress intensity factor (Mode I)
K_{II}	stress intensity factor (Mode II)
K_{III}	stress intensity factor (Mode III)
K_{IC}	fracture toughness (Mode I)
K_{IIC}	fracture toughness (Mode II)
K_{IIIC}	fracture toughness (Mode III)
K_{ISO}	stress intensity factor component for the wing crack
K_{SLI}	stress intensity factor component for the main crack (Mode II)
K_{TEN}	stress intensity factor component for the main crack (Mode I)
l	wing crack length
l^*	effective wing crack length
l_c	critical wing crack length
l_{eq}	equivalent wing crack length
n	stress corrosion index
P	initial vertical pressure
r	distance from the tip of the crack
R	gas constant (Boltzmann constant)
S	area of the zone
t_{zone}	lifetime of a zone
T	absolute temperature
u	displacement (x direction)
v	crack propagation velocity/ displacement (y direction)
v_0	material constant
W_s	work for new surfaces' creation
x	crack size
x_{cr}	critical crack size

α	microcrack inclination from the vertical direction
β	orientation of the initial crack
γ_s	surface energy
θ	kink angle from the tip of the crack
κ	Lamé constant
μ	shear modulus
υ	Poisson's ratio
Π	potential energy
σ	remote normal stress σ
σ_1	maximum principal stress
σ_2	minimum principal stress
σ_{eff}	effective shear stress on the crack
σ_f	failure stress
σ_H	horizontal stress applied on the zone
σ_M	maximal tensile stress within the zone
σ_N	normal stress on the crack
σ_T	shear stress on the crack
σ_V	vertical stress applied on the zone
σ_{xx}	normal stress in x direction
σ_{yy}	normal stress in y direction
σ_z	normal stress in z direction
σ_θ	circumferential stress near the crack tip
$\sigma_{\theta\theta}$	circumferential stress near the crack tip (Mode I/ Mode II)
τ	in-plane shear stress
τ'	out-of-plane shear stress
τ_M	maximal shear stress within the zone
τ_{xy}	shear stress in xy plane
τ_{xz}	shear stress in xz plane
τ_{yz}	shear stress in yz plane
φ	friction angle

1 Introduction

Rock is the main material which bears loads in geotechnical projects such as civil engineering constructions, mining structures, underground storage facilities etc. It is necessary for the rock mass to maintain stability in such structures during certain long time for safety reason. So behavior of rock under load and the service time (lifetime) prediction is of great practical interest for the above industries. In other structures such as historical buildings and monuments where rock is also commonly used, predicted life time could also provide important information for plans on further maintenance work or other necessary measures. The purpose of this study is to provide possible lifetime prediction schemes based on the existing theories in fracture mechanics through numerical simulation of the microcrack propagations inside the rock body. Results of this study are supposed to give practical reference to the construction work in the field of rock engineering.

A solid body responds to extreme loading by undergoing large deformation and/or fracture (Hellan 1985). The second phenomenon has been the focus of this study. It is understood that under loads, microcracks in the natural rock would propagate and coalesce and form macroscopic fractures. This process decreases the stability of the rock body, and could with ongoing time, finally lead to the failure of the rock mass. In view of this, it is considered in this study that the lifetime or time to failure of rocks is governed by such micro structural defects as microcracks or voids. The lifetime can be predicted by empirical exponential laws or physical laws based on damage and fracture mechanics. Based on subcritical crack growth and linear elastic fracture mechanical approach, a lifetime prediction scheme has been proposed with a numerical cellular automate developed to simulate the rock behavior containing initial microcracks (Konietzky et al. 2009). Based on this research work, this study aims to further develop the existing approach and make improvement on the numerical simulation, and finally apply the developed scheme to geotechnical problems. Improvements have been made on the basis of the developed cellular automate, including incorporation of the orientation of the microcracks, development of distinct lifetime prediction schemes with corresponding numerical model schemes, inclusion of anisotropy into the numerical model. Investigations of the factors influencing the lifetime have been included. Possible applications of the proposed model schemes have also been discussed.

A brief introduction into fracture mechanics and the state of the art of time related studies of solids is included in Chapter 2. The basic theories and current laboratory results are introduced in Chapter 3. A detailed study of the lifetime prediction schemes corresponding to different numerical models are given in Chapter 4. In Chapter 5, some examples of possible applications of the proposed numerical models

have been given and discussions have been made about their applicability. Conclusions of this study and possible future work have been given in Chapter 6.

2 State of the art

In rock mechanics, fracture is one of the results for rocks bearing load to a certain magnitude. Fracture causes failure of the rock, and may finally leads to instability and failure of the rocks. Thus fracture has always been an important issue that researchers and engineers deal with considering the safety of the structures, especially man made structures.

Experiments and researches on the phenomenon of fracture could date back to centuries ago. But no quantitative result has been acquired during such early ages. It was the great work of Griffith (1921) that had lead to the onset of modern fracture mechanics. Griffith analyzed the stresses of a cracked plate, which was studied before by Inglis (1913), and applied it to the crack propagation. According to Griffith's theory, the fracture propagates when the change of the strain energy overcomes the material's surface energy. Griffith's theory has shown agreement with data from experiments for brittle materials, but was also considered to be limited to certain brittle materials such as glasses and ceramics. Orowan (1949) modified Griffith's theory to include the influence of plasticity in the energy balance theory. An extension of Griffith's theory had been made by Irwin (1948), who found that plasticity had an indispensible role in ductile materials such as metals, and included a dissipative term to Griffith's energy balance relation, thus applying Griffith approach to metals successfully. Later on, Irwin (1956) put forward the concept of energy release rate in his study of fast crack propagation in high strength steel and aluminum alloys. Another of Irwin's contribution was to have introduced the parameter later known as the stress intensity factor (K), which was related to the energy release rate, and was used to describe the stress conditions and displacements near the crack tip in his analysis of the stress field and strains near the crack tip (Irwin 1957). After the fundamentals of linear elastic fracture mechanics were well established around 1960 (Anderson 2005), researchers had focused more on the influence of materials' plasticity on the fracture analysis. Researchers following this trend also include Irwin, who proposed the plastic zone correction as a further improvement of linear elastic fracture mechanics (Irwin 1961). Rice (1968) introduced the parameter of J integral to describe the plastic characteristics around the crack tip. Later, Rice and Rosengren (1968), Hutchinson (1968) applied the J integral to stress field in nonlinear materials. Mindess et al. (1977) tested and verified the applicability of the J integral to concrete. Shih (1981) studied the relationship between J integral and the crack opening displacement. In recent times, fracture mechanics has become more complete. And with the development of computer technology, more complicated material models have been applied to fracture mechanical analyses. With the help of advancing computing power, the development of numerical models of a microscopic scale has been made possible, which allows researchers to study both the microscopic and

macroscopic fracture behavior easily. It is shown that the boundary of development and application of fracture mechanics has been and will be greatly extended with the help of computer.

Recent fracture mechanical researches have also been extensive. One trend in this research field of both theory and applications is the time-related or time-dependent study on material behavior and parameters, within which lifetime prediction is a comparatively new topic with practical application prospects. The lifetime or time dependent study on solids has been studied by many researchers. By using the empirical Charles power law for the relation between crack propagation velocity and stress intensity factor at the crack tip, Kemeny (1991) modeled subcritical crack growth in rock under compression. The model can predict the dependence of the stress-strain curve on certain applied strain rate and both transient and tertiary creep, which makes a time-to-failure prediction possible. Mishnaevsky (1996) developed a method to determine the time to fracture on the basis of physical mechanisms of microcracks and fractal model of fracture. Based on the dependence of the distribution of the maximum crack lengths on the accrued lifetime, a method was proposed by Ignatovich (1996) to determine the useful lifetime, and the results of prediction of cracks of maximum sizes have been compared with experiments of chromium-nickel alloys. Based on the split tension tests on the saturated granite from Three Gorges Project in China, Sun and Hu (1997) confirmed time dependency of the Three Gorges granite and put forward two criteria for the time-dependent theory of rock strength: the failure criterion of stress and the failure criterion of time. Shao et al. (1999) studied anisotropic damage in granites through numerical modeling. The time dependent microcrack growth can be simulated by the proposed model, and the model's numerical result has been compared with the test data. The time-dependent behavior of tabular excavations in the gold mines in South Africa has been studied by Malan (1999). Elasto-viscoplastic approach has been used for the simulation of the time-dependent stope closure and the numerical results have shown good accordance with the experimental data. Later on, Malan (2002) implemented the developed continuum viscoplastic approach into the finite difference code to investigate the time-dependent closure of stopes and squeezing of tunnels in hard rocks. Aubertin et al. (2000) proposed a multiaxial criterion for short and long term rock strength including time effects, and applied the proposed criterion to the analysis of failure around an underground tunnel. Ritter et al. (2000) studied subcritical crack growth in soda-lime glass under mixed-mode loading. The conclusion that subcritical crack growth rates are much less than those under Mode I loading at the same energy release rates was drawn and possible mechanics for this phenomenon were also discussed. Masuda (2001) studied the time-dependent failure strength of granitic rocks. The effects of water on rock strength have been studied through tests on both

wet and dry samples. Based on the Three Gorges Project in China, Feng et al. (2001) studied the effects of water on compressive strength and microcracking of granite, and confirmed the reduction of the compressive strength on presence of water. They concluded that the pH value has great effect on rock strength. Based on the creep tests and analytical modeling, Maranini and Yamaguchi (2001) studied viscoplastic behavior of granite in triaxial compression and compared the modelling results and test data. Time effects on rock strength and transient creep behavior have been discussed. Miura et al. (2003) proposed a model based on the micromechanics for predicting the creep failure of hard rock, where the time to failure of the proposed model is also studied for different stress and environmental conditions such as water and temperature. Kemeny (2003) has developed a model with the degradation of the joint cohesion of rock dependent on time. Later on, Kemeny (2005) developed a fracture mechanics model in UDEC to simulate the time-dependent failure of rock bridges. Chen et al. (2004) proposed a damage-coupled time-dependent constitutive model and applied it to the stability study of underground caverns. The numerical result has shown good accordance with the field measurements. Chandler (2004) developed a modified PFC model to simulate the time-dependence of the rock strength, and calibrated the model to laboratory time to failure data for Lac du Bonnet granite. Based on strength tests and creep tests on several Japanese rocks including igneous rocks, Shin et al. (2005) studied the relation between variations in strength and creep under dry and wet conditions as well as different loading conditions, and presented the equation describing the time dependency of strength. Lifetime prediction of composite materials under constant and monotonic load has been studied by Guedes (2006). A numerical model has been proposed by Amitrano and Helmstetter (2006) to study the time-dependent damage and deformation of rock under creep. Lei et al. (2006) studied pre-failure damage in rock under stress. Based on simultaneous measurements of time-to-failure energy release, seismic b value etc. accompanying pre-failure damage, they concluded these parameters are functions of the time-to-failure and can be used as indicators of the critical point of damage. As an improvement to the previous model, Golshania et al. (2007) developed a damage model for the simulation of the excavation damaged zone (EDZ) problem in brittle rock. The development of the excavation damaged zone around the opening by time has been studied through a numerical model. Li et al. (2008) studied the time dependence of crack growth in granite under compressive-shear stress state, using parameters of subcritical crack growth obtained by the double torsion constant displacement load relaxation method. A turning point has been located on the curve of crack relative length and crack growth time which describes the boundary between the stable and rapid growth of crack. The conclusion that there is no gradual change from stable to instable crack in granite was drawn. Le et al. (2009) studied the size effect on the lifetime of quasibrittle structures. Damjanac and Fairhurst (2010) found clear

evidence of a long-term strength threshold for silicate crystalline rock under long-duration compression loading, and the laboratory value has been compared with the field result. Jiang et al. (2012) investigated the time-dependent damage of rock mass. A damage viscoelastic-plastic model was developed to describe the time-dependent deterioration of rock mass. Time-dependent rock mechanical properties have been investigated by Eberhardt (1998); Szczepanik et al. (2003); Alehossein and Boland (2004); Lau and Chandler (2004); Jeong et al. (2007). Time-dependent behavior of rocks has been investigated by Cristescu and Hunsche (1998); Fujii et al. (1999); Challamel et al. (2006).

It is clearly noticed that limitations exist in the former researches of lifetime. For instance, the phenomenological approaches are often used to describe the time-related behavior of brittle materials. Time effect on strength or failure criterion is also often considered by former researchers. However, in contrast this study uses explicit fracture mechanics to describe the time-dependent crack growth. The innovations also include simulating specific initial fractures with certain distributions at the micro-scale. The microcrack propagation process is simulated by incorporating the subcritical crack growth theory into the time marching calculations of the numerical code. Thus the real “time” is connected to the crack propagation step wisely in the simulation. This study assumes the lifetime (time to failure) of rocks is dependent on the development of these initial microcracks, which propagate and coalesce under loads, and the macroscopic fractures formed by these microcracks could finally lead to the failure of the rock. This process has been simulated by Konietzky et al. (2009) based on the linear elastic fracture mechanical theory (LEFM) using data from Westerly Granite. As a further development of this research work, this study improved the crack propagation scheme by considering orientation of the initial cracks and including anisotropy into the numerical model. The stress intensity factor calculation has also been modified according to the different crack simulation schemes. The numerical simulations in this study were performed by the 2D Finite Difference Code FLAC (Itasca Consulting Group 2005). Lifetime (time to failure of rocks) prediction schemes have been proposed for each numerical model and analytical results have been compared with the numerical calculations. The factors influencing lifetime have also been investigated through the numerical models. More detailed aspects of the theoretical basis adopted in this study are discussed in the following chapter.

3 Theoretical concepts

The numerical model of this research is based on the linear elastic fracture mechanical theory. The linear elastic fracture mechanics (LEFM) studies the propagation of cracks in a brittle material under load from continuum mechanical point of view. That is, the body contains the crack is considered to be linear elastic as a whole. In this case, plastic behavior near the crack tip is not considered, which makes it necessary to restrict the inelastic region near the crack tip to a negligible size.

The applicability of the continuum mechanical approach is influenced to a large part by the concept of process zone (Gross 2006), which denotes the region near the crack tip. Within the process zone, the microscopic bond breaking process is too complex as to be described by continuum mechanics. So for the continuum mechanics to be applicable, the size of the process zone should be small enough as to be negligible comparing with the size of the crack and the solid body. Continuum mechanics is applicable for metals and brittle materials. The object in this research is brittle rock, so this approach suits our research very well and thus is adopted in the numerical model.

3.1 Griffith energy balance theory and the energy criterion

The energy balance theory and the energy criterion for fracture were proposed by Griffith (1920) based on the earlier work of Inglis (1913). Irwin (1956) further developed the energy criterion approach. The Griffith energy balance theory assumes that the total energy does not change or decreases during the formation or propagation of a crack. We consider an infinitely wide plate under a remote tensile stress σ, with a crack inside of length 2a, as shown in Fig. 3-1.

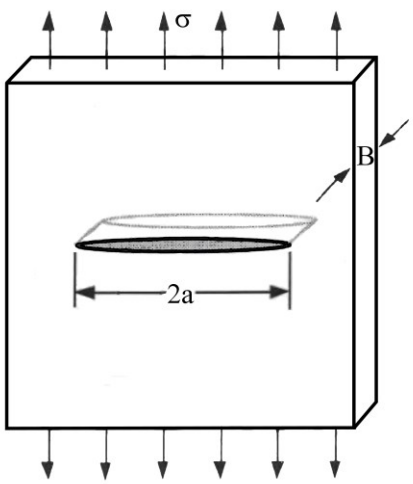

Figure 3-1 An infinitely wide plate subjected to a remote tensile stress

For an increase dA of the crack area, the balance of the energy could be expressed as:

$$\frac{dE}{dA} = \frac{d\Pi}{dA} + \frac{dW_s}{dA} = 0 \tag{3-1}$$

where E denotes the total energy, Π is the potential energy of the internal strain energy and external force and W_s describes the work need for the creation of new surfaces. The components of the expression are describes as:

$$-\frac{d\Pi}{dA} = \frac{\pi\sigma^2 a}{E} \tag{3-2}$$

$$\frac{dW_s}{dA} = 2\gamma_s \tag{3-3}$$

where E is Young's modulus, σ is the remote tensile stress, a is the half crack length. For the infinite plane, the released energy is related to the unit thickness. Thus parameter a denoting the half crack length is used in the equations instead of the parameter A denoting the crack area. γ_s denotes the surface energy. So the energy balance could be further expressed as:

$$\frac{\pi\sigma^2 a}{E} = 2\gamma_s \tag{3-4}$$

Solving the above equation for fracture stress, the following expression is obtained:

$$\sigma_f = \left(\frac{2E\gamma_s}{\pi a}\right)^{1/2} \tag{3-5}$$

Equation (3-2) represents an important parameter first proposed by Griffith (1920), known as the energy release rate G. As can be shown by equation (3-2), the energy release rate describes the potential energy change for an incremental crack surface increase. For the same plate example, the energy release rate is given by:

$$G = \frac{\pi\sigma^2 a}{E} \tag{3-6}$$

The energy criterion can be described as: the fracture occurs if the released energy is enough to overcome the resistance of the material, which includes the surface energy and other energy dissipation related to the crack propagation. To be specific, when

fracture happens, the energy release rate reaches the critical value, known as the critical energy release rate G_c. In the above example shown in Fig. 3-1, the Griffith's energy criterion for fracture is defined by:

$$G = G_c \tag{3-7}$$

and

$$G_c = \frac{\pi \sigma_f^2 a_c}{E} \tag{3-8}$$

where σ_f denotes the failure stress and a_c describes the half crack length. The critical energy release rate G_c could be deemed as the material's resistance to fracture. As compared with the factors in the traditional material strength approach, energy release rate G is the driving force for the fracture while the critical energy release rate G_c is the fracture toughness, which is a material parameter independent of the crack geometry. This feature gives the G parameter a characteristic of global applicability within the same linear elastic material.

3.2 Crack opening modes

Three types of opening modes, or loading types, known as Mode I, Mode II and Mode III are illustrate in Fig. 3-2, respectively, can be distinguished.

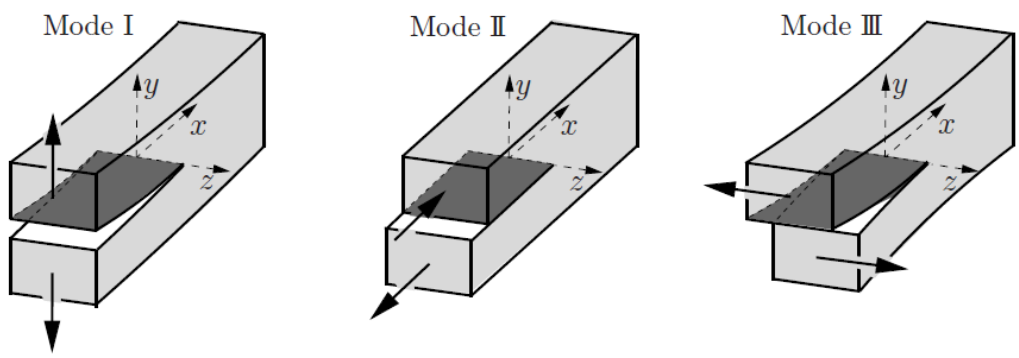

Figure 3-2 Three crack opening modes with corresponding stress conditions (Gross 2006)

According to the coordinate system shown in Fig. 3-2, Mode I describes the crack surfaces separating from each other and the movement is perpendicular to the x-z plane, where the crack tip is subjected to the stress normal to the crack plane. Mode II describes in-plane shear loading mode involving a sliding movement of the crack surfaces. This relative movement is caused by the shear stress within the x-z plane. Mode III describes the out-of-plane shear loading mode involving a relative

movement of the crack surfaces within the x-z plane, as a result by the shear stress in the x-z plane.

In reality, the rock materials are often subjected to more complex stress conditions than any single case of the three basic loading types shown in Fig. 3-2. In such cases, a so called mixed-loading mode is required to describe the real stress situation. The mixed-mode loading is a combination of some or all of these basic modes (Fig. 3-3). For example, a mixed-loading situation of Mode I and Mode II describes the situation of the crack tip being subjected to both normal and shear stresses. Crack under different modes of loading and mixed-mode loading has been studied by many researchers: Erdogan and Sih (1963); Sih (1973, 1974); Ingraffca (1981); Nemat-Nasser and Horii (1983); Watkins and Liu (1985); Ouchterlony (1988); Lam (1989); Hakami and Stephansson (1990); Ashby and Sammis (1990); Kemeny (1991); Davenport and Smith (1993); Shen and Stephansson (1993, 1994); Chen and Wang (1994); Pang (1995); Kong et al. (1995); Baud et al. (1996); Zhu et al. (1997); Lauterbach and Gross (1998); Bobet and Einstein (1998); Ritter et al. (2000); Chang et al. (2002); Backers et al. (2002); Sahouryeh et al. (2002); Rao et al. (2003); Yoon and Jeon (2003); Zhu et al. (2006); Napier and Backers (2006); Ko and Kemeny (2006); Li et al. (2008); Ayatollahi and Aliha (2009); Ayatollahi and Sedighiani (2010); Bhat et al. (2011); Zhou and Yang (2012); Backers and Stephansson (2012).

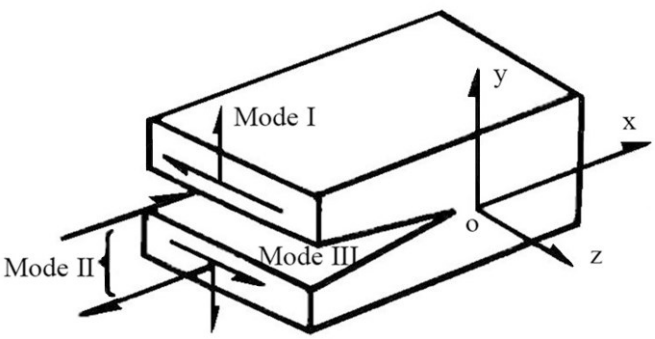

Figure 3-3 Crack under mixed-mode loadings (modified from Li 1988)

3.3 Crack-tip field and stress intensity factor

Stress analysis of the crack tip region is based on the understanding of the different crack opening modes described above. Analysis on the stresses and strains close to a crack tip, also known as crack-tip field (Gross 2006), has its indispensible role in the constitution of linear elastic fracture mechanics. Each of the three different crack opening modes has its own crack-tip field. Consider a two-dimensional problem containing a straight crack, as shown in Fig. 3-4.

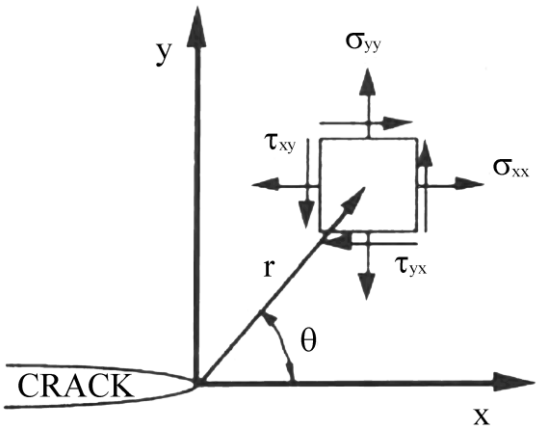

Figure 3-4 Stresses near the crack tip in a two-dimensional problem (modified from Anderson 1995)

With the geometry and stresses depicted in Fig. 3-4, the crack-tip field can be described as, for Mode I:

$$\begin{Bmatrix} \sigma_{xx} \\ \sigma_{yy} \\ \tau_{xy} \end{Bmatrix} = \frac{K_I}{\sqrt{2\pi r}} \cos(\theta/2) \begin{Bmatrix} 1 - \sin(\theta/2)\sin(3\theta/2) \\ 1 + \sin(\theta/2)\sin(3\theta/2) \\ \sin(\theta/2)\sin(3\theta/2) \end{Bmatrix} \tag{3-9}$$

$$\begin{Bmatrix} u \\ v \end{Bmatrix} = \frac{K_I}{2G}\sqrt{\frac{r}{2\pi}}(\kappa - \cos\theta) \begin{Bmatrix} \cos(\theta/2) \\ \sin(\theta/2) \end{Bmatrix} \tag{3-10}$$

For Mode II:

$$\begin{Bmatrix} \sigma_{xx} \\ \sigma_{yy} \\ \tau_{xy} \end{Bmatrix} = \frac{K_{II}}{\sqrt{2\pi r}} \cos(\theta/2) \begin{Bmatrix} -\sin(\theta/2)[2 + \cos(\theta/2)\cos(3\theta/2)] \\ \sin(\theta/2)\cos(\theta/2)\cos(3\theta/2) \\ \cos(\theta/2)[1 - \sin(\theta/2)\sin(3\theta/2)] \end{Bmatrix} \tag{3-11}$$

$$\begin{Bmatrix} u \\ v \end{Bmatrix} = \frac{K_{II}}{2G}\sqrt{\frac{r}{2\pi}} \begin{Bmatrix} \sin(\theta/2)[\kappa + 2 + \cos\theta] \\ \cos(\theta/2)[\kappa - 2 + \cos\theta] \end{Bmatrix} \tag{3-12}$$

where $\sigma_z = \upsilon\,(\sigma_x + \sigma_y)$, $\kappa = 3 - 4\upsilon$ for plane strain and $\sigma_z = 0$, $\kappa = (3 - \upsilon) / (1 + \upsilon)$ for plane stress.

For Mode III:

$$\begin{Bmatrix} \tau_{xz} \\ \tau_{yz} \end{Bmatrix} = \frac{K_{III}}{\sqrt{2\pi r}} \begin{Bmatrix} -\sin(\theta/2) \\ \cos(\theta/2) \end{Bmatrix} \tag{3-13}$$

$$\omega = \frac{2K_{III}}{G}\sqrt{\frac{r}{2\pi}}\sin(\theta/2) \tag{3-14}$$

The factors K_I, K_{II} and K_{III} in these expressions are defined as stress intensity factors. For the straight crack of length 2a, which is subjected to uniaxial remote tensile stress σ, in-plane shear stress τ and out-of-plane shear stress τ', respectively, they are expressed as:

$$K_I = \sigma\sqrt{\pi a} \tag{3-15}$$

$$K_{II} = \tau\sqrt{\pi a} \tag{3-16}$$

and

$$K_{III} = \tau'\sqrt{\pi a} \tag{3-17}$$

The value of stress intensity factor depends on the remote stress and the size of the crack. For each of the crack opening modes, if the K factor is known, the stress distribution and displacements near the crack tip can be solely determined by the above expressions containing corresponding K factors. So the stress intensity factor can be deemed as a parameter describing the stress condition in a cracked linear elastic material. Research works concerning stress intensity factor include: Wilson (1971); Cartweight and Rooke (1974); Rybicki and Kanninen (1977); Waza et al. (1980); Horii and Nemat-Nasser (1983); Huang and Wang (1985); Costin (1985); Ashby and Hallam (1986); Ouchterlony (1988); Hakami and Stephansson (1990); Lim et al. (1993); Fowell (1995); Baud et al. (1996); Khan and Al-Shayea (2000); Guinea et al. (2000); Chao et al. (2001); Chang et al. (2002); Backers et al. (2002); Isaksson and Ståhle (2002); Rao et al. (2003); Yoon and Jeon (2003); Liu and Chao (2003); Zhu et al. (2006); Ko and Kemeny (2006); Morais (2007); Sun and Qian (2009); Kumar et al. (2011); Backers and Stephansson (2012); Ayatollahi and Sedighiani (2012). A more detailed description about the stress intensity factor is discussed in the following section.

3.4 Fracture criterion based on the stress intensity factor

Earlier work of Griffith (1920) has formed a strong basis and essential tool to analyze fracture for the subsequent researchers. While Griffith (1920) and Orowan (1949) studied the material strength and behavior through energy approach, Irwin (1957) proposed a criterion based on the analysis of the stress field around the crack tip. Irwin (1957) had shown that the stress distribution and displacements near the crack

tip could be determined by a single parameter, known as the stress intensity factor. Expressions for different loading modes have been described above. Fracture criteria in linear elastic body have also been discussed by several researchers, including Erdogan and Sih (1963); Sih (1973, 1974); Theocaris and Andrianopoulos (1982); Shen and Stephansson (1994); Ukadgaonker and Awasare (1995).

The stress intensity factor criterion of fracture is based on the assumption that the fracture starts when the stress intensity factor reaches the critical value K_C, also known as fracture toughness, which is a material property. Its specific value can be determined by experiments. Fracture toughness value controls the fracture initiation criterion for corresponding loading mode introduced in the last subsection. For example if the material is subjected to Mode I loading, in which case only K_I value is considered, it fails when $K_I = K_{IC}$. Correspondingly for Mode II, the criterion is $K_{II} = K_{IIC}$ and for Mode III, $K_{III} = K_{IIIC}$. The criterion for a mixed-mode loading condition is more complicated. In this case, a more generalized expression such as $f(K_I, K_I, K_I) = 0$ must be utilized. Expression of such criterion is further discussed in the next chapter.

The logic of stress intensity factor approach lies in the fact that it allows a description of the stress condition and displacements. So the judgment that the material would fail when the stress intensity factor comes to its critical value is based on the stress intensity factor's indication that the stress and strain combination has come to a critical condition. As described above, the stress intensity factor is a local parameter, so it's necessary to study the region near the crack tip where K factor dominates.

Take Mode I crack opening as shown in Fig. 3-2(3) for example. As described above, the K_I factor characterizes the region near the crack tip, which is limited by the radius R in Fig. 3-5. The region where K_I dominates also has its limit inwards. According to Equation 3-9, the stress values would become infinite if r becomes infinitely small, and could not be sustained by any material. That means linear elastic theory could not describe the real stress and displacement situation inside this region. Actually, inelastic deformations happen within the region of radius r_p, and there is an additional zone within the radius of ρ, where de-bonding process at the crack tip is supposed to occur (Gross 2006).

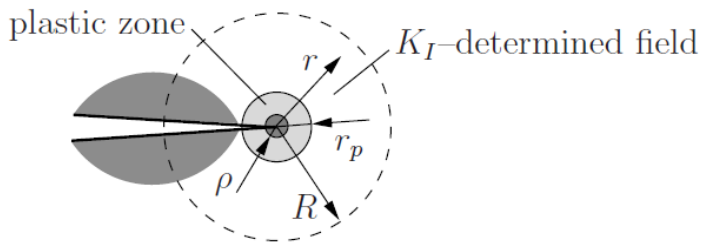

Figure 3-5 K_I-determined field near the crack tip (Gross 2006)

The processes within the inelastic zone is not considered within this study, but assumed to be controlled by the K_I-determined field, thus indirectly characterized by K_I factor. The case applies to Mode II and Mode III as well. So the fracture criterion described above would only apply to the K-determined region. And the stress intensity factor becomes a state variable or a 'loading parameter' (Gross 2006) whose value changes with propagation of crack. The above facts make it necessary that K value be always recalculated and updated with the new crack geometry and stress conditions during crack propagation process when using this crack criterion, which is the case in this research.

3.5 Stress intensity factor and Griffith's energy release rate

In Irwin's work (Irwin 1957), the relationship between the local parameter stress intensity factor K and global energy parameter, Griffith's energy release rate G, had also been given:

$$G_I = \frac{K_I^2}{E'} \tag{3-18}$$

$$G_{II} = \frac{K_{II}^2}{E'} \tag{3-19}$$

$$G_{III} = \frac{K_{III}^2}{2\mu} \tag{3-20}$$

where E' = E for plane stress condition and E' = E / (1 - υ^2) for plane strain condition. G_I, G_{II} and G_{III} are the energy release rates in Mode I, Mode II and Mode III conditions, respectively. μ is the shear modulus:

$$\mu = \frac{E}{2(1+\upsilon)} \tag{3-21}$$

Energy release rates are scalar quantities, so they are additive for mixed-mode loading conditions. For example, for a material subjected to all three loading modes the energy release rate becomes:

$$G = \frac{K_I^2}{E'} + \frac{K_{II}^2}{E'} + \frac{K_{III}^2}{2\mu} \tag{3-22}$$

Although the relationship between K and G is unique, the difference between these two factors is obvious. The energy release is a global behavior parameter that describes the potential energy change in the process of crack propagation. The stress intensity factor as a local parameter describes the stress distribution and displacements in the crack tip region.

3.6 Subcritical crack growth

It was assumed by the classical fracture mechanics that in a linear elastic material, the crack will propagate ultrasonically when the stress intensity factor K reached the fracture toughness K_C. Otherwise the crack will remain stable. The critical stress intensity factor approach has long been applied to predict catastrophic crack propagation in brittle materials. However, the classical fracture mechanics could not hold for the long-term constant loading condition, where crack propagates at certain velocity when stress intensity factor is lower than the critical value K_C. This phenomenon is called subcritical crack growth, which was first found in materials such as glasses and ceramics, and later in rocks and minerals (Atkinson 1982, 1984). Charles and Hillig (1962) proposed that stress-corrosion could be the mechanism for the fatigue phenomenon in silicate glass, where propagation of crack was observed when the loads were less than the critical value for the fast fracture propagation. Wiederhorn (1967) studied static fatigue of glass using a new experimental approach and related the measured crack velocity with stress and water vapor concentration. Later on, Wiederhorn and Bloz (1970) studied stress corrosion cracking of six glasses using fracture mechanical techniques, and concluded that the chemical reaction between the glass and water could be the reason for the stress corrosion of glass. The effect of water on subcritical crack growth in silicate rocks has been investigated by Waza et al. (1980). Swanson (1985) studied subcritical fracture propagation in Westerly granite. Kemeny (1991) modeled time dependency in rock deformation under compression considering cracks inside the elastic body growing due to subcritical crack growth. Yoshida and Horii (1992) proposed an analytical model of microcrack growth under compression on the basis of micromechanics to study the creep behavior of rock. Dill et al. (1997) investigated subcritical crack growth behavior of borosilicate glass under cyclic loads. Mechanical fatigue effect was found at low growth rates in both moist and dry environments. Ritter et al. (2000) studied

subcritical crack growth in soda-lime glass under mixed-mode loading. Aubertin et al. (2000) proposed the damage initiation threshold (DIT) of rocks and introduced it into the subcritical crack growth theory. Kemeny (2003) developed a fracture mechanical model using subcritical crack growth to simulate degradation of joint cohesion in brittle fractured rock. Miura et al. (2003) developed a micromechanical-based model for predicting the creep failure of hard rock under compression. Liu (2003) proposed to explain rock burst mechanisms by considering time dependency of sub-critical crack growth in brittle rock under compression. Lau and Chandler (2004) developed laboratory test techniques and used the test data for the calibration of Itasca's PFC stress-corrosion model. Dependence of subcritical crack growth on anisotropy, grain size and environment has been investigated by Nara et al. (2004). The dependence of subcritical crack growth on water vapor pressure was studied by Nara and Kaneko (2004) using double torsion test. Subcritical crack growth in andesite was investigated by Nara and Kaneko (2005) using the double torsion test. The effects of water on subcritical crack growth have also been discussed. Kemeny (2005) modeled the time dependence of the rock bridge failure process using subcritical crack growth. Cao et al. (2006) analyzed the behavior of subcritical crack growth for different rocks. Nara and Kaneko (2006) studied the subcritical crack growth in granite using the double torsion test. Yuan et al. (2006) applied double torsion specimens to study the subcritical crack growth of flabby and intricate ore rock. Nara et al. (2006) studied the relation between subcritical crack growth behavior and crack paths in granite. Li et al. (2008) presented the curves of crack relative length and crack growth time of granite under compressive stresses according to subcritical crack growth parameters. Rinne (2008) modeled time-dependent failure in brittle rock based on subcritical crack growth approach. Ciccotti (2009) reviewed the researches of the mechanisms of subcritical crack growth in silicate glasses. Le et al. (2009) studied the consequences of subcritical crack growth law for the lifetime statistics of quasibrittle structures. Damjanac and Fairhurst (2010) have done numerical analysis on the effect of fracture toughness decrease due to stress corrosion of a crystalline rock.

The mechanisms having been proposed which could cause subcritical crack growth include stress corrosion, dissolution, diffusion, ion-exchange and micro plasticity (Atkinson 1984). Specific environmental and material conditions decide which of the possible mechanism is dominant. Subcritical crack growth could be further described by the relationship between local stress intensity factor K and corresponding crack propagation speed v, as shown in Fig. 3-6.

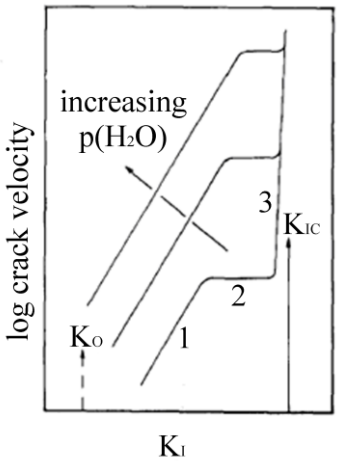

Figure 3-6 Schematic stress intensity factor/crack velocity diagram for tensile crack growth (Atkinson 1987)

The main mechanism in region 1 of the curve is the stress corrosion, which is a process of weakening in bond structure caused by certain chemical reaction (Anderson and Grew 1977). The stress corrosion theory postulates that for crystalline silicates and for silicate glasses the strained Si-O bonds at crack tips can react more readily with the environmental agents than unstrained bonds because of a strain-induced reduction in the overlap of atomic orbitals (Michalske and Freiman in Atkinson 1987). For silicate rocks, the strained Si-O bonds will produce a weakened state during the reaction with the environmental agent. Based on the expression for silicate glasses and quartz, with water as an environmental corrosive agent, the chemical reaction could be described as (Scholz 1972; Martin 1972; Atkinson 1979, Atkinson and Meredith 1987):

$$[\equiv Si - O - Si \equiv] + H_2O = 2[\equiv Si - OH] \tag{3-23}$$

In basic environment, the chemical reaction in silica glasses could be described as (Charles 1958):

$$\equiv Si - O - Si \equiv + OH^- = Si - O^- + \equiv Si - OH \tag{3-24}$$

The second part of the *K-v* curve is also caused by stress corrosion. The speed is controlled by the rate of transport of reactive species to crack tips. Crack propagation in region 3 is mainly controlled by thermally activated process and it is relatively insensitive to the chemical environment (Atkinson 1982, Freiman 1984 in Atkinson 1987). It is shown in the *K-v* curve that there exists an upper bound of K_{IC} value (K_C value in general cases). When this critical stress intensity factor value K_C is reached, the crack propagation speed reaches ultrasonic speed (Konietzky et al. 2009). Theoretically there also exists a lower threshold value K_O below which no crack

propagation could be observed in practice. A stress corrosion limit has been observed in soda-lime silicate and borosilicate glasses, but it is not yet clear whether in fact all materials behave in this way (Freiman 1984). Experiments have certainly not yet confirmed the existence of a stress corrosion limit in ceramics or rocks (Atkinson 1984). It is assumed that K_O value is about 10 ~ 20 % of K_C. However, whether this stress corrosion limit K_O exists in rocks is not confirmed (Atkinson in Rinne 2008).

3.7 Charles equation

In Charles' study on delayed failure problem of glass (Charles 1958), the relationship describing the crack velocity was derived by assuming the corrosion rate to conform to an arbitrary power function of stress:

$$v = k^{'}(\sigma_m)^n + k \tag{3-25}$$

where k' and n are constants , σ_m is the tensile stress at the crack tip and k is the corrosion rate of the material under zero stress.

The above expression was further developed for stress-activated corrosion assuming the temperature dependence of the crack growth process is an Arrhenious one. The relationship is:

$$v = C(x / x_{cr})^{n/2} e^{-A/RT} \tag{3-26}$$

where C is a constant, x and x_{cr} are flaw depth and critical flaw depth respectively, A is the activation energy term and R is a gas constant (Boltzmann constant).

The Charles equation is often referred to with the form where stress intensity factor is involved:

$$v = v_0 K^n \exp\left(\frac{-u}{RT}\right) \tag{3-27}$$

where v_0 is a material constant, K is the stress intensity factor, n is the stress corrosion index, T is the absolute temperature and R is the gas constant.

There have been many attempts to characterize the K-v curve by means of the stress corrosion process. Charles equation described above is one of the most acknowledged expressions to describe the stress corrosion data. With respect to the life time study in this research, a general relation between the natural logarithm of life time t and load σ

for brittle solids has been given in Fig. 3-7. The linear part of the curve can also be explained by Charles equation.

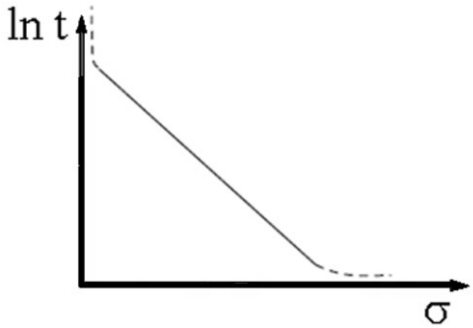

Figure 3-7 General relation between life time and load for brittle solids (Konietzky et al. 2009)

3.8 Lab and field results

In this study, it is assumed the failure of the model is caused by macroscopic fractures formed by the coalescence of microcracks, rather than caused by any single crack's propagation through the model. The assumption is that under load, the initial microcracks grow simultaneously based on the subcritical crack growth (their distinct propagation velocity is controlled by Charles equation). When the coalescence of microcracks has reached a critical level (e.g. coalesced area penetrating the model), failure is considered to happen in the model. This simulation idea is supported by the observation of laboratory tests (Fortin et al. 2011, Mayr et al. 2011, Yang et al. 2012, Yoon et al. 2012, Zietlow and Labuz 1998). Exemplary, Fig. 3-8 shows acoustic emission (AE) locations observed during laboratory tests of red sandstone under compressive load. It is seen in Fig. 3-8 that the acoustic emission locations (considered to be identical to growing micro-cracks) were more concentrated at an inclined plane, which coincides with the position of the shear plane observed in the laboratory test. Nevertheless, growth of micro-cracks is observed within the whole sample. The structure of the rock at the grain size level determines location, size and orientation of the micro-cracks. Also, the structure at grain size level is responsible for temporary crack arrest. For the rock specimen under tension, the macroscopic fracture is observed perpendicular to the direction of major tensile load (Fig. 3-9). The concentration of the acoustic emission locations also shows agreement with the macroscopic fracture in the test (Fig. 3-10). But even in this case, additional local micro-crack growth is observed in areas far away from the final macroscopic fracture. These observations support the proposed modeling idea described within this thesis.

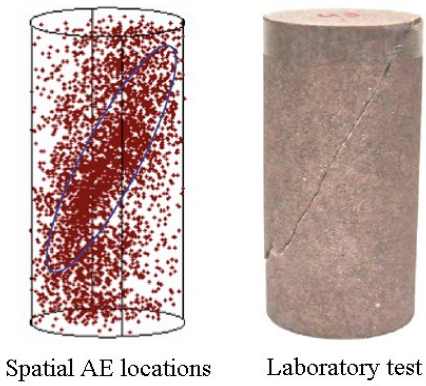

Figure 3-8 Spatial acoustic emission (AE) locations and experimental failure of red sandstone at a confining pressure of 35 MPa (Yang et al. 2012)

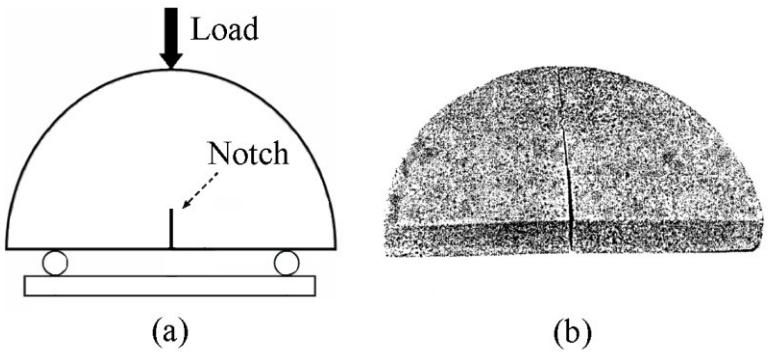

Figure 3-9 Three-point bending test on semi-circular rock specimen (a) experimental set-up; (b) fracture pattern of Johnstone in the three point bending test (Ayatollahi and Aliha 2007)

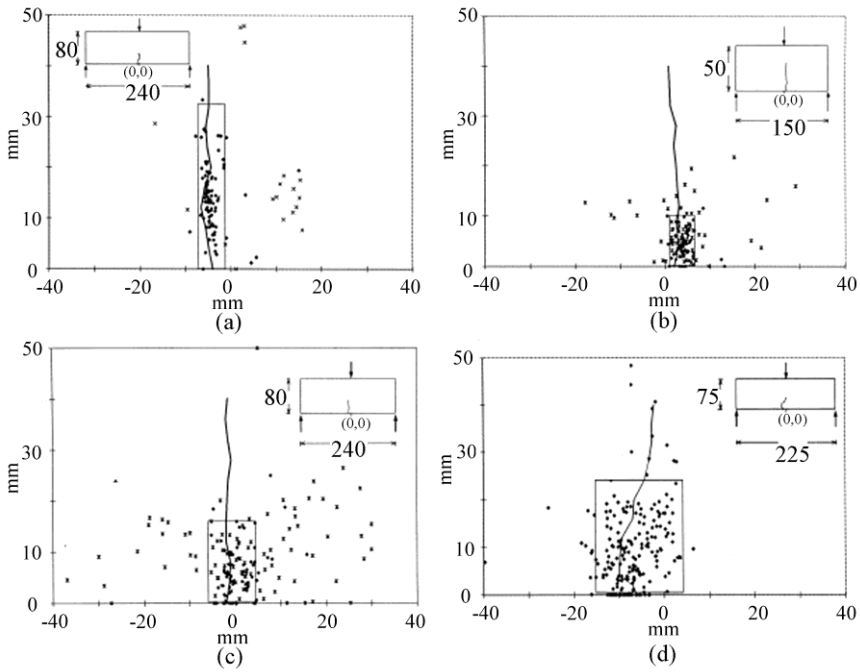

Figure 3-10 Acoustic emission (AE) locations and final macroscopic fracture pattern in the three-point bending test (a) Berea sandstone; (b) Sioux quartzite; (c) Charcoal granite; (d) Rockville granite (Zietlow and Labuz 1998)

3.9 Life time prediction idea

In this study, the life time prediction is done with numerical models based on subcritical growth using Charles equation. The numerical model is divided by zones and it is assumed that each zone contains a microcrack. One can get a rough idea about the approximate life time of a zone t_{zone} by integration over the crack length (Konietzky et al. 2009):

$$t_{zone} = \int_{a_o}^{a_c} \frac{da}{v} \tag{3-28}$$

where the initial crack length is given by a_o and the critical crack length is given by a_c, which is deduced by either the fracture toughness or the zone edge length. The crack propagation velocity v is obtained from Charles equation as expressed in Equation 3-27. Life time prediction schemes are discussed in detail in the next Chapter.

4 Numerical cellular automate for lifetime prediction

The modeling and calculations in this study are done with the ITASCA code FLAC (Itasca Consulting Group 2005). In this chapter, an introduction to the basic model is first given. Following that the realization of life time counting scheme and the technique of a changeable time step scheme are explained. Four new numerical model schemes are proposed including their properties. The calculation schemes are introduced and the corresponding calculation results are analyzed. Influences of particular parameters and properties on the calculation result are also investigated.

4.1 Basic model

4.1.1 Model idea

(1) Realization of real time counting in FLAC

FLAC (Itasca Consulting Group 2005) performs a static analysis by default. The calculation procedure takes into account the displacement and stress state after each step while not after certain time. Because life time prediction is the focus of this study, a certain period of time (time step) is attached additionally to each calculation step. The time step values are recorded during calculation and added up. The lifetime is reached when the model reaches its macroscopic failure stage. Through crack propagation velocity obtained from Charles equation, the time step controls the crack propagation length in each zone for each step, and the crack length in turn defines the mechanical status of the zone, which influences the stress field of nearby zones if failure happens. So the realization of lifetime counting is dependent on the simulation of propagation of individual crack inside each zone of the model.

(2) Microscopic crack propagation and calculation cycle

The numerical calculation scheme is designed in such a way that each zone inside the model contains an initial crack with its length and orientation following certain probability distributions. For each calculation step, the following procedures are executed within each zone: the stresses of the zone are first calculated using Mohr-Coulomb constitutive law; if this zone has already been breached (failed) in the last step, the calculation cycle jumps to the end and goes on to the next zone. Otherwise, the stresses on the crack are calculated and the stress intensity factor is obtained according to the current crack propagation condition; whether the zone is failed or not is then determined by examining if the current crack length has reached the zone's dimension or the crack's fracture toughness has been reached. If the zone has failed by either or both of these criterions, post failure regime is then applied to this zone and the calculation cycle for this zone jumps to the end and goes on to the next zone. Otherwise the new crack propagation velocity is obtained according to the Charles equation; by multiplying the current velocity and the time span (time step) assigned to

the step, and adding the previous crack length, the new crack length is obtained. Thus, both the stress condition and crack propagation condition is "updated" for this zone and ready for the next calculation step. This calculation cycle iterates itself through all the zones within each calculation step. The flow chart for the calculation cycle is shown in Fig. 4-1.

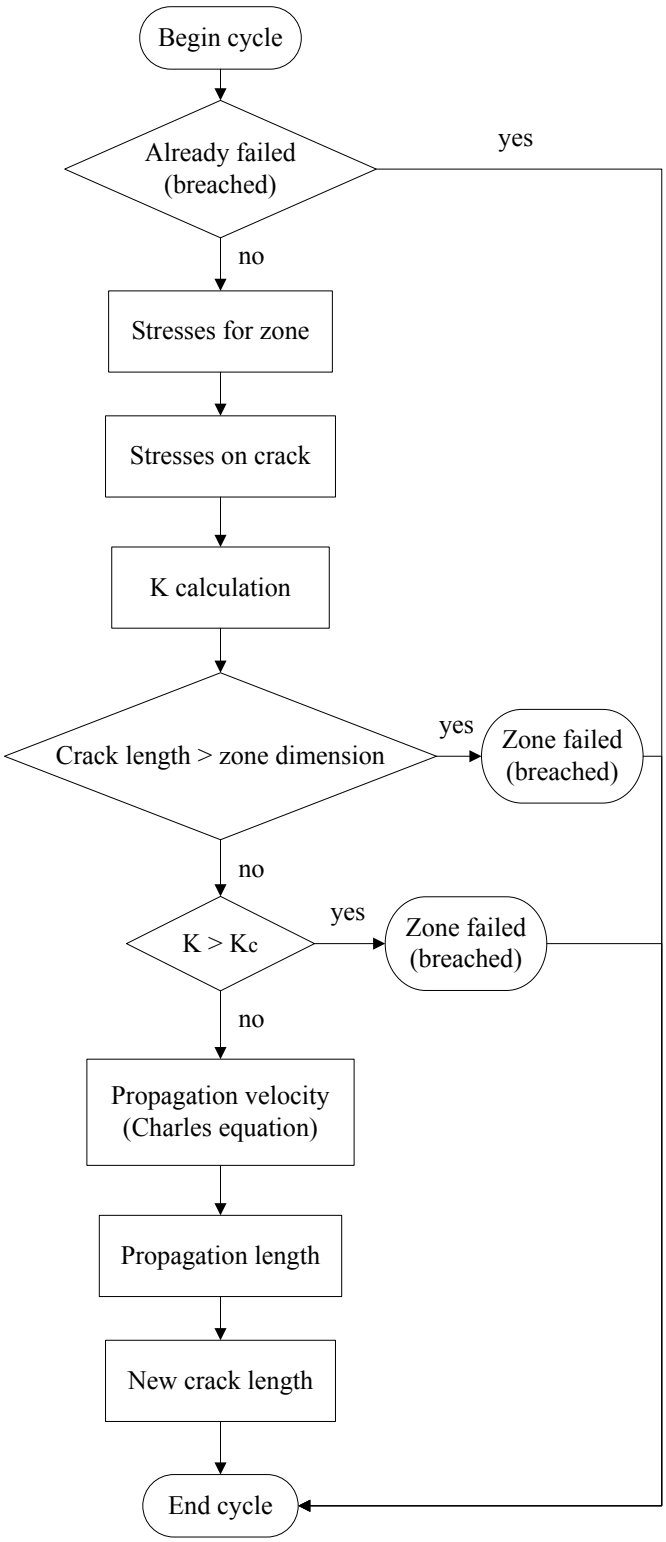

Figure 4-1 Flow chart for one calculation cycle in a zone

(3) Macroscopic fracture simulation

The macroscopic fractures of the numerical models are represented by the coalescence of failed zones. The macroscopic fracturing process is explained using a zoomed in area of the numerical model (Fig. 4-2) as an example. In this example, the orientation of the initial microcrack inside each zone follow uniform distribution, and the microcrack propagates along its original orientation. The difference of the crack conditions inside one zone before and after its failure is clearly seen from the crack illustration. The calculation cycle of each zone is as introduced in the former section.

It is shown in Fig.4-2 (left), at an earlier calculation step (time), no zone in this area has failed. At a later calculation step, as shown in the middle of Fig. 4-2, some zones have failed. After one zone fails by either the crack length reaching the zone's dimension or the crack's fracture toughness being reached, the post failure regime is applied to this zone by assigning residual strength values to this zone, which is illustrated by gray zones in Fig. 4-2. Stress redistributions in the whole model are caused by the failed zones. The zones in the vicinity of the failed zones are more influenced by the stress redistributions. It is seen in Fig. 4-2 (right), at an even later calculation step, more zones have failed in the vicinity of the already failed zones. These failed zones coalesce and form the macroscopic fracture for the whole model. The calculations continue until macroscopic fractures (formed by failed zones) penetrate the model. Then the whole model is considered to be failed. The accumulation of time spans from all the calculation steps is then recorded as the lifetime of the model.

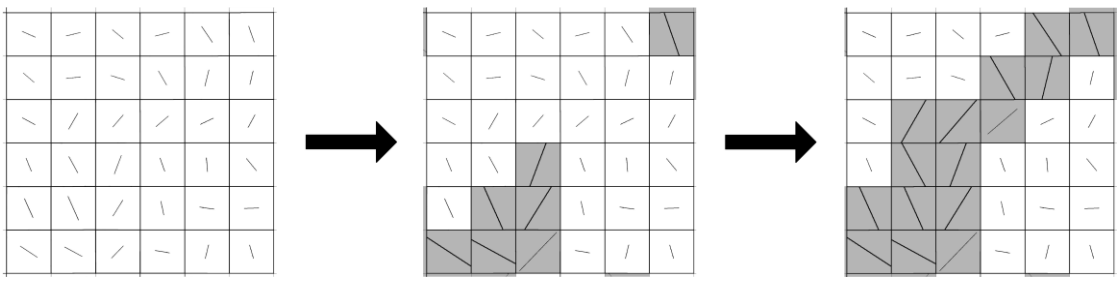

Figure 4-2 The macroscopic fracturing process (zones in gray: failed zones)

4.1.2 Application

Life time prediction studies on rocks with two dimensional numerical models have been performed by Konietzky et al. (2009) with the model idea described above. The 2D numerical simulations were done using FLAC with the extensive use of its internal program language FISH (Itasca Consulting Group 2005). These simulations do not consider crack orientation. It is always assumed, that the crack orientation is the most critical one (Konietzky et al. 2009). Data from Westerly Granite were used for simulation of uniaxial compression and tensile tests. Table 4-1 shows the material

parameters used in the numerical model. In this study, the fracture toughness under Mode I and II has been given the same value for the convenience of comparison between the numerical results under these loading modes.

Table 4-1 Material parameters (Konietzky et al. 2009)

Young's modulus	73.8 GPa
Poisson's ratio	0.22
Bulk modulus	43.9 GPa
Shear modulus	30.2 GPa
Density	2700 kg / m^3
Initial cohesion	45 MPa
Initial friction angle	30°
Initial tensile strength	15 MPa
Residual cohesion	0
Residual friction angle	30°
Residual tensile strength	0
Stress corrosion index n	33.7234
Fracture toughness K_{IC}	1.79 MPa-$m^{1/2}$
Fracture toughness K_{IIC}	1.79 MPa-$m^{1/2}$
Fracture growth constant C	8.8552×10^{-214} m s^{-1} (Pa-$m^{1/2}$)$^{-n}$

A square shaped model with a size of 2×2 m^2 was used for the simulation. The model was divided by a 50 by 50 element mesh, with each element containing an initial crack. A constant tensile load of 12 MPa was applied in model A, B and C in the uniaxial tensile tests, and constant compressive load of the same magnitude in A', B' and C' in the uniaxial compressive tests. The initial crack lengths of the models follow normal distribution with a mean value of 0.013 m and a standard deviation of 0.0001 m (Fig. 4-3). The only difference between these models is the different realization for the initial crack lengths. Studies on the different model sets are described in the following subsections.

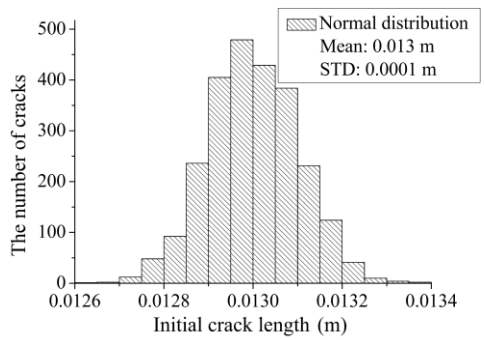

(a) model A

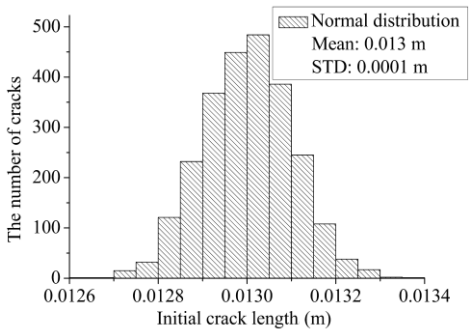

(b) model B

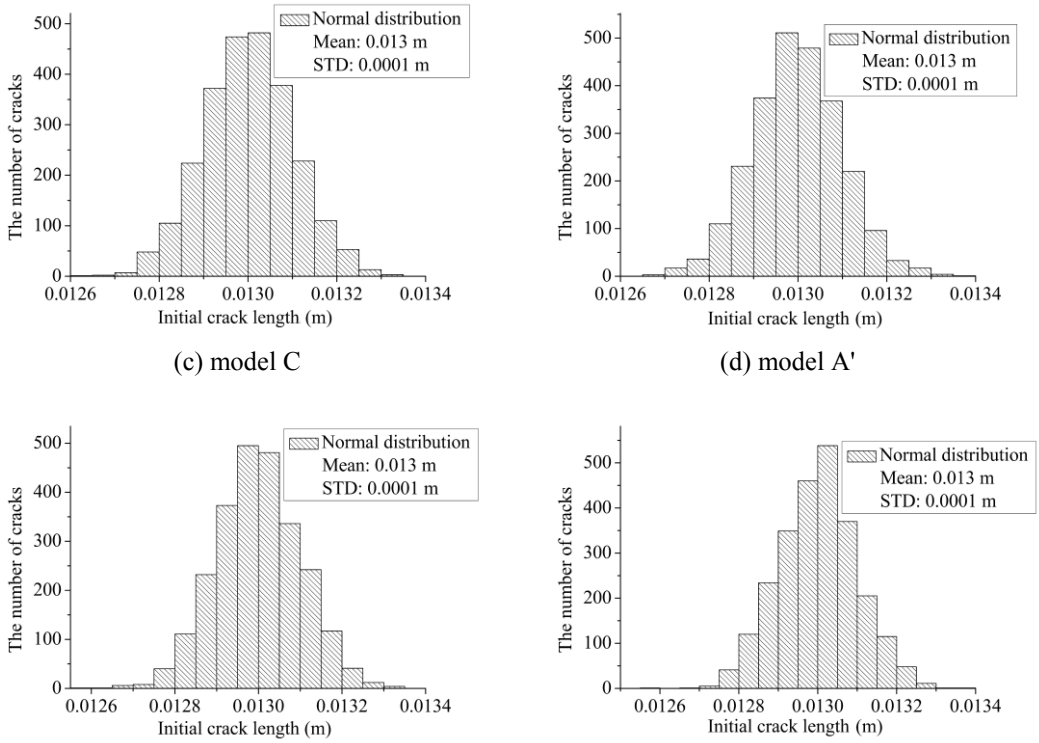

(c) model C (d) model A'

(e) model B' (f) model C'

Figure 4-3 Initial crack length distributions of the models

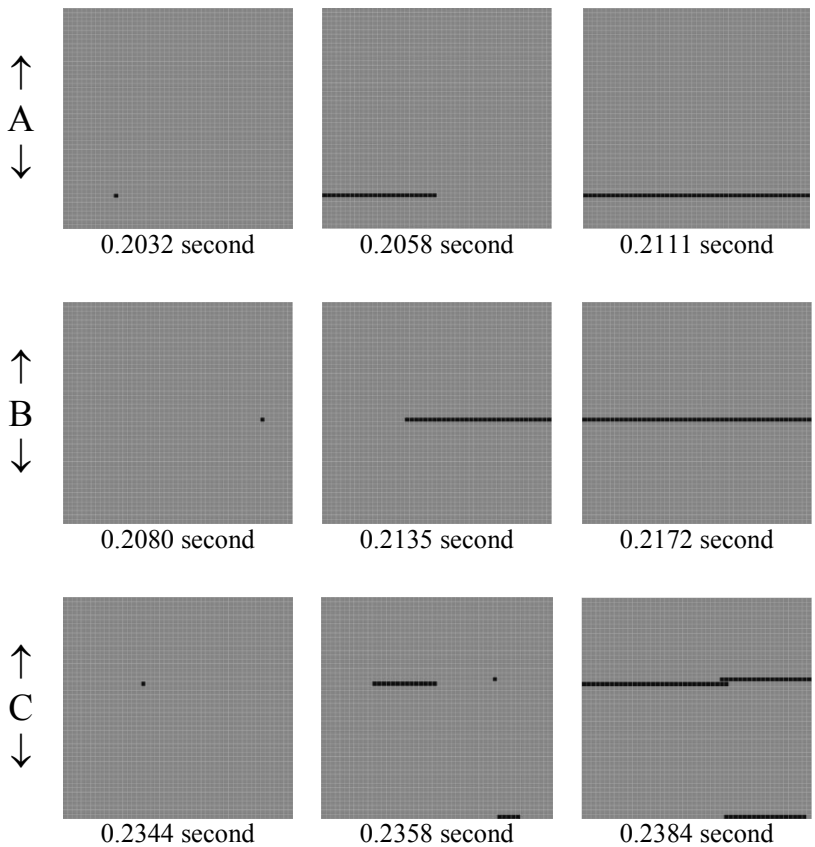

Figure 4-4 Uniaxial tensile test of model A, B and C under tensile load of 12 MPa (Initial crack lengths: normal distribution, mean = 0.013 m, standard deviation = 0.0001 m) (Konietzky et al. 2009)

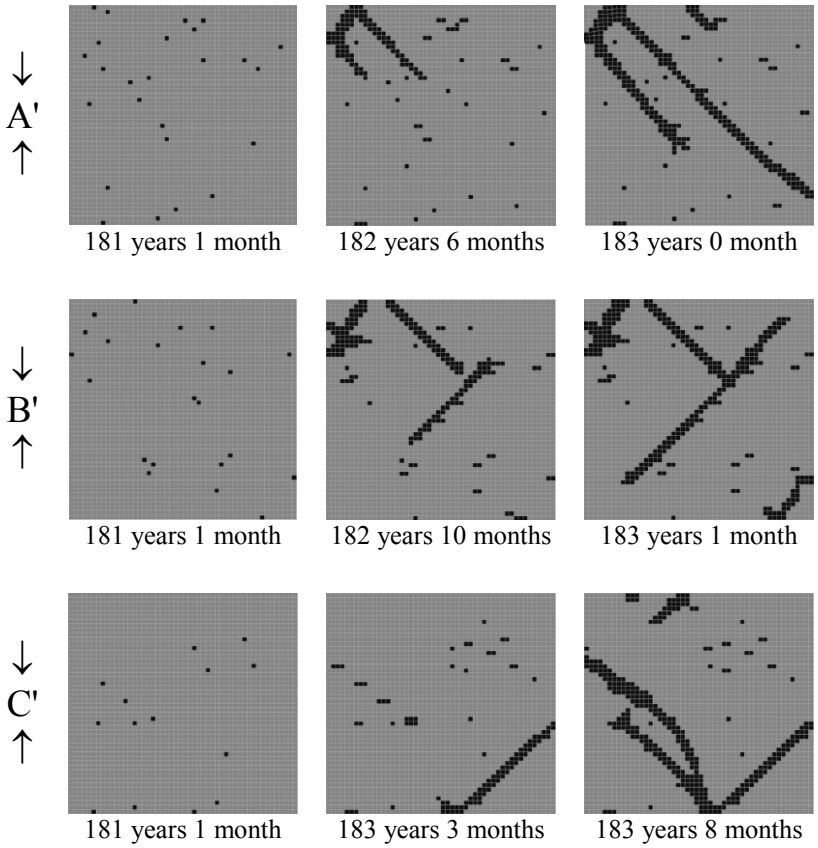

Figure 4-5 Uniaxial compressive test of model A, B and C under compressive load of 12 MPa (Initial crack lengths: normal distribution, mean = 0.013 m, standard deviation = 0.0001 m) (Konietzky et al. 2009)

The predicted life times for the tensile tests are: model A: 0.2111 seconds, model B: 0.2172 seconds and model C: 0.2384 seconds. The results for the compressive tests are respectively: model A': 183 years, model B': 183 years and 1 month, and model C': 183 years and 8 months (Konietzky et al. 2009). The macroscopic fracture patterns of models in tensile tests and compressive tests are shown in Fig. 4-4 and Fig. 4-5, respectively.

4.2 Time-dependent studies

4.2.1 The lifetime prediction scheme and results (single zone)

Consider a rock structure simulated by a single zone model with constant loadings. The idea of predicting life time of this single zone model can be explained by integration over the crack propagation length (Konietzky et al. 2009):

$$t_{zone} = \int_{a_o}^{a_c} \frac{da}{v} \tag{4-1}$$

where a_o and a_c denote the initial crack length and critical crack length of the zone respectively. Letting $C = v_0 \exp(-\mu / (RT))$ as a rock-specific parameter, Charles equation (Eq. 3-27) could be simplified into Eq. 4-2. If only crack opening Mode I and Mode II are considered, Eq. 4-1 can be rewritten in terms of stress intensities (Eq. 4-3):

$$v = CK^n \tag{4-2}$$

$$t_{zone} = \int_{a_o}^{a_c} \frac{da}{CK^n} = \int_{a_o}^{a_c} \frac{da}{CK_I^n + CK_{II}^n} \tag{4-3}$$

In the basic model, the stress intensity factors are expressed as:

$$K_I = \sigma_M \sqrt{\pi a} \tag{4-4}$$

$$K_{II} = \tau_M \sqrt{\pi a} \tag{4-5}$$

σ_M and τ_M are the maximal tensile stress and maximal shear stress within the zone. If the maximal tensile stress σ_M is minus, a compressive stress is applied on the crack. In this case a zero is given to σ_M instead and only K_{II} contributes to the crack propagation velocity.

Substituting Eq. 4-4 and Eq. 4-5 into Eq. 4-3, the lifetime of the zone is calculated:

$$t_{zone} = \frac{\sqrt{(2/\pi)^n}\left(a_c^{1-n/2} - a_0^{1-n/2}\right)}{C(1-n/2)\left(\sigma_M^n + \tau_M^n\right)} \tag{4-6}$$

The critical crack length a_c is determined by the minimum of these three values: the critical length calculated by K_{IC} and K_{IIC} and the dimension of the zone d_{zone}. It can be described as:

$$a_c = \min\left\{\frac{2}{\pi}\left(\frac{K_{IC}}{\sigma_M}\right)^2, \frac{2}{\pi}\left(\frac{K_{IIC}}{\tau_M}\right)^2, d_{zone}\right\} \tag{4-7}$$

In this study, the d_{zone} is expressed as:

$$d_{zone} = 2\sqrt{\frac{S}{\pi}} \tag{4-8}$$

where S is the area of the zone. When a_c is determined and substituted into Eq. 4-6, the predicted life time for this single zone model (t_{zone}) is obtained.

The life time prediction idea has been applied and verified in the code. A square shaped single zone model with the size of 0.04 × 0.04 m^2 (the same size as a single zone in the multi-zone basic model in this study) was used in the tests. The material parameters follow Table 4-1. To verify the calculation results, a comparison has been made between the numerical calculation and the analytical solution (Table 4-2).

Table 4-2 Calculation results for uniaxial tests (initial crack length: 0.013 m)

Uniaxial tensile stress: 6 MPa			
	Analytical solution	**Numerical calculation**	**Error**
K_I	1.5976e6	1.5976e6	< 0.006 %
K_{II}	7.9880e5	7.9881e5	0.001 %
Critical crack length (m)	0.0451	0.0451	0.002 %
Life time	240 y, 56 d, 3 h, 59 min.	240 y, 130 d, 2 h, 3 min.	0.08 %
Failure mode	Crack length > zone size	Crack length > zone size	0
Uniaxial tensile stress: 12 MPa			
	Analytical solution	**Numerical calculation**	**Error**
K_I	1.7900e6	1.7900e6	< 0.005 %
K_{II}	8.9500e5	8.9502e5	0.002 %
Critical crack length (m)	1.4165e-2	1.4166e-2	0.007 %
Life time	0.3972 s	0.3976 s	0.1 %
Failure mode	$K_I \geq K_{IC}$	$K_I \geq K_{IC}$	0
Uniaxial compressive stress: 12 MPa			
	Analytical solution	**Numerical calculation**	**Error**
K_I	0	0	0
K_{II}	1.5976e6	1.5976e6	< 0.006 %
Critical crack length (m)	0.0451	0.0451	0.002 %
Life time	240 y, 56 d, 3 h, 59 min.	240 y, 130 d, 2 h, 3 min.	0.08 %
Failure mode	Crack length > zone size	Crack length > zone size	0

It can be seen from Table 4-2 that the numerical calculation has shown great accordance with the analytical solution. The numerical calculation has predicted a slightly longer life time than the analytical solution for both uniaxial tensile and compressive tests, but the error is negligible as compared to the magnitude of the life time. For the compressive test, a compressive load of 12 MPa renders 6 MPa of the maximum shear stress in a zone, which has the same magnitude as the maximum tensile stress of the zone in the tensile test. No tensile stress is caused in this

compressive case. For the tensile test, both tensile and shear stress are caused, but the crack propagation velocity caused by the maximum shear stress is negligible to that caused by the maximum tensile stress. So for this stress configuration, the predicted life time in the tensile test is the same as the compressive test. The life time prediction idea for the single zone model is applied in multi-zone models for the life time study of more complicated cases, which is included in the following subsections.

4.2.2 Time step study on multi-zone models

The life time prediction scheme is applied to the multi-zone models. The program is designed in such a way that the scheme is carried out for every zone of the model. The critical crack length a_c and predicted life time t_{zone} for each zone is obtained. The lifetime prediction scheme requires that the external stresses should be constant. So it is only possible to predict the life time of the zone which would be the first to fail within the model. After that, the stress conditions for other zones will change because of the elasto-plastic stress redistributions.

In view of this situation, the minimum t_{zone} value is identified as the life time of the "most critical zone", which would clearly be the first to reach failure within the model. The life time of this "most critical zone" (also referred to "the first zone failure time" or "first failure time" in this study) could serve as a reference when choosing the time step value. When the life time of "the most critical zone" is determined, the upper boundary of all possible time steps is defined (the time step should at least be smaller than the life time of "the most critical zone"; also sufficient steps should be carried out before that zone fails). Tests have been made to determine the appropriate time step.

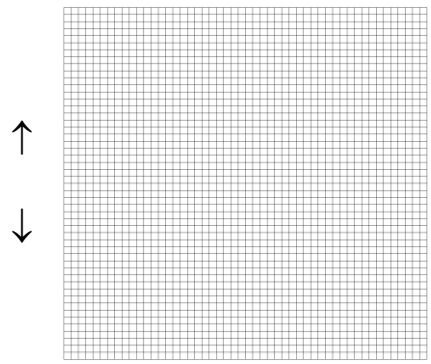

Figure 4-6 Geometry of model A

The uniaxial tensile test is first studied. Model A of Subsection 4.1.2 is used with the model parameters taken from Table 4-1. The geometry of the numerical model is shown in Fig. 4-6. The initial crack lengths of model A follow normal distribution, as is shown in Fig. 4-3 (a). As the life time and failing span of model A are too small for

analysis with tensile stress of 12 MPa, the tensile loading has been changed to 6 MPa, but the other parameters remain unchanged. Using the scheme described above, the "most critical zone" is determined as Zone (12, 8), which is the intersecting zone of 12th vertical line of zones from the left and the 8th horizontal line of zones from the bottom. The analytical life time prediction of this zone is 4,801,063,122 seconds (about 152 years 87 days 20 hours 38 minutes). Therefore, for the numerical calculation, the time step should at least be smaller than this value. With this analytical solution, different time steps have been tried for the uniaxial tensile tests. All the numerical results also showed that the first failure happened in Zone (12, 8). The model's macroscopic failure pattern predicted with different time steps are shown in Fig. 4-7. It is seen that macroscopic fractures have formed with direction perpendicular to the applied tensile load (Fig. 4-7). With a time step equal to or bigger than 15 days, multiple macroscopic tensile fractures have formed in the model, while single tensile fracture formed if the time step is smaller than this value. The predicted first zone failure time has certain differences with the analytical result (Eq. 4-3), and the extent of the difference depends on the value of time step. It can be seen from Table 4-3 and Fig. 4-8 that the first zone failure time descreases and approaches the analytical value when the time step becomes smaller. Coinciding time steps ranging from 1 year to 6 hours, the error of the numerical result of first zone failure time drops from 3.78 % to 0.004 % of the analytical result of 4,801,063,122 seconds (about 152 years 87 days 20 hours 38 minutes).

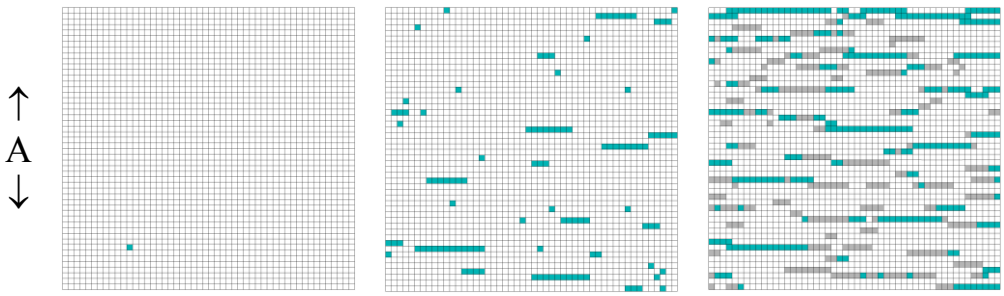

4.9827e9 (s) 6.0234e9 (s) 7.2217e9 (s)

Timestep: 1 year
Lifetime: 229 years

(a)

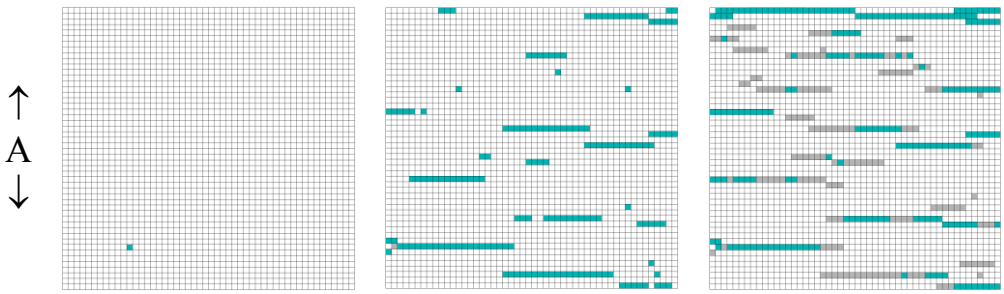

4.9038e9 (s) 5.9130e9 (s) 6.9064e9 (s)

Timestep: 182 days 12 hours
Lifetime: 219 years

(b)

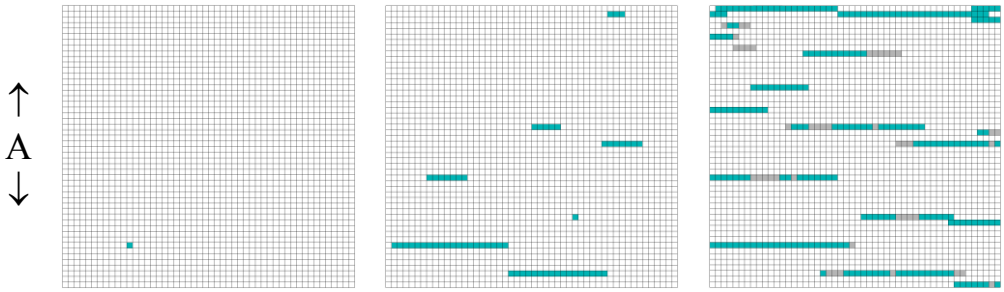

4.8522e9 (s) 5.3577e9 (s) 6.2364e9 (s)

Timestep: 90 days
Lifetime: 197 years 275 days

(c)

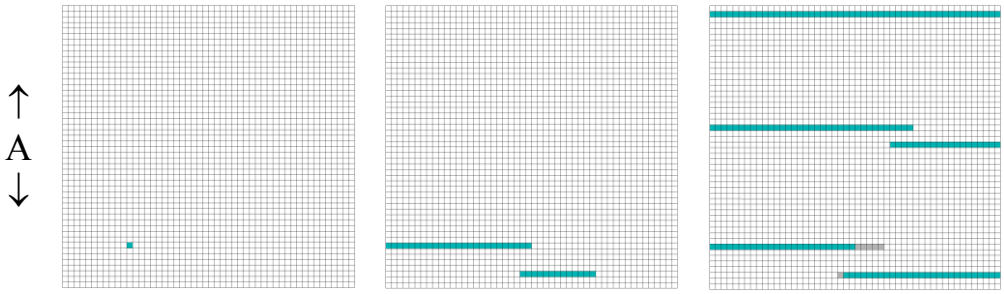

4.8185e9 (s) 5.0492e9 (s) 5.9979e9 (s)

Timestep: 30 days
Lifetime: 190 years 70 days

(d)

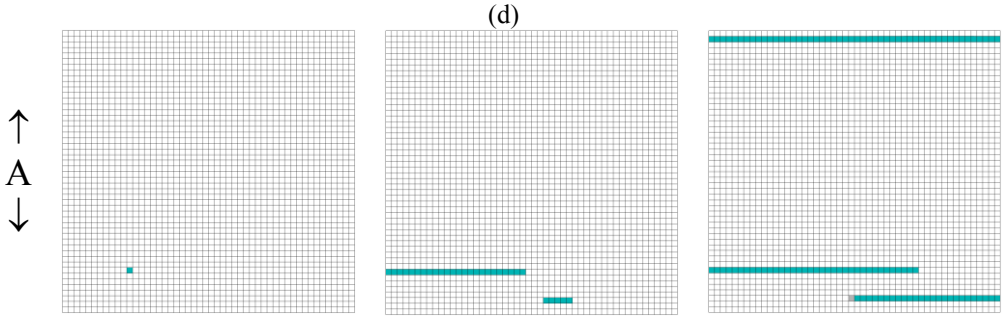

4.8108e9 (s) 4.9391e9 (s) 5.6661e9 (s)

Timestep: 15 days
Lifetime: 179 years 245 days

(e)

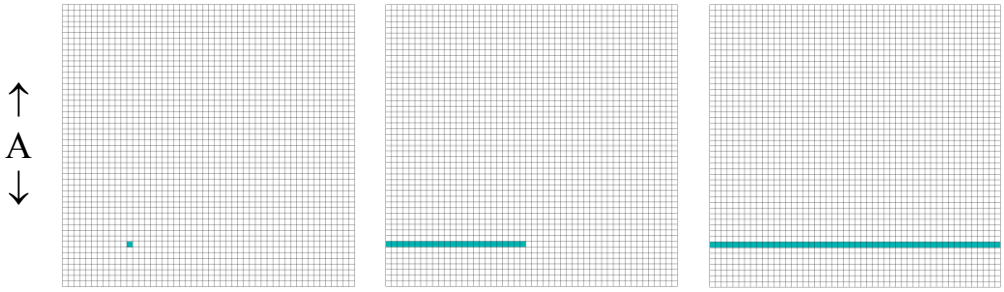

4.8057e9 (s) 4.8614e9 (s) 4.9757e9 (s)

Timestep: 7 days
Lifetime: 157 years 284 days

(f)

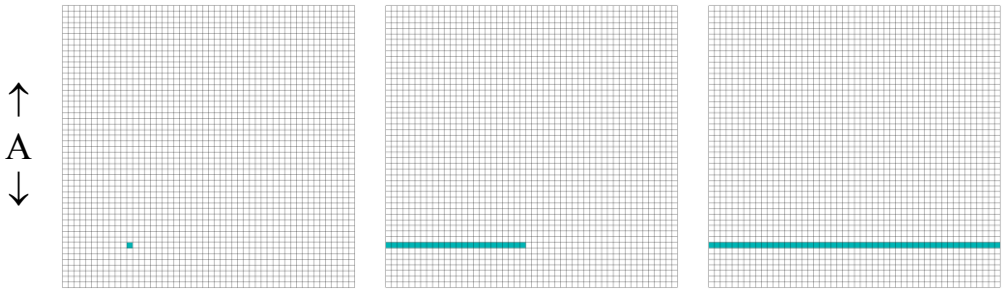

4.8019e9 (s) 4.8106e9 (s) 4.8310e9 (s)

Timestep: 1 day
Lifetime: 153 years 69 days
(g)

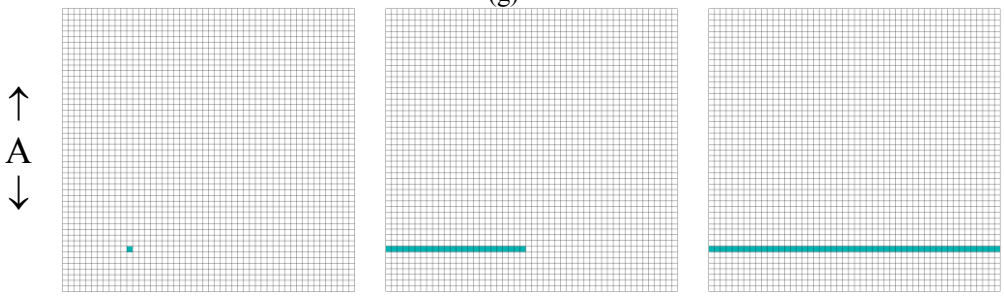

4.8015e9 (s) 4.8061e9 (s) 4.8170e9 (s)

Timestep: 12 hours
Lifetime: 152 years 272 days
(h)

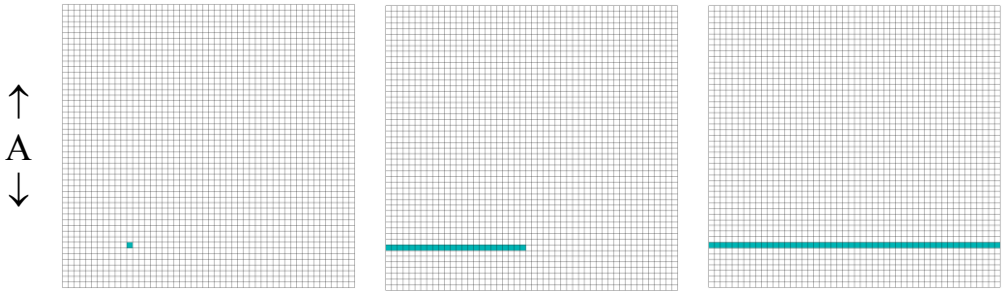

4.8013e9 (s) 4.8037e9 (s) 4.8094e9 (s)

Timestep: 6 hours
Lifetime: 152 years 184 days
(i)

Figure 4-7 Uniaxial tensile tests (6 MPa) with different time steps (Zones in green: tensile failure; zones in gray: failed in the past)

Table 4-3 Calculated life times with different constant time steps (corresponding to Fig. 4-7) (analytical 1st failure time: 4,801,063,122 seconds)

	Time step	**1st failure time (s)**	**1st failure time error**	**Time span to failure (s)**	**Life time (s)**	**1st failure step**	**Total steps**
(a)	1 year	4.9827e9	3.78 %	2.2706e9	7.2217e9	158	229
(b)	182 days	4.9038e9	2.14 %	2.0025e9	6.9064e9	311	438
(c)	90 days	4.8522e9	1.07 %	1.3841e9	6.2364e9	624	802
(d)	30 days	4.8185e9	0.36 %	1.1794e9	5.9979e9	1,859	2,314
(e)	15 days	4.8108e9	0.20 %	8.5536e8	5.6661e9	3,712	4,372
(f)	7 days	4.8057e9	0.10 %	1.6995e8	4.9757e9	7,946	8,227
(g)	1 days	4.8019e9	0.02 %	2.9117e7	4.8310e9	55,577	55,914
(h)	12 hours	4.8015e9	0.008 %	1.5552e7	4.8170e9	111,145	111,505
(i)	6 hours	4.8013e9	0.004 %	8.1432e6	4.8094e9	222,281	222,658

Uniaxial compressive tests on model A with different time steps have also been done. A compressive load of 12 MPa is applied on the numerical model. With the model unchanged, zone (12, 8) is again determined as "the most critical zone", and the analytical solution of the lifetime of this zone is also 4.8011e9 seconds (152 years 87 days 20 hours 38 minutes and 42 seconds). Different time steps have been applied in the test. All the numerical results also showed the first failure happened in Zone (12, 8). It is seen from the model's macroscopic failure pattern in Fig. 4-9 that shear bands have formed with the inclination 45º to the direction of applied compressive load. The shear bands were more ubiquitously formed in the model with comparatively bigger time steps, while with a smaller time step, less shear bands were formed (Fig. 4-9). It is noticed from the simulation results (Table 4-4) that the predicted lifetime of the model descends when the time step is set smaller; it is also recognized that the predicted failure time of "the most critical zone" is the same as that in the tensile tests with tensile loading of 6 MPa. But the time span between the first zone failure and the macroscopic failure is much longer in the compressive tests. The predicted first zone failure time results using different constant time steps are the same as shown in Fig. 4-8. As can be seen in Table 4-4, the predicted first zone failure time becomes more precise if the time step is set smaller. But at the same time, much more computing steps (computing time) are needed if the time step is set too small, thus making the simulation neither efficient nor practical. So to choose a time step scheme which guarantees a precise simulation and an acceptable computing time has been a focus in this study. Therefore, a new scheme for the changeable time step has been developed.

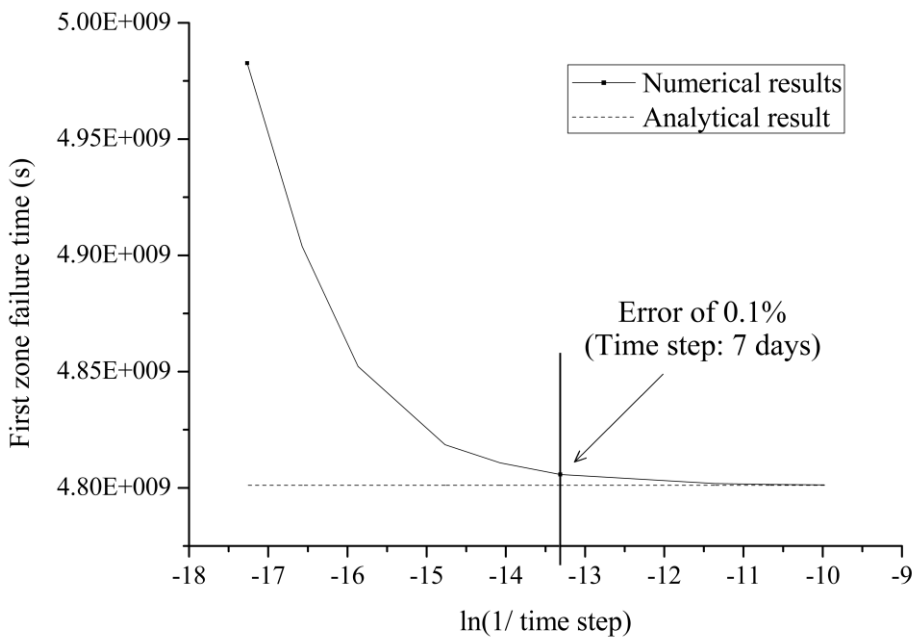

Figure 4-8 First zone failure time results with different constant time steps

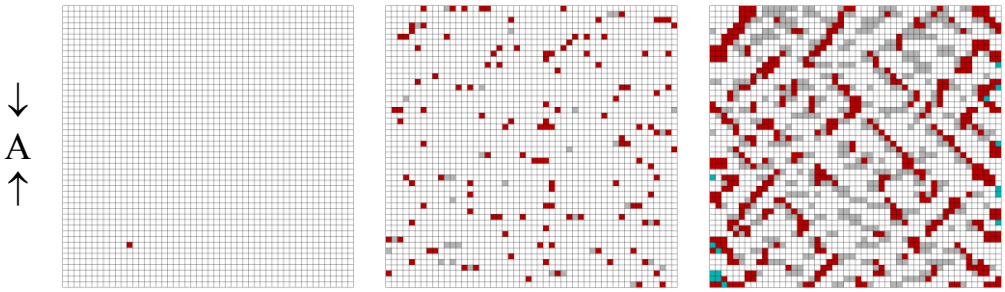

4.9827e9 (s) 6.4649e9 (s) 9.7762e9 (s)

Timestep: 1 year
Lifetime: 310 years
(a)

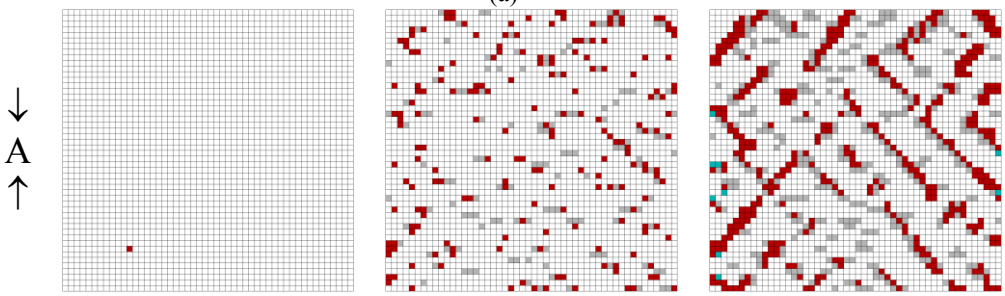

4.9038e9 (s) 6.6226e9 (s) 8.4201e9 (s)

Timestep: 182 days 12 hours
Lifetime: 267 years
(b)

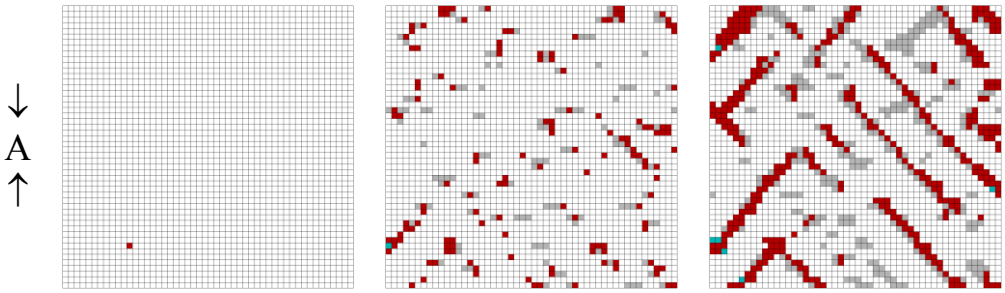

4.8522e9 (s) 6.3763e9 (s) 8.1104e9 (s)

Timestep: 90 days
Lifetime: 257 years 65 days
(c)

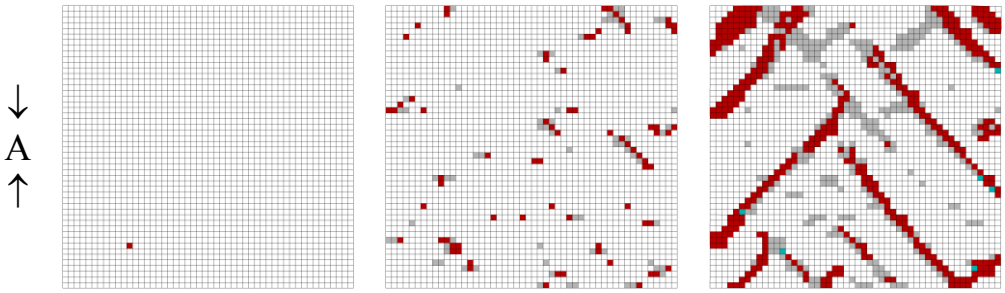

4.8185e9 (s) 5.9357e9 (s) 7.7371e9 (s)

Timestep: 30 days
Lifetime: 245 days 125 days
(d)

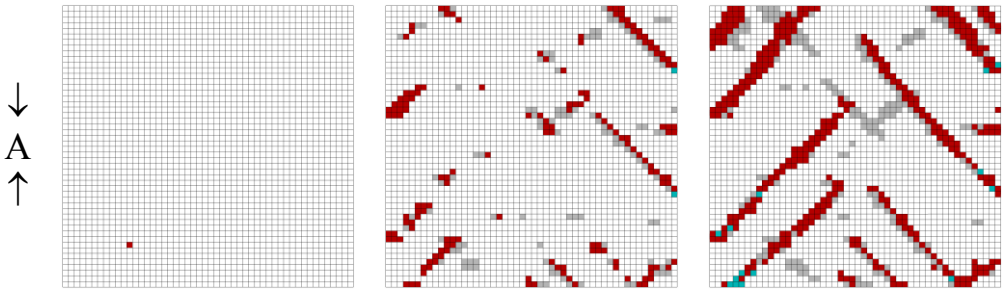

4.8108e9 (s) 5.9823e9 (s) 6.7262e9 (s)

Timestep: 15 days
Lifetime: 213 years 105 days

(e)

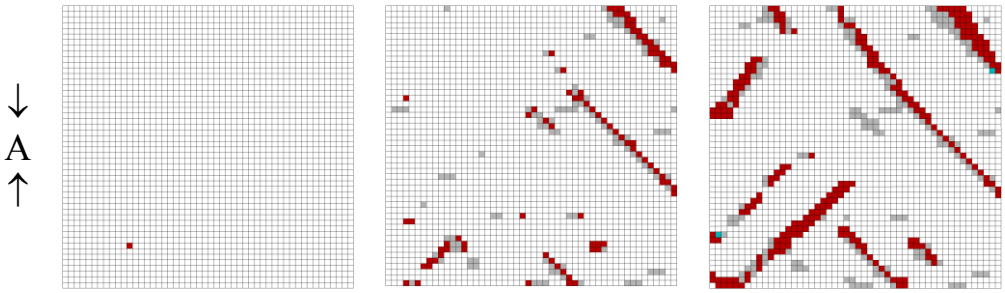

4.8057e9 (s) 5.7662e9 (s) 6.0190e9 (s)

Timestep: 7 days
Lifetime: 190 years 314 days

(f)

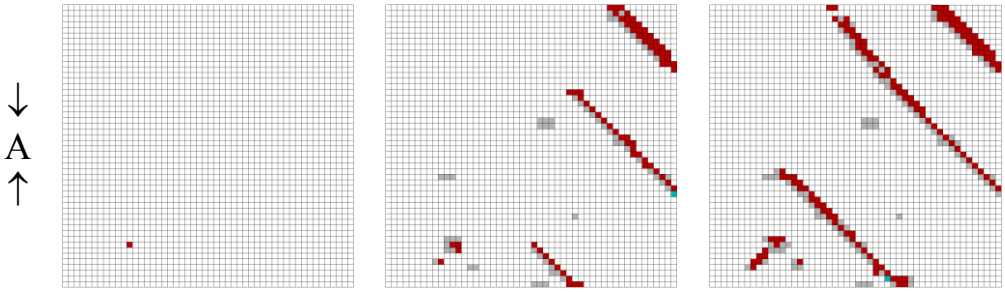

4.8019e9 (s) 5.4398e9 (s) 5.4864e9 (s)

Timestep: 1 days
Lifetime: 173 years 355 days

(g)

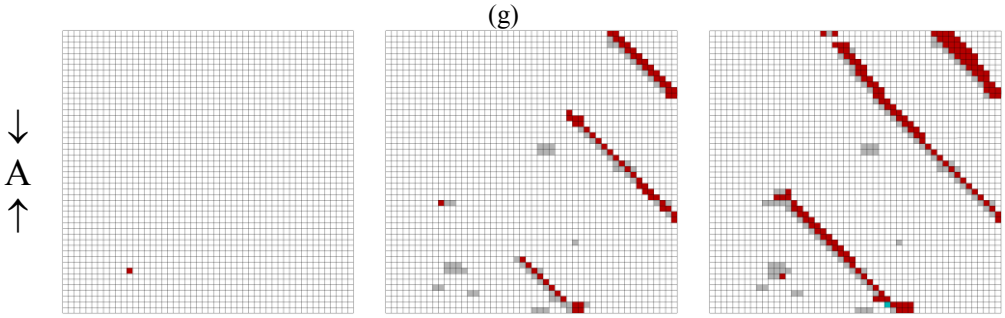

4.8015e9 (s) 5.3982e9 (s) 5.4224e9 (s)

Timestep: 12 hours
Lifetime: 171 years 344 days

(h)

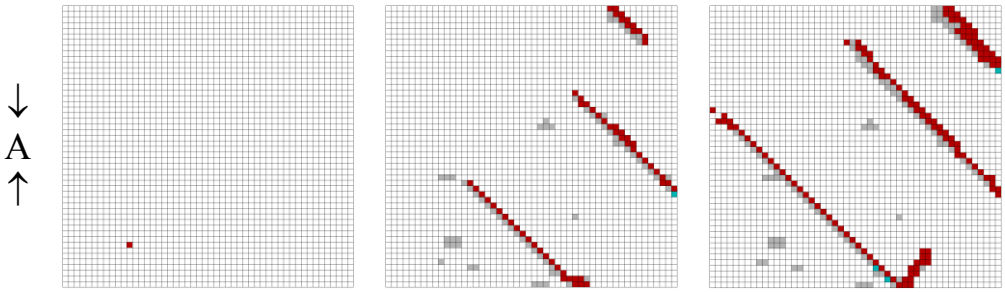

4.8013e9 (s) 5.3748e9 (s) 5.3841e9 (s)

Timestep: 6 hours

Lifetime: 170 years 266 days

(i)

Figure 4-9 Uniaxial compressive tests (12 MPa) with different time steps (zones in green: tensile failure; zones in red: shear failure; zones in gray: failed in the past)

Table 4-4 Calculated life times with different constant time steps (corresponding to Fig. 4-9) (analytical 1st failure time: 4.8011e9 seconds)

	Time step (s)	**1st failure time (s)**	**1st failure time error**	**Time span to failure(s)**	**Life time (s)**	**1st failure step**	**Total steps**
(a)	1 year	4.9827e9	3.78 %	4.7935e9	9.7762e9	158	310
(b)	182 days	4.9038e9	2.14 %	3.5163e9	8.4201e9	311	534
(c)	90 days	4.8522e9	1.07 %	3.2581e9	8.1104e9	624	1,043
(d)	30 days	4.8185e9	0.36 %	2.9186e9	7.7371e9	1,859	2,985
(e)	15 days	4.8108e9	0.20 %	1.9155e9	6.7262e9	3,712	5,190
(f)	7 days	4.8057e9	0.10 %	1.2132e9	6.0190e9	7,946	9,952
(g)	1 days	4.8019e9	0.02 %	6.8455e8	5.4864e9	55,577	63,500
(h)	12 hours	4.8015e9	0.008 %	6.2096e8	5.4224e9	111,145	125,519
(i)	6 hours	4.8013e9	0.004 %	5.8283e8	5.3841e9	222,281	249,264

4.2.3 Calculation scheme with changeable time steps

Calculation with small time step value but more steps gives better results than one with larger time step value but less steps. A procedure with a larger time step is more prone to great imbalance caused by insufficient updates. This assumption is supported by the calculation results obtained in subsection 4.2.2. However, more computing time is needed for a smaller time step value. Efforts have been made to avoid consuming more computing time while keeping the calculation result to an acceptable precision as well.

It is assumed that for the steps before any zone of the model fails, the influence of the time step value is not obvious because of the comparatively static condition of motion and stress/strain state. This is also supported by the predicted first zone failure time obtained by different constant time steps (subsection 4.2.2), with errors between 3.78 % and 0.004 %, while the predicted life time for the whole model varies greatly. This feature makes the application of a larger time step at the beginning of the calculation possible. Based on this observation, the scheme with a changeable time step has been proposed and adopted in the program. In this scheme, the maximum

local equilibrium ratio (the maximum equilibrium ratio for each grid point) is used as a criterion of whether the time step value is changed in a descendent or ascending manner in the coming steps. In FLAC (Itasca Consulting Group 2005), a mechanical equilibrium state is considered to be achieved by default when the maximum unbalanced force ratio drops below 0.001. Therefore, 0.001 was used as the limit value in the calculation. For each of the calculation steps, the maximum unbalanced force ratio is detected. If it exceeds this limit value, the time step is decreased in the next step and increased if otherwise. The changing of the time step will be continued stepwise till the defined minimum or maximum is reached. The minimum and maximum time step is set earlier in the program for each specific model under study.

For comparison, the same model as in subsection 4.2.2 is used here, with a tensile load of 6 MPa in the uniaxial tensile tests and compressive load of 12 MPa in the uniaxial compressive tests. The maximum time step value is set to 7 days. As listed in Table 4-3 and 4-4, with 7 days as a constant time step, the program renders first zone failure in 4.8057e9 seconds (about 152 years 142 days), whose error is about 54 days from the analytical first zone failure time of $4.8011e^9$ seconds (about 152 years 87 days 20 hours), or with other words only 0.1 %. A comparison between the predicted life times obtained by changeable and constant time step for the uniaxial tensile test is shown in Table 4-5. In the scheme with the changeable time step, the maximum value of 7 days is kept unchanged, and the minimum value is set 1 day, 12 hours and 6 hours, respectively. Comparisons have been made between these results and those obtained by the constant time step of 1 day, 12 hours and 6 hours. As can be seen from Table 4-5, a considerable number of calculation steps could be saved using changeable time step, while only negligible degree of precision is lost. For example, using time step ranging from 7 days to 6 hours, the predicted life time is 4,813,901,280 seconds, which has 0.09 % of difference with the life time of 4,809,412,800 seconds obtained using constant time step of 6 hours, but has only used 8,322 steps, reducing the calculation steps by 96.26 %.

Table 4-5 Comparison between life time results

New scheme (changeable time step)			**Old scheme (constant time step)**		
Time step range	**Life time (s)**	**Total step**	**Time step (s)**	**Life time (s)**	**Total step**
7 days ~ 1 day	4.8348e9	8,282	**1 day**	4.8310e9	55,914
7 days ~ 12 hours	4.8218e9	8,318	**12 hours**	4.8170e9	111,505
7 days ~ 6 hours	4.8139e9	8,322	**6 hours**	4.8094e9	222,658

To further study the influence of the changeable time step on the predicted life time and fracture pattern with the maximum time step value of 7 days, more different minimum time steps have been tested. The macroscopic failure pattern of the model with different minimum time step limit has not changed and results in a macroscopic

tensile fracture perpendicular to the direction of the applied tensile load. The fracture pattern for different points in time for a minimum time step limit of 1 day is shown in Fig. 4-10 as an example. The life time results of tests with different minimum time steps are listed in Table 4-6. The life times corresponding to these different minimum time steps are also shown in Fig. 4-11. It is seen from Table 4-6 that the lifetime decreases when the minimum time step descends from 1 day to 20 seconds. For values smaller than 20 seconds the predicted lifetime is nearly constant with only very small fluctuations (numerical noise).

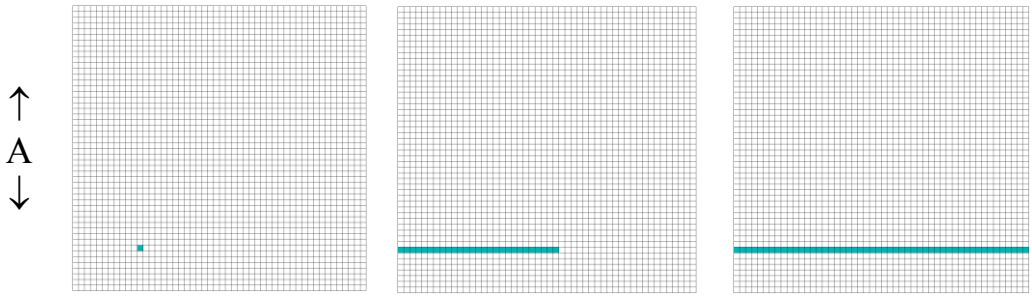

4.8057e9 (s) 4.8170e9 (s) 4.8348e9 (s)

Maximum time step: 7 days; Minimum time step: 1 day; Lifetime: 153 years 113 days

Figure 4-10 Uniaxial tensile test (6 MPa applied on model A) with changeable time steps (Zones in green: tensile failure)

Table 4-6 Predicted life time results with changeable time steps

Time step (s)		First failure time (s)	Life time (s)	Time span to failure(s)	First failure step	Total steps
Max.	Min.					
7 days	1 day	4.8057e9	4.8348e9	2.9030e7	7,946	8,282
7 days	12 hours	4.8057e9	4.8218e9	1.6088e7	7,946	8,318
7 days	6 hours	4.8057e9	4.8139e9	8.1605e6	7,946	8,322
7 days	3 hous	4.8057e9	4.8101e9	4.3157e6	7,946	8,341
7 days	1 hour	4.8057e9	4.8074e9	1.6253e6	7,946	8,381
7 days	30 min.	4.8057e9	4.8066e9	8.9093e5	7,946	8,406
7 days	10 min.	4.8057e9	4.8061e9	3.7793e5	7,946	8,467
7 days	5 min.	4.8057e9	4.8060e9	2.4053e5	7,946	8,527
7 days	100 s	4.8057e9	4.8059e9	1.4713e5	7,946	8,749
7 days	60 s	4.8057e9	4.8059e9	1.2749e5	7,946	8,955
7 days	50 s	4.8057e9	4.8059e9	1.2674e5	7,946	9,141
7 days	40 s	4.8057e9	4.8059e9	1.2103e5	7,946	9,296
7 days	30 s	4.8057e9	4.8059e9	1.1528e5	7,946	9,553
7 days	20 s	4.8057e9	4.8058e9	1.0911e5	7,946	10,046
7 days	10 s	4.8057e9	4.8059e9	1.1300e5	7,946	11,307
7 days	5 s	4.8057e9	4.8064e9	6.9514e5	7,946	11,320
7 days	1 s	4.8057e9	4.8066e9	8.5373e5	7,946	11,376
7 days	0.5 s	4.8057e9	4.8064e9	6.8003e5	7,946	11,400
7 days	0.1 s	4.8057e9	4.8059e9	1.8977e5	7,946	11,458
7 days	0.05 s	4.8057e9	4.8059e9	1.2912e5	7,946	11,838
7 days	0.01 s	4.8057e9	4.8060e9	2.1390e5	7,946	11,690
7 days	0.005 s	4.8057e9	4.8064e9	6.9055e5	7,946	11,758
7 days	0.001 s	4.8057e9	4.8066e9	8.5276e5	7,946	12,092

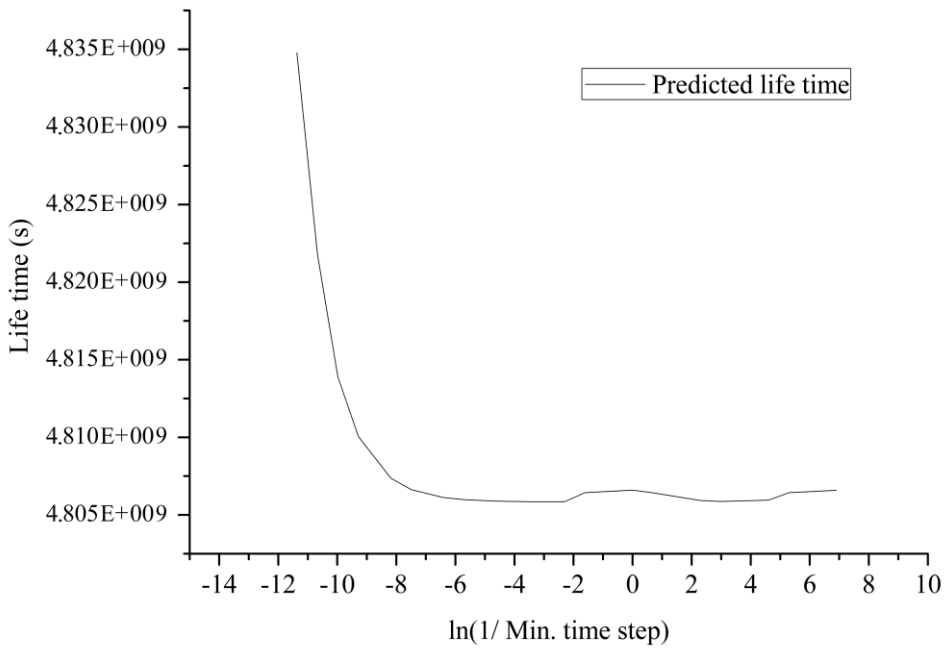

Figure 4-11 Life time predictions with different Min. time steps

The scheme with changeable time step has also been applied in the uniaxial compressive tests. The maximum time step value is also set to 7 days. Comparisons between predicted life times obtained from the constant and changeable time step are shown in Table 4-7. It can be recognized, that similar to the tensile tests, large numbers of calculation steps are saved using changeable time step, especially when the time step value is comparatively small. For example, it takes 29,698 steps for the scheme with time step ranging from 7 days to 6 hours to obtain the life time of the model, while more than 249,264 steps are necessary for the scheme with the constant time step of 6 hours to obtain the result (Table 4-7). The predicted life time obtained by these two different time step schemes differs only by 0.06 %. It is concluded that the changeable time step scheme can produce acceptable simulation results with much less computing time.

Table 4-7 Comparison between predicted life times

New scheme (changeable time step)			**Old scheme (constant time step)**		
Time step range	**Life time (s)**	**Total step**	**Time step (s)**	**Life time (s)**	**Total step**
7 days ~ 1 day	5.4885e9	15,842	**1 day**	5.4864e9	63,500
7 days ~ 12 hours	5.4227e9	22,213	**12 hours**	5.4224e9	125,519
7 days ~ 6 hours	5.3876e9	29,698	**6 hours**	5.3841e9	249,264

With a time step of 7 days as the upper time step limit, more different minimum time steps have been tested in the changeable time step scheme. The observed macroscopic fracture pattern is similar for different ranges of time steps (Fig. 4-12). Multiple shear bands were formed with a minimum time step of 3 hours and higher. Single shear

band was form with a minimum time step less than 3 hours. The shear bands have an inclination of 45º from the direction of the applied compressive load. Especially, additional tensile fractures have been formed following the loading direction if the minimum time step is set equal or less than 0.1 second. The lifetime results corresponding to the models shown in Fig. 4-12 are listed in Table 4-8. The lifetimes corresponding to different minimum time steps are also shown in Fig. 4-13. It can be recognized that the lifetime is becoming smaller with decreasing minimum time step values as long as the time step is bigger than 60 seconds. The lifetime results are more or less constant for time steps smaller than 60 seconds (Fig. 4-13, Table 4-8).

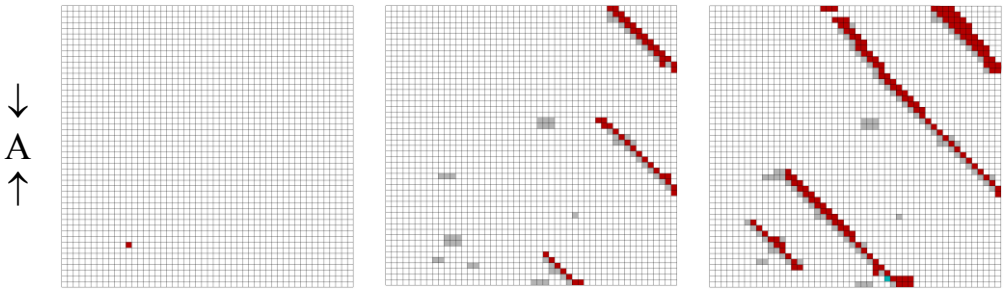

4.8057e9 (s) 5.4264e9 (s) 5.4885e9 (s)

Timestep: 7 days ~ 1 day
Lifetime: 174 years 14 days

(a)

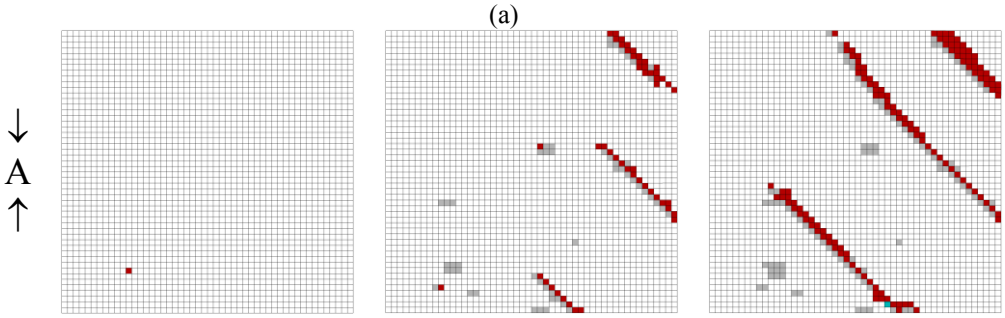

4.8057e9 (s) 5.3903e9 (s) 5.4227e9 (s)

Timestep: 7 days ~ 12 hours
Lifetime: 171 years 347 days

(b)

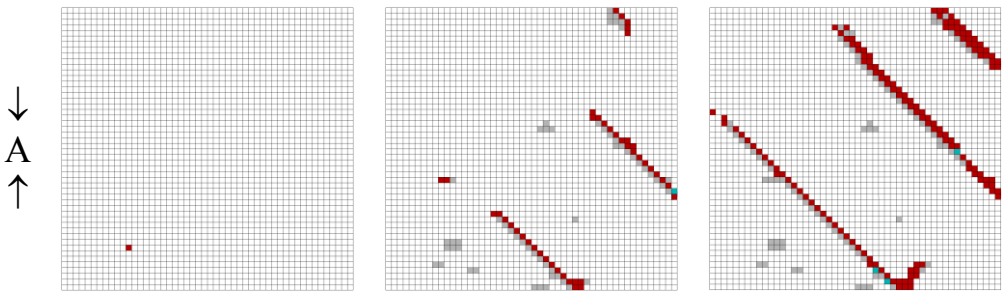

4.8057e9 (s) 5.3731e9 (s) 5.3876e9 (s)

Timestep: 7 days ~ 6 hours
Lifetime: 170 years 306 days

(c)

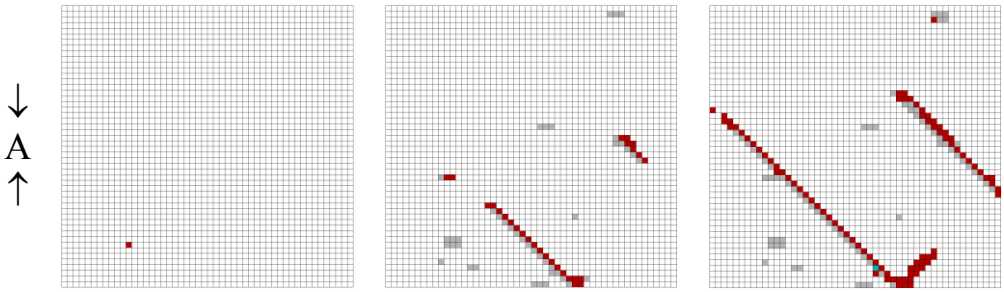

4.8057e9 (s) 5.3547e9 (s) 5.3617e9 (s)

Timestep: 7 days ~ 3 hours
Lifetime: 5361716160 (s)
(d)

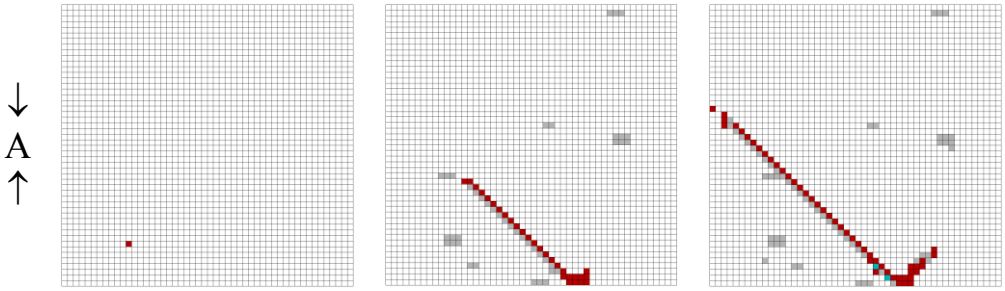

4.8057e9 (s) 5.3400e9 (s) 5.3417e9 (s)

Timestep: 7 days ~ 1 hour
Lifetime: 169 years 140 days
(e)

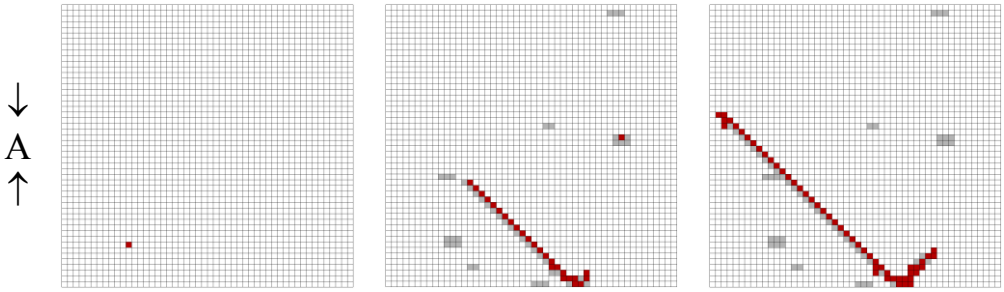

4.8057e9 (s) 5.3379e9 (s) 5.3389e9 (s)

Timestep: 7 days ~30 min.
Lifetime: 169 years 107 days
(f)

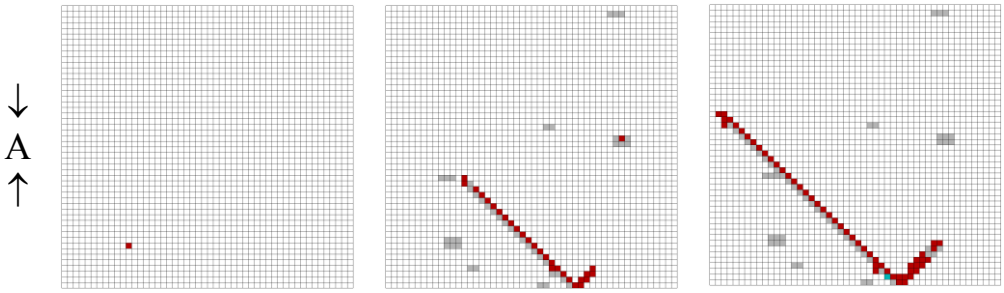

4.8057e9 (s) 5.3328e9 (s) 5.3332e9 (s)

Timestep: 7 days ~ 10 min.
Lifetime: 169 years 41 days
(g)

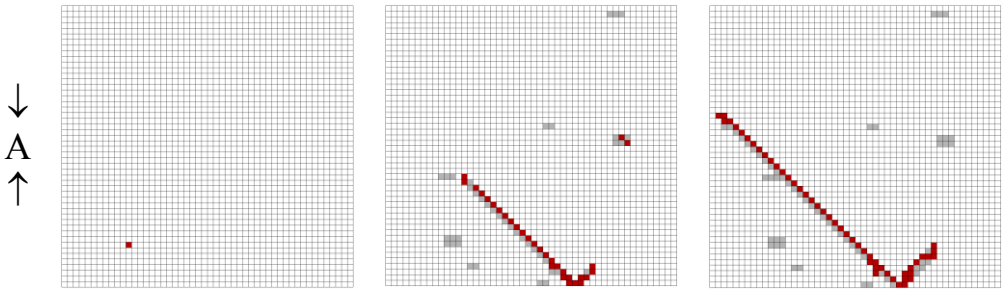

4.8057e9 (s) 5.3328e9 (s) 5.3330e9 (s)

Timestep: 7 days ~ 5 min.
Lifetime: 169 years 39 days

(h)

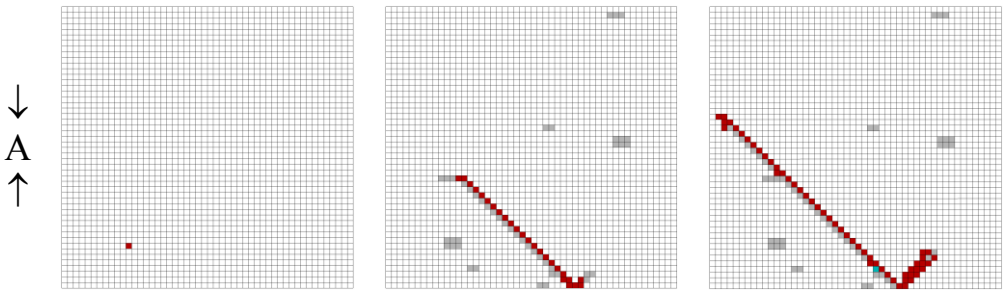

4.8057e9 (s) 5.3318e9 (s) 5.3319e9 (s)

Timestep: 7 days ~ 100 s
Lifetime: 169 years 26 days

(i)

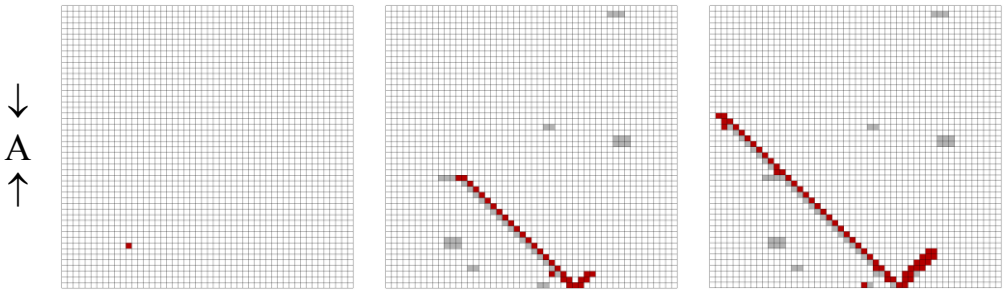

4.8057e9 (s) 5.3323e9 (s) 5.3323e9 (s)

Timestep: 7 days ~ 60 s
Lifetime: 169 years 31 days

(j)

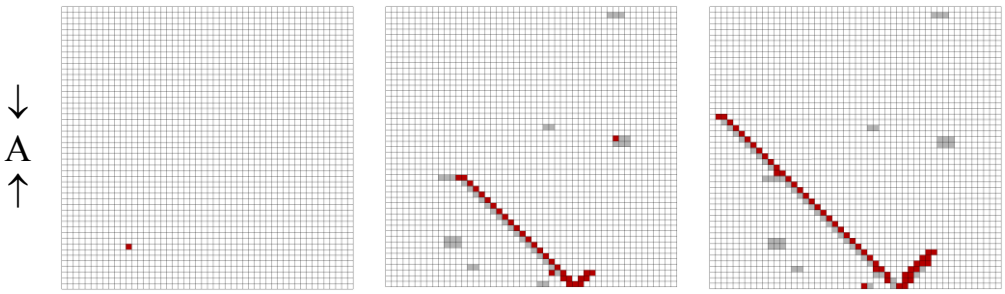

4.8057e9 (s) 5.3325e9 (s) 5.3325e9 (s)

Timestep: 7 days ~ 50 s
Lifetime: 169 years 34 days

(k)

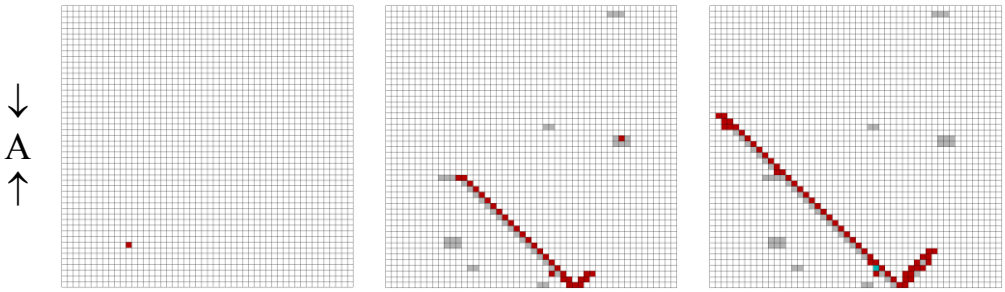

4.8057e9 (s) 5.3341e9 (s) 5.3342e9 (s)

Timestep: 7 days ~ 40 s
Lifetime: 169 years 53 days

(l)

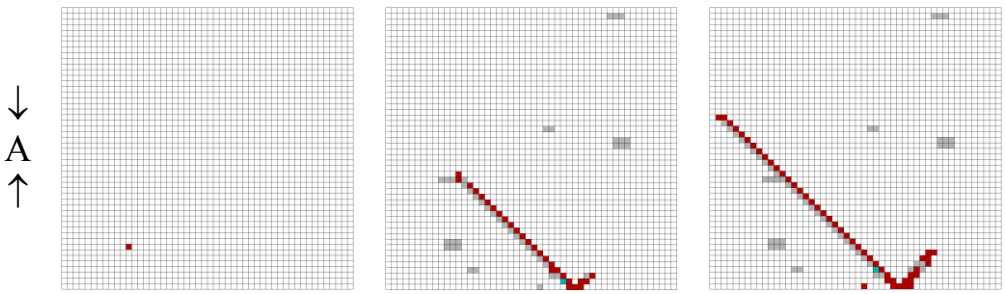

4.8057e9 (s) 5.3331e9 (s) 5.3331e9 (s)

Timestep: 7 days ~ 30 s
Lifetime: 169 years 41 days

(m)

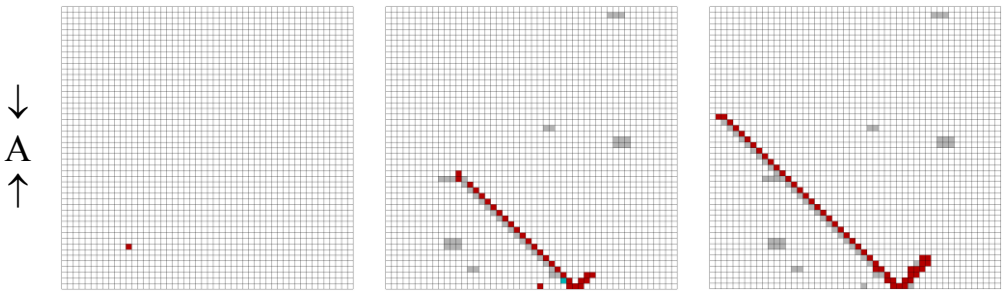

4.8057e9 (s) 5.3320e9 (s) 5.3320e9 (s)

Timestep: 7 days ~ 20 s
Lifetime: 169 years 28 days

(n)

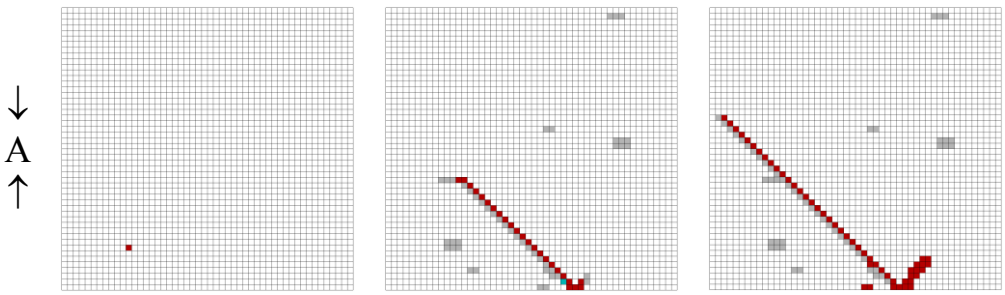

4.8057e9 (s) 5.3335e9 (s) 5.3335e9 (s)

Timestep: 7 days ~ 10 s
Lifetime: 169 years 45 days

(o)

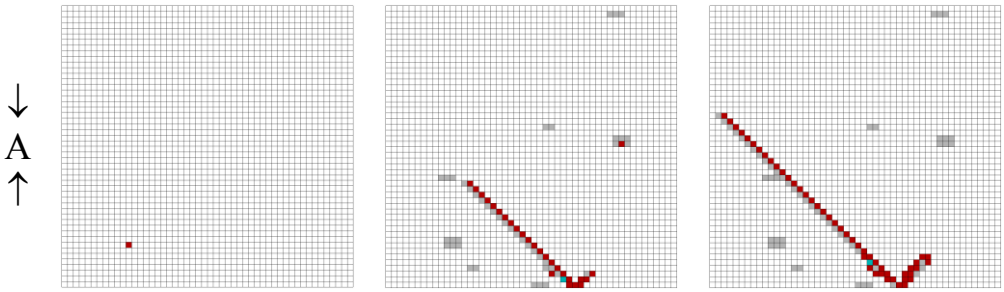

4.8057e9 (s) 5.3356e9 (s) 5.3356e9 (s)

Timestep: 7 days ~ 5 s
Lifetime: 169 years 69 days

(p)

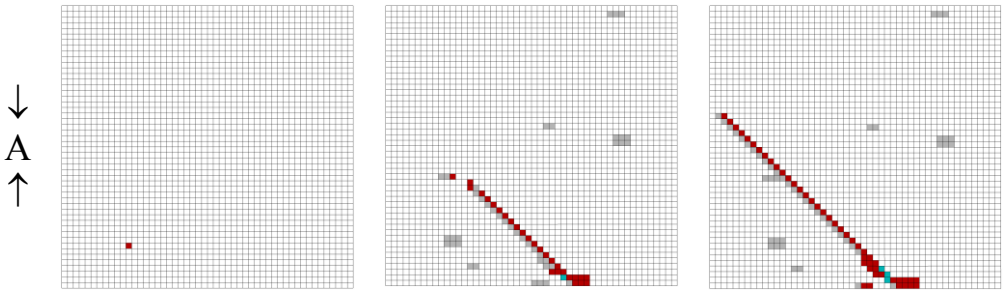

4.8057e9 (s) 5.3373e9 (s) 5.3373e9 (s)

Timestep: 7 days ~ 1 s
Lifetime: 169 years 89 days

(q)

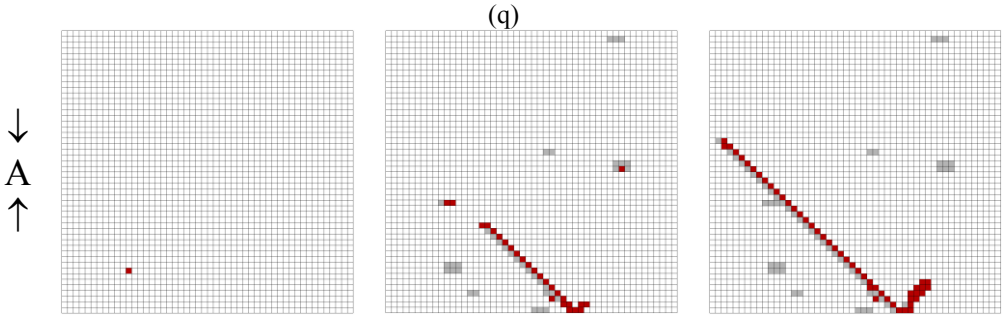

4.8057e9 (s) 5.3365e9 (s) 5.3365e9 (s)

Timestep: 7 days ~ 0.5 s
Lifetime: 169 years 80 days

(r)

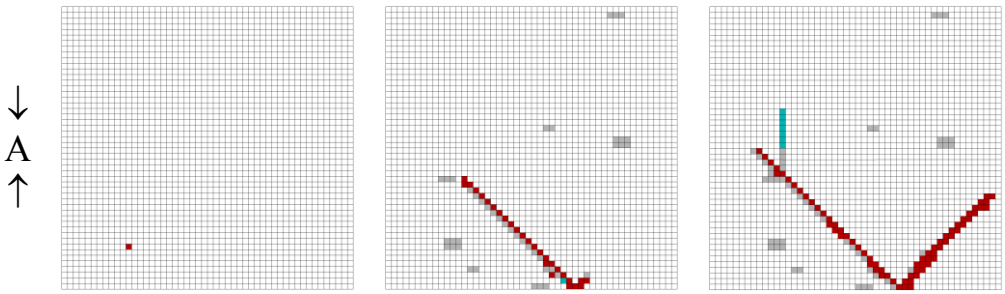

4.8057e9 (s) 5.3350e9 (s) 5.3350e9 (s)

Timestep: 7 days ~ 0.1 s
Lifetime: 169 years 62 days

(s)

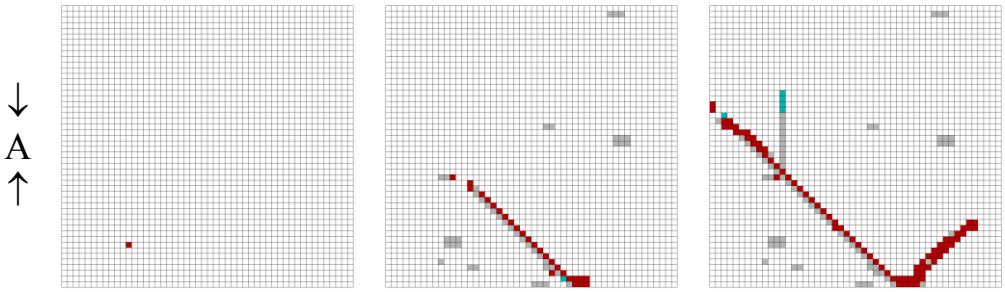

Timestep: 7 days ~ 0.05 s
Lifetime: 169 years 101 days

(t)

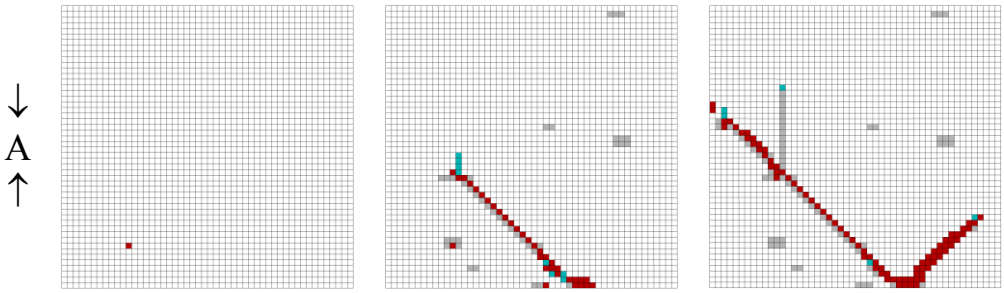

Timestep: 7 days ~ 0.01 s
Lifetime: 169 years 90 days

(u)

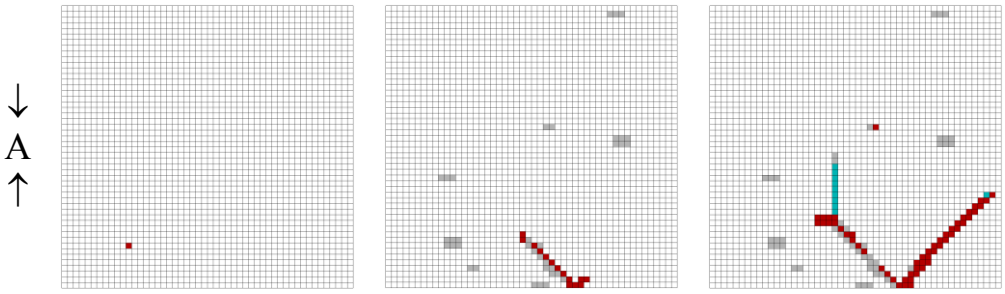

Timestep: 7 days ~ 0.005 s
Lifetime: 169 years 83 days

(v)

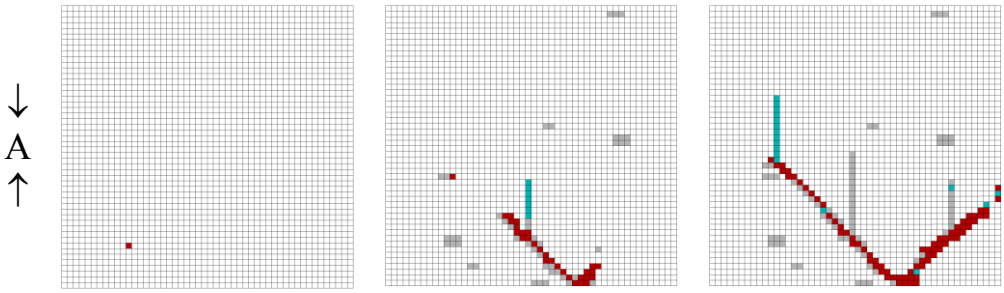

Timestep: 7 days ~ 0.001 s
Lifetime: 169 years 83 days

(w)

Figure 4-12 Uniaxial compressive tests (12 MPa) with different minimum time steps (zones in green: tensile failure; zones in red: shear failure; zones in gray: failed in the past)

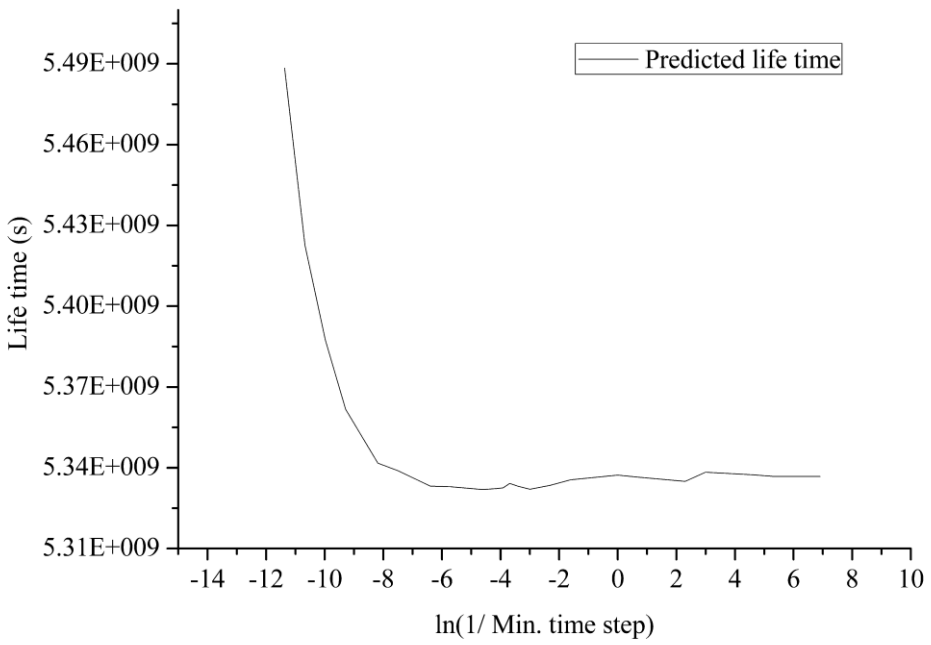

Figure 4-13 Life time predictions with different min. time steps

Table 4-8 Predicted life times with changeable time steps (corresponding to Fig. 4-12)

	Time step (s)		First failure time (s)	Lifetime (s)	Failing time span(s)	First failure step	Total steps
	Max.	Min.					
(a)	7 days	1 days	4.8057e9	5.4885e9	6.8273e8	7,946	15,842
(b)	7 days	12 hours	4.8057e9	5.4227e9	6.1691e8	7,946	22,213
(c)	7 days	6 hours	4.8057e9	5.3876e9	5.8182e8	7,946	29,698
(d)	7 days	3 hours	4.8057e9	5.3617e9	5.5598e8	7,946	35,577
(e)	7 days	1 hour	4.8057e9	5.3417e9	5.3597e8	7,946	46,051
(f)	7 days	30 min.	4.8057e9	5.3389e9	5.3311e8	7,946	51,151
(g)	7 days	10 min.	4.8057e9	5.3332e9	5.2744e8	7,946	63,033
(h)	7 days	5 min.	4.8057e9	5.3330e9	5.2722e8	7,946	65,246
(i)	7 days	100 s	4.8057e9	5.3319e9	5.2616e8	7,946	74,300
(j)	7 days	60 s	4.8057e9	5.3323e9	5.2660e8	7,946	79,199
(k)	7 days	50 s	4.8057e9	5.3325e9	5.2680e8	7,946	78,320
(l)	7 days	40 s	4.8057e9	5.3342e9	5.2842e8	7,946	82,410
(m)	7 days	30 s	4.8057e9	5.3331e9	5.2740e8	7,946	77,534
(n)	7 days	20 s	4.8057e9	5.3320e9	5.2628e8	7,946	83,372
(o)	7 days	10 s	4.8057e9	5.3335e9	5.2775e8	7,946	92,570
(p)	7 days	5 s	4.8057e9	5.3356e9	5.2982e8	7,946	88,104
(q)	7 days	1 s	4.8057e9	5.3373e9	5.3154e8	7,946	90,041
(r)	7 days	0.5 s	4.8057e9	5.3365e9	5.3078e8	7,946	95,057
(s)	7 days	0.1 s	4.8057e9	5.3350e9	5.2923e8	7,946	106,342
(t)	7 days	0.05 s	4.8057e9	5.3383e9	5.3258e8	7,946	109,009
(u)	7 days	0.01 s	4.8057e9	5.3374e9	5.3165e8	7,946	105,888
(v)	7 days	0.005 s	4.8057e9	5.3368e9	5.3107e8	7,946	119,457
(w)	7 days	0.001 s	4.8057e9	5.3368e9	5.3105e8	7,946	169,522

4.2.4 Conclusions

Time-dependency of the numerical model has been the focus of this section. Specifically, the lifetime prediction scheme has been introduced using the basic model. The lifetime prediction scheme has been tested on a single zone, and the calculation results have shown great accordance between the numerical calculation and the analytical solution, with respect to both the lifetime and failure mode. For the multi-zone numerical model, the lifetime prediction scheme has also been applied to predict the first zone failure and correct results with high precision were obtained. Different time step values have been used for the uniaxial tensile and compressive tests for the model, to study its influence on the lifetime. The macroscopic fracture patterns have also been studied accordingly. It was shown that a lifetime result with better precision can be obtained with a smaller time step value. To save computing time and to guarantee a precise simulation, a changeable time step scheme has been proposed and applied to the model. Macroscopic fracture pattern of the model with changeable time step scheme have also been discussed for tensile and compressive tests. It can be concluded that, these calculations can still render results with more or less the same precision, but can save considerable calculation time, which is especially the case when the time step is set very small. The time-related study of the numerical model has formed a valuable base for the other models. For reason of efficiency, the changeable time step scheme has been used in the modeling strategies of all subsequent studies.

4.3 New modeling strategies

The basic model scheme has given reasonable results under uniaxial tensile and compressive loading in terms of fracture evolution and damage pattern as well as for the predicted lifetime. Nevertheless, some simplifications have been made in the numerical simulations making further studies necessary. The purpose of this study is to improve this two dimensional modeling scheme in respect to the following aspects: inclusion of orientation of initial micro cracks; inclusion of different crack propagation schemes and the corresponding K value calculation and inclusion of anisotropic elasto-plastic constitutive law with softening into the model.

Four sets of numerical models are proposed in addition to the basic model. The new models are named fixed orientation model, wing crack model, fixed orientation combined ubiquitous-joint model and wing crack combined ubiquitous-joint model, respectively. The model schemes are illustrated in Fig. 4-14.

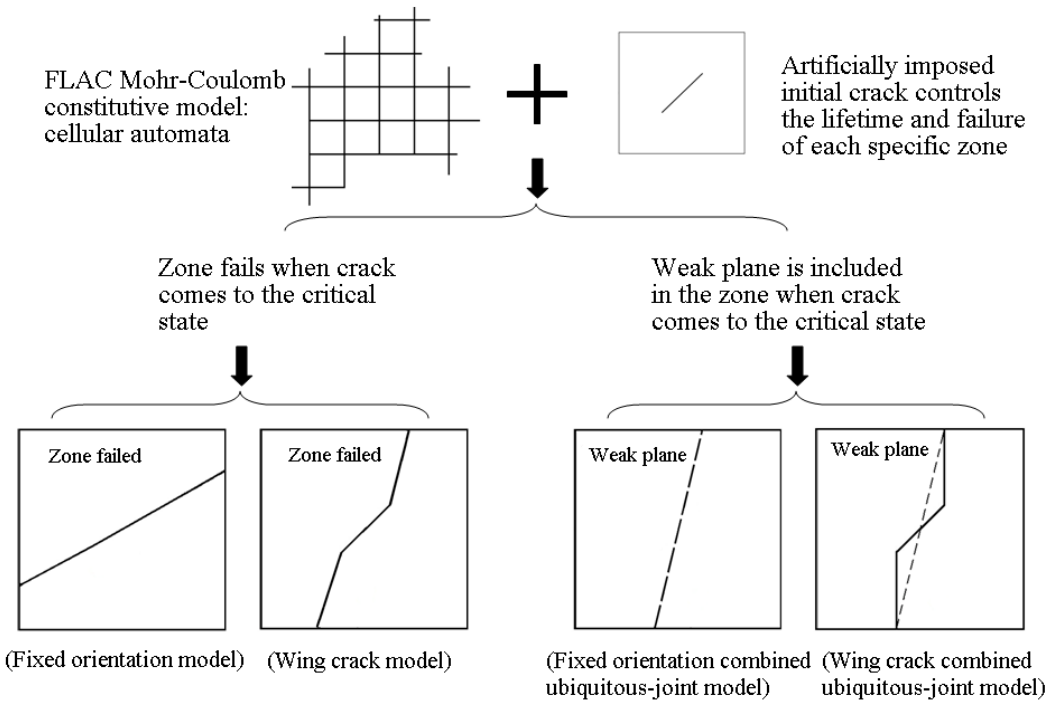

Figure 4-14 Different new model schemes

The fixed orientation model has included initial crack orientation and the cracks inside each zone are considered to propagate in their original planes. That means the cracks have constant propagation directions. Wing crack model assumes that the crack inside each zone propagates towards the direction of the maximum circumferential stress and a superposition method for K calculation has been adopted. In both of these two model schemes hold: when the crack inside a zone has reached the critical condition (crack reaches the zone boundary or stress intensity factor of the crack tip reaches the fracture toughness), the zone is considered to be failed and residual strength values are assigned to the whole zone. The fixed orientation combined ubiquitous-joint model and wing crack combined ubiquitous-joint model have included anisotropic elasto-plastic constitutive law with softening (ubiquitous-joint constitutive model) on the basis of the former two models. In this case, when the crack inside a zone has reached the critical condition, residual strength values are assigned only to the direction described by the crack, representing the weak plane inside the zone. For the fixed orientation combined ubiquitous-joint model, the orientation of the weak plane is the same as the orientation of the initial crack. While for the wing crack combined ubiquitous-joint model, as illustrated by the dashed line in Fig. 4-14, the weak plane is simplified by connecting the two wing crack tips, and the orientation value is obtained accordingly. The distinct characteristics of these models are also listed in Table 4-9.

Table 4-9 Distinct characteristics of numerical models

Model	Lifetime prediction	Crack length	Crack orientation	Anisotropy
Basic model	√	√	×	×
	Key characteristics			
	Microcrack orientation is not considered, but most critical orientation is used. Maximal tensile stress and shear stress within the zone are used for the calculation of KI and KII, respectively.			
Fixed orientation model	**Lifetime prediction**	**Crack length**	**Crack orientation**	**Anisotropy**
	√	√	√ (constant)	×
	Key characteristics			
	Microcrack orientation is defined, and crack propagates in its own plane. The normal stress and shear stress on the crack is used for the calculation of KI and KII, respectively.			
Fixed orientation combined ubiquitous-joint model	**Lifetime prediction**	**Crack length**	**Crack orientation**	**Anisotropy**
	√	√	√ (constant)	√
	Key characteristics			
	Based on the fixed orientation model, material strength anisotropy is included by assigning residual strength values on the direction represented by the crack orientation if the crack has reached critical condition, rather than assigning residual strength values to the entire zone.			
Wing crack model	**Lifetime prediction**	**Crack length**	**Crack orientation**	**Anisotropy**
	√	√	√ (wing)	×
	Key characteristics			
	Orientation of the initial crack is defined, and the crack propagates by forming “wing crack”. Only KI at the wing crack tip is used to calculate the crack propagation velocity since the wing crack propagates in pure Mode I.			
Wing crack combined ubiquitous-joint model	**Lifetime prediction**	**Crack length**	**Crack orientation**	**Anisotropy**
	√	√	√ (wing)	√
	Key characteristics			
	This model is a further extension of wing crack model. When the propagating crack has reached critical condition, instead of assigning residual strength values to the entire zone, this model assigns the residual strength values only to the plane represented by the direction of the crack’s geometry. Thus this model includes strength anisotropy by including a ‘weak plane’ into the zone.			

4.4 Fixed orientation model

4.4.1 Initial microcracks

Study on microcracks in rocks has long been the focus of geoscientists and engineers (Hadley 1976, Tapponier and Brace 1976, Costin 1983, Wong 1985, Wong et al. 1996, Wong et al. 2006). Kranz (1983) summarized studies on microcrack population in different rock types, and performed an additional study on intracrystalline microcrack length probability density distributions for three types of granites. It was concluded that for the natural, unstressed rock, micro cracks in plan view are more or less randomly oriented. For a stressed rock, a normal distribution may describe observations on the microcrack orientation. Acceptable assumptions of initial microcrack lengths include lognormal or exponential distribution. The assumption of an exponential distribution of crack lengths was also supported earlier by Dienes (1978).

Since microcrack characteristics are of great importance for mechanical behavior of rock, inclusion of initial crack parameters has been one of the keys for appropriate numerical modeling. In this research, crack characteristics including initial length and orientation have been considered in the numerical model. As has been already introduced, an initial crack is defined in each zone to simulate the universally existing microcracks in the rock specimen. One zone of the model with initial crack is shown in Fig. 4-15 as an example. Uniform, normal and lognormal distribution functions have been programmed to describe the lengths of initial cracks. The initial crack orientation is defined by the angle β (the angle between the crack and horizontal direction). Numerical calculations with different distributions of initial crack length and orientation have been performed and results are compared. The simulations are discussed in detail in the following subsections.

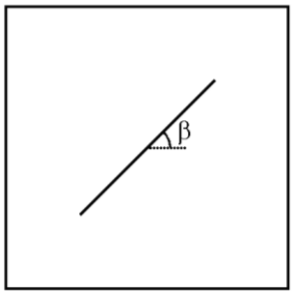

Figure 4-15 Zone of the model with initial crack

4.4.2 The lifetime prediction scheme for fixed orientation model (single zone)

In this subsection, lifetime prediction scheme for fixed orientation model has been introduced. The initial crack orientation is considered and crack within the zone

propagates along its original orientation. This means Mode I and Mode II loading conditions are superimposed on the crack. Consider a zone with an initial crack under biaxial loading, the normal and shear stresses on the crack are given as:

$$\sigma_N = \frac{1}{2}\left[\left(\sigma_v + \sigma_H\right) + \left(\sigma_v - \sigma_H\right)\cos 2\beta\right] \tag{4-9}$$

$$\sigma_T = \frac{1}{2}\left(\sigma_V - \sigma_H\right)\sin 2\beta \tag{4-10}$$

where β denotes the orientation of the initial crack (from horizontal direction); σ_V denotes the vertical stress applied on the zone and σ_H denotes the horizontal stress applied on the zone; σ_N and σ_T denote the normal stress and shear stress on the crack, respectively. The stress intensity factors of the crack in this case are:

$$K_I = \sigma_N \sqrt{\pi a} \tag{4-11}$$

$$K_{II} = \sigma_{eff} \sqrt{\pi a} \tag{4-12}$$

where $|\sigma_{eff}| = |\sigma_T| - \mu|\sigma_N|$, denoting the effective shear stress on the crack. μ is the coefficient of friction. The determination of crack propagation velocity is based on the superposition of both K_I and K_{II} components. Consulting Charles equation, the crack propagation velocity is expressed as:

$$v = CK^n = CK_I^n + CK_{II}^n \tag{4-13}$$

where parameter C and n have the same meanings as in Equation 4-2. Similar to Eq. 4-3 in Subsection 4.2.1, the life time of the zone is given:

$$t_{zone} = \int_{a_o}^{a_c} \frac{da}{v} = \frac{\sqrt{(2/\pi)^n}\, a_c^{1-n/2} - a_0^{1-n/2}}{C(1-n/2)\left(\sigma_N^n + \sigma_{eff}^n\right)} \tag{4-14}$$

The critical crack length a_c is determined by the minimum of these three values: the critical length determined by K_{IC} and K_{IIC} and the dimension of the zone d_{zone}, as shown in Eq.4-15:

$$a_C = \min\left\{\frac{2}{\pi}\left(\frac{K_{IC}}{\sigma_N}\right)^2, \frac{2}{\pi}\left(\frac{K_{IIC}}{\sigma_{eff}}\right)^2, a\left(d_{zone}\right)\right\} \tag{4-15}$$

where d_{zone} denotes the length of the zone; $a(d_{zone})$ is expressed as:

$$a(d_{zone}) = \frac{d_{zone}}{\cos\beta} \tag{4-16}$$

if the orientation of the crack β is less than or equal to 45º (Fig. 4-16 (c), (d)), and

$$a(d_{zone}) = \frac{d_{zone}}{\sin\beta} \tag{4-17}$$

if β is bigger than 45º (Fig. 4-16 (e)).

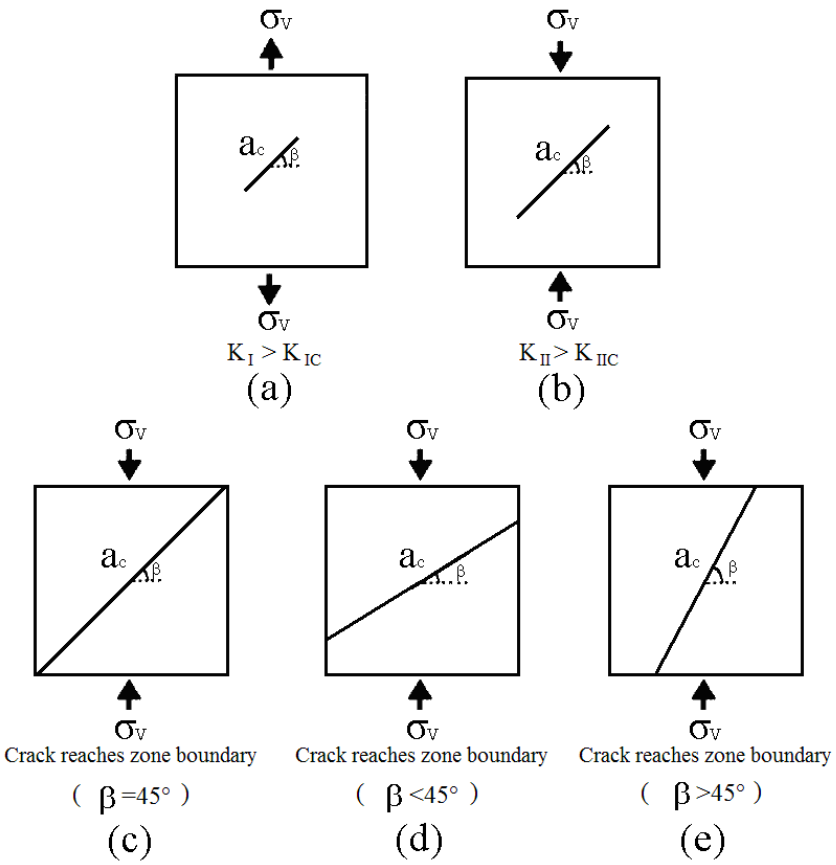

Figure 4-16 Cases of the critical crack length in single zone models

The lifetime prediction idea has first been studied on a single zone model of the size 0.04×0.04 m^2. The material parameters follow Table 4-1. The zone is put under the tensile load of 12 MPa and the compressive load of 18 MPa, respectively. The crack conditions of the model at failure in the uniaxial tests are shown in Fig. 4-17. It is seen that both failure modes have been detected: in the tensile tests, with the crack orientation being 0º, the model fails by K_I value reaching the critical value K_{IC} (Fig. 4-17 (a)), while with the crack orientation of 45º, the model fails by crack propagation

reaching the zone boundary (Fig. 4-17 (b)). In the compressive tests, with the crack orientation of 45º, the model fails by K_{II} value reaching the critical value K_{IIC} (Fig. 4-17 (c)), while with the crack orientation of 60º, the model fails by crack propagation reaching the zone boundary (Fig. 4-17 (d)).

Table 4-10 Calculation results under uniaxial loads (corresponding to Fig. 4-17)

(a) Under uniaxial tensile load of 12 MPa			
	Analytical solution	**Numerical calculation**	**Error**
K_I	1.7900e6	1.7901e6	0.006 %
K_{II}	0	0	0
Critical crack length (m)	0.0142	0.0142	0.007 %
Life time	0.3972 (s)	0.3976 (s)	0.1 %
Failure mode	$K_I \geq K_{IC}$	$K_I \geq K_{IC}$	0
(b) Under uniaxial tensile load of 12 MPa			
	Analytical solution	**Numerical calculation**	**Error**
K_I	1.7885e6	1.7886e6	0.006 %
K_{II}	1.7885e6	1.7886e6	0.006 %
Critical crack length (m)	0.0566	0.0566	0.002 %
Life time	3.7867e9 (s) (120 y, 28 d, 1 h, 59 min.)	3.7898e9 (s) (120 y, 62 d, 20 h, 27 min.)	0.08 %
Failure mode	Crack length > zone size	Crack length > zone size	0
(c) Under uniaxial compressive load of 18 MPa			
	Analytical solution	**Numerical calculation**	**Error**
K_I	0	0	0
K_{II}	1.7900e6	1.7900e6	< 0.005 %
Critical crack length (m)	0.0514	0.0514	0.002 %
Life time	1.4612e9 (s) (46 y, 122 d, 11 h, 29 min.)	1.4624e9 (s) (46 y, 135 d, 21 h, 29 min.)	0.08 %
Failure mode	$K_{II} \geq K_{IIC}$	$K_{II} \geq K_{IIC}$	0
(d) Under uniaxial compressive load of 18 MPa			
	Analytical solution	**Numerical calculation**	**Error**
K_I	0	0	0
K_{II}	1.7358e6	1.7358e6	< 0.005 %
Critical crack length (m)	0.046188	0.046189	0.002 %
Life time	6.8109e8 (s) (21 y, 218 d, 40 min.)	6.8163 (s) (21 y, 224 d, 6 h, 45 min.)	0.08 %
Failure mode	Crack length > zone size	Crack length > zone size	0

The lifetime is influenced greatly by the crack condition. For example, under the same tensile load (12 MPa), the zone fails in less than 1 second if the crack orientation is 0º; while with crack orientation of 45º, the lifetime of the zone is more than 120 years (Table 4-10). This feature is also seen in the compressive tests: under the compressive load of 18 MPa, the zone fails in more than 46 years if the crack orientation is 45º,

while with crack orientation of 60º, the lifetime of the zone is less than 22 years (Table 4-10). The analytical solution of the lifetime for each case in Fig. 4-17 is also listed in Table 4-10. It is seen that the predicted lifetimes and other related parameters have shown good agreement with the analytical solutions (Eq. 4-14) in all cases (deviations no bigger than 0.1 % for lifetimes; deviations no bigger than 0.006 % for K values; deviation no bigger than 0.007 % for critical crack lengths). In all cases the correct fracture mode was predicted.

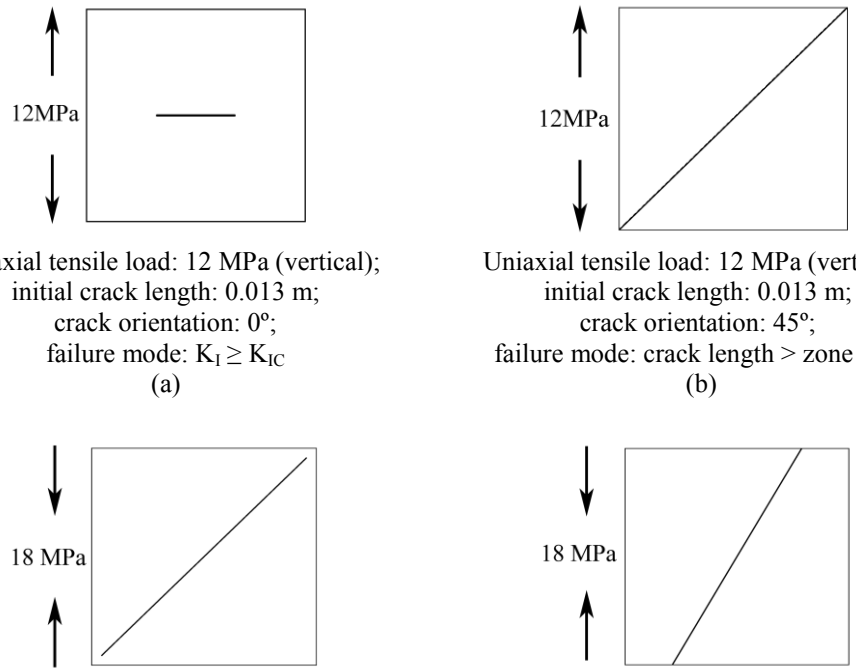

Uniaxial tensile load: 12 MPa (vertical);
initial crack length: 0.013 m;
crack orientation: 0º;
failure mode: $K_I \geq K_{IC}$
(a)

Uniaxial tensile load: 12 MPa (vertical);
initial crack length: 0.013 m;
crack orientation: 45º;
failure mode: crack length > zone size
(b)

Uniaxial compressive load: -18 MPa (vertical);
initial crack length: 0.013 m;
crack orientation: 45º;
failure mode: $K_{II} \geq K_{IIC}$
(c)

Uniaxial compressive load: -18 MPa (vertical);
initial crack length: 0.013 m;
crack orientation: 60º;
failure mode: crack length > zone size
(d)

Figure 4-17 Crack condition at failure under uniaxial loads

To further test the applicability of the lifetime prediction for the fixed orientation model, biaxial loading condition has also been investigated (major principal stress applied vertically). Still considering one zone with different biaxial loading configurations, the simulation results are shown in Fig. 4-18. It is seen that under biaxial tensile loads, the zone fails by $K_I \geq K_{IC}$ if the crack orientation is 45º, and fails by crack reaching the zone boundary if the crack orientation is 50º (magnitudes of loads are seen in Fig. 4-18 (a), (b)). Zone failure by $K_{II} \geq K_{IIC}$ has not been found in the numerical simulations. This phenomenon is supported by the theory: under biaxial tensile loads, it is known from the stresses condition on the crack (Eq. 4-9 and 4-10) that the normal stress on the crack is always bigger than the shear stress. This makes the K_I value always bigger than K_{II} value (Eq. 4-11 and 4-12) (in this case the effective shear stress is equal to the shear stress). So in biaxial tensile loading condition, failure by $K_{II} \geq K_{IIC}$ is not possible. With the major principal stress being tensile and minor principal stress being compressive, cases where zone fails by $K_I \geq K_{IC}$, by $K_{II} \geq K_{IIC}$ and by crack reaching the zone boundary have all been found

with different magnitudes of loads and crack characteristics (Fig. 4-18 (c), (d) and (e)), such is also the case if the major principal stress is compressive and the minor principal stress is tensile (Fig. 4-18 (f), (g) and (h)). Under biaxial compressive loads, only zone failure by $K_{II} \geq K_{IIC}$ or by crack reaching the zone boundary has been found. This phenomenon is also supported by theory: in this case, the normal stress on the crack is always compressive, so the crack is not under Mode I loading condition, thus failure by $K_I \geq K_{IC}$ is not possible. The numerical predicted lifetimes have shown excellent agreement with the analytical solutions in all cases. It is shown (Table 4-11) that the deviations between the numerical predicted lifetime and the analytical solution has been no bigger than 0.08 % for all loading configurations. For the stress intensity factor K_I and K_{II} at failure, the deviations between the numerical calculation and analytical result has been no bigger than 0.009 %. For the critical crack length, the deviations have been no bigger than 0.005 %. In all cases the correct fracture mode was predicted.

The failure of the zone under different loading configurations has been studied exhaustively, where every possible loading condition has been modeled, and every possible failure mode under corresponding loads has been found. The numerical results have shown excellent agreement with the analytical results with respect to the important parameters related to lifetime. Especially, the numerical predicted lifetime has been found in good agreement with the analytical solution. The simulation results proved the applicability of the lifetime prediction scheme for fixed orientation model to any complex stress conditions, and formed the base for extending this model scheme to a multi-zone numerical model.

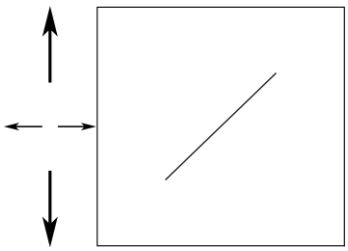

Principal stresses: 12 MPa, 6 MPa;
crack orientation: 45º;
failure mode: $K_I \geq K_{IC}$
(a)

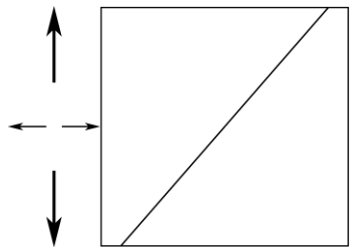

Principal stresses: 12 MPa, 2 MPa;
crack orientation: 50º;
failure mode: crack length > zone size
(b)

Loading case I: major principal stress (vertical): tensile;
minor principal stress (horizontal): tensile

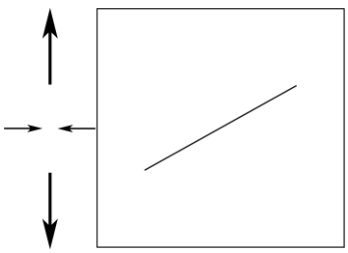

Principal stresses: 12 MPa, -2 MPa;
crack orientation: 30º;
failure mode: $K_I \geq K_{IC}$
(c)

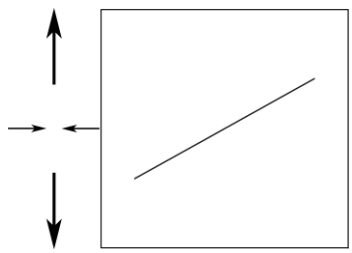

Principal stresses: 12 MPa, -6 MPa;
crack orientation: 30º;
failure mode: $K_{II} \geq K_{IIC}$
(d)

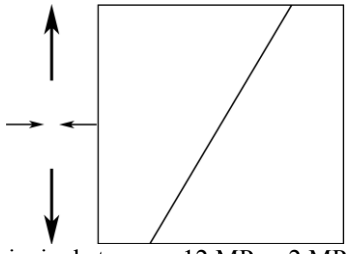

Principal stresses: 12 MPa, -2 MPa;
crack orientation: 60º;
failure mode: crack length > zone size

(e)

Loading case II: major principal stress (vertical): tensile;
minor principal stress (horizontal): compressive

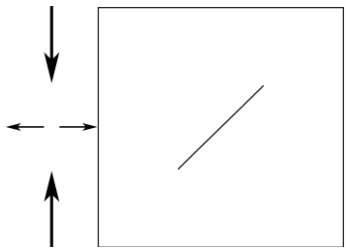

Principal stresses: -18 MPa, 6 MPa;
crack orientation: 45º;
failure mode: $K_{II} \geq K_{IIC}$

(f)

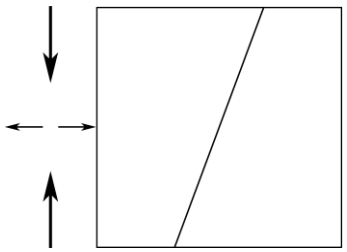

Principal stresses: -18 MPa, 2 MPa;
crack orientation: 70º;
failure mode: crack length > zone size

(g)

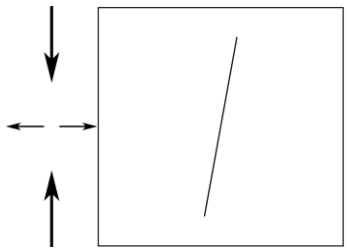

Principal stresses: -18 MPa, 9 MPa;
crack orientation: 80º;
failure mode: $K_I \geq K_{IC}$

(h)

Loading case III: major principal stress (vertical): compressive;
minor principal stress (horizontal): tensile

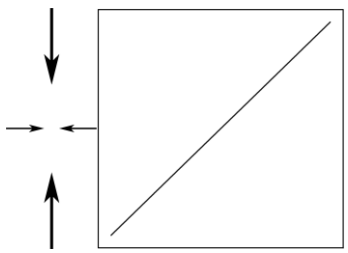

Principal stresses: -20 MPa, -1 MPa;
crack orientation: 45º;
failure mode: $K_{II} \geq K_{IIC}$

(i)

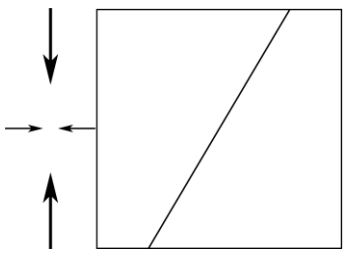

Principal stresses: -20 MPa, -1 MPa;
crack orientation: 60º;
failure mode: crack length > zone size

(j)

Loading case IV: major principal stress (vertical): compressive;
minor principal stress(horizontal): compressive

Figure 4-18 Crack condition at failure under biaxial loads (Initial crack length: 0.013 m)

Table 4-11 Calculation results under biaxial loads (corresponding to Fig. 4-18)

Loading case I			
(a)			
	Analytical solution	**Numerical calculation**	**Error**
K_I	1.7900e6	1.7900e6	< 0.005 %
K_{II}	5.9667e5	5.9668e5	0.002 %
Critical crack length (m)	0.025183	0.025184	0.004 %
Life time (s)	8,727 (2 h, 25 min.)	8,734 (2 h, 25 min.)	0.08 %
Failure mode	$K_I \geq K_{IC}$	$K_I \geq K_{IC}$	0
(b)			
	Analytical solution	**Numerical calculation**	**Error**
K_I	1.7561e6	1.7561e6	< 0.005 %
K_{II}	1.4102e6	1.4102e6	< 0.006 %
Critical crack length (m)	0.052216	0.052217	0.002 %
Life time (s)	3.6382e9 115 y, 134 d, 1 h, 5 min.)	3.6411e9 (115 y, 167 d, 10 h, 49 min.)	0.08 %
Failure mode	Crack length > zone size	Crack length > zone size	0
Loading case II			
(c)			
	Analytical solution	**Numerical calculation**	**Error**
K_I	1.7900e6	1.7900e6	< 0.005 %
K_{II}	1.2766e6	1.2766e6	< 0.007 %
Critical crack length (m)	0.028232	0.028233	0.004 %
Life time (s)	5.9983e4 (16 h, 39 min.)	6.0031e4 (16 h, 40 min.)	0.08 %
Failure mode	$K_I \geq K_{IC}$	$K_I \geq K_{IC}$	0
(d)			
	Analytical solution	**Numerical calculation**	**Error**
K_I	1.7224e6	1.7225e6	0.006 %
K_{II}	1.7900e6	1.7900e6	< 0.005 %
Critical crack length (m)	0.033577	0.033578	0.003 %
Life time (s)	8.7639e5 (10 d, 3 h, 26 min.)	8.7708e5 (10 d, 3 h, 38 min.)	0.08 %
Failure mode	$K_{II} \geq K_{IIC}$	$K_{II} \geq K_{IIC}$	0
(e)			
	Analytical solution	**Numerical calculation**	**Error**
K_I	4.0403e5	4.0404e5	0.002 %
K_{II}	1.6329e6	1.6329e6	< 0.006 %
Critical crack length (m)	0.046188	0.046189	0.002 %
Life time (s)	5.3494e9 (169 y, 228 d, 23 h, 6 min.)	5.3536e9 (169 y, 278 d, 1 h, 54 min.)	0.08 %
Failure mode	Crack length > zone size	Crack length > zone size	0

Loading case III			
(f)			
	Analytical solution	**Numerical calculation**	**Error**
K_I	0	0	0
K_{II}	1.7900e6	1.7900e6	< 0.005 %
Critical crack length (m)	0.019606	0.019607	0.005 %
Life time (s)	127 (2 min, 7 s)	128 (2 min, 8 s)	0.08 %
Failure mode	$K_{II} \geq K_{IIC}$	$K_{II} \geq K_{IIC}$	0
(g)			
	Analytical solution	**Numerical calculation**	**Error**
K_I	0	0	0
K_{II}	1.6358e6	1.6358e6	< 0.006 %
Critical crack length (m)	0.042567	0.042567	< 0.002 %
Life time (s)	1.2717e9 (40 y, 118 d, 14 h, 22 min.)	1.2727e9 (40 y, 130 d, 6 h, 36 min.)	0.08 %
Failure mode	Crack length > zone size	Crack length > zone size	0
(h)			
	Analytical solution	**Numerical calculation**	**Error**
K_I	1.7900e6	1.7900e6	< 0.005 %
K_{II}	1.0097e6	1.0097e6	< 0.009 %
Critical crack length (m)	0.030441	0.030442	0.003 %
Life time (s)	2.1359e5 (2 d, 11 h, 19 min.)	2.1376e5 (2 d, 11 h, 22 min.)	0.08 %
Failure mode	$K_I \geq K_{IC}$	$K_I \geq K_{IC}$	0
Loading case IV			
(i)			
	Analytical solution	**Numerical calculation**	**Error**
K_I	0	0	0
K_{II}	1.7900e6	1.7900e6	< 0.005 %
Critical crack length (m)	0.050587	0.050588	0.002 %
Life time (s)	1.1193e9 (35 y, 179 d, 17 h, 54 min.)	1.1202e9 (35 y, 190 d, 33 min.)	0.08 %
Failure mode	$K_{II} \geq K_{IIC}$	$K_{II} \geq K_{IIC}$	0
(j)			
	Analytical solution	**Numerical calculation**	**Error**
K_I	0	0	0
K_I	1.7514e6	1.7514e6	< 0.005 %
Critical crack length (m)	0.046188	0.046189	0.002 %
Life time (s)	5.0344e8 (15 y, 351 d, 21 h, 19 min.)	5.0384e8 (15 y, 356 d, 12 h, 16 min.)	0.08 %
Failure mode	Crack length > zone size	Crack length > zone size	0

Before the fixed orientation model scheme is extended to a multi-zone numerical model, more simulations have been performed with the same material parameters but different loadings or crack conditions (length and orientation) to study how they influence the lifetime. Lifetime results of the zone under different constant uniaxial

loads, initial crack lengths and crack orientations are listed in Table 4-12, 4-13 and 4-14, respectively. To illustrate how these factors influence the lifetime, the numerical results corresponding to the tables are also shown in Fig. 4-19, 4-20 and 4-21, respectively.

Table 4-12 Uniaxial tests under different constant loads (corresponding to Fig. 4-19)

(a) Under tensile loads			
Load (MPa)	**Lifetime (s) (Analytical solution)**	**Lifetime (s) (Numerical calculation)**	**Failure mode**
11	7.1224e10 (2,258 y, 179 d, 5 h, 16 min.)	7.1280e10 (2,260 y, 103 d, 4 h, 22 min.)	Crack length > zone size
15	2.0424e6 (23 d, 15 h, 19 min.)	2.0440e6 (23 d, 15 h, 46 min.)	$K_I \geq K_{IC}$
20	124 (2 m, 4 s)	124 (2 m, 4 s)	$K_I \geq K_{IC}$
22	4.9	4.9	$K_I \geq K_{IC}$
24	0.2	0.2	$K_I \geq K_{IC}$
(b) Under compressive loads			
Load (MPa)	**Lifetime (s) (Analytical solution)**	**Lifetime (s) (Numerical calculation)**	**Failure mode**
16	7.7581e10 (2,460 y, 33 d, 15 h, 14 min.)	7.7643e10 (2,462 y, 15 d, 23 h, 20 min.)	Crack length > zone size
20	4.1843e7 (1 y, 119 d, 7 h, 3 min.)	4.1876e7 (1 y, 119 d, 16 h, 16 min.)	$K_{II} \geq K_{IIC}$
22	1.6816e6 (19 d, 11 h, 6 min.)	1.6829e6 (19 d, 11 h, 28 min.)	$K_{II} \geq K_{IIC}$
24	8.9405e4 (1 d, 50 min.)	8.9475e4 (1 d, 51 min.)	$K_{II} \geq K_{IIC}$

It is seen in Table 4-12 that, with the initial crack length of 0.013 m and crack orientation of 45º unchanged, in the tensile tests, the zone fails by crack reaching the zone boundary under tensile load of 11 MPa, while fails by $K_I \geq K_{IC}$ under bigger load. In the compressive tests, the zone fails by crack reaching the zone boundary under compressive load of 16 MPa, while fails by $K_{II} \geq K_{IIC}$ under bigger load. It is seen in Table 4-13 that, with the crack orientation of 45º unchanged, under the tensile load of 12 MPa, the zone fails by crack reaching the zone boundary with the initial crack length ranging from 0.011 m to 0.033 m; while under the compressive load of 18 MPa, the zone fails by $K_{II} \geq K_{IIC}$ with the initial crack length ranging from 0.011 m to 0.027 m. It is seen in Table 4-14 that, with the initial crack length of 0.013 m unchanged, under the tensile load of 12 MPa, the zone fails by $K_I \geq K_{IC}$ if the crack orientation is smaller than 45º, while the zone fails by crack reaching the zone boundary if the crack is equal to or bigger than 45º. Under the compressive load of 18 MPa, the zone fails by $K_{II} \geq K_{IIC}$ for the crack orientation ranging from 45º to 55º,

while for crack orientation smaller than 45º or bigger than 55º, the zone fails by crack reaching the zone boundary.

Table 4-13 Uniaxial tests with different initial crack lengths (corresponding to Fig. 4-20)

(a) Under tensile load of 12 MPa			
Initial crack length (m)	**Lifetime (s) (Analytical solution)**	**Lifetime (s) (Numerical calculation)**	**Failure mode**
0.011	5.3585e10 (1,699 y, 61 d, 14 h, 50 min.)	5.3627e10 (1,700 y, 188 d, 15 h)	Crack length > zone size
0.013	3.7867e9 (120 y, 28 d, 1 h, 59 min.)	3.7898e9 (120 y, 62 d, 20 h, 27 min.)	Crack length > zone size
0.015	3.9129e8 (12 y, 148 d, 18 h, 40 min.)	3.9160e8 (12 y, 152 d, 8 h, 53 min.)	Crack length > zone size
0.017	5.3739e7 (1 y, 256 d, 23 h, 30 min.)	5.3782e7 (1 y, 257 d, 11 h, 21 min.)	Crack length > zone size
0.025	1.1847e5 (1 d, 8 h, 54 min.)	1.1856e5 (1 d, 8 h, 56 min.)	Crack length > zone size
0.033	1,448 (24 min., 8 s)	1,449 (24 min., 9 s)	Crack length > zone size
(b) Under compressive load of 18 MPa			
Initial crack length (m)	**Lifetime (s) (Analytical solution)**	**Lifetime (s) (Numerical calculation)**	**Failure mode**
0.011	2.0677e10 (655 y, 247 d, 20 h, 36 min.)	2.0694e10 (656 y, 72 d, 17 h, 9 min.)	$K_{II} \geq K_{IIC}$
0.015	1.5099e8 (4 y, 287 d, 13 h, 47 min.)	1.5111e8 (4 y, 288 d, 23 h, 4 min.)	$K_{II} \geq K_{IIC}$
0.019	3.5526e6 (41 d, 2 h, 50 min.)	3.5555e6 (41 d, 3 h, 37 min.)	$K_{II} \geq K_{IIC}$
0.023	1.7157e5 (1 d, 23 h, 39 min.)	1.7170e5 (1 d, 23 h, 41 min.)	$K_{II} \geq K_{IIC}$
0.027	1.3486e4 (3 h, 44 min.)	1.3496e4 (3 h, 44 min.)	$K_{II} \geq K_{IIC}$

Table 4-14 Uniaxial tests with different crack orientations (corresponding to Fig. 4-21)

(a) Under tensile load of 12 MPa			
Crack orientation	**Lifetime (s) (Analytical solution)**	**Lifetime (s) (Numerical calculation)**	**Failure mode**
0º	0.4	0.4	$K_I \geq K_{IC}$
10º	1.4	1.4	$K_I \geq K_{IC}$
20º	35	35	$K_I \geq K_{IC}$
30º	8,727 (2 h, 25 min.)	8,734 (2 h, 25 min.)	$K_I \geq K_{IC}$
40º	3.4125e7 (1 y, 29 d, 23 h, 8 min.)	3.4152e7 (1 y, 30 d, 6 h, 39 min.)	$K_I \geq K_{IC}$
45º	3.7867e9 (120 y, 28 d, 1 h, 59 min.)	3.7898e9 (120 y, 62 d, 20 h, 27 min.)	Crack length > zone size
50º	1.2657e10 (401 y, 130 d, 14 h, 15 min.)	1.2667e10 (401 y, 246 d, 19 h, 26 min.)	Crack length > zone size

(b) Under compressive load of 18 MPa			
Crack orientation	**Lifetime (s) (Analytical solution)**	**Lifetime (s) (Numerical calculation)**	**Failure mode**
40º	4.4145e10 (1,399 y, 297 d, 13 h, 51 min.)	4.4180e10 (1,400 y, 337 d, 21 h, 42 min.)	Crack length > zone size
45º	1.4612e9 (46 y, 122 d, 11 h, 29 min.)	1.4624e9 (46 y, 135 d, 21 h, 29 min.)	$K_{II} \geq K_{IIC}$
50º	2.5840e8 (8 y, 70 d, 17 h, 28 min.)	2.5860e8 (8 y, 73 d, 2 h, 25 min.)	$K_{II} \geq K_{IIC}$
55º	2.0204e8 (6 y, 148 d, 8 h, 54 min.)	2.0220e8 (6 y, 150 d, 5 h, 26 min.)	$K_{II} \geq K_{IIC}$
60º	6.8109e8 (21 y, 218 d, 40 min.)	6.8163e8 (21 y, 224 d, 6 h, 45 min.)	Crack length > zone size
65º	1.1255e10 (356 y, 327 d, 19 h, 42 min.)	1.1264e10 (357 y, 66 d, 3 h, 55 min.)	Crack length > zone size

Fig. 4-19 shows that the zone fails faster under a bigger load under both tensile and compressive load. It is also noticed that under the same magnitude of load, the zone fails much faster under tension than under compression. With other factors remaining the same, a longer initial crack length would also cause the zone to fail faster under both tensile load and compressive load (Fig. 4-20). It is also seen in Fig. 4-21 that under a constant tensile load (12 MPa), the lifetime ascends while the orientation becomes bigger (the lifetime is less than one second at 0º and over 400 years at 50º). While under a compressive load (18 MPa), the lifetime descends first and then ascends as the crack orientation becomes bigger, and the shortest lifetime (less than 6 years 6 months) is obtained at an orientation of about 55º.

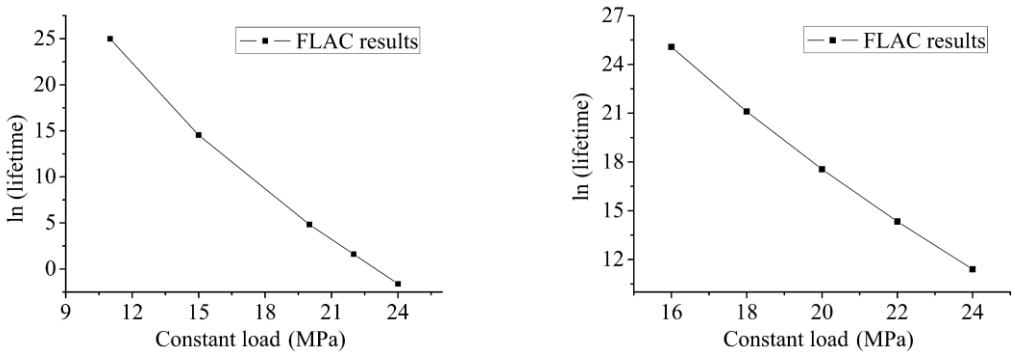

(a) Initial crack length: 0.013 m; Crack orientation: 45º (Uniaxial tensile loads)

(b) Initial crack length: 0.013 m; Crack orientation: 45º (Uniaxial compressive loads)

Figure 4-19 Natural logarithm of lifetimes (seconds) with different constant loads

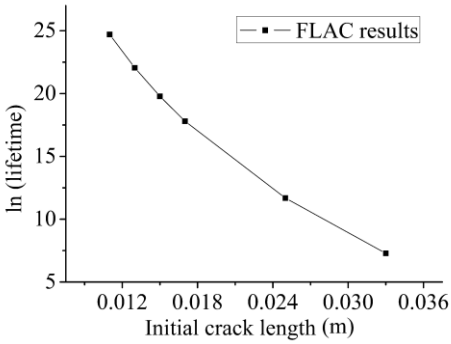

(a) Uniaxial tensile load: 12 MPa; Crack orientation: 45º

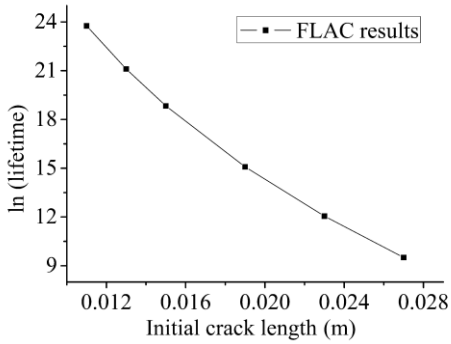

(b) Uniaxial compressive load: 18 MPa; Crack orientation: 45º

Figure 4-20 Natural logarithm of lifetimes (seconds) with different initial crack lengths

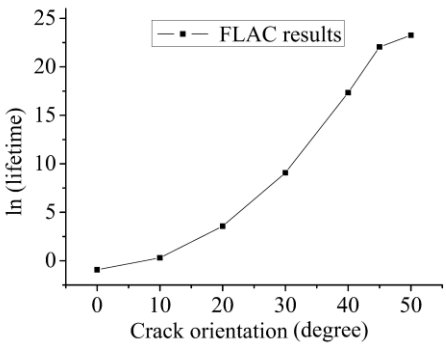

(a) Uniaxial tensile load: 12MPa; Initial crack length: 0.013 m

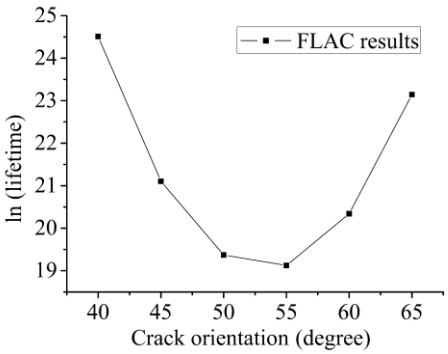

(b) Uniaxial compressive load: 18 MPa; Initial crack length: 0.013 m

Figure 4-21 Natural logarithm of lifetimes (seconds) with different crack orientations

4.4.3 Study on the multi-zone models

The lifetime prediction scheme for fixed orientation model has been extended to the multi-zone model. The geometry is the same as for the basic model. The material parameters follow Tabel 4-1, except that the tensile strength has been assigned larger for some cases. This measure was taken to put the focus on the crack's subcritical crack growth instead of triggering a sudden tensile failure. A zone's sudden tensile failure could be otherwise caused by the stress exceeding the tensile strength due to the stress redistributions. The initial crack lengths follow the normal distribution (initial crack length data from realizations of model A, B and C in Fig. 4-3). Another model (named model D) with initial crack lengths following lognormal distribution (Fig. 4-22) has also been tested. As for the crack orientation, both the uniform and normal distributions of crack orientation have been applied to the numerical model. The crack orientation distribution patterns are seen in Fig. 4-23 and 4-24; the corresponding initial crack conditions are illustrated in Fig. 4-25 and 4-26, respectively.

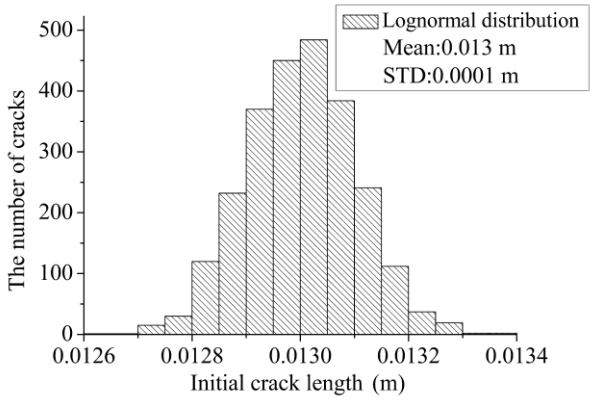

Figure 4-22 Lognormal distribution of initial crack lengths (model D)

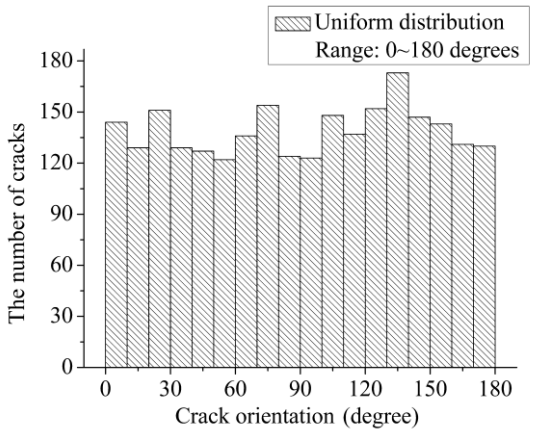

Figure 4-23 Uniform distribution of crack orientation

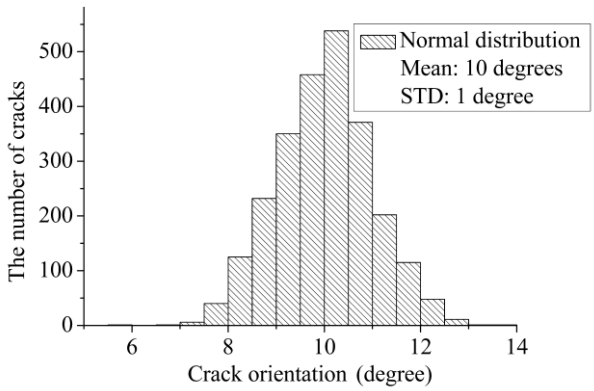

Figure 4-24 Normal distribution of crack orientation (Mean value: 10º; standard deviation: 1º)

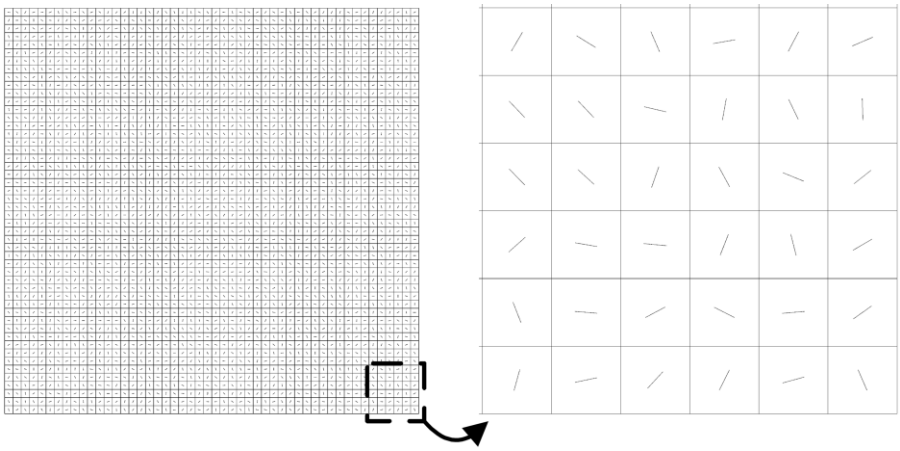

Figure 4-25 Initial crack conditions of fixed orientation model (Initial crack lengths (realization: model A): normal distribution, mean = 0.013 m, STD = 0.0001 m; initial crack orientation: uniform distribution)

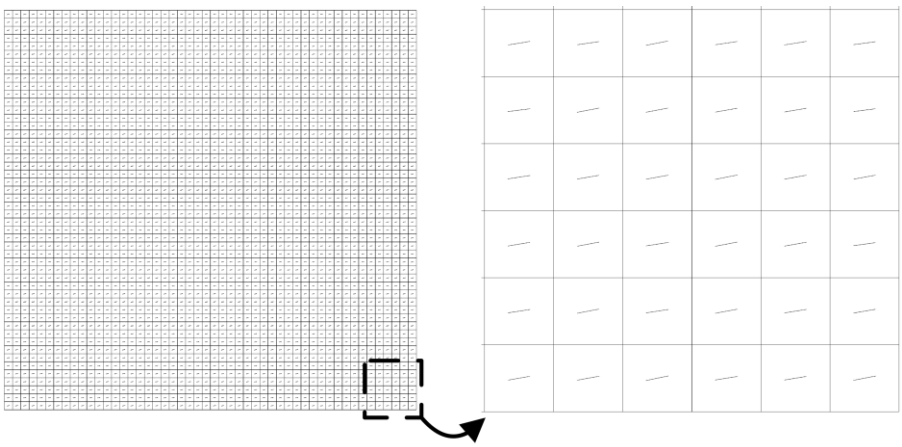

Figure 4-26 Initial crack conditions of fixed orientation model (Initial crack lengths (realization: model A): normal distribution, mean = 0.013 m, STD = 0.0001 m; initial crack orientation: normal distribution, mean = 10º, STD = 1º)

For the tensile tests, the failure process of the models under a constant load of 12 MPa is shown in Fig. 4-27 to Fig. 4-30, where for the normal crack orientation distribution, the mean orientation was set to 10º and standard deviation (STD) 1º. The corresponding lifetime results are listed in Table 4-15.

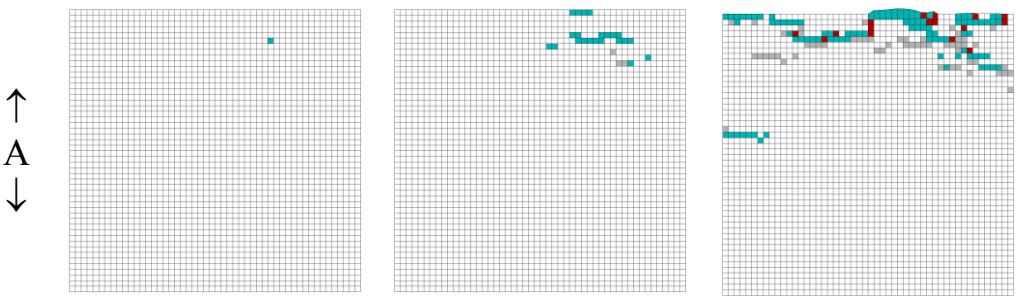

0.2864 second 0.3040 second 0.3600 second

Initial crack lengths: normal distribution, mean = 0.013 m, STD = 0.0001 m

Initial crack orientation: uniform distribution

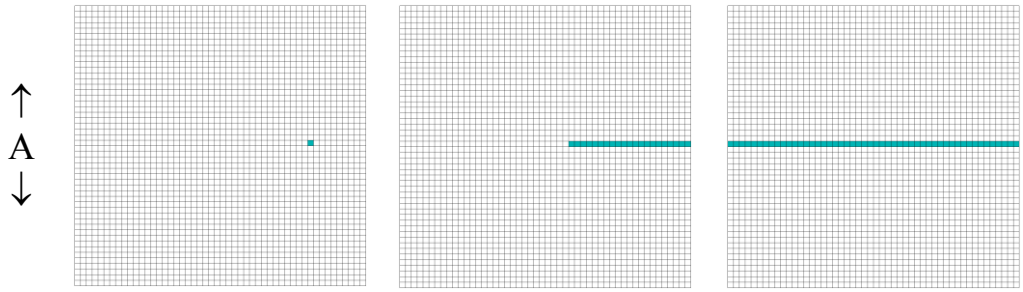

0.4704 second 0.4739 second 0.4826 second

Initial crack lengths: normal distribution, mean = 0.013 m, STD = 0.0001 m

Initial crack orientation: normal distribution, mean = 10º, STD = 1º

Figure 4-27 Uniaxial tensile tests (12 MPa) of model A (zones in green: tensile failure; zones in red: shear failure; zones in gray: failed in past)

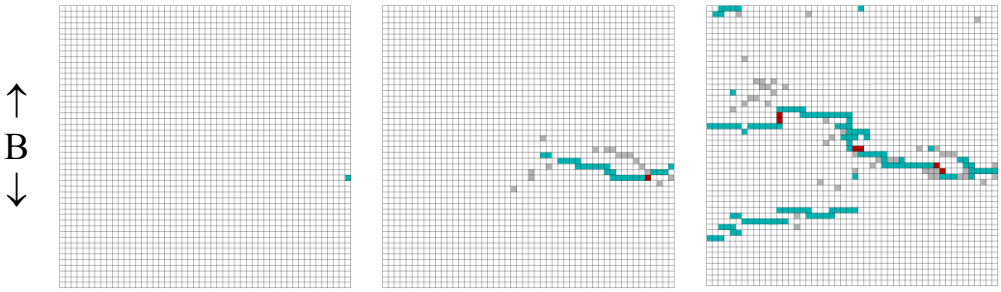

0.2496 second 0.2931 second 0.3734 second

Initial crack lengths: normal distribution, mean = 0.013 m, STD = 0.0001 m

Initial crack orientation: uniform distribution

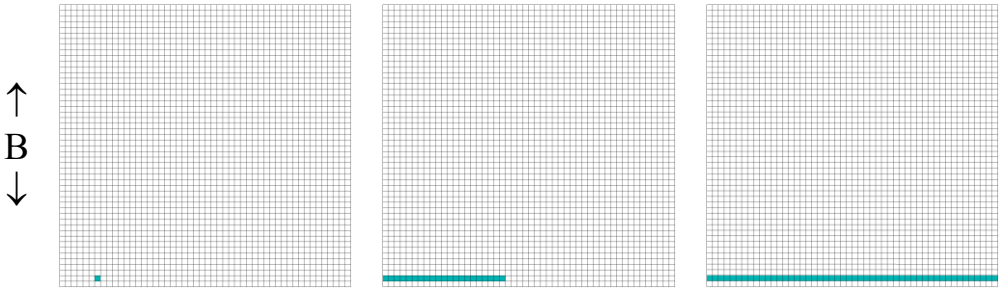

0.5800 second 0.5804 second 0.5811 second

Initial crack lengths: normal distribution, mean = 0.013 m, STD = 0.0001 m

Initial crack orientation: normal distribution, mean = 10º, STD = 1º

Figure 4-28 Uniaxial tensile tests (12 MPa) of model B (zones in green: tensile failure; zones in red: shear failure; zones in gray: failed in the past)

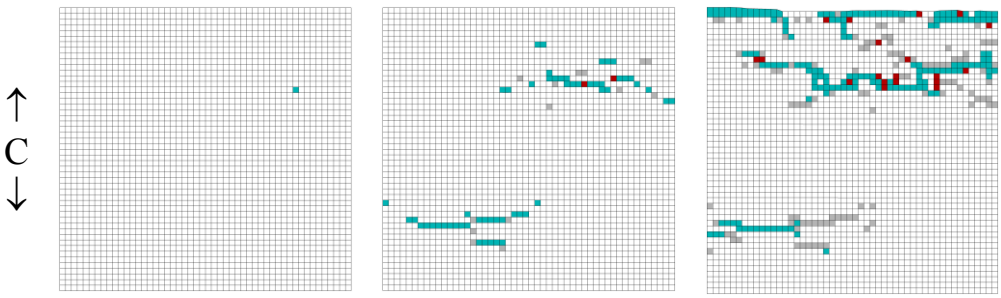

0.2488 second 0.3202 second 0.4224 second

Initial crack lengths: normal distribution, mean = 0.013 m, STD = 0.0001 m

Initial crack orientation: uniform distribution

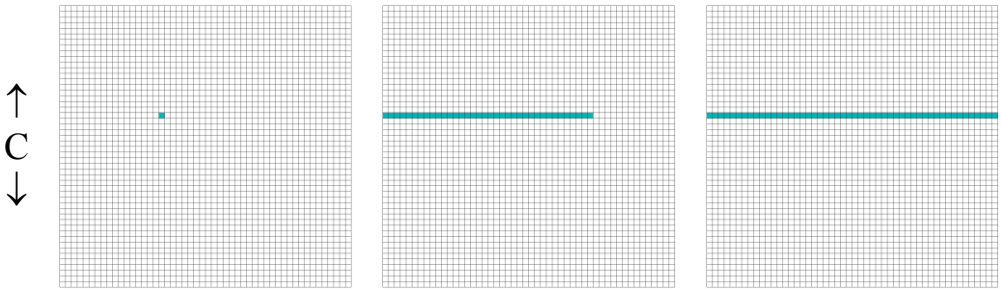

0.5968 second 0.6023 second 0.6064 second

Initial crack lengths: normal distribution, mean = 0.013 m, STD = 0.0001 m

Initial crack orientation: normal distribution, mean = 10º, STD = 1º

Figure 4-29 Uniaxial tensile tests (12 MPa) of model C (zones in green: tensile failure; zones in red: shear failure; zones in gray: failed in the past)

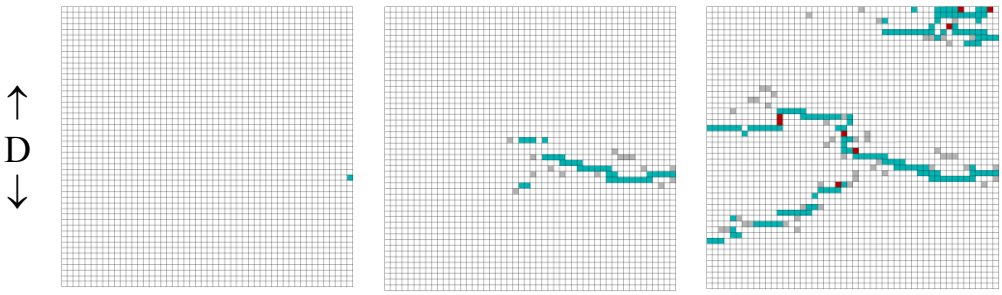

0.2480 second 0.2986 second 0.3620 second

Initial crack lengths: lognormal distribution, mean = 0.013 m, STD = 0.0001 m

Initial crack orientation: uniform distribution

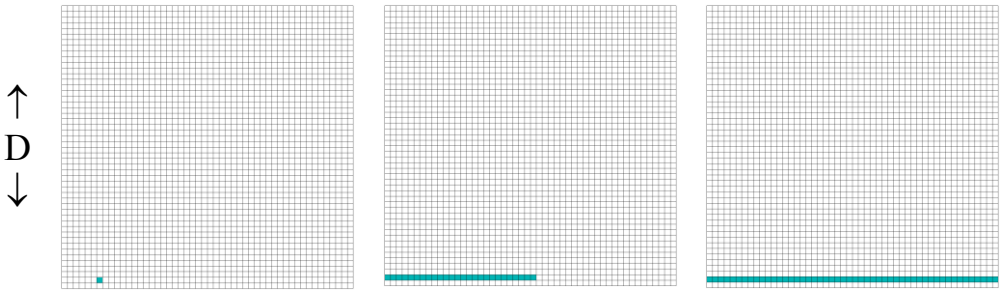

0.5776 second 0.5813 second 0.5858 second

Initial crack lengths: lognormal distribution, mean = 0.013 m, STD = 0.0001 m

Initial crack orientation: normal distribution, mean = 10º, STD = 1º

Figure 4-30 Uniaxial tensile tests (12 MPa) of model D (zones in green: tensile failure; zones in red: shear failure; zones in gray: failed in the past)

Coalescence of the microcracks has been detected in each model. It is seen that under a tensile load, the macroscopic fracture was formed perpendicular to the applied load for normally distributed orientation. It is also seen that the macroscopic fracture pattern is greatly influenced by the initial crack orientation: if crack orientation follows the uniform distribution, despite the fact that the main trend of macroscopic fracture growing direction is still perpendicular to the applied tensile force, the macroscopic fracture showed a more uneven pattern. As is seen from the lifetime

results shown in Table 4-15, for each case, the numerical predicted first zone failure time revealed great agreement with the analytical solution (Eq. 4-14), and the position of the first failure zone also matches the analytical solution. For model A to D, the first zone failure time ranges from 0.2466 seconds to less than 0.2844 seconds, and the lifetimes ranges from 0.3600 seconds to 0.4224 seconds if the initial crack orientation follows uniform distribution. If the initial crack orientation follows normal distribution (mean orientation: 10º, standard deviation (STD: 1º) the first zone failure time ranges from 0.4682 seconds to 0.5948 seconds, and the lifetimes ranges from 0.4826 seconds to 0.6064 seconds. It is concluded that the initial crack orientation also influences the lifetimes. Both the first zone failure time and the lifetime are longer if the initial crack orientation follows normal distribution (mean orientation: 10º, standard deviation (STD: 1º) than if the initial crack orientation follows uniform distribution. The lifetime results and macroscopic failure patterns revealed similarity between the models with different realizations of normal distribution (model A, B and C) and lognormal distribution (model D) of initial crack lengths.

Table 4-15 Lifetime results of models in uniaxial tensile tests (12 MPa)

	Analytical results		**Numerical results**		
Model	**First failure zone**	**First failure time (s)**	**First failure zone**	**First failure time (s)**	**Lifetime (s)**
Initial crack orientation: uniform distribution					
A	(35, 45)	0.2844	(35, 45)	0.2864	0.3600
B	(50, 20)	0.2480	(50, 20)	0.2496	0.3734
C	(41, 36)	0.2469	(41, 36)	0.2488	0.4224
D	(50, 20)	0.2466	(50, 20)	0.2480	0.3620
Initial crack orientation: normal distribution (mean = 10º, STD = 1º)					
A	(41, 26)	0.4682	(41, 26)	0.4704	0.4826
B	(7, 2)	0.5778	(7, 2)	0.5800	0.5811
C	(18, 31)	0.5948	(18, 31)	0.5968	0.6064
D	(7, 2)	0.5761	(7, 2)	0.5776	0.5858

The crack condition of each model at the stage of failure has been studied. Exemplary, the macroscopic fracture of model A with a zoomed in area presenting the microcracks forming the macroscopic fracture is shown in Fig. 4-31 and Fig. 4-32. It is seen that most of the zones forming the macroscopic fracture failed by tension and some of them failed by shear if the crack orientation follows uniform distribution, while all zones failed by tension if the crack orientation follows normal distribution. This indicates the influence of the crack orientation on the failure model of the zone. And it is clearly seen from the zoomed in area that in the failed zones, the microcracks have not reached the zone boundary, which means these zones fail by $K_I \geq K_{IC}$ (zone fails immediately as the crack propagates ultrasonically). Such

phenomenon is also supported by the comparatively short lifetime results (Table 4-15), which implied a sudden failure of the model.

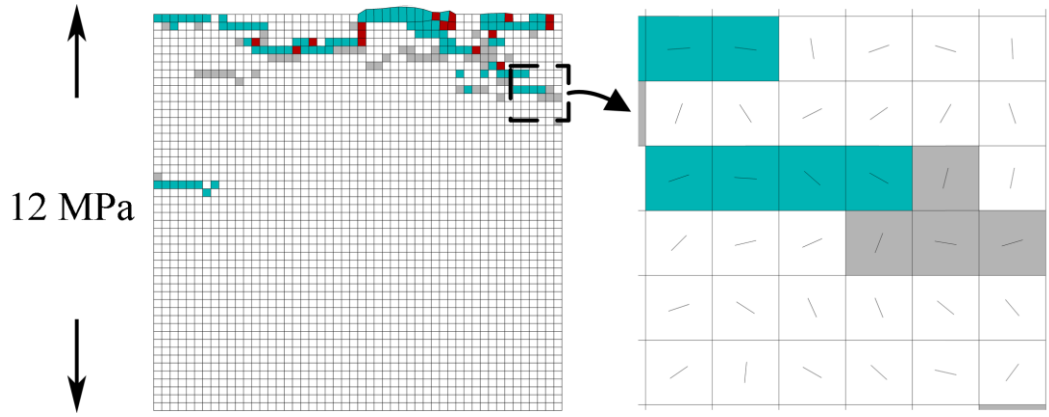

Figure 4-31 Crack condition of model A at failure (zones in green: tensile failure; zones in red: shear failure; zones in gray: failed in the past; initial crack lengths: normal distribution, mean = 0.013 m, STD = 0.0001 m; initial crack orientation: uniform distribution)

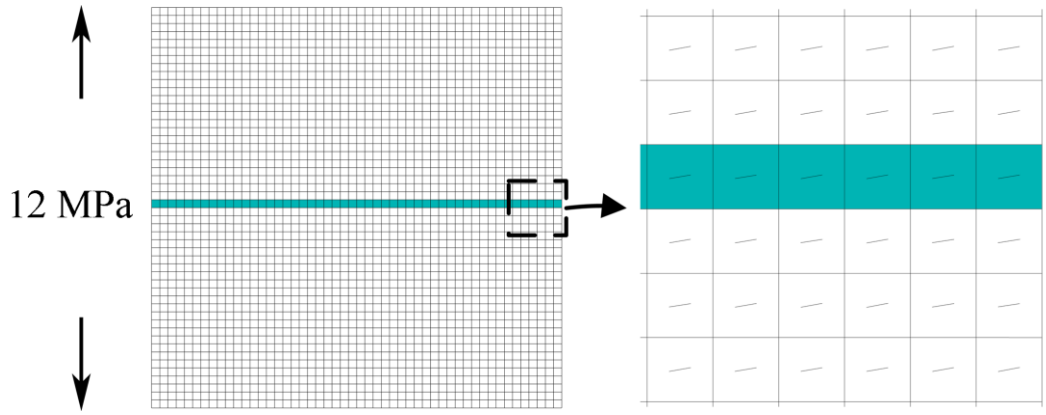

Figure 4-32 Crack condition of model A at failure (zones in green: tensile failure; initial crack lengths: normal distribution, mean = 0.013 m, STD = 0.0001 m; initial crack orientation: normal distribution, mean = 10º, STD = 1º)

The influence of the crack orientation on lifetime has also been studied. For this purpose the initial crack length data of model A (initial crack lengths are normally distributed; mean length: 0.013 m, STD: 0.0001 m) are used. Uniaxial tensile tests have been conducted on the model with different mean orientations. The numerical lifetime results are listed in Table 4-16. Analytical solutions of the position of the first failure zone and first failure time have also been given for comparison. The numerical results have shown great agreement with the analytical solutions with respect to the first zone failure time, and for each mean orientation tried in the test, the position of the first failure zone was predicted correctly (Table 4-16). The predicted lifetime results with different mean orientations of cracks are also shown in Fig. 4-33. It is seen that in principal, the numerical results show the same trends as shown in Fig. 4-21 (a). It takes longer time for the zone to fail if the mean initial crack orientation is

bigger. It is also noticed that the mean orientation has great influence on the lifetime of the model: the lifetime changes from about 0.2 second if the mean crack orientation is 0º to more than 166 years if the mean crack orientation is 50º.

Table 4-16 Lifetime of model A with different mean orientations under tensile load of 12 MPa (initial crack orientation following normal distribution)

	Analytical results		**Numerical results**		
Mean orientation	**First failure zone**	**First failure time (s)**	**First failure zone**	**First failure time (s)**	**Lifetime (s)**
0º	(12, 8)	0.2028	(12, 8)	0.2040	0.2049
5º	(3, 32)	0.2909	(3, 32)	0.2928	0.2941
10º	(41, 26)	0.4682	(41, 26)	0.4704	0.4826
15º	(45, 48)	1.5589	(45, 48)	1.5608	1.5626
20º	(45, 48)	6.4926	(45, 48)	6.5200	6.5231
30º	(45, 48)	550.8	(45, 48)	554.5	554.6
40º	(45, 48)	5.8122e5 (6 d, 17 h, 26 min.)	(45, 48)	5.8422e5 (6 d, 18 h, 16 min.)	5.85315e5 (6 d, 18 h, 35 min.)
50º	(45, 48)	5.0181e9 (159 y, 45 d, 5 h, 20 min.)	(45, 48)	5.2111e9 (165 y, 88 d, 15 h, 46 min.)	5.2558e9 (166 y, 240 d, 13 h, 11 min.)

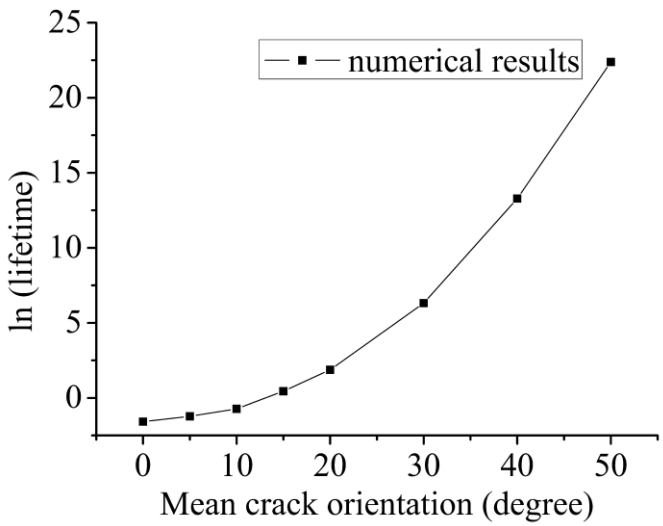

Figure 4-33 Natural logarithm of lifetime (seconds) in uniaxial tensile test (tensile load of 12 MPa) with different mean crack orientation

Uniaxial compressive tests have also been performed on model A, B, C and D. The compressive load of 18 MPa is applied vertically to the model. The crack orientation follows uniform and normal distributions. For those cases where crack orientation follows normal distribution, the mean angle is 45º and the standard deviation is 1º. An additional set of calculations with a standard deviation of initial crack orientation of

5º has been included in each model to study its influence on the macroscopic crack pattern and life time. The failure process of the specific model is documented in Fig. 4-34 to Fig. 4-37. The corresponding lifetime results are also listed in Table 4-17.

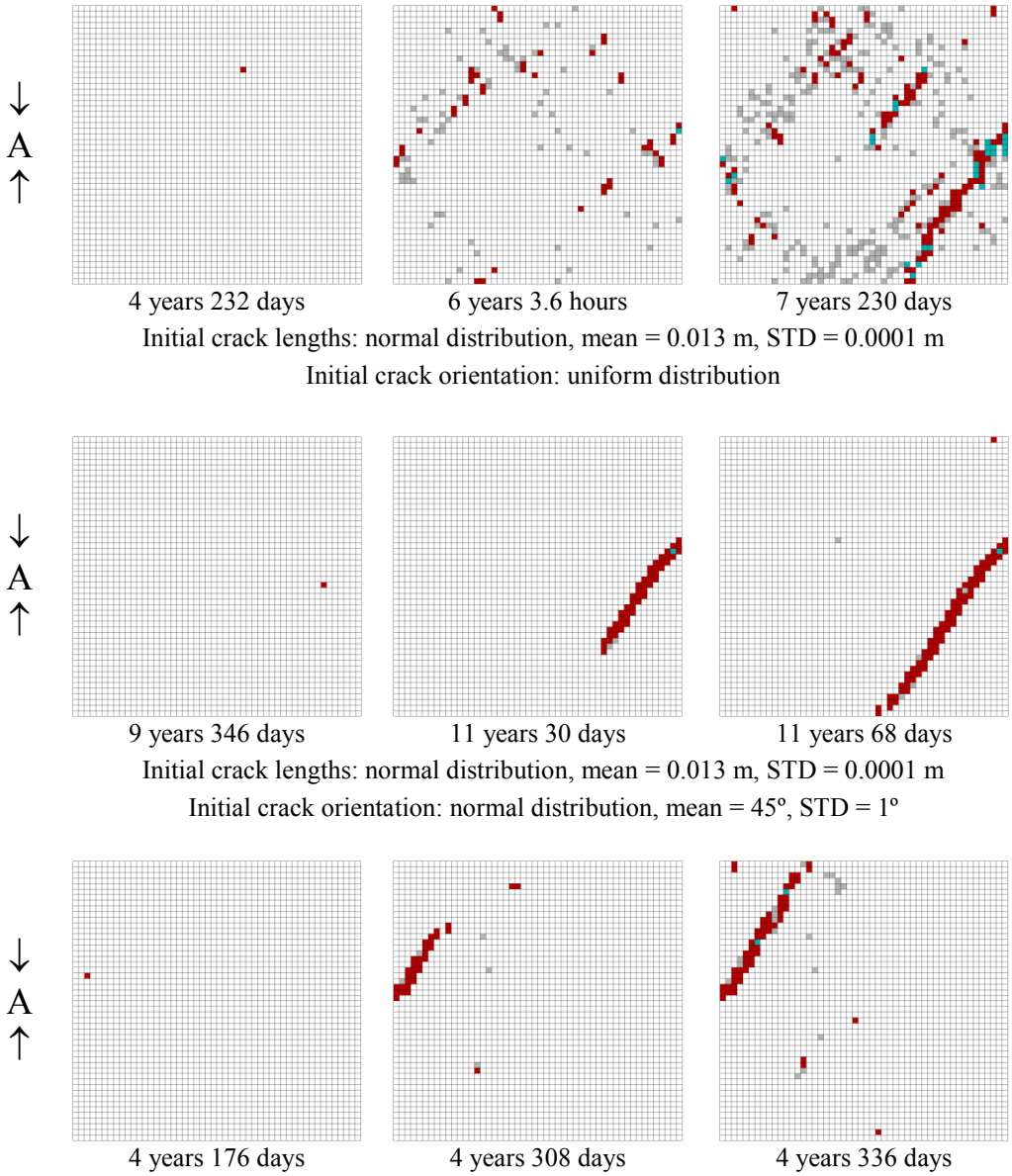

Figure 4-34 Uniaxial compressive tests (18 MPa) of model A (zones in green: tensile failure; zones in red: shear failure; zones in gray: failed in the past)

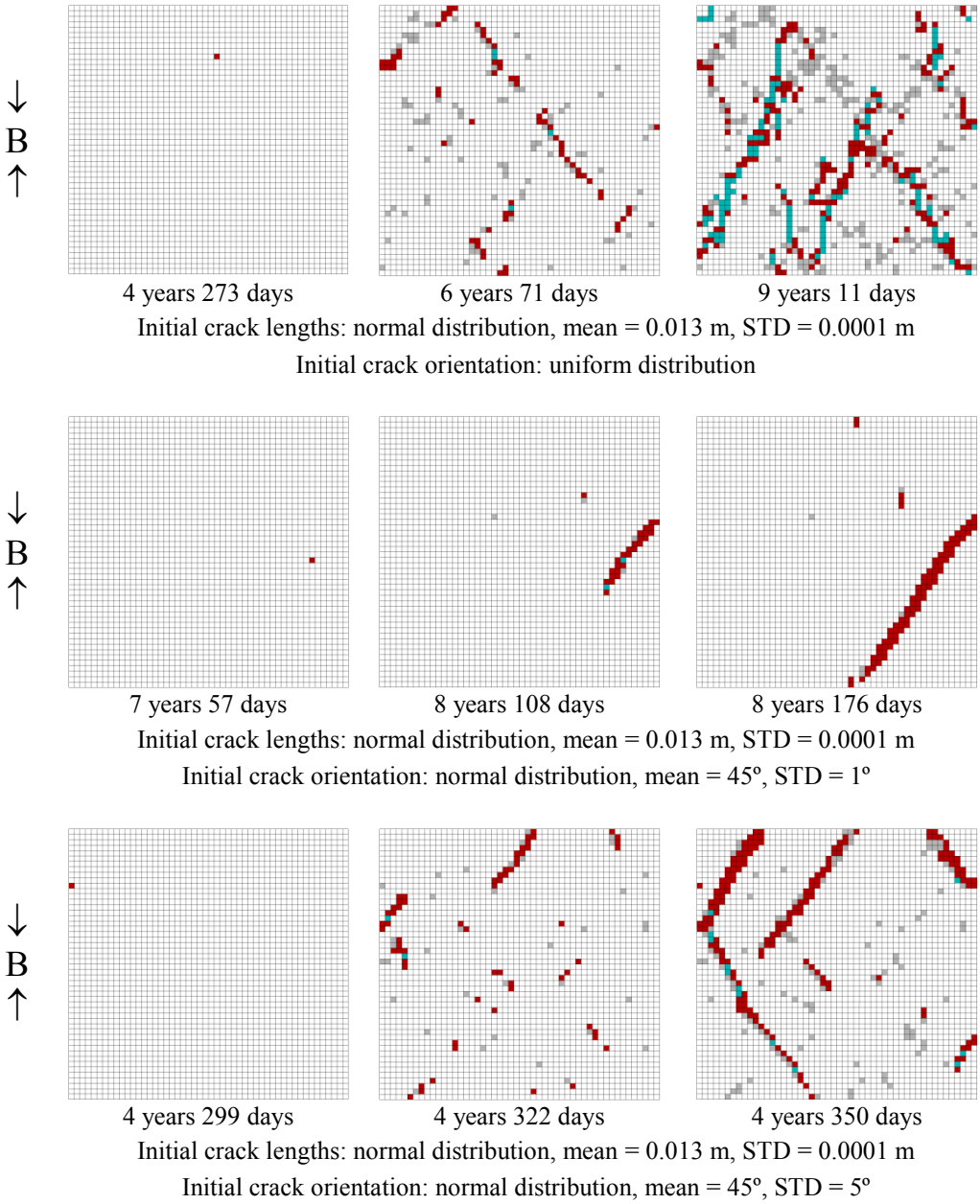

Figure 4-35 Uniaxial compressive tests (18 MPa) of model B (zones in green: tensile failure; zones in red: shear failure; zones in gray: failed in the past)

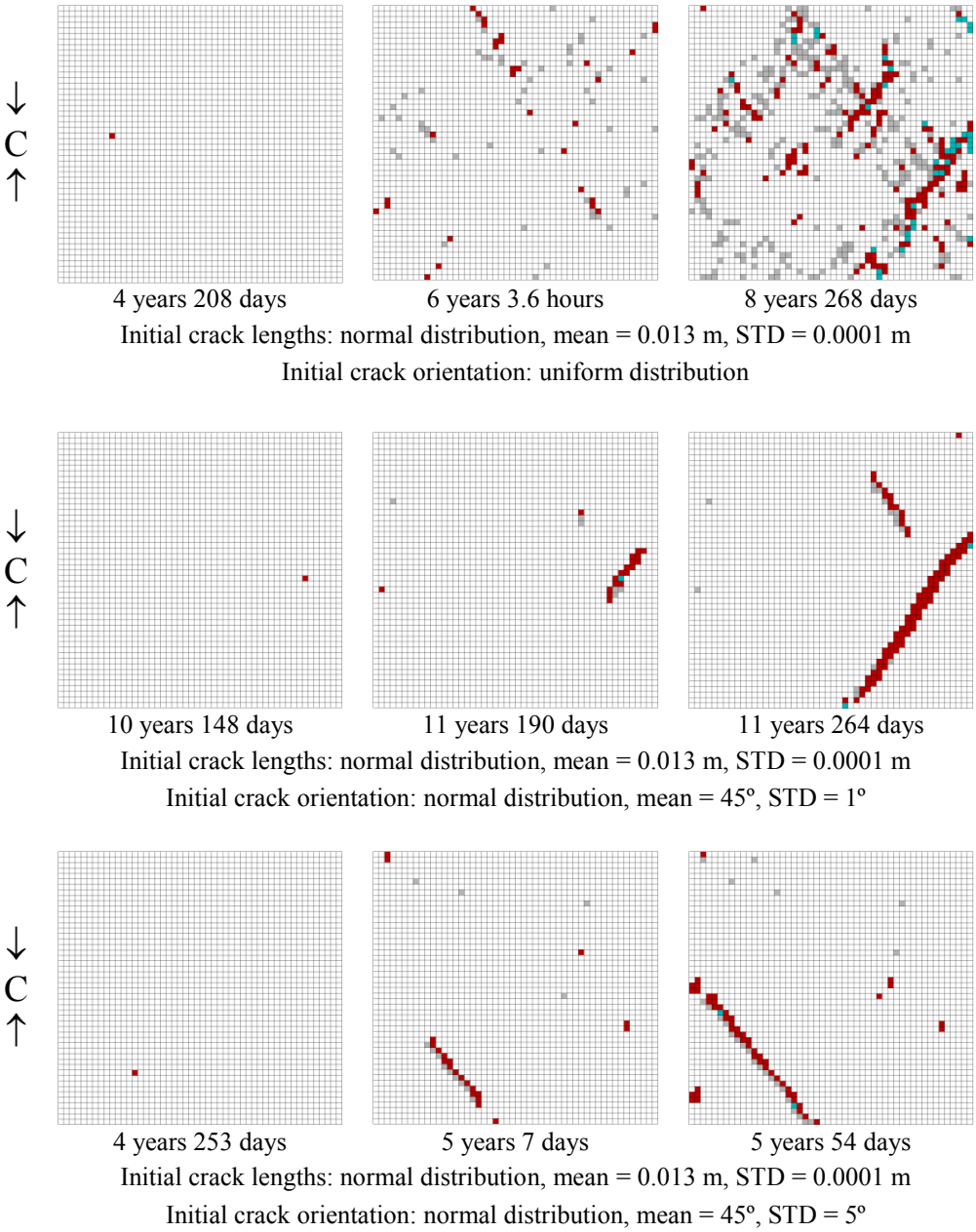

Figure 4-36 Uniaxial compressive tests (18 MPa) of model C (zones in green: tensile failure; zones in red: shear failure; zones in gray: failed in the past)

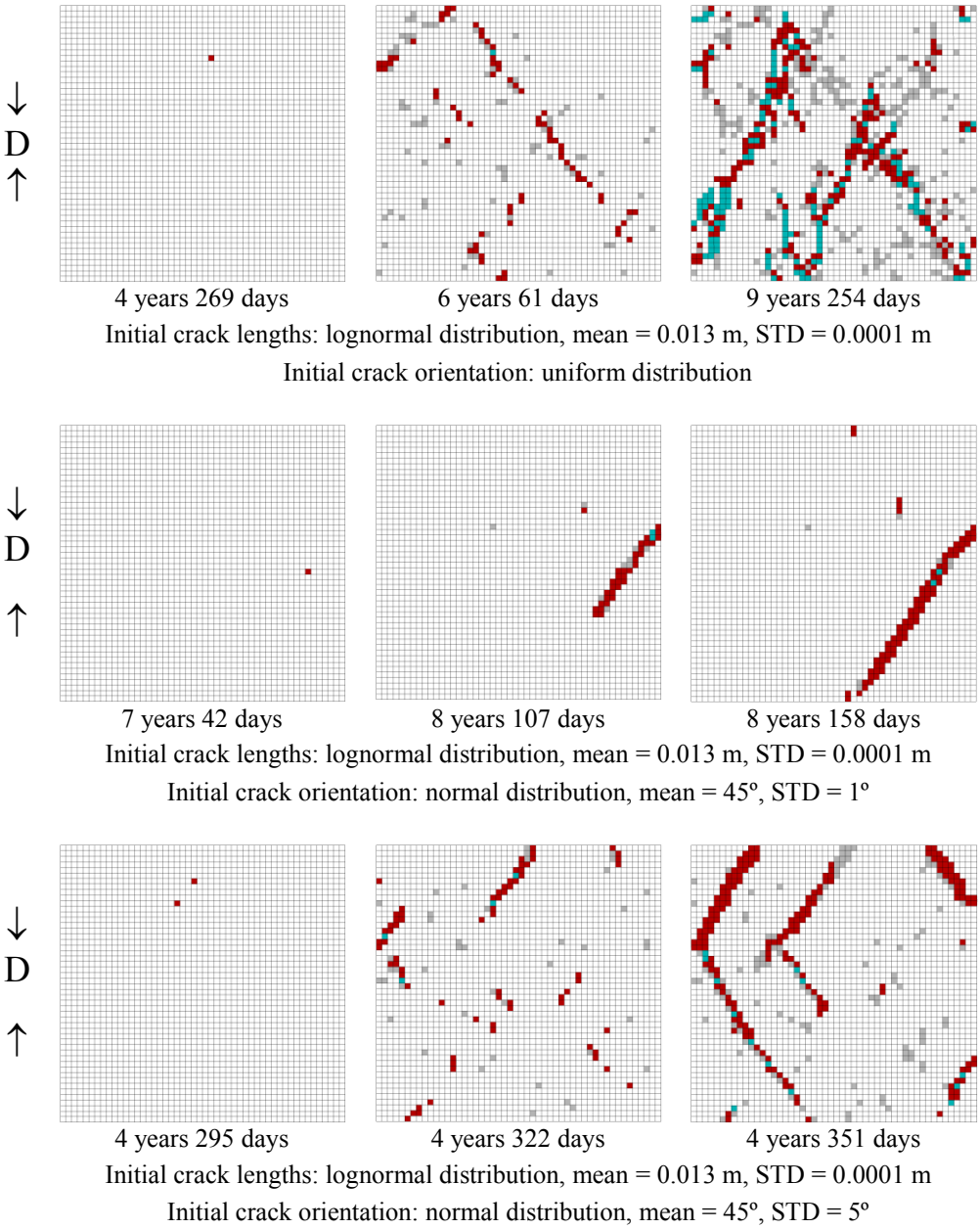

Figure 4-37 Uniaxial compressive tests (18 MPa) of model D (zones in green: tensile failure; zones in red: shear failure; zones in gray: failed in the past)

It is seen (Fig. 4-34 to Fig. 4-37) that shear band has been formed with an inclination of about 60º to the horizontal direction (30º to the loading direction). The inclination of the shear band confirms Mohr-Coulomb theory, where inclination (β) of the weak plan to the applied compressive load is expressed as $\beta = (\pi / 4) + (\varphi / 2)$. $\varphi = 30º$ denotes the friction angle in this study. The zones forming the shear bands showed a more scattered pattern if the crack orientation follows uniform distribution than if the crack orientation follows normal distribution. It is clearly observed that with a bigger standard deviation of the crack orientation (5º instead of 1º), the shear band is more scattered but the inclination is the same. Especially, multiple shear bands appeared in

two models (model B and model D) in such case. Most of the failed zones forming the shear bands have shear failure. More zones failed by tension have been found in the case where the crack orientation follows uniform distribution than normal distribution. In the case where the crack orientation follows normal distribution, more zones failed by tension if the standard deviation of the crack orientation is 5º instead of 1º (Fig. 4-34 to Fig. 4-37). This phenomenon indicates that the crack orientation has its influence on the failure mode of the zone. As can be seen from Table 4-17, the numerical predicted first zone failure time and position revealed good agreement with the analytical solutions (Eq. 4-14) for each case. For model A to D, the numerical predicted lifetime ranges from about 7 years 230 days (model A) to 9 years 254 days (model D) if the crack orientation follows uniform distribution. For the case where crack orientation follows normal distribution, and standard deviation is 1º, the numerical predicted lifetime ranges from about 8 years 158 days (model D) to 11 years 264 days (model C). If the standard deviation is 5º, the numerical predicted lifetimes are shortened by about half the amount: lifetime ranges from about 4 years 336 days (model A) to 5 years 54 days (model C). Considering the first zone failure time, the results have the same magnitude in the cases where the crack orientation follows uniform distribution and normal distribution. But with the standard deviation of 5º, the first zone failure times are more than 4 years but less than 5 years for both cases. For the cases where the crack orientation follows normal distribution but with the standard deviation of 1º, the first zone failure times are over 7 years but less than 11 years (Table 4-17). This finding is explained by consulting Fig. 4-21 (b), where the shortest lifetime is found at a crack orientation of 55º under compressive load. In the multi-zone model, the cases where the mean crack orientation follows uniform distribution and normal distribution (mean orientation: 45º) but with the standard deviation of 5º have more zones with crack orientation closer to 55º than the case where the mean crack orientation follows normal distribution (mean orientation: 45º) but with the standard deviation of 1º. So the first zone failure time is longer for the case where the standard deviation is 1º than the other two cases. Similar to the observations in the tensile tests, the lifetime results and macroscopic failure patterns showed similarity between the models with different realizations of normal distribution (model A, B and C) and lognormal distribution (model D) of initial crack lengths.

Table 4-17 Lifetime results of models under compressive load of 18 MPa

	Analytical results		Numerical results		
Model	**First failure zone**	**First failure time (s)**	**First failure zone**	**First failure time (s)**	**Lifetime (s)**
Initial crack orientation: uniform distribution					
A	(30, 39)	1.4586e8 (4 y, 228 d, 3 h, 54 min.)	(30, 39)	1.4625e8 (4 y, 232 d, 17 h)	2.4063e8 (7 y, 230 d, 42 min.)
B	(27, 41)	1.4939e8 (4 y, 269 d, 58 min.)	(27, 41)	1.4975e8 (4 y 273 d 5 h 13 min.)	2.8484e8 (9 y 11 d 17 h 14 min.)
C	(10, 27)	1.4379e8 (4 y, 204 d, 6 h, 18 min.)	(10, 27)	1.4415e8 (4 y, 208 d, 9 h, 40 min.)	2.7548e8 (8 y, 268 d, 10 h, 6 min.)
D	(27, 41)	1.4903e8 (4 y, 264 d, 21h, 48 min.)	(27, 41)	1.4940e8 (4 y, 269 d, 4 h)	3.0581e8 (9 y, 254 d, 11 h, 14 min.)
Initial crack orientation: normal distribution (mean = 45º, STD = 1º)					
A	(44, 24)	3.1336e8 (9 y, 341 d, 21 h, 2 min.)	(44, 24)	3.1375e8 (9 y, 346 d, 8 h, 46 min.)	3.5280e8 (11 y, 68 d, 6 h, 38 min.)
B	(44, 24)	2.2536e8 (7 y, 53 d, 6 h, 56 min.)	(44, 24)	2.2575e8 (7 y, 57 d, 20 h, 20 min.)	2.6750e8 (8 y, 176 d, 2 h, 52 min.)
C	(44, 24)	3.2775e8 (10 y, 143 d, 8 h, 59 min.)	(44, 24)	3.2815e8 (10 y, 148 d, 46 min.)	3.6976e8 (11 y, 264 d, 15 h, 19 min.)
D	(44, 24)	2.2402e8 (7 y, 37 d, 20 h, 45 min.)	(44, 24)	2.2440e8 (7 y, 42 d, 5 h, 20 min.)	2.6597e8 (8 y, 158 d, 8 h, 58 min.)
Initial crack orientation: normal distribution (mean = 45º, STD = 5º)					
A	(3, 30)	1.4101e8 (4 y, 172 d, 1 h, 27 min.)	(3, 30)	1.4140e8 (4 y, 176 d, 13 h, 46 min)	1.5518e8 (4 y, 336 d, 1 h, 56 min)
B	(1, 40)	1.5176e8 (4 y, 296 d, 11 h, 16 min)	(1, 40)	1.5198e8 (4 y, 299 d, 40 min)	1.5641e8 (4 y, 350 d, 6 h)
C	(14, 10)	1.4766e8 (4 y, 249 d, 2 h, 2 min)	(14, 10)	1.4805e8 (4 y, 253 d, 13 h)	1.6242e8 (5 y, 54 d, 20 h, 47 min)
D	(21, 40)	1.5148e8 (4 y, 293 d, 6 h, 51 min)	(21, 40)	1.5171e8 (4 y, 295 d, 21 h, 40 min)	1.5648e8 (4 y, 351 d, 2 h)

The fracture pattern of each model at the stage of failure has also been studied. The fracture pattern of model A is shown in Fig. 4-38 and Fig. 4-39 as an example. It is

seen that most of the zones forming the shear band failed in shear. From the zoomed in area in Fig. 4-38 and Fig. 4-39, it is seen that in most of the failed zones the microcracks have reached the zone boundary, which means these zones fail in the subcritical crack propagation phase, which is also supported by the comparatively long lifetimes of the models (Table 4-17).

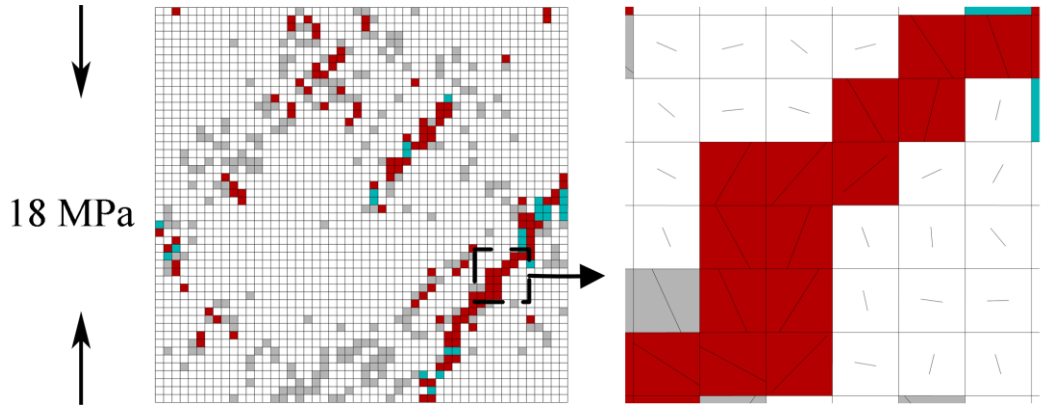

Figure 4-38 Fracture pattern of model A at failure (zones in green: tensile failure; zones in red: shear failure; zones in gray: failed in the past; initial crack lengths: normal distribution, mean = 0.013 m, STD = 0.0001 m; initial crack orientation: uniform distribution)

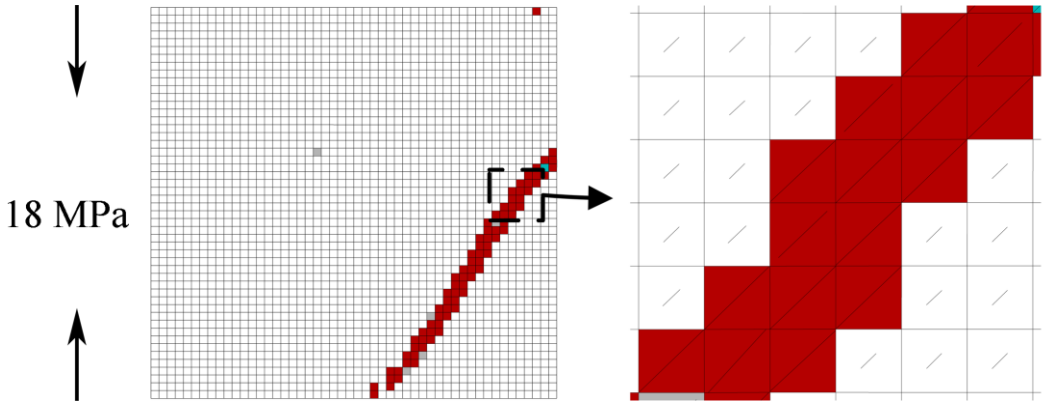

Figure 4-39 Fracture pattern of model A at failure (zones in green: tensile failure; zones in red: shear failure; zones in gray: failed in the past; initial crack lengths: normal distribution, mean = 0.013 m, STD = 0.0001 m; initial crack orientation: normal distribution, mean = 45º, STD = 1º)

To study the influence of the crack orientation on the lifetime, uniaxial compressive tests on models with different orientations have also been performed. With initial crack length and orientation following normal distribution (different mean values, STD: 1º), uniaxial compressive test were performed. Model A's realization of initial crack lengths has been used here. Both the analytical and numerical predicted lifetimes are listed in Table 4-18. The numerical predicted lifetime results are also shown in Fig. 4-40. It is seen from Table 4-18 that the numerical results are in good agreement with the analytical results with respect to both the first zone failure time and position. In principal, the numerical results show the same trends as already documented in Fig. 4-21 (b). The shortest lifetime is found at a mean crack orientation

of about 55º. It takes longer time for the zone to fail if the mean initial crack orientation is bigger or smaller. The influence of the mean orientation on the lifetime is also great: the lifetime is only about 4 years 26 days if the mean orientation is 55º, while ascends to about 110 years 45 days if the mean orientation is 40º.

Table 4-18 Lifetime of model A with different mean orientations under compressive load of 18 MPa (initial crack orientation follow normal distribution)

	Analytical results		**Numerical results**		
Mean orientation	**First failure zone**	**First failure time (s)**	**First failure zone**	**First failure time (s)**	**Lifetime (s)**
40º	(44, 24)	2.6821e9 (85 y, 17 d, 20 h, 11 min.)	(44, 24)	2.6849e9 (85 y, 50 d, 14 h, 8 min.)	3.4729e9 (110 y, 45 d, 18 h, 35 min.)
45º	(44, 24)	3.1336e8 (9 y, 341 d, 21 h, 2 min.)	(44, 24)	3.1375e8 (9 y, 346 d, 8 h, 46 min.)	3.5280e8 (11 y, 68 d, 6 h, 38 min.)
50º	(37, 7)	1.4233e8 (4 y, 187 d, 6 h, 45 min.)	(37, 7)	1.4256e8 (4 y, 190 d)	1.5111e8 (4 y, 289 d, 20 min.)
55º	(12, 8)	1.2248e8 (3 y, 322 d, 14 h, 5 min.)	(12, 8)	1.2264e8 (3 y, 324 d, 10 h, 40 min.)	1.2847e8 (4 y, 26 d, 23 h, 16 min.)
60º	(41, 26)	1.9086e8 (6 y, 19 d, 1 h, 33 min.)	(41,26)	1.9110e8 (6 y, 21 d, 19 h, 20 min.)	2.0481e8 (6 y, 180 d, 10 h, 40 min.)
65º	(41, 26)	1.2313e9 (39 y, 15 d, 16 h, 23 min.)	(41, 26)	1.2327e9 (39 y, 32 d, 17 h, 15 min.)	1.3811e9 (43 y, 290 d, 4 h, 37 min.)

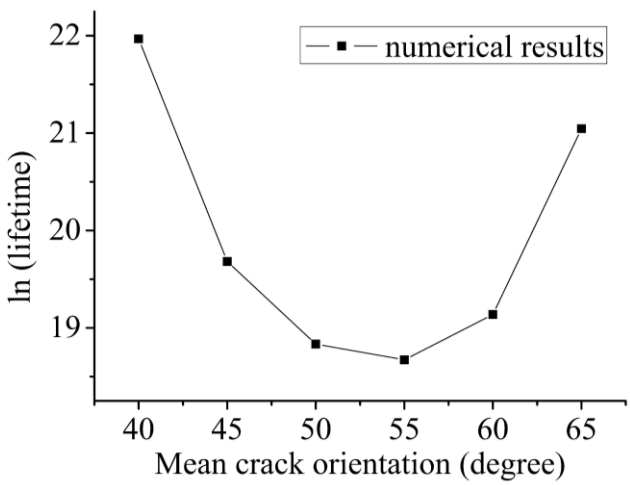

Figure 4-40 Natural logarithm of lifetime (seconds) in uniaxial compressive test with different mean crack orientation

4.4.4 Conclusions

The lifetime prediction scheme for fixed orientation model has been proposed and the application of this scheme to both the single zone and multi-zone model has been successful. The single zone model under different load configuration has been studied exhaustively, and precise lifetime predictions were obtained with correct fracture mode predicted for every case, which ensured the applicability of this model scheme to the multi-zone model with more complex stress conditions. For a single zone, the lifetime is shorter if the load becomes bigger or the initial crack is longer under both tensile and compressive loading conditions. In tensile tests, the lifetime is longer the more the crack axis is parallel to the applied tensile stress (the same holds for the mean orientation in multi zone models); while in compressive tests the lifetimes have a U-shaped curve with ascending crack orientation. The shortest lifetime was found at a crack orientation of about 55º (the same holds for the mean orientation in multi zone models). The numerical predicted lifetimes of the first zone failure also showed good agreement with the analytical solutions in multi-zone models. Especially, the position of the first failure zone has been predicted correctly for each case in the multi-zone model under both tensile and compressive load. It is observed from multiple zone models that the macroscopic fractures grow perpendicularly to the tensile loading directions; while under compressive loads, shear bands are formed with the inclination of about 60º to the horizontal direction (30º to the loading direction), which confirms Mohr-Coulomb theory. The macroscopic fracture pattern formed under tensile load is more uneven and the shear band has a more scattered pattern with uniformly distributed crack orientation compared to normally distributed crack orientation. Also, the influence of the standard deviation of the crack orientation has been studied under compressive load. The shear band is found more scattered and the lifetime is shorter with bigger standard deviation (5º instead of 1º). Similar to the basic model, it is observed that under tensile loads, the zones are more likely to fail by $K_I > K_{IC}$, while in compressive tests, the zones often fail by crack lengths reaching the zone dimensions (subcritical crack propagation phase).

4.5 Wing crack model

It's more commonly seen in natural rock structures that more than one loading mode is present, known as mixed-mode loading condition. Considering only 2D model again, this means Mode I and Mode II loading are superimposed on the crack. In the basic model and the fixed orientation model, the mixed-mode loading condition is considered, but the technique was to calculate the stress intensity factor under each loading mode separately, and to include both contributions into the crack propagation velocity through Charles equation. In this section, the wing crack model strategy is proposed where the crack does not extend in its own plane but forms a wing crack in the direction of the maximum circumferential stress. The stress intensity factor at the

wing crack tip is obtained through a superposition method. Lifetime prediction scheme for wing crack model is also proposed and tested. Various initial crack orientations, wing crack propagation and corresponding stress intensity factor calculation scheme under mixed load loading is also introduced.

4.5.1 Crack initiation (Kink model)

Consider a single crack with the length of 2a under biaxial loading with the major stress being vertical. The normal and shear stresses on the crack are described by Eq. 4-9 and Eq. 4-10, respectively. The stress intensity factors of the crack in this case are expressed by Eq. 4-11 and Eq. 4-12. By using these two stress intensity factors K_I and K_{II} differentiated by different loading modes on the initial main crack, the circumferential stress near the crack tip is given (Gross 2006):

$$\sigma_\theta = \frac{1}{4\sqrt{2\pi r}}\left[K_1\left(3\cos\frac{\theta}{2}+\cos\frac{3\theta}{2}\right)-K_{II}\left(3\sin\frac{\theta}{2}+3\sin\frac{3\theta}{2}\right)\right] \tag{4-18}$$

where r and θ are the polar coordinates originated at the tip of the crack, as shown in Fig. 4-41.

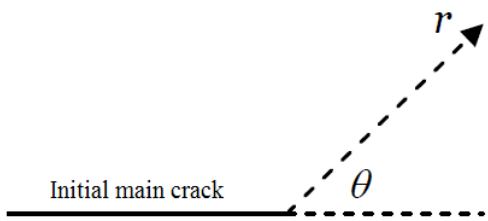

Figure 4-41 Initiation of the crack under mixed-mode loading

A small kink forms at the tip of the crack in the initial phase of the propagation. The direction of the kink is affected by the comparative dominance of either of the two loading modes. Research done by Erdogan and Sih (1963) has shown that the crack would kink to the direction of the maximum circumferential stress (maximum hoop stress). The denotation of the kink direction θ is the angle between the kink and the initial main crack, which can be deduced from

$$\frac{\partial\sigma_\theta}{\partial\theta} = 0 \tag{4-19}$$

and leads to

$$K_I \sin\theta + K_{II}\left(3\cos\theta - 1\right) = 0 \tag{4-20}$$

or

$$\theta = 2\arctan\left(-\frac{2K_{II}/K_I}{1+\sqrt{1+8(K_{II}/K_I)^2}}\right) \tag{4-21}$$

if $K_I \neq 0$.

Under pure Mode I loading ($K_I \neq 0$ and $K_{II} = 0$), according to the equation, θ equals to 0, which means the propagation starts in the tangential direction from the crack tip. For pure Mode II ($K_I = 0$ and $K_{II} \neq 0$), the equation leads to cosθ = 1 / 3, which means approximately ± 70.5º for the kink direction. The positive or negative direction depends on the sign of K_{II}.

The crack tip stress fields (in polar coordinates) for pure Mode I and Mode II loading are given by Anderson (1995):

$$\sigma_{\theta\theta} = \frac{K_I}{\sqrt{2\pi r}}\left[\frac{3}{4}\cos\left(\frac{\theta}{2}\right)+\frac{1}{4}\cos\left(\frac{3\theta}{2}\right)\right] \tag{4-22}$$

$$\sigma_{\theta\theta} = \frac{K_{II}}{\sqrt{2\pi r}}\left[-\frac{3}{4}\sin\left(\frac{\theta}{2}\right)-\frac{3}{4}\sin\left(\frac{3\theta}{2}\right)\right] \tag{4-23}$$

The local Mode I stress intensity factor at the kink tip can be deduced by the nominal K values of the main crack through summing the normal and shear stresses, as is shown below

$$k_{1\theta} = \frac{1}{4}K_1\left(3\cos\frac{\theta}{2}+\cos\frac{3\theta}{2}\right)-\frac{3}{4}K_{II}\left(\sin\frac{\theta}{2}+\sin\frac{3\theta}{2}\right) \tag{4-24}$$

which is also in agreement with the expression of circumferential stress.

Take biaxial compression as an example: in this case K_I will be ignored since the main crack is closed, and pure Mode II ($K_I = 0$ and $K_{II} \neq 0$) condition occure. The stress intensity factor for the kink is

$$k_{1\theta} = -\frac{3}{4}K_{II}\left(\sin\frac{\theta}{2}+\sin\frac{3\theta}{2}\right) = -\frac{3}{2}K_{II}\left(\sin\theta\cos\frac{\theta}{2}\right) \tag{4-25}$$

Thus substituting $\theta = \pm 70.5^{o}$ (sign of θ depends on that of K_{II}), the local stress intensity factor at the crack tip is calculated.

4.5.2 Crack propagation model (Wing crack model)

In consideration that the crack propagates along a curved path under general loading conditions, an approximation scheme is needed for the further crack propagation simulation. An improved wing crack model proposed by Baud et al. (1996) has been adopted in this research. This innovative model simplified the exact local stress intensity factor derivation for the wing crack system proposed by Nemat-Nasser and Horii (1982), Horii and Nemat-Nasser (1985). The simplification involves replacing the curved crack by a straight one by connecting the original main crack tip to the wing crack tip, as shown in Fig. 4-42. It is observed that the curved wing crack orientation is related to its length. Thus the orientation of the simplified straight crack also depends on its length.

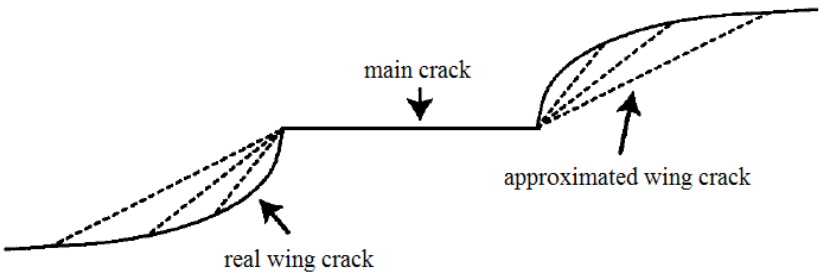

Figure 4-42 Replacement of the real wing crack with a straight one (Baud et al. 1996)

To decide which direction the wing crack tip is propagating for different time span, a propagation path simplification for each time step is applied in the code. The 'time step' is used as a parameter in the code representing a real time span. It has been demonstrated by Cotterell and Rice (1980) that the crack propagation follows the direction where crack tip is under pure Mode I condition ($K_{II} = 0$ and the energy release rate has a local maximum). For each time step, the crack (simplified to a straight crack) propagates from the former crack tip and follows the direction where pure Mode I condition is met. Then the main crack tip and this new wing crack tip are connected to replace the real wing crack. The numerical simulation scheme for the simplified wing crack propagation is illustrate in Fig.4-43.

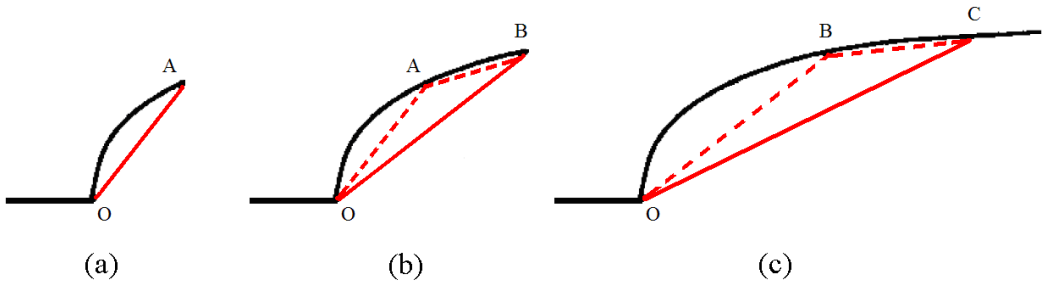

Figure 4-43 Simplified propagation scheme for wing crack

Point O in Fig.4-43 is the original main crack tip. After one time step the real crack propagation path is represented by Curve OA. The real crack propagates in a real-time pattern so that a pure Mode I condition is satisfied for any infinitesimal time span within this time step. The simulation of this process is done by replacing Curve OA by the straight red line OA with its orientation in accordance with the pure Mode I condition of this time step (Fig. 4-43 (a)). Local stress intensity factor K_A is then calculated using the length OA and its orientation. Within the next time step the real crack path (Curve AB) is replaced by straight dashed red line AB. Point B becomes the current wing crack tip. Then, Point O and Point B are connected (solid red line OB) as the simplified wing crack substituting real wing crack (Curve OAB) in this step (Fig. 4-43 (b)). With the length of line OB and its own orientation the local stress intensity factor K_B is calculated for the next time step. Using K_B, the wing crack propagates along the curve BC in the next step, which was simplified by the dashed red line BC. Connecting Point O and Point C, the straight solid red line OC represents the wing crack (Curve OBC) at this step (Fig. 4-43 (c)). This process goes on until the crack propagation halts or the zone containing the crack fails.

4.5.3 Stress intensity factor calculation

Baud et al. (1996) proposed a superposition method for the stress intensity factor calculation for the simplified straight wing crack. The stress intensity factor is studied for the case where the normal stress on the crack is compressive. It is assumed that the stress intensity factor is composed of two parts: a component K_{ISO} for the two straight wing cracks on both ends of the main crack, and a component K_{SLI} for the main crack subjected to the same stress conditions. This superposition method is illustrated for biaxial compression in Fig. 4-44.

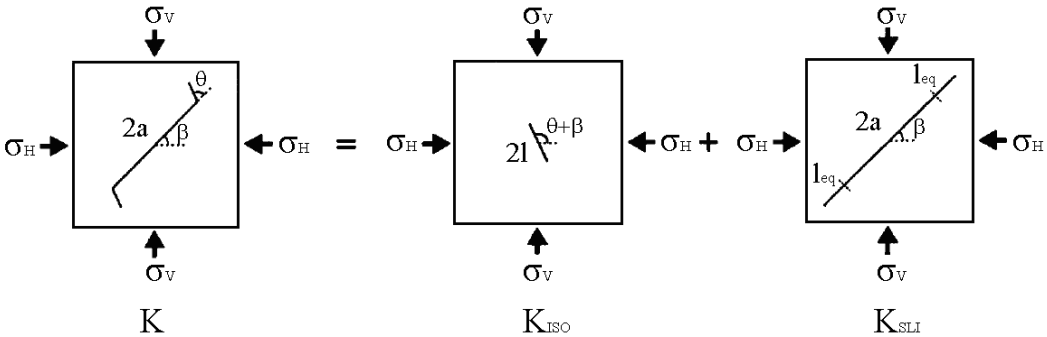

Figure 4-44 Superposition method for K value under biaxial compression (Baud et al. 1996)

Assuming the length of each wing crack is l, they are regarded as a single straight crack of length 2l. The main crack orientation is β related to the horizontal direction. The angle between the main crack and the wing crack is θ, as shown in Fig. 4-44. Assuming the major principal stress is σ_V and the minor principal stress is σ_H, the component K_{ISO} is given as:

$$K_{ISO} = \frac{1}{2}\left[(\sigma_V + \sigma_H) + (\sigma_V - \sigma_H)\cos 2(\theta + \beta)\right]\sqrt{\pi l} \tag{4-26}$$

For the calculation of K_{SLI}, the initial system of the main crack with a wing crack pair is substituted by an equivalent straight crack of the length 2 (a + l_{eq}) with the same orientation as the initial main crack (Fig. 4-44). This equivalent crack consists of a central part with length 2a and two equivalent wing lengths l_{eq} on both ends. But since only the shear stress contributes to the K value at the wing crack tip (main crack is closed under compressive normal stress) and wing crack propagates under pure Mode I condition (no shear stress), only the central part with length equal to the initial crack length is subjected to the same effective shear stress. Thus the stress intensity factor of the equivalent crack is written as (Sih and Liebowitz 1968):

$$K = 2\sigma_{eff}\sqrt{\frac{a + l_{eq}}{\pi}}\sin^{-1}\left(\frac{a}{a + l_{eq}}\right) \tag{4-27}$$

where σ_{eff} is the effective shear stress on the main crack ($|\sigma_{eff}| = |\sigma_T| - \mu|\sigma_N|$, consulting Eq. 4-9 and Eq. 4-10 for σ_T and σ_N). By implementing this K value into the transformed stress intensity factor for wing crack initiation (Equation 4-25), the component K_{SLI} is given as (Baud et al. 1996)

$$K_{SLI} = -3\sigma_{eff}\sqrt{\frac{a + l_{eq}}{\pi}}\sin^{-1}\left(\frac{a}{a + l_{eq}}\right)\sin\theta\cos\frac{\theta}{2} \tag{4-28}$$

To determine the value of l_{eq}, Horii and Nemat-Nasser (1986) introduced a pair of collinear splitting forces F = 2a σ_{eff} to represent the shear effect of the main crack on the wing crack. The angle between the forces and the wing crack is θ due to its orientation. In this case the K_I value for a long wing crack with a length l is:

$$K_1 = -\frac{2a\sigma_{eff}\sin\theta}{\sqrt{\pi l}} \tag{4-29}$$

Considering the expressions of K_{SLI} and K_I (Equation 4-28 and 4-29), the wing crack equivalent length l_{eq} is deduced:

$$l_{eq} = \frac{9}{4} l \cos^2\frac{\theta}{2} \tag{4-30}$$

Zhao and Wang (2011) have proposed a new scheme to obtain l_{eq}, where an effective crack length l^* has been applied to equation 4-29 for the case of crack initiation when wing crack length l is rather small:

$$K_1 = -\frac{2a\sigma_{eff}\sin\theta}{\sqrt{\pi(l+l^*)}} \tag{4-31}$$

This expression is equal to the stress intensity factor at initiation of the original crack under pure shear loading (maximum θ = 0.392π):

$$K_1 = \sigma_{eff}\sqrt{\pi a}\left(-\frac{3}{4}\right)\left[\sin\left(\frac{\theta}{2}\right)+\sin\left(\frac{3\theta}{2}\right)\right] \tag{4-32}$$

An effective crack length of $l^* = 0.27a$ can be obtained by identifying Equation 4-31 and 4-32 at $\theta = 0.392\pi$ and $l = 0$. By substituting $l^* = 0.27a$ into Equation 4-31, equaling it to Equation 4-28 and letting $l \to 0$, l_{eq} for the case of a rather short wing crack length is obtained:

$$l_{eq} = \left(\frac{0.667}{\cos^2\left(\frac{\theta}{2}\right)} - 1\right)a \tag{4-33}$$

A general expression of l_{eq} supposed to satisfy both long and short wing crack length conditions was given (Zhao and Wang 2011):

$$l_{eq} = \left(\frac{0.667}{\cos^2\left(\frac{\theta}{2}\right)} - 1 \right) a e^{-\frac{l}{a}} + \frac{9}{4} l \cos^2 \frac{\theta}{2} \left(1 - e^{-\frac{l}{a}} \right) \tag{4-34}$$

With l_{eq} obtained, by adding K_{SLI} and K_{ISO}, the Mode I stress intensity factor at the wing crack tip is:

$$\begin{aligned} K &= K_{SLI} + K_{ISO} \\ &= -3\sigma_{eff} \sqrt{\frac{a + l_{eq}}{\pi}} \sin^{-1}\left(\frac{a}{a + l_{eq}} \right) \sin\theta \cos\frac{\theta}{2} \\ &\quad + \frac{1}{2}\left[(\sigma_V + \sigma_H) + (\sigma_V - \sigma_H) \cos 2(\theta + \beta) \right] \sqrt{\pi l} \end{aligned} \tag{4-35}$$

The expression of K at wing crack tip is different if the main crack is subjected to tensile normal stress rather than compressive. In this case the crack is considered open, so both shearing and tensile load from the main crack should contribute to the K value at the wing crack tip. Thus, a K_{TEN} as the tensile contribution from the main crack should also be included in the K expression for the wing crack tip, while the K_{ISO} and K_{SLI} component remain the same. With the major principal stress σ_V being compressive and minor principal stress σ_H tensile, the superposition is shown in Fig. 4-45.

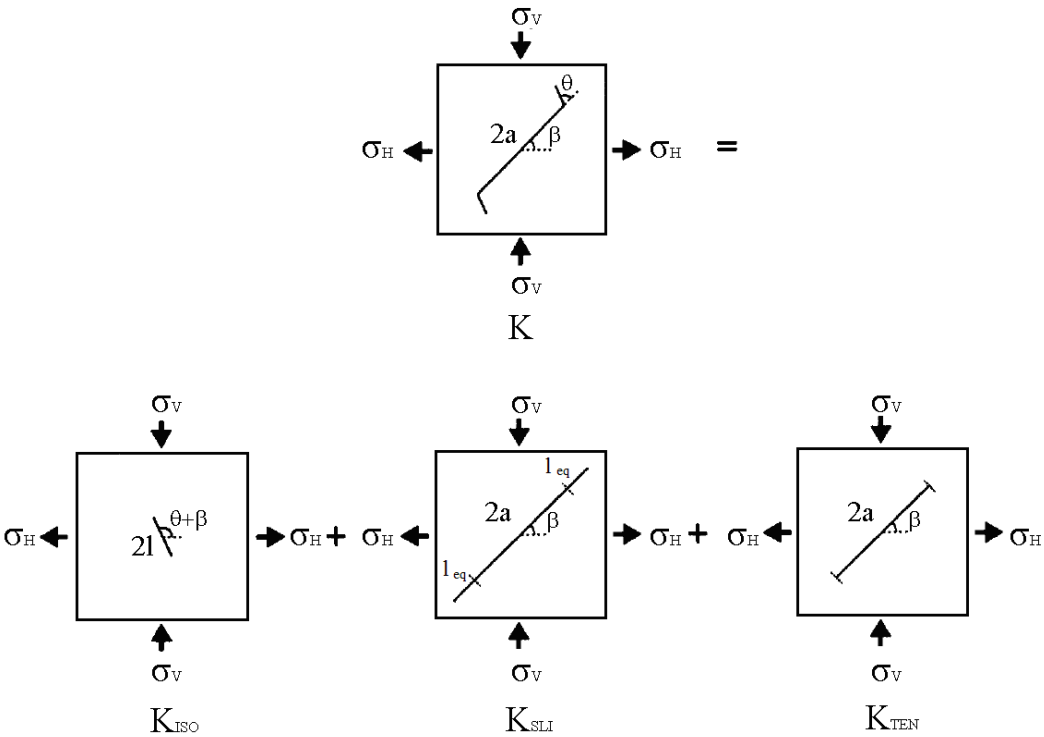

Figure 4-45 The superposition method for K value with tensile normal stress on the main crack

Using the kink model at the crack initiation and kink direction θ of the wing crack, K_{TEN} is given as:

$$K_{TEN} = \sigma_N \sqrt{\pi a}\left[\frac{3}{4}\cos\left(\frac{\theta}{2}\right) + \frac{1}{4}\cos\left(\frac{3\theta}{2}\right)\right] \tag{4-36}$$

where σ_N is the normal tensile stress on the main crack. By adding K_{SLI}, K_{ISO} and K_{TEN}, the Mode I stress intensity factor at the wing crack tip is obtained:

$$\begin{aligned} K &= K_{SLI} + K_{ISO} + K_{TEN} \\ &= -3\sigma_{eff}\sqrt{\frac{a+l_{eq}}{\pi}}\sin^{-1}\left(\frac{a}{a+l_{eq}}\right)\sin\theta\cos\frac{\theta}{2} \\ &\quad + \frac{1}{2}\left[(\sigma_V + \sigma_H) + (\sigma_V - \sigma_H)\cos 2(\theta+\beta)\right]\sqrt{\pi l} \\ &\quad + \sigma_N\sqrt{\pi a}\left[\frac{3}{4}\cos\left(\frac{\theta}{2}\right) + \frac{1}{4}\cos\left(\frac{3\theta}{2}\right)\right] \end{aligned} \tag{4-37}$$

where the expression of l_{eq} remains the same. Thus K value expressions at the wing crack tip of both cases have been given: Equation 4-35 for main crack under compressive normal stress (closed crack), and Equation 4-37 for main crack under

tensile normal stress (open crack). The calculation program is designed to choose one of the two K calculating procedures according to the normal stress state on the main crack.

4.5.4 K value verification for wing crack model

For the wing crack model, the superposition method of stress intensity factor calculation is tested in this subsection. A square shaped single-element model with the size of 0.04 × 0.04 m was built for the verification. The initial crack length is set to 0.004 m; orientation is set to 45º from the horizontal direction and coefficient of friction $\mu = 0.3$. Other material parameters remain unchanged as given in Table 4-1.

For the cases where the initial main crack is subjected to compressive normal stress, biaxial and uniaxial tests have been performed. The normalized stress intensity factors ($K_I / (|\sigma_V| (\pi a)^{1/2})$, where a denotes the half initial crack length) for different horizontal and vertical stress ratios are illustrated in Fig. 4-46.

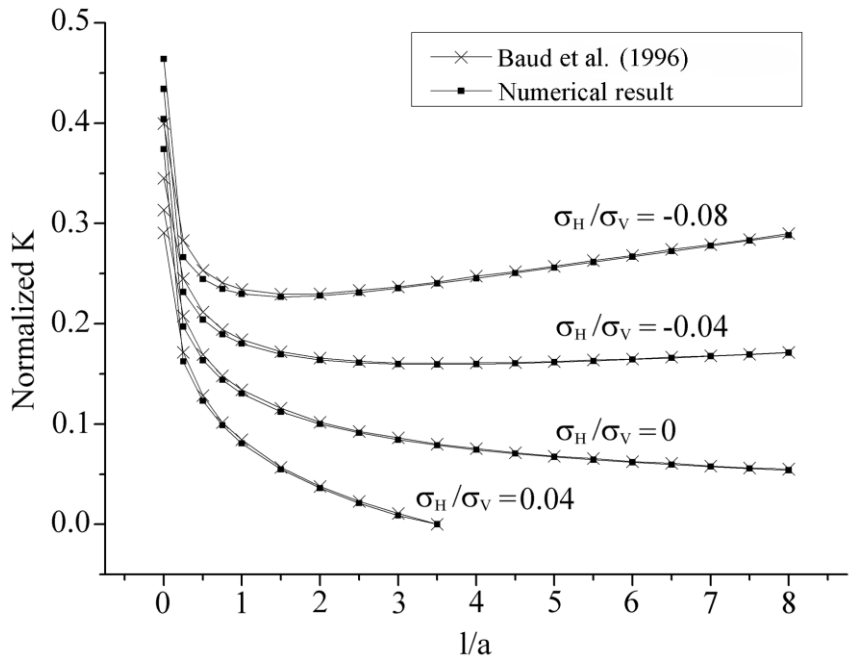

Figure 4-46 Comparison of normalized K values between numerical model and results from Baud et al. (1996) (l: wing crack length; a: half initial crack length)

It can be seen from Fig. 4-46 that the numerical results are in good agreement with those of Baud et al. (1996) in each loading case, which documents the applicability of the superposition method implemented into FLAC. The slight difference in the results is caused by the further simplification in the numerical model that for each time step, the propagation is also considered to be straight rather than curved as described in Subsection 3.1.4.

The equivalent wing crack scheme proposed by Zhao and Wang (2011) (Eq. 4-34) has also been applied to the superposition method. A comparison between this scheme and the numerical results using Baud et al. (1996) (Eq. 4-30) is given in Fig. 4-47:

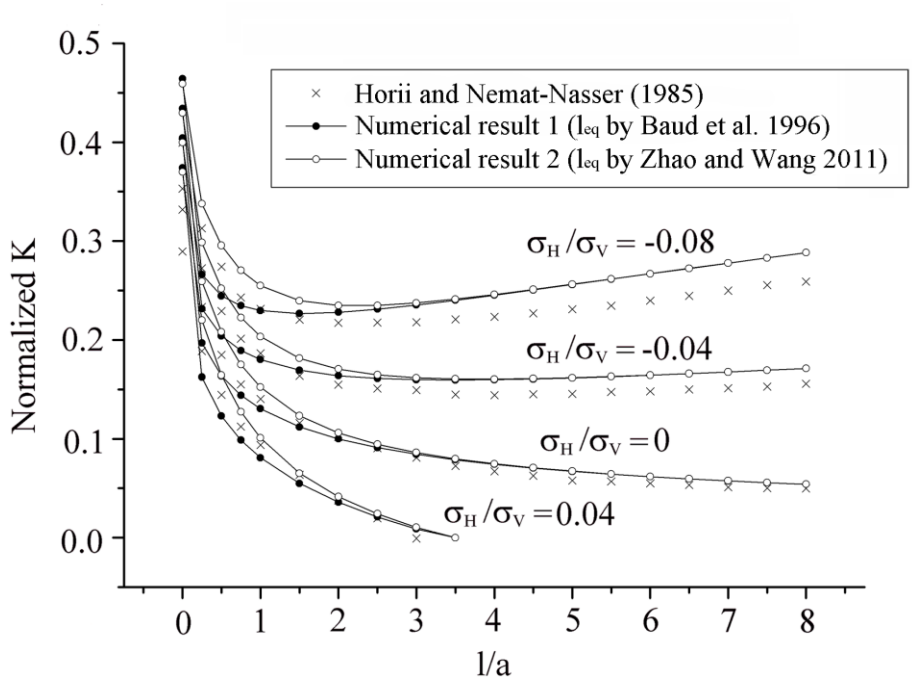

Figure 4-47 Normalized K values with different l_{eq} schemes compared to exact solution (Horii and Nemat-Nasser 1985)

Both numerical results have shown reasonable agreement with the exact solution (Horii and Nemat-Nasser 1985), especially in the uniaxial test ($\sigma_H / \sigma_V = 0$) and biaxial compressive test ($\sigma_H / \sigma_V = 0.04$). The K values from two different l_{eq} schemes agree well when the wing crack length is comparatively long. Although Zhao and Wang's scheme has led a slightly better result when the wing crack length l is very small, the scheme of Baud et al. (1996) results in a better agreement with the exact solution in general. So the l_{eq} scheme introduced by Baud et al. (1996) has been adopted in this research.

4.5.5 Life time prediction for wing crack model (single zone)

(1) Life time prediction scheme

In the wing crack model, the crack propagation velocity is defined by stress intensity factor at the wing crack tip through Charles equation:

$$v = CK_I^n \tag{4-38}$$

It is assumed in wing crack model that the crack only propagates in Mode I condition. For simplicity, the stress intensity factor at the wing crack tip is also expressed as K_I in this study. Considering a single zone containing an initial crack under constant stress, with length of each wing crack l, the life time can be calculated by:

$$t_{zone} = \int_0^{l_c} \frac{dl}{v} = \int_0^{l_c} \frac{dl}{CK_I^n} \tag{4-39}$$

where C is a rock-specific parameter as introduced in Subsection 2.3.2. n is the stress corrosion index. If the crack is under a compressive normal stress with $l_{eq} = (9 / 4)\, l \cos^2(\theta / 2)$, the K_I is obtained by Equation 4-35. So the crack propagation velocity in this case is expressed as:

$$\begin{aligned} v(l) &= CK_I^n \\ &= C(-3\sigma_{eff}\sqrt{\frac{a+\frac{9}{4}l\cos^2\frac{\theta}{2}}{\pi}}\sin^{-1}\left(\frac{a}{a+\frac{9}{4}l\cos^2\frac{\theta}{2}}\right)\sin\theta\cos\frac{\theta}{2} \\ &+\frac{1}{2}[(\sigma_V+\sigma_H)+(\sigma_V-\sigma_H)\cos 2(\theta+\beta)]\sqrt{\pi l})^n \end{aligned} \tag{4-40}$$

If the crack is under tensile normal stress, K_I is obtained by Equation 4-37. The crack propagation velocity in this case is expressed as:

$$\begin{aligned} v(l) &= CK_I^n \\ &= C(-3\sigma_{eff}\sqrt{\frac{a+\frac{9}{4}l\cos^2\frac{\theta}{2}}{\pi}}\sin^{-1}\left(\frac{a}{a+\frac{9}{4}l\cos^2\frac{\theta}{2}}\right)\sin\theta\cos\frac{\theta}{2} \\ &+\frac{1}{2}[(\sigma_V+\sigma_H)+(\sigma_V-\sigma_H)\cos 2(\theta+\beta)]\sqrt{\pi l} \\ &+\sigma_N\sqrt{\pi a}\left[\frac{3}{4}\cos\left(\frac{\theta}{2}\right)+\frac{1}{4}\cos\left(\frac{3\theta}{2}\right)\right])^n \end{aligned} \tag{4-41}$$

Due to the complexity of the expression of $\upsilon(l)$, the life time of the zone t_{zone} can only be obtained through numerical integration. The composite trapezoidal rule is used to solve these equations. With the integrating domain $[0\ l_c]$ is divided into "N" equally spaced panels, the approximation can be expressed as:

$$t_{zone} = \int_0^{l_c} \frac{dl}{CK_I^n} = \frac{l_c}{2N}\left[f(0) + 2\sum_{k=2}^{N} f(l_k) + f(l_c) \right] \tag{4-42}$$

where $f(l) = 2 / (CK_I^n)$ denotes the reciprocal of the crack propagation velocity for one side of the wing crack. Measures have been taken to make the approximation result precise. The code is programmed in such a way that after one approximation the integrating domain is subdivided into "N" equally spaced panels, another one with "2N" divisions is also conducted. The approximation is considered acceptable if the percentage of the error of these two consecutive calculations is below a certain value which is set for the specific precision requirements of the model (0.01 % in this study). Otherwise, another approximation will be performed (two times the former divisions). This process is repeated until the error is below this limit.

The critical wing crack length l_c is determined by the minimum of two limiting values: the critical length determined by K_{IC} and the critical length determined by the dimension of the zone d_{zone} (Fig. 4-48).

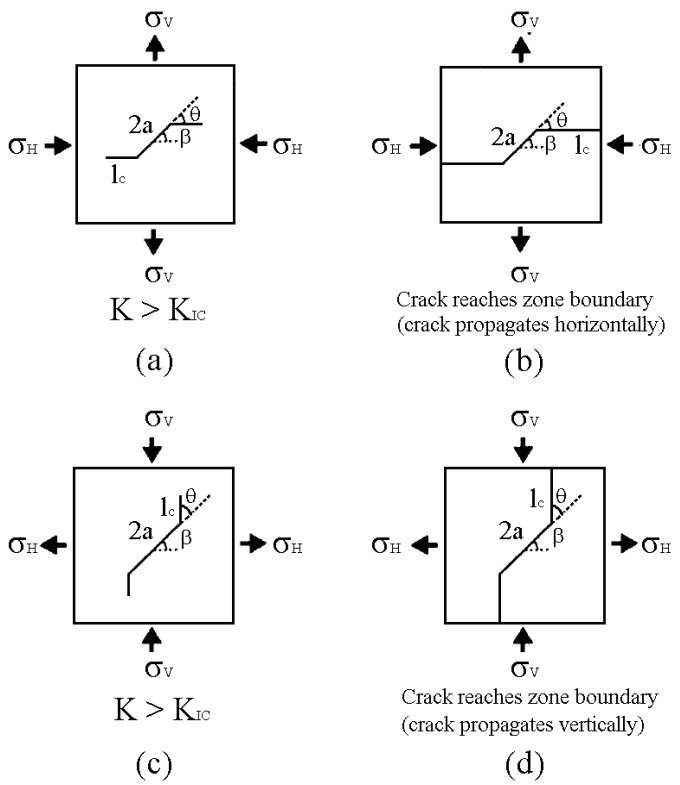

Figure 4-48 Cases of the critical wing crack length in single zone models (major principal stress: σ_V; minor principal stress: σ_H; $\beta = 45°$)

If the main crack is under compressive stress (Fig. 4-48 (c)), according to Equation 4-35, the critical wing crack length l_c determined by K_{IC} is obtained by solving the equation:

$$K_{SLI} + K_{ISO} = -3\sigma_{eff}\sqrt{\frac{a+l_{eq}}{\pi}}\sin^{-1}\left(\frac{a}{a+l_{eq}}\right)\sin\theta\cos\frac{\theta}{2} + \frac{1}{2}\left[(\sigma_V+\sigma_H)+(\sigma_V-\sigma_H)\cos 2(\theta+\beta)\right]\sqrt{\pi l} = K_{IC} \tag{4-43}$$

If the main crack is under the tensile stress (Fig. 4-48 (a)), according to Equation 4-37, the critical wing crack length l_c determined by K_{IC} is obtained by solving the equation:

$$K_{SLI} + K_{ISO} + K_{TEN} = -3\sigma_{eff}\sqrt{\frac{a+l_{eq}}{\pi}}\sin^{-1}\left(\frac{a}{a+l_{eq}}\right)\sin\theta\cos\frac{\theta}{2} + \frac{1}{2}\left[(\sigma_V+\sigma_H)+(\sigma_V-\sigma_H)\cos 2(\theta+\beta)\right]\sqrt{\pi l} + \sigma_N\sqrt{\pi a}\left[\frac{3}{4}\cos\left(\frac{\theta}{2}\right)+\frac{1}{4}\cos\left(\frac{3\theta}{2}\right)\right] = K_{IC} \tag{4-44}$$

The Newton's method is applied to obtain the approximation of the root l_c of Equation 4-43 and 4-44. In the single zone model, the major principal stress is set vertical. So for the compressive case, the wing crack propagates vertically. In this case, $\theta + \beta = \pi / 2$, and the K_{ISO} component in the wing crack K_I is expressed as $K_{ISO} = \sigma_H (\pi l)^{1/2}$. Letting $x = a / (a + l_{eq})$ (satisfying $x \in (0\ 1]$) and $l = 4l_{eq} / (9\cos^2(\theta / 2))$ derived from Equation 4-30, the function of x is expressed:

$$f(x) = -3\sigma_{eff}\sqrt{\frac{a}{\pi x}}\sin^{-1}(x)\sin\theta\cos\frac{\theta}{2} + \frac{2\sigma_H}{3\cos\frac{\theta}{2}}\sqrt{\pi\left(\frac{a}{x}-a\right)} - K_{IC} \tag{4-45}$$

The derivative of the function f(x) is:

$$f'(x) = -3\sigma_{eff}\sqrt{\frac{a}{\pi}}\sin\theta\cos\frac{\theta}{2}\left(-\frac{\sin^{-1}(x)}{2x\sqrt{x}}+\frac{1}{\sqrt{x-x^3}}\right) - \frac{a\sigma_H\sqrt{\pi}}{3\cos\frac{\theta}{2}x^2\sqrt{\frac{a}{x}-a}} \tag{4-46}$$

As the major principal stress is set vertical, for the tensile case, the wing crack propagates horizontally, which means $\theta + \beta = 0$. In this case, the K_{ISO} component in the wing crack K_I is expressed as $K_{ISO} = \sigma_V (\pi l)^{1/2}$. The function of x is expressed:

$$f(x) = -3\sigma_{eff}\sqrt{\frac{a}{\pi x}}\sin^{-1}(x)\sin\theta\cos\frac{\theta}{2} + \frac{2\sigma_V}{3\cos\frac{\theta}{2}}\sqrt{\pi\left(\frac{a}{x}-a\right)}$$
$$+\sigma_N\sqrt{\pi a}\left(\frac{3}{4}\cos\frac{\theta}{2}+\frac{1}{4}\cos\frac{3\theta}{2}\right)-K_{IC} \tag{4-47}$$

The derivative of f (x) is:

$$f'(x) = -3\sigma_{eff}\sqrt{\frac{a}{\pi}}\sin\theta\cos\frac{\theta}{2}\left(-\frac{\sin^{-1}(x)}{2x\sqrt{x}}+\frac{1}{\sqrt{x-x^3}}\right)-\frac{a\sigma_V\sqrt{\pi}}{3\cos\frac{\theta}{2}x^2\sqrt{\frac{a}{x}-a}} \tag{4-48}$$

Giving a start value for x_o, with the expressions of f(x) and f'(x), a better approximation x_1 is obtained:

$$x_1 = x_0 - \frac{f(x_0)}{f'(x_0)} \tag{4-49}$$

The calculation is repeated until a sufficiently precise approximation is reached:

$$x_{k+1} = x_k - \frac{f(x_k)}{f'(x_k)} \tag{4-50}$$

In this study, the approximation is considered acceptable if the percentage of the error between x_{k+1} and x_k is below 0.01 %. This limiting value could also be changed depending on the precision requirement of each specific model. When an acceptable x_{k+1} value is reached, the approximation of the critical wing crack length l_c is obtained by:

$$l_c = \frac{4a(1-x_{k+1})}{9x_{k+1}\cos^2\frac{\theta}{2}} \tag{4-51}$$

The critical wing crack length determined by the dimension of the zone d_{zone} is expressed as:

$$l_c = \min\left\{\frac{d_{zone} - 2a\sin(|\beta|)}{2\sin(|\beta| + |\theta|)}, \frac{d_{zone} - 2a\cos(|\beta|)}{2\cos(|\beta| + |\theta|)}\right\} \tag{4-52}$$

where d_{zone} denotes the length of the zone in this case and 2a denotes the length of the initial main crack. Especially, if the wing crack propagates horizontally (Fig.4-48 (b)), the critical wing crack length is obtained:

$$l_c = \frac{d_{zone} - 2a\cos(|\beta|)}{2} \tag{4-53}$$

If the wing crack propagates vertically (Fig.4-48 (d)), the critical wing crack length is obtained:

$$l_c = \frac{d_{zone} - 2a\sin(|\beta|)}{2} \tag{4-54}$$

The minimum of the three l_c values (Eq. 4-51 and Eq. 4-52) is considered to be the critical wing crack length, and used as the upper limit of the integrating domain in Equation 4-42.

(2) Application of the lifetime prediction scheme

The lifetime prediction scheme for wing crack model has been tested. A square shaped single zone with the size of 0.04 × 0.04 m^2 (the same size as a single zone in the former models) containing an initial crack was used in the tests. The material parameters follow Table 4-1. Both uniaxial and biaxial tests have been studied.

In the uniaxial tensile tests, both failure modes have been detected: failure by K_I value reaching the critical value K_{IC} (Fig. 4-49 (a)), and failure by crack propagation reaching the zone boundary (Fig. 4-49 (b)). For the uniaxial compressive test, only failure by crack propagation reaching the zone boundary has been detected (Fig. 4-49 (c)). The fact that no failure has occurred by $K_I \geq K_{IC}$ in the uniaxial compressive test agrees with the K_I calculation scheme. As can be seen in Fig. 4-48, for the uniaxial compressive loading case, the K_I descends as the crack propagates. So if the model didn't fail by $K_I \geq K_{IC}$ at the wing crack initiation stage, it is no likely to fail in this way when the wing crack propagates even further. The lifetime results of the model under uniaxial loads corresponding to Fig. 4-49 are shown in Table 4-19. As can be seen in the table, the numerical predicted lifetimes showed good agreement with the analytical solutions (Eq. 4-39) in all cases (deviations equal to or smaller than 0.37 %).

The error between the numerical calculation and analytical solution is kept to a very low range also for other important parameters related to the lifetime: the deviations of stress intensity factor at failure are no bigger than 0.006 %; the deviations of critical half wing crack propagation length are no bigger than 0.05 %. In addition, correct failure mode of the zone was predicted for every case.

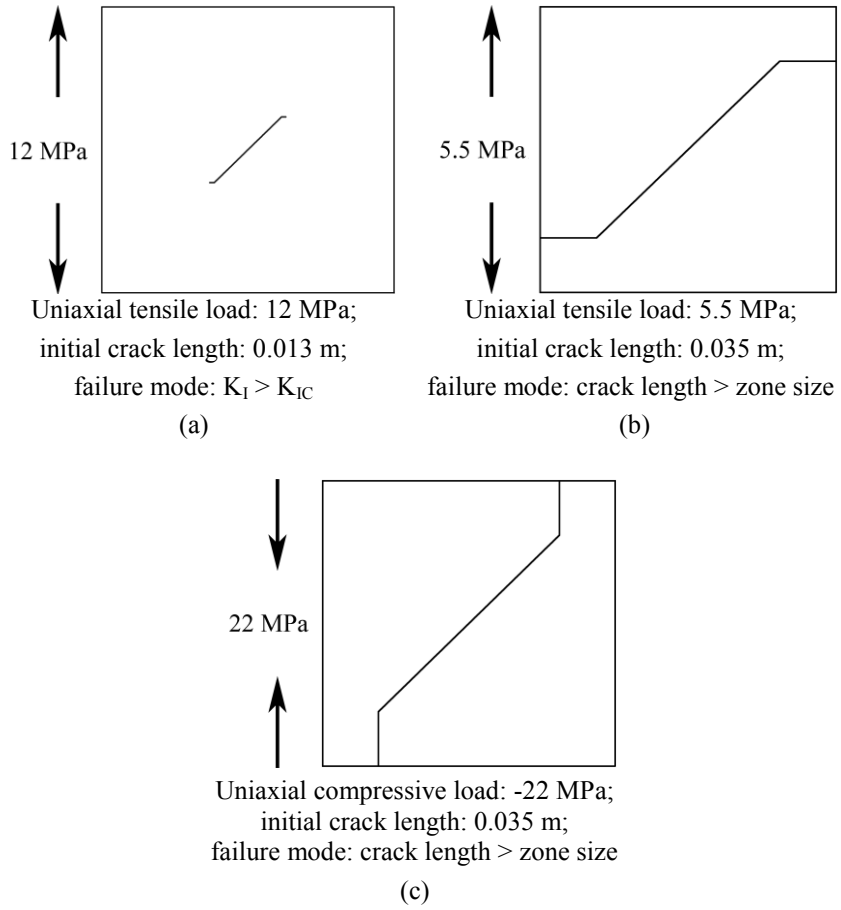

Figure 4-49 Crack condition at failure under uniaxial loads (initial crack orientation: 45º)

Table 4-19 Calculation results under uniaxial loads (corresponding to Fig. 4-49)

(a) Uniaxial tensile load of 12 MPa			
	Analytical results	**Numerical results**	**Error**
K_I	1.7900e6	1.7901e6	0.006 %
Half crack propagation (m)	6.1427e-4	6.1458e-4	0.05 %
Life time (s)	3.7131	3.7270	0.37 %
Failure mode	$K_I > K_{IC}$	$K_I > K_{IC}$	0
(b) Uniaxial tensile load of 5.5 MPa			
	Analytical results	**Numerical results**	**Error**
K_I	1.6736e6	1.6737e6	0.006 %
Half crack propagation (m)	7.6256e-3	7.6265e-3	0.01 %
Life time (s)	1.5180e5 (1 d, 18 h, 9 min.)	1.5236e5 (1 d, 18 h, 19 min.)	0.37 %
Failure mode	Crack length > zone size	Crack length > zone size	0

(c) Uniaxial compressive load of 22 MPa			
	Analytical results	**Numerical results**	**Error**
K_I	8.7878e5	8.7875e5	0.003 %
Half crack propagation (m)	7.6256e-3	7.6265e-3	0.01 %
Life time (s)	5.9352e9 (188 y, 74 d, 13 h, 38 min.)	5.9386e9 (188 y, 113 d, 5 h, 24 min.)	0.06 %
Failure mode	Crack length > zone size	Crack length > zone size	0

The lifetime prediction scheme has been further tested on a single zone for biaxial loading conditions (major principal stress is applied vertically). The crack pattern of the model at failure in each case is shown in Fig. 4-50 and the calculation results are listed in Table 4-20. It is seen in Fig. 4-50 that both zone failure modes: failure by $K_I \geq K_{IC}$ and failure by crack reaching the zone boundary, have been observed under biaxial tensile loads (Fig. 4-50 (a), (b)), under major tensile load and minor compressive load (Fig. 4-50 (c), (d)), and under major compressive load and minor tensile load (Fig. 4-50 (e), (f)) with different load magnitudes and crack conditions. However, only failure by crack length reaching the zone boundary has been observed under biaxial compressive loads (Fig. 4-50 (g)). This phenomenon is supported by Fig. 4-46 for the biaxial compressive loading case, where the K_I descends as the crack propagates. If K_I of the wing crack tip did not reach K_{IC} at wing crack's initiation, it is not possible to reach K_{IC} when the wing crack propagates even further. The numerical predicted lifetimes have shown accordance with the analytical solutions in all cases: the deviations between the numerical predicted lifetime and the analytical solution range from 0.003 % to 1.7 % (Table 4-20). For the stress intensity factor at failure, the deviations between the numerical calculation and analytical result has been less than 0.05 %; the deviations of the half crack propagation length between the numerical calculation and analytical result has been no bigger than 0.01 % in all cases. In addition, the correct failure mode for the zone was predicted in all cases.

The wing crack model has been studied exhaustively under both uniaxial and biaxial loads, where all possible loading configurations have been applied and all possible failure modes have been observed. The lifetime prediction scheme for wing crack models is thus verified by the well agreement between the numerical results and the analytical solutions, which also proved the applicability of the lifetime prediction scheme for wing crack model to more complex stress conditions (multi-zone model).

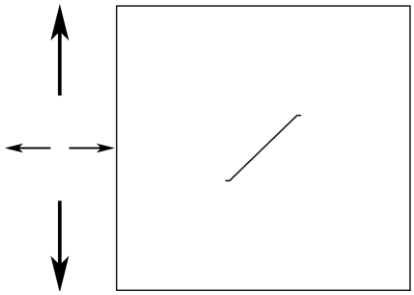

Principal stresses: 12 MPa , 6 MPa;
initial crack length: 0.013 m;
failure mode: $K_I > K_{IC}$
(a)

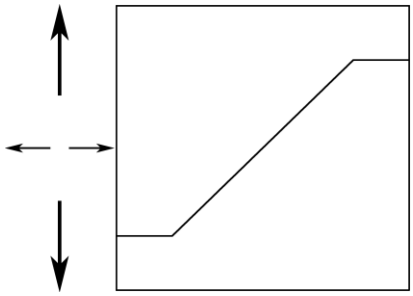

Principal stresses: 5 MPa, 4 MPa;
initial crack length: 0.035 m;
failure mode: crack length > zone size
(b)

Loading case I: major principal stress (vertical): tensile;
minor principal stress (horizontal): tensile

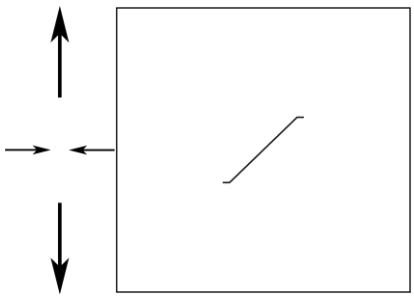

Principal stresses: 12 MPa, -6 MPa;
initial crack length: 0.013 m;
failure mode: $K_I > K_{IC}$
(c)

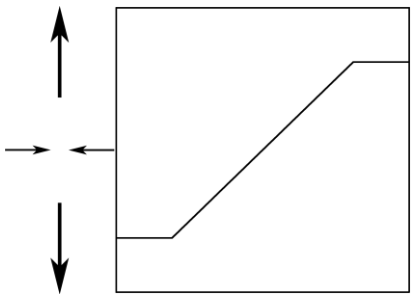

Principal stresses: 5 Mpa, -4 MPa;
initial crack length: 0.035 m;
failure mode: crack length > zone size
(d)

Loading case II: major principal stress (vertical): tensile;
minor principal stress (horizontal): compressive

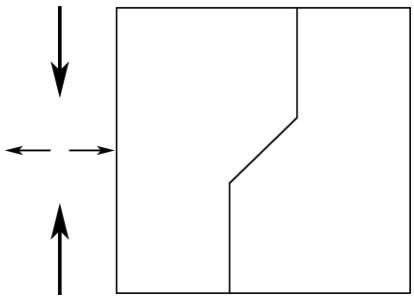

Principal stresses: -12 MPa, 6 MPa;
initial crack length: 0.013 m;
failure mode: crack length > zone size
(e)

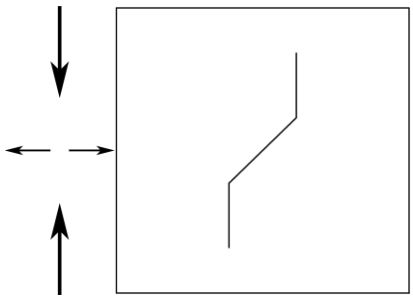

Principal stresses: -12 MPa, 8 MPa;
initial crack length: 0.013 m;
failure mode: $K_I > K_{IC}$
(f)

Loading case III: major principal stress (vertical): compressive;
minor principal stress (horizontal): tensile

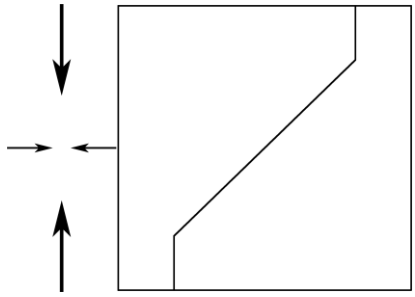

Principal stresses: -22 MPa, -0.12 MPa;
initial crack length: 0.035 m;
failure mode: crack length > zone size
(g)

Loading case IV: major principal stress (vertical): compressive;
minor principal stress(horizontal): compressive

Figure 4-50 Crack pattern at failure for the biaxial test (initial crack orientation: 45º)

Table 4-20 Calculation results for the biaxial tests (corresponding to Fig. 4-50)

Loading case I			
(a)			
	Analytical results	**Numerical results**	**Error**
K_I	1.7900e6	1.7901e6	0.006 %
Half crack propagation (m)	4.9255e-4	4.9270e-4	0.03 %
Life time (s)	9.1	9.2	1 %
Failure mode	$K_I > K_{IC}$	$K_I > K_{IC}$	0
(b)			
	Analytical results	**Numerical results**	**Error**
K_I	1.6630e6	1.6631e6	0.006 %
Half crack propagation (m)	7.6256e-3	7.6265e-3	0.01 %
Life time (s)	1.8184e7 (s) (210 d, 11 h, 3 min.)	1.8494e7 (s) (214 d, 1 h, 20 min.)	1.7 %
Failure mode	Crack length > zone size	Crack length > zone size	0
Loading case II			
(c)			
	Analytical results	**Numerical results**	**Error**
K_I	1.7900e6	1.7900e6	< 0.05 %
Half crack propagation (m)	8.5410e-4	8.5410e-4	< 0.001 %
Life time (s)	2.3	2.3	0.09 %
Failure mode	$K_I > K_{IC}$	$K_I > K_{IC}$	0
(d)			
	Analytical results	**Numerical results**	**Error**
K_I	1.3799e6	1.3799e6	< 0.006 %
Half crack propagation (m)	7.6256e-3	7.6265e-3	0.01 %
Life time (s)	2.3837e6 (27 d, 14 h, 7 min.)	2.3846e6 (27 d, 14 h, 22 min.)	0.04 %
Failure mode	Crack length > zone size	Crack length > zone size	0

Loading case III			
(e)			
	Analytical results	**Numerical results**	**Error**
K_I	1.6281e6	1.6281e6	< 0.006 %
Half crack propagation (m)	1.5404e-2	1.5404e-2	< 0.006 %
Life time	2.6513e7 (s) (306 d, 20 h, 39 min.)	2.6514e7 (s) (306 d, 20 h, 53 min.)	0.003 %
Failure mode	Crack length > zone size	Crack length > zone size	0
(f)			
	Analytical results	**Numerical results**	**Error**
K_I	1.7900e6	1.7900e6	< 0.005 %
Half crack propagation (m)	9.0195e-3	9.0197e-3	0.002 %
Life time (s)	4.2916e4 (11 h, 55 min.)	4.2919e4 (11 h, 55 min.)	0.007 %
Failure mode	$K_I > K_{IC}$	$K_I > K_{IC}$	0
Loading case IV			
(g)			
	Analytical results	**Numerical results**	**Error**
K_I	8.6987e5	8.6985e5	0.002 %
Half crack propagation (m)	7.6256e-3	7.6265e-3	0.01 %
Life time	8.3667e9 (s) (265 y, 111 d, 16 h, 14 min.)	8.3714e9 (s) (265 y, 166 d, 4 h, 6 min.)	0.06 %
Failure mode	Crack length > zone size	Crack length > zone size	0

Factors influencing lifetime have been investigated. Lifetime results of the zone under different constant loads, initial crack lengths and initial crack orientations have been investigated. The results are seen in Table 4-21, 4-22 and 4-23. The corresponding lifetime results obtained by FLAC are also seen in Fig. 4-51, 4-52 and 4-53.

Table 4-21 Uniaxial tests with different constant loads (corresponding to Fig. 4-51)

(a) Under tensile loads			
Load (MPa)	**Lifetime (s)** **(Analytical solution)**	**Lifetime (s)** **(Numerical calculation)**	**Failure mode**
6	5.3638e10 (1,700 y, 314 d, 19 h, 22 min.)	5.3829e10 (1,706 y, 336 d, 8 h, 52 min.)	$K_I > K_{IC}$
8	3.2815e6 (37 d, 23 h, 31 min.)	3.2935e6 (38 d, 2 h, 52 min.)	$K_I > K_{IC}$
9	6.1808e4 (17 h, 10 min.)	6.2033e4 (17 h, 13 min.)	$K_I > K_{IC}$
10	1,769 (29 min., 29 s)	1,776 (29 min., 36 s)	$K_I > K_{IC}$
11	71.0320 (1 min., 11 s)	71.2930 (1 min., 11 s)	$K_I > K_{IC}$
12	3.7	3.7	$K_I > K_{IC}$

(b) Under compressive loads			
Load (MPa)	**Lifetime (s) (Analytical solution)**	**Lifetime (s) (Numerical calculation)**	**Failure mode**
20	1.4769e11 (4,683 y, 29 d, 8 h, 6 min.)	1.4777e11 (4,685 y, 261 d, 5 h, 51 min.)	Crack length > zone size
20.5	6.4223e10 (2,036 y, 185 d, 21 h, 57 min.)	6.4260e10 (2,037 y, 239 d, 5 h, 9 min.)	Crack length > zone size
21	2.8495e10 (903 y, 203 d, 22 h, 47 min.)	2.8511e10 (904 y, 24 d, 12 h, 58 min.)	Crack length > zone size
21.5	1.2887e10 (408 y, 230 d, 8 h, 22 min.)	1.2894e10 (408 y, 314 d, 6 h, 45 min.)	Crack length > zone size
22	5.9352e9 (188 y, 74 d, 13 h, 38 min.)	5.9386e9 (188 y, 113 d, 5 h, 24 min.)	Crack length > zone size

Table 4-22 Uniaxial tests with different initial crack lengths (corresponding to Fig. 4-52)

(a) Under tensile load of 12 MPa			
Initial crack length (m)	**Lifetime (s) (Analytical solution)**	**Lifetime (s) (Numerical calculation)**	**Failure mode**
0.006	8.0151e5 (9 d, 6 h, 38 min.)	8.0445e5 (9 d, 7 h, 27 min.)	$K_I > K_{IC}$
0.008	8,359 (2 h, 19 min.)	8,389 (2 h, 19 min.)	$K_I > K_{IC}$
0.01	242 (4 min., 2 s)	243 (4 min., 3 s)	$K_I > K_{IC}$
0.013	3.7	3.7	$K_I > K_{IC}$
0.015	0.3	0.3	$K_I > K_{IC}$
(b) Under compressive load of 22 MPa			
Initial crack length (m)	**Lifetime (s) (Analytical solution)**	**Lifetime (s) (Numerical calculation)**	**Failure mode**
0.0338	2.6248e10 (832 y, 115 d, 15 h, 6 min.)	2.6247e10 (832 y, 107 d, 5 h, 44 min.)	Crack length > zone size
0.034	2.0451e10 (648 y, 180 d, 4 h, 37 min.)	2.0456e10 (648 y, 234 d, 6 h, 59 min.)	Crack length > zone size
0.0345	1.0994e10 (348 y, 220 d, 12 h, 30 min.)	1.0996e10 (348 y, 251 d, 9 h, 42 min.)	Crack length > zone size
0.035	5.9352e9 (188 y, 74 d, 13 h, 38 min.)	5.9386e9 (188 y, 113 d, 5 h, 24 min.)	Crack length > zone size
0.0355	3.2171e9 (102 y, 5 d, 10 h, 40 min.)	3.2187e9 (102 y, 23 d, 21 h, 33 min.)	Crack length > zone size
0.0358	2.2319e9 (70 y, 281 d, 20 h, 56 min.)	2.2326e9 (70 y, 289 d, 20 h, 33 min.)	Crack length > zone size

Table 4-23 Uniaxial tests with different initial crack orientations (corresponding to Fig. 4-53)

(a) Under tensile load of 12 MPa			
Crack orientation	**Lifetime (s) (Analytical solution)**	**Lifetime (s) (Numerical calculation)**	**Failure mode**
0º	0.0066	0.0068	$K_I > K_{IC}$
10º	0.0061	0.0063	$K_I > K_{IC}$
20º	0.0073	0.0075	$K_I > K_{IC}$
30º	0.0309	0.0312	$K_I > K_{IC}$
40º	0.5305	0.5328	$K_I > K_{IC}$
45º	3.7131	3.7270	$K_I > K_{IC}$
50º	44.1	44.3	$K_I > K_{IC}$
60º	6.2805e4 (17 h, 26 min.)	6.3274e4 (17 h, 34 min.)	$K_I > K_{IC}$
(b) Under compressive load of 22 MPa			
Crack orientation	**Lifetime (s) (Analytical solution)**	**Lifetime (s) (Numerical calculation)**	**Failure mode**
42º	1.9433e10 (616 y, 82 d, 19 h, 3 min.)	1.9432e10 (616 y, 69 d, 17 h, 46 min.)	Crack length>zone size
45º	5.9352e9 (188 y, 74 d, 13 h, 38 min.)	5.9386e9 (188 y, 113 d, 5 h, 24 min.)	Crack length>zone size
46º	4.7612e9 (150 y, 355 d, 23 h, 9 min.)	4.7619e9 (150 y, 364 d, 23 h, 49 min.)	Crack length>zone size
48º	3.9522e9 (125 y, 117 d, 22 h, 28 min.)	3.9534e9 (125 y, 131 d, 16 h, 48 min.)	Crack length>zone size
50º	4.5910e9 (145 y, 211 d, 14 h, 49 min.)	4.5924e9 (145 y, 227 d, 21 h, 45 min.)	Crack length>zone size
52º	7.4697e9 (236 y, 314 d, 18 h, 4 min.)	7.4651e9 (236 y, 261 d, 14 h, 46 min.)	Crack length>zone size

It is seen in Table 4-21 that with an initial crack length of 0.013 m and initial crack orientation of 45º the zones failed all by $K_I \geq K_{IC}$ under the tensile load ranging from 6 MPa to 12 MPa. With an initial crack length of 0.035 m and initial crack orientation of 45º the zones failed all by crack reaching the zone boundary under the compressive load ranging from 20 MPa to 22 MPa. It is seen in Table 4-22 that with an initial crack orientation of 45º, the zone failed by $K_I \geq K_{IC}$ under the tensile load of 12 MPa with an initial crack length ranging from 0.006 m to 0.015 m. The zones failed by crack reaching the zone boundary under the compressive load of 22 MPa with an initial crack length ranging from 0.0338 m to 0.0358 m. It is seen in Table 4-23 that with an initial crack length of 0.013 m under tensile load of 12 MPa, all zones failed by $K_I \geq K_{IC}$ with an initial crack orientation ranging from 0º to 60º. With an initial crack length of 0.035 m under compressive load of 22 MPa, all zones failed by crack reaching the zone boundary with an initial crack orientation ranging from 42º to 52º. The numerical predicted lifetimes have shown good agreement with the analytical solutions. Similar to the fixed orientation model, the lifetime of the zone is shorter with a bigger load under both tensile and compressive regime (Fig. 4-51). The

lifetime is also shorter with a longer initial crack length with other factors remaining unchanged (Fig. 4-52). It is seen in Fig. 4-53 that under a constant tensile load, the lifetime is longer if the initial crack orientation is bigger. Under a constant compressive load the shortest lifetime is obtained for an initial crack orientation of app. 48º, and the lifetime becomes longer with a bigger or smaller orientation than app. 48º.

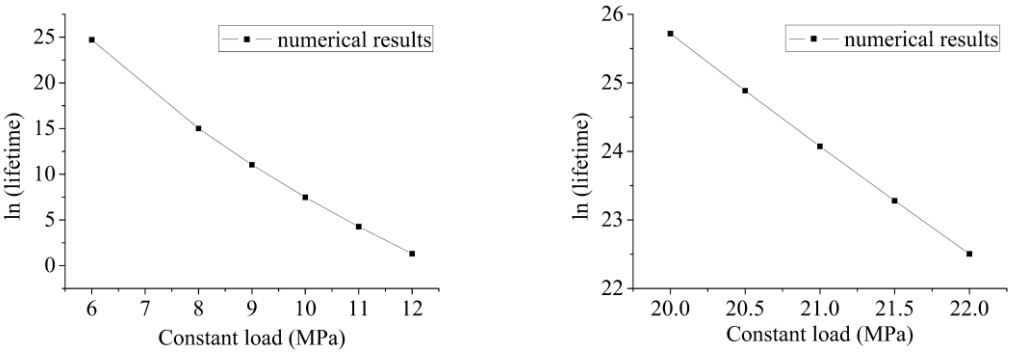

(a) Initial crack length: 0.013 m; Initial crack orientation: 45º (Uniaxial tensile loads)

(b) Initial crack length: 0.035 m; Initial crack orientation: 45º (Uniaxial compressive loads)

Figure 4-51 Natural logarithm of lifetime (seconds) with different constant loads

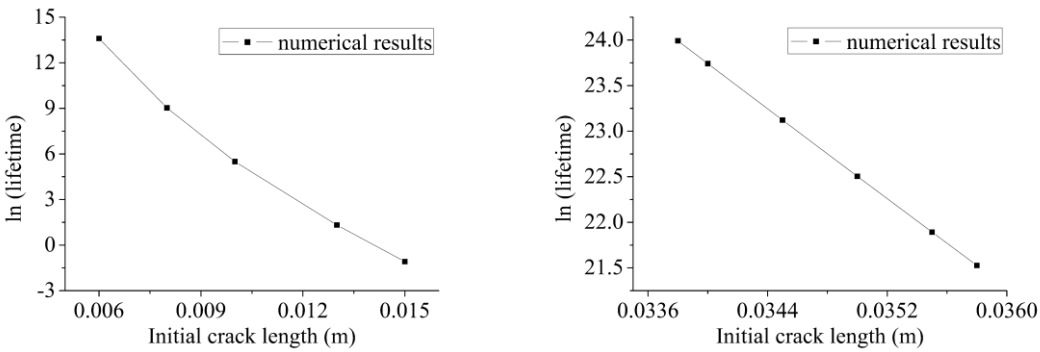

(a) Uniaxial tensile load: 12 MPa; Initial crack orientation: 45º

(b) Uniaxial compressive load: 22 MPa; Initial crack orientation: 45º

Figure 4-52 Natural logarithm of lifetime (seconds) with different initial crack lengths

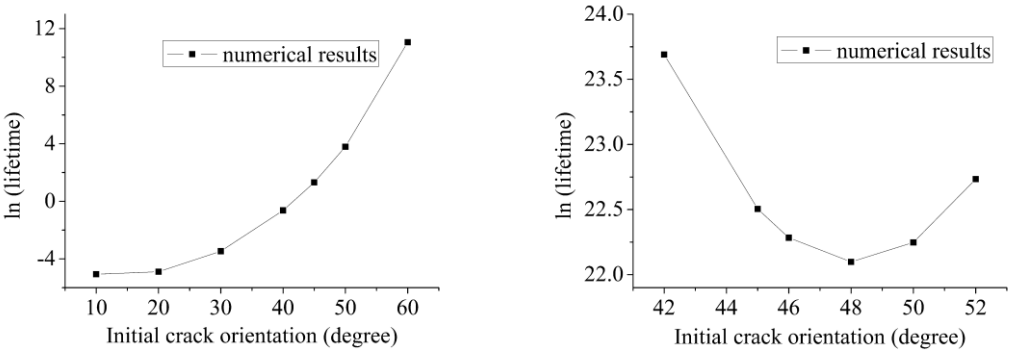

(a) Uniaxial tensile load: 12MPa; Initial crack length: 0.013 m

(b) Uniaxial compressive load: 22 MPa Initial crack length: 0.035 m

Figure 4-53 Natural logarithm of lifetime (seconds) with different initial crack orientations

4.5.6 Study on the multi-zone wing crack model

In this subsection, the lifetime prediction scheme has been applied to the multi-zone wing crack model with its corresponding K superposition calculation scheme under different loading conditions. Models with the same geometry as used in former subsections and parameters as given in Table 4-1 have been studied. (It can be seen from former subsections that models with normal and lognormal distribution of initial crack lengths have rendered very similar results with respect to both macroscopic fracture pattern and lifetime. For simplicity, only normal distribution of initial crack lengths has been applied in this subsection.) The initial crack lengths of the models follow the normal distribution with a mean length of 0.035 m and standard deviation of 0.0001 m. For the Initial crack orientation, two distributions have been applied: uniform distribution, and normal distribution with a mean value of 45º from the horizontal direction and a standard deviation of 1º. Both uniaxial and biaxial tests have been studied.

(1) A tensile load of 5.5 MPa is applied to the model in the uniaxial tensile test. The failure process of the model is shown in Fig. 4-54. Corresponding to the two cases with different initial crack orientations, Fig. 4-55 and Fig. 4-56 shows the microscopic crack conditions at failure with a zoomed in area of the macroscopic fractures. It is seen that macroscopic fracture was formed perpendicular to the applied load for the case with normally distributed initial crack orientation; while multiple macroscopic fractures formed in the case with uniformly distributed initial crack orientation have shown a more uneven pattern, but it is also clearly seen that the trend is still perpendicular to the applied load (Fig. 4-54). It is also observed from the failure process (Fig. 4-54) that for the case where the initial crack orientation follows normal distribution, it took about 7 hours 35 minutes for the first zone to fail, while only after less than 1 minutes the macroscopic fracture has penetrated the whole model (at about 7 hours 36 minutes). While for the case where the initial crack orientation follows uniform distribution, the first zone failed in a much shorter time (10 minutes 1 second), and after farther 5 minutes (at 15 minutes 51 seconds), which was longer than the case with a normal distribution, macroscopic fractures have formed massively. It is worth noticing that afterwards, the macroscopic fractures have been halted and the progress has been very slow: after more than 23 days and 21 hours the appearance of the macroscopic fractures has not changed much and a penetration through the model still did not occur. The influence of the initial crack orientation on the macroscopic fractures is clearly seen by the comparison of the two cases: if the initial crack orientation follows uniform distribution (Case 1), the model contains more zones with more favorable initial crack orientation for a short failure time than an orientation of about 45º (for example, 20º, 10º and 0º etc., consulting Fig. 4-53 (a)), which is the mean angle for the case with a normal distribution (Case 2). So it takes

much shorter time for some zones to fail and form macroscopic fractures in Case1 than Case 2, but at the same time Case 1 also contains more zones with less favorable initial crack orientation than those in case 2 (for example, 50º, 60º and 70º etc., consulting Fig. 4-53 (a)). When the macroscopic fracture in Case 1 reaches a zone with an unfavorable initial crack orientation, the progress of the macroscopic fracture growth is stopped and eventually a longer lifetime is obtained for Case 1. According to lifetime results shown in Table 4-24, the numerical predicted first zone failure time has shown good agreement with the analytical solution (Eq. 4-39), and numerical results of the failure mode and the position of the first failure zone also match the analytical solution.

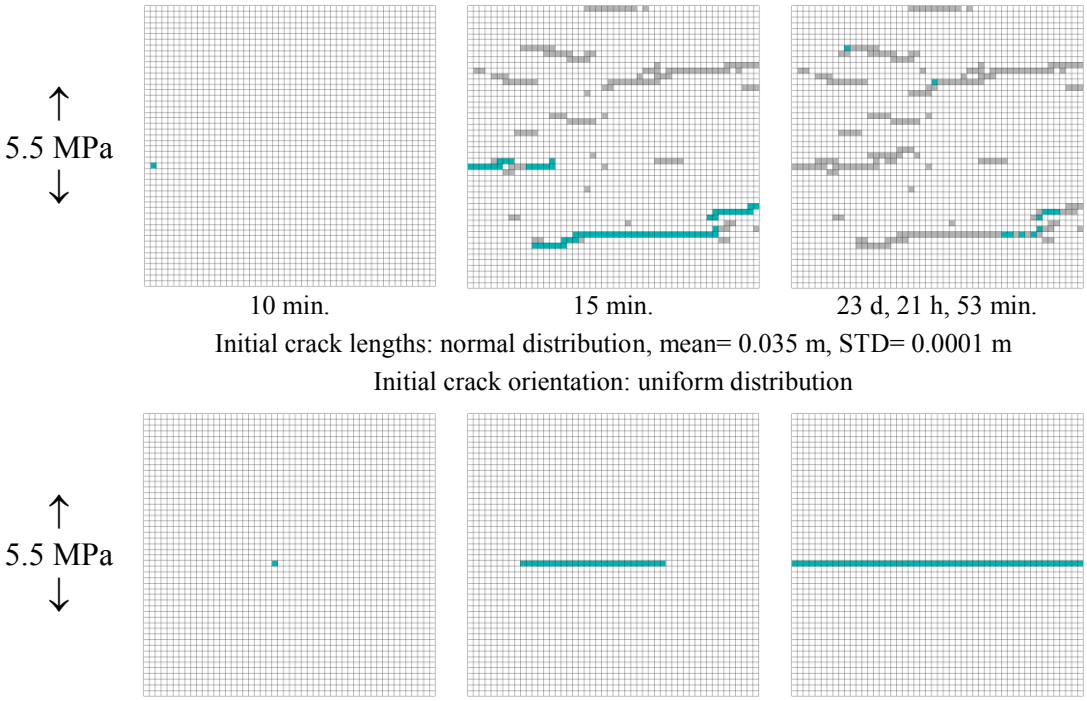

Figure 4-54 Uniaxial tensile test of the wing crack model (zones in green: tensile failure; zones in gray: failed in the past)

Table 4-24 Lifetime results of uniaxial tensile test

Analytical results		**Numerical results**		
First failure zone	**First failure time (s)**	**First failure zone**	**First failure time (s)**	**Lifetime (s)**
Initial crack orientation: uniform distribution				
(2, 22)	578 (9 min., 38 s)	(2, 22)	601 (10 min., 1 s)	2.0660e6 /NA (23 d, 21 h, 53 min.)
Initial crack orientation: normal distribution (mean= 45º, STD= 1º)				
(23, 24)	2.7266e4 (7 h, 34 min.)	(23, 24)	2.7321e4 (7 h, 35 min.)	2.7361e4 (7 h, 36 min.)

The analysis of the microcrack characteristics has revealed that in most of the tension failure zones forming the macroscopic fractures the microcracks inside have not reached the zone boundary, which means these zones fail by $K_I \geq K_{IC}$. Especially, in the case where initial crack orientation follows normal distribution, as can be seen from Fig. 4-56, the first failure zone (Zone (23, 24), consulting Table 4-24) failed by crack reaching the zone boundary (the middle zone of the 5 failed zones), and other zones failed afterwards by $K_I \geq K_{IC}$. This is explained by the comparative longer time before Zone (23, 24) failed (7 hours 35 minutes 21 seconds), as the microcrack in this zone was in the subcritical crack grow phase, and afterwards sudden failure occurred for the other zones which leads to a comparative short time span (less than 1 minutes from 7 hours 35 minutes to 7 hours 36 mintues, consulting Table 4-24).

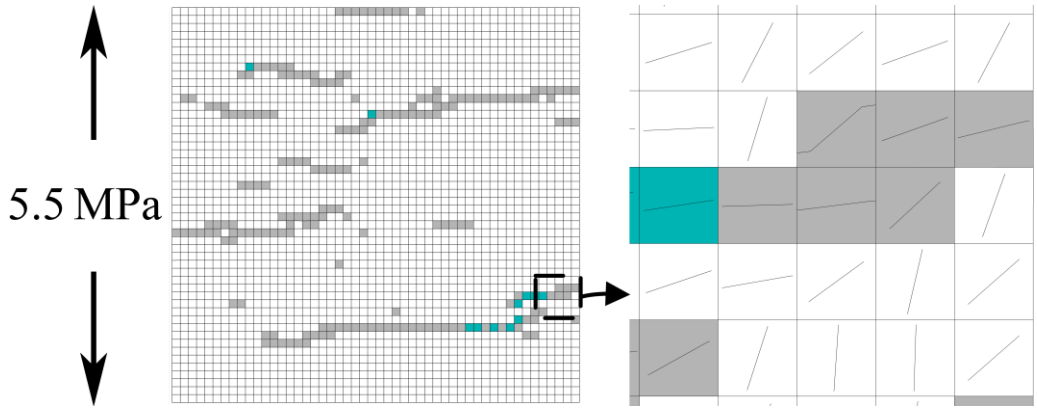

Figure 4-55 Crack characteristics after 23 days in the uniaxial tensile test (zones in green: tensile failure; zones in gray: failed in the past; initial crack lengths: normal distribution, mean = 0.035 m, STD = 0.0001 m; initial crack orientation: uniform distribution)

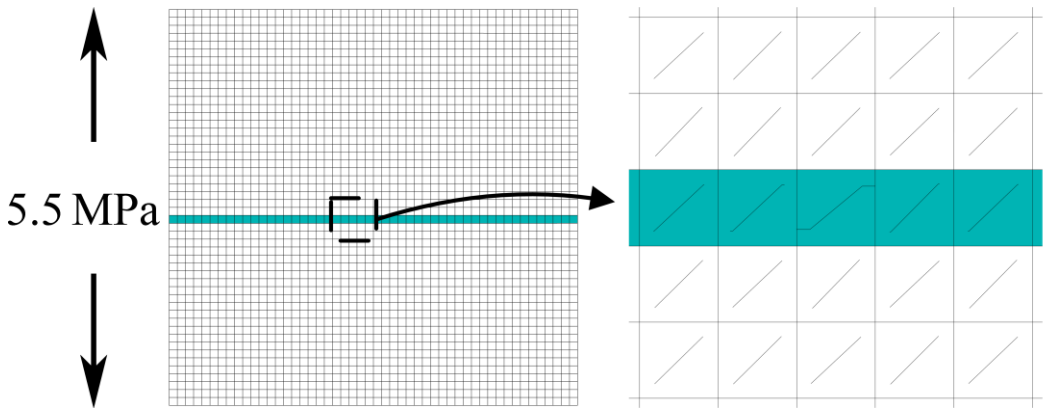

Figure 4-56 Crack characteristics at failure in the uniaxial tensile test (zones in green: tensile failure; initial crack lengths: normal distribution, mean = 0.035 m, STD = 0.0001 m; initial crack orientation: normal distribution, mean = 45º, STD = 1º)

To study the influence of the crack orientation on the lifetime, tests have also been done on models with different initial crack orientations under uniaxial tension. The same tensile load of 5.5 MPa was applied. The calculation results using different

mean initial crack orientations are listed in Table 4-25. It is seen that the numerical predicted first zone failure time showed great precision as compared with the analytical solution (Eq. 4-39) for all mean orientations tested. The first zone failure time is shorter with a smaller mean initial crack orientation. The numerical prediction of the position of the first failure zone also matches the analytical solution for all cases. With the mean orientation ranging from 20º to 60º, the lifetime of the model ranges from about 11 minutes to more than 1 year. Especially, the time span between the first zone failure to the failure of the model becomes longer with a bigger mean orientation: the time span is only 3 seconds (from 11 minutes 19 seconds to 11 minutes 22 seconds) if the mean orientation is 20º, and becomes more than 1 day (from 1 year 322 days 1 hour to 1 year 323 days 23 hours) if the mean orientation is 60º. The numerical predicted lifetime results are shown in Fig. 4-57. The pattern is similar to the single zone study (Fig. 4-53 (a)): the lifetime becomes longer if the mean initial crack orientation becomes bigger.

Table 4-25 Lifetime results of unaxial tensile test (tensile load of 5.5 MPa) with different mean initial crack orientations

	Analytical results		**Numerical results**		
Mean orientation	**First failure zone**	**First failure time (s)**	**First failure zone**	**First failure time (s)**	**Lifetime (s)**
20º	(4, 32)	676 (11 min., 16 s)	(4, 32)	679 (11 min., 19 s)	682 (11 min., 22 s)
30º	(48, 24)	1,219 (20 min., 19 s)	(48, 24)	1,224 (20 min., 24 s)	1,253 (20 min., 53 s)
40º	(48, 24)	6,379 (1 h, 46 min., 19 s)	(48, 24)	6,406 (1 h, 46 min.)	6,448 (1 h, 47 min.)
45º	(23, 24)	2.7266e4 (7 h, 34 min., 26 s)	(23, 24)	2.7321e4 (7 h, 35 min.)	2.7361e4 (7 h, 36 min.)
50º	(48, 24)	1.8147e5 (2 d, 2 h, 24 min.)	(48, 24)	1.8211e5 (2 d, 2 h, 35 min.)	1.8228e5 (2 d, 2 h, 37 min.)
60º	(48, 24)	5.9035e7 (1 y, 318 d, 6 h, 43 min.)	(48, 24)	5.9361e7 (1 y, 322 d, 1 h, 11 min.)	5.9529e7 (1 y, 323 d, 23 h, 47 min.)

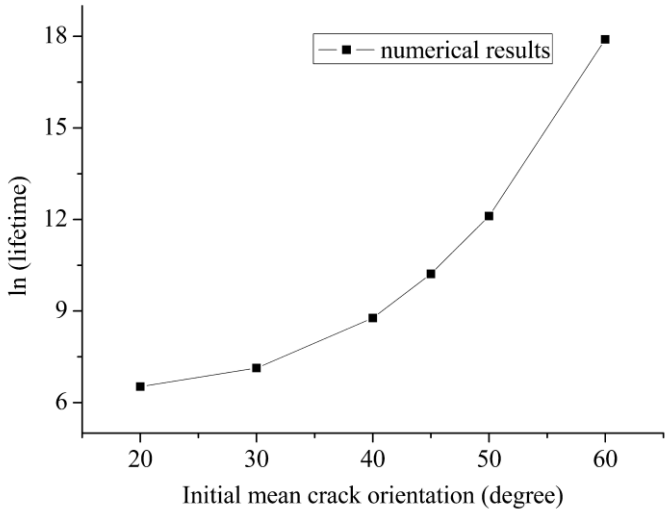

Figure 4-57 Natural logarithm of lifetime (seconds) in tensile test (tensile load of 5.5 MPa) with different mean initial crack orientations (initial crack lengths: normal distribution, mean = 0.035 m, STD = 0.0001 m)

(2) For the uniaxial compressive test, a compressive load of 22 MPa is applied to the model. The macroscopic failure stages of the model are shown in Fig. 4-58. It is seen that shear band was formed at an inclination of 65º to the direction of the applied load if the initial crack orientation follows uniform distribution. In the failed zones forming the shear band (upper in Fig. 4-58), more zones under tensile failure have been found than in the models mentioned above. If the initial crack orientation follows normal distribution, instead of a shear band, the straight macroscopic fracture was formed following the direction of the applied compressive load (Fig. 4-58). As for the first zone failure time, the numerical result is in good agreement with the analytical solution for both cases. Also, the numerical calculation has predicted the same position of the first failure zone as the analytical solution in each case (Table 4-26). It is also seen from Table 4-26 that, the time span between the first failure zone and final failure of the model is about 1 year (from 90 years 33 days to 91 years 34 days) if the initial crack orientation follows uniform distribution, while with normal distribution, the time span is only about 68 days (from 94 years 29 days to 94 years 97 days).

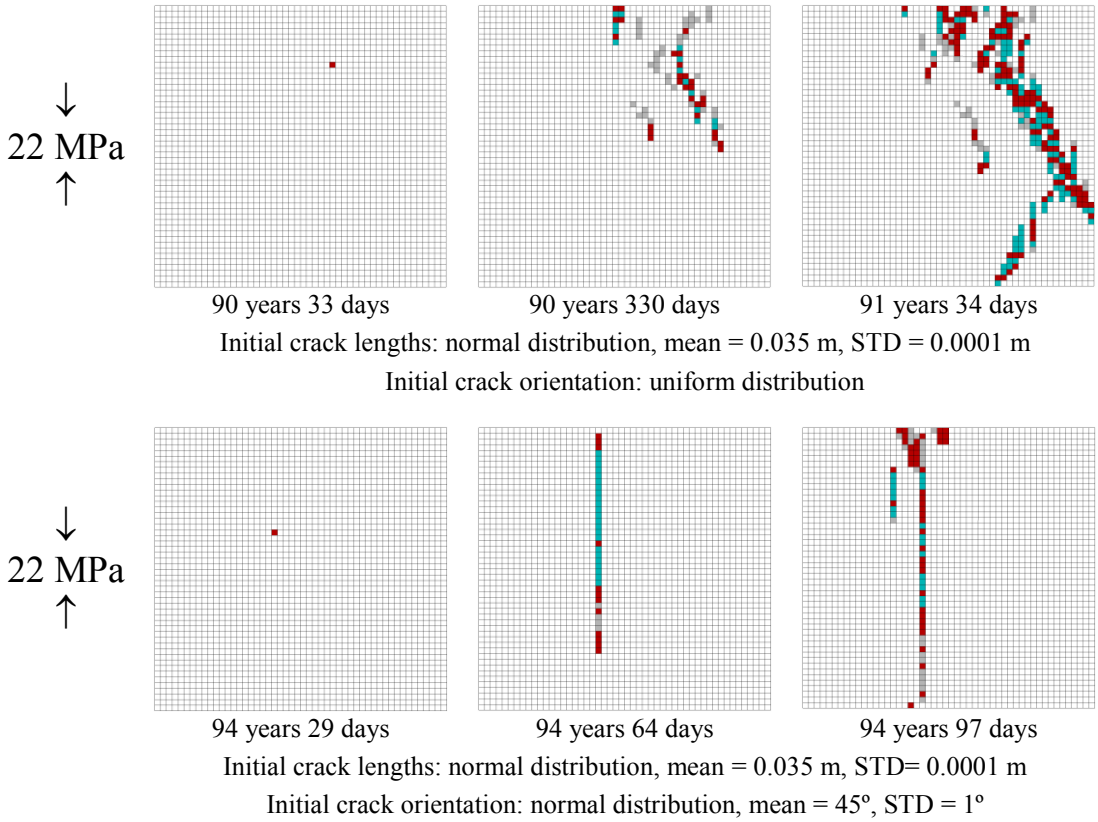

Figure 4-58 Uniaxial compressive test of the wing crack model (zones in green: tensile failure; zones in red: shear failure; zones in gray: failed in the past)

Table 4-26 Lifetime results of uniaxial compressive test

Analytical results		**Numerical results**		
First failure zone	**First failure time (s)**	**First failure zone**	**First failure time (s)**	**Lifetime (s)**
Initial crack orientation: uniform distribution				
(31, 40)	2.8427e9 (s) (90 y, 51 d, 20 h, 9 min.)	(31, 40)	2.8412e9 (s) (90 y, 33 d, 18 h, 51 min.)	2.8727e9 (s) (91 y, 34 d, 6 h, 7 min.)
Initial crack orientation: normal distribution (mean= 45º, STD= 1º)				
(21, 32)	2.9685e9 (94 y, 48 d, 34 min.)	(21, 32)	2.9670e9 (94 y, 29 d, 18 h, 51 min.)	2.9728e9 (94 y, 97 d, 1 h, 12 min.)

Fig. 4-59 and Fig. 4-60 show the fracture pattern with a zoomed in area, corresponding to the failure stages of the model with two different distributions of initial crack orientation shown in Fig. 4-58. It is seen that for both the initial crack orientations following uniform and normal distribution, the microcracks inside most of the failed zones forming the macroscopic fracture have reached the zone boundaries, which denotes that zones failed in the subcritical crack propagation phase.

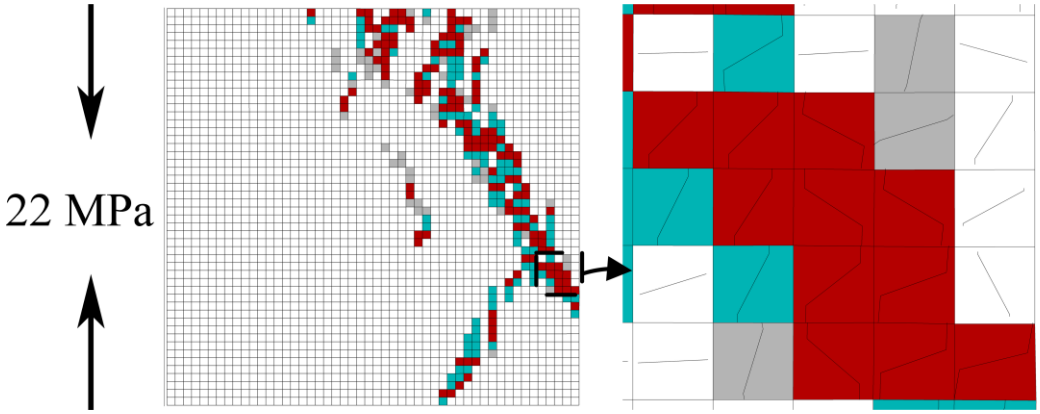

Figure 4-59 Crack characteristics at failure in the uniaxial compressive test (zones in green: tensile failure; zones in red: shear failure; zones in gray: failed in the past; initial crack lengths: normal distribution, mean = 0.035 m, STD = 0.0001 m; initial crack orientation: uniform distribution)

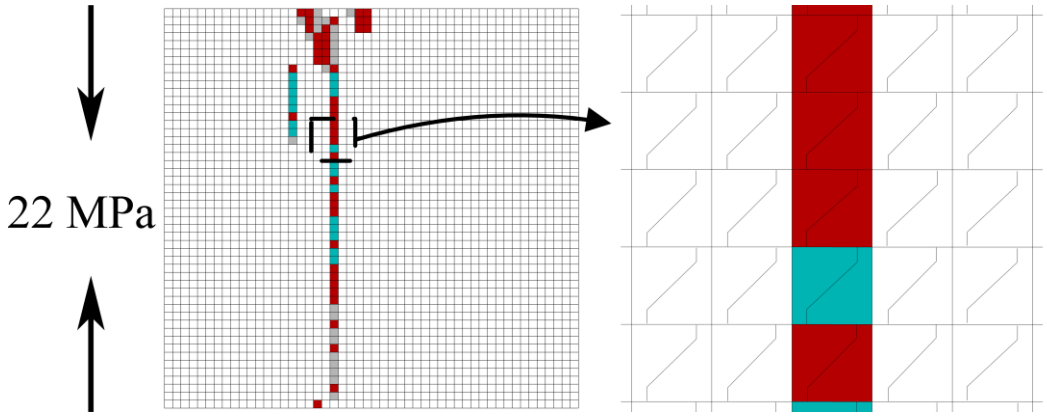

Figure 4-60 Crack characteristics at failure in the uniaxial compressive test (zones in green: tensile failure; zones in red: shear failure; zones in gray: failed in the past; initial crack lengths: normal distribution, mean = 0.035 m, STD = 0.0001 m; initial crack orientation: normal distribution, mean = 45º, STD = 1º)

Influence of mean initial crack orientation on the lifetime under uniaxial compressive load has been studied. The same compressive load of 22 MPa was applied. With respect to the first failure zone, the numerical calculation has predicted the same zone position for each mean orientation value, and the first zone failure time has been in good agreement with the analytical solution in all cases (Table 4-27). The time span between the first zone failure and final failure of the model has been about 239 days, 68 days, 51 days, 1 year 240 days and 4 years 135 days for mean initial crack orientation of 40º, 45º, 50º, 55º and 58º, respectively (Table 4-27). This means the shortest time span within the mean orientation range is found with 50º. The numerical predicted lifetime results are also shown in Fig. 4-61. It is seen that similar to the single zone case shown in Fig. 4-53 (b), the lifetimes have a U-shaped curve with ascending mean initial crack orientation. The shortest lifetime is found with a mean orientation of app. 50º (same value with the shortest time span). Longer lifetime is obtained if mean orientation is smaller or bigger than this angle.

Table 4-27 Lifetime results of unaxial compressive test (compressive load of 22 MPa) with different mean orientations

	Analytical results		Numerical results		
Mean orientation	**First failure zone**	**First failure time (s)**	**First failure zone**	**First failure time (s)**	**Lifetime (s)**
40º	(22, 37)	8.5274e9 (270 y, 146 d, 10 h, 27 min.)	(22, 37)	8.5214e9 (270 y, 76 d, 20 h, 45 min.)	8.5420e9 (270 y, 315 d, 19 h, 3 min.)
45º	(21, 32)	2.9685e9 (94 y, 48 d, 34 min.)	(21, 32)	2.9670e9 (94 y, 29d, 18 h, 51 min.)	2.9728e9 (94 y, 97 d, 1 h, 12 min.)
50º	(37, 35)	2.6704e9 (84 y, 247 d, 3 h, 27 min.)	(37, 35)	2.6689e9 (84 y, 230 d, 4 h, 11 min.)	2.6733e9 (84 y, 281 d, 5 h, 56 min.)
55º	(48, 24)	4.4195e9 (140 y, 52 d, 23 min.)	(48, 24)	4.4177e9 (140 y, 30 d, 21 h, 58 min.)	4.4700e9 (141 y, 270 d, 22 h, 48 min.)
58º	(48, 24)	1.1817e10 (374 y, 262 d, 23 h, 23 min.)	(48, 24)	1.1809e10 (374 y, 169 d, 12 h, 38 min.)	1.1947e10 (378 y, 304 d, 7 h, 55 min.)

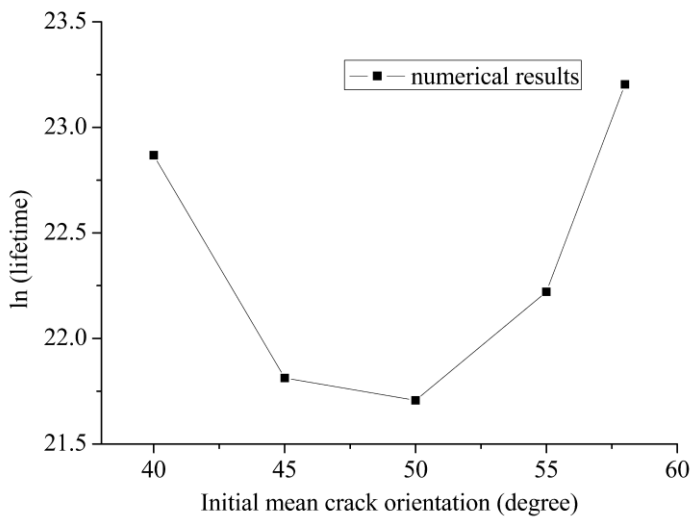

Figure 4-61 Natural logarithm of lifetime (seconds) in compressive test (compressive load of 22 MPa) with different mean initial crack orientations (initial crack lengths: normal distribution, mean = 0.035 m, STD = 0.0001 m; initial crack orientation: normal distribution, mean = 45º, STD = 1º)

(3) Models under biaxial compressive loads have also been studied. The model is under a major principal load of 22 MPa applied vertically and a minor principal load of 0.5 MPa applied horizontally. It is seen from Fig. 4-62 that shear band has formed for both uniform and normal distribution of initial crack orientation. The shear band has an inclination of 65º to the applied major compressive load. Especially, macroscopic fractures following the direction of the applied major compressive load

have been observed for the case with normal distribution of initial crack orientation as well. The first zone failed at about 375 years 233 days for the case where initial crack orientation follows uniform distribution, and after about 24 years (at about 399 years 229 days) the shear band has connected two boundaries of the model (upper Fig. 4-62). While if the initial crack orientation follows normal distribution, the first zone failed at about 398 years 28 days (later than the first case), and only after about 1 year (at about 399 years 129 days), the shear band has caused the final failure for the model (time span much shorter than the first case). The shorter first zone failure time for the case of uniformly distributed initial crack orientation is explained by more zones containing initial cracks with a more favorable orientation (for example 48º, 50º etc., consulting Fig. 4-53 (b), Fig. 4-61) than the case with the normally distributed initial crack orientation where the mean angle is 45º, so under the same loads, there would be zones failed earlier in the first case than the second case. The longer time span for failure for the first case is explained by the fact that it also contains more zones with a less favorable orientation than the second case, which prevent a faster formation of the shear band. As can been seen from the lifetime results shown in Table 4-28, the numerical calculation has given precise first zone failure time compared with the analytical solution (Eq. 4-38) for all cases. Besides, numerical predicted position of the first failure zone has been the same as the analytical solution for each case. The microcrack characteristics at failure of the models are shown in Fig. 4-63 and Fig. 4-64, corresponding to the final failure stage of the model in Fig. 4-62. Similar to the uniaxial compressive loading case, the microcracks inside most of the failed zones forming the shear bands have reached the zone boundaries, denoting the zones failed during the subcritical crack propagation. In addition, the lifetimes under biaxial compressive load have been considerably longer than under uniaxial compressive load when other parameters were kept unchanged. It is seen from Table 4-28 that the lifetimes have a magnitude of about 400 years under biaxial compressive load for both initial crack orientation distributions, while under uniaxial compressive load, the lifetimes have a magnitude of only about 90 years.

Table 4-28 Lifetime results of biaxial compressive test

Analytical results		**Numerical results**		
First failure zone	**First failure time (s)**	**First failure zone**	**First failure time (s)**	**Lifetime (s)**
Initial crack orientation: uniform distribution				
(31, 40)	1.1850e10 (375 y, 274 d, 10 h, 42 min.)	(31, 40)	1.1846e10 (375 y, 233 d, 18 h, 51 min.)	1.2603e10 (399 y, 229 d, 20 h, 51 min.)
Initial crack orientation: normal distribution (mean= 45º, STD= 1º)				
(21, 32)	1.2558e10 (398 y, 76 d, 23 h, 55 min.)	(21, 32)	1.2554e10 (398 y, 28 d, 18 h, 51 min.)	1.2594e10 (399 y, 129 d, 10 h, 27 min.)

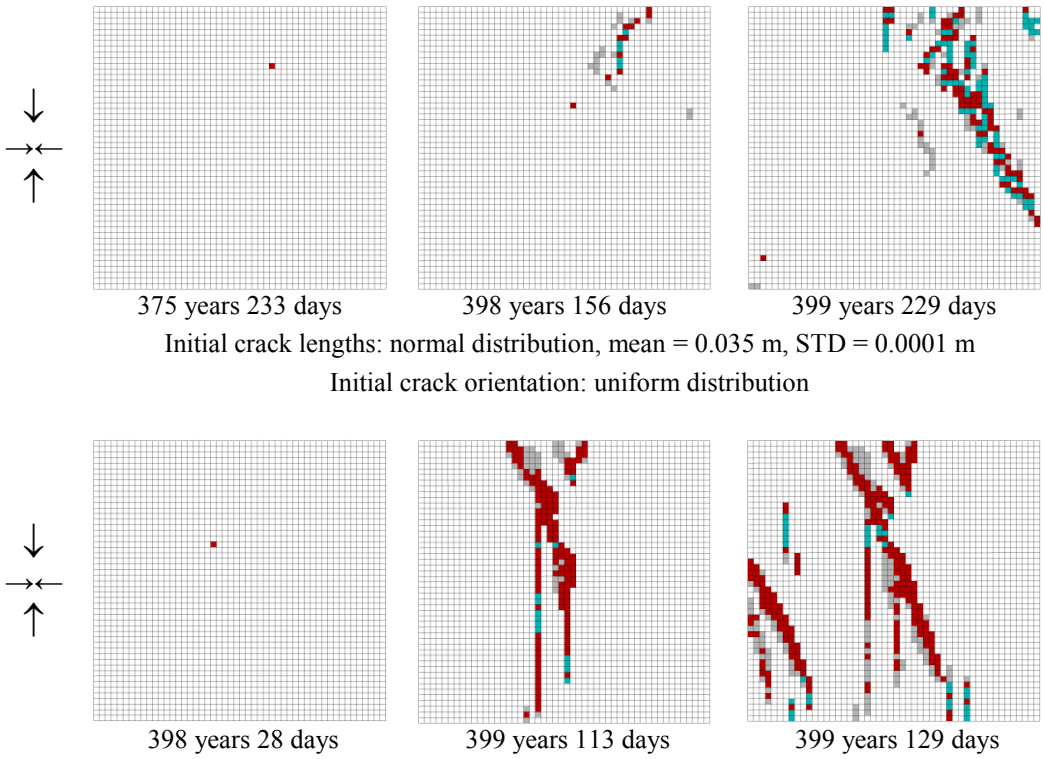

Figure 4-62 Biaxial compressive test of the wing crack model (major compressive load of 22 MPa applied vertically; minor compressive load of 0.5 MPa applied horizontally; zones in green: tensile failure; zones in red: shear failure; zones in gray: failed in the past)

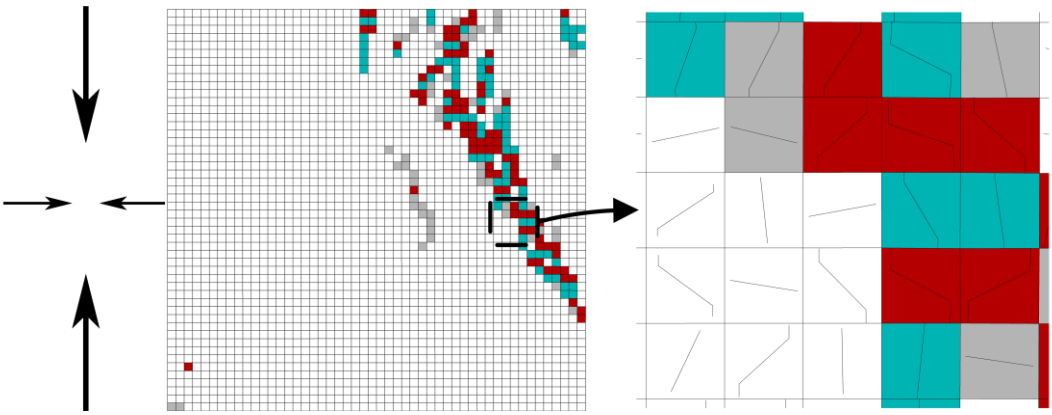

Figure 4-63 Crack characteristics at failure in the biaxial compressive test (major compressive load of 22 MPa applied vertically; minor compressive load of 0.5 MPa applied horizontally; zones in green: tensile failure; zones in red: shear failure; zones in gray: failed in the past; initial crack lengths: normal distribution, mean = 0.035 m, STD = 0.0001 m; initial crack orientation: uniform distribution)

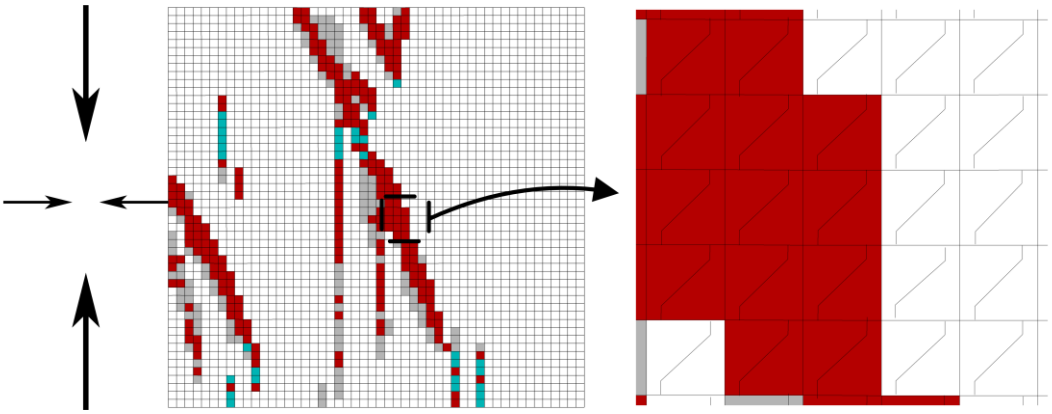

Figure 4-64 Crack characteristics at failure in the biaxial compressive test (major compressive load of 22 MPa applied vertically; minor compressive load of 0.5 MPa applied horizontally; zones in green: tensile failure; zones in red: shear failure; zones in gray: failed in the past; initial crack lengths: normal distribution, mean = 0.035 m, STD = 0.0001 m; initial crack orientation: normal distribution, mean = 45º, STD = 1º)

4.5.7 Conclusions

Simulation techniques for the wing crack propagation have been developed and implemented into the numerical models. A superposition method for calculating the stress intensity factor has been incorporated into the program. The numerical calculations have been compared with the exact solutions. Acceptable results have been obtained. The lifetime prediction scheme for wing crack model has been proposed and studied in this section. The application of the scheme has shown precise results with very low deviations from the analytical results for both single zone and multi-zone models. In the single zone study, the lifetime prediction scheme is investigated exhaustively with all possible loading configurations, and all possible zone failure modes have been observed and results tested. The numerical results have shown excellent agreement with the analytical solutions in all cases. The influences of load magnitude, initial crack length and initial crack orientation on the lifetime have been investigated through a single zone containing an initial crack. Similar to the fixed orientation model, the result shows that lifetime is shorter if the load becomes bigger or the initial crack is longer for both tensile and compressive loads. Under tensile load, the lifetime is longer if the axis of the crack is more perpendicular to the direction of the applied tensile load. Under compressive load, the lifetime value descends first and then ascends with ascending crack orientation, the shortest lifetime is found at an initial crack orientation of app. 48º. The lifetime prediction scheme was also applied to the multi-zone wing crack model. Uniaxial tensile tests, uniaxial compressive tests and biaxial compressive tests have been studied. The numerical results have shown good agreement with the analytical solutions with respect to the first zone failure time and position. If the initial crack orientation follows uniform instead of normal distribution, the first zone failure happens earlier, but the time span from first zone failure to final failure of the model is much longer. In addition, the

considerable prolonged lifetime under biaxial compressive load (with horizontal compressive load of only 0.5 MPa) compared to uniaxial compressive load indicates the resistance of the wing crack propagation under compression. The influence of mean initial crack orientation on lifetime has been investigated. The lifetime has shown similar pattern as in the single zone study. Under tensile load, both the first zone failure time and the lifetime of the model is shorter when the mean initial crack orientation is smaller, and under compressive load, the lifetimes have a U-shaped curve with the shortest lifetime found at a mean initial crack orientation of app. 50º.

4.6 Combined ubiquitous-joint model

In the fixed orientation model scheme and wing crack model scheme the initial crack orientation is known and crack propagation pattern is programmed. However, when the crack has reached the critical condition, the whole zone is considered as failed by assigning the residual strengths to the zone. Based on these two model schemes, two new model schemes are proposed to include anisotropy into the models on the zone level. This improvement is accomplished by incorporating into the model scheme the anisotropic elasto-plastic constitutive law with softening, which contains both the elasto-plastic matrix for the solid and an elasto-plastic line element (weak plane) with softening. The ubiquitous-joint constitutive model in FLAC is utilized for this purpose, which includes the presence of weakness of a certain orientation in a Mohr-Coulomb zone. Yield may occur in either the solid or alone the weak plane, or both, depending on the stress state, the orientation of the weak plane, and material properties of the solid and weak plane (Itasca Consulting Group 2005). The combined ubiquitous-joint model scheme is introduced in subsection 4.6.1. Applications of fixed orientation combined ubiquitous-joint model and wing crack combined ubiquitous-joint model are given in subsections 4.6.2 and 4.6.3, respectively.

4.6.1 Modeling scheme

The modeling scheme of the combined ubiquitous-joint model is programmed such that when the stress intensity factor of the crack inside a zone has reached the critical value ($K \geq K_C$) or the crack has reached the zone dimension, the FLAC ubiquitous-joint constitutive model will be assigned to this zone, substituting the previous Mohr-Coulomb constitutive model. Rather than assigning the residual strength values to the whole zone of Mohr-Coulomb constitutive model, the joint residual strength values will be assigned on the joint (weak plane) only (Fig. 4-65 and Fig.4-66). The joint angle is obtained by consulting the crack's final propagation condition, which is known from the calculation scheme of the fixed orientation model (Section 4.4) or wing crack model (Section 4.5). The simulation schemes for the weak plane are shown in Fig. 4-65 and Fig. 4-66, where the solid line denotes the real crack condition. The dashed line on the left of each figure is the auxiliary line; the dashed line on the

right of each figure denotes the weak plane. For the fixed orientation model, since the crack propagates along its own orientation, the joint angle θ for the ubiquitous-joint constitutive model is the same as the crack's angle (Fig. 4-65), regardless whether the zone fails by crack stress intensity factor reaching fracture toughness (Fig. 4-65 (a)), or the crack reaching the zone boundary (Fig. 4-65 (b)). For the wing crack model, if the crack has reached the zone dimension, the weak plane is defined by connecting the two wing crack tips (Fig. 4-66 (b)); while if the crack's intensity factor has reached the critical value, and crack propagates with ultrasonic velocity. The weak plane is defined by connecting the anticipated location of crack tips at the zone boundary (Fig. 4-66 (a)). The joint angle θ is thus obtained for each case.

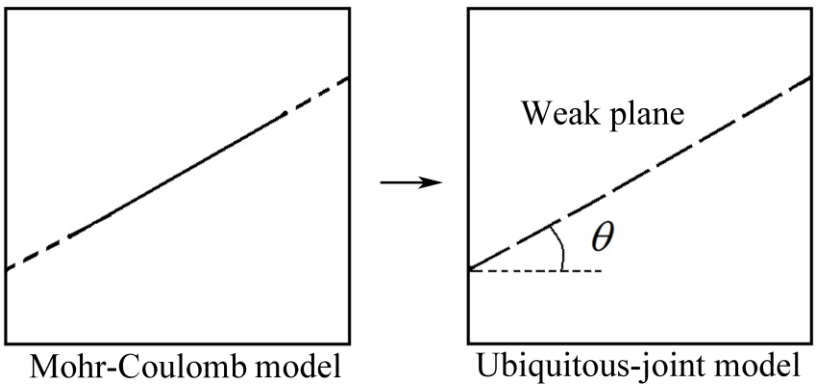

(a) $K \geq K_c$ ($K_I \geq K_{IC}$ or $K_{II} \geq K_{IIC}$)

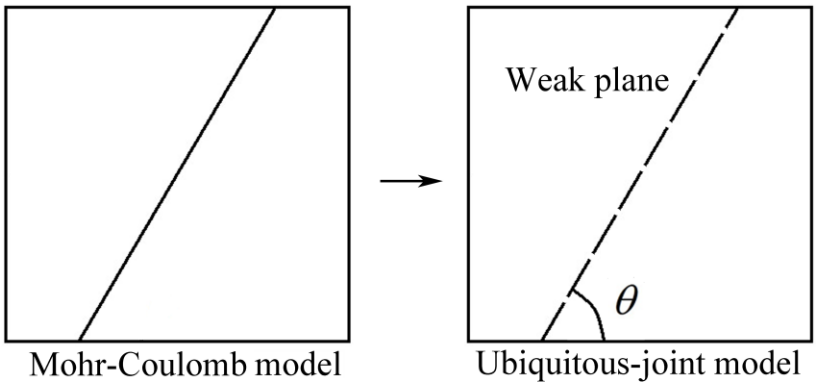

(b) Crack reaching the zone dimension

Figure 4-65 Model scheme for fixed orientation combined ubiquitous-joint model (the solid line in the zone is the actual crack)

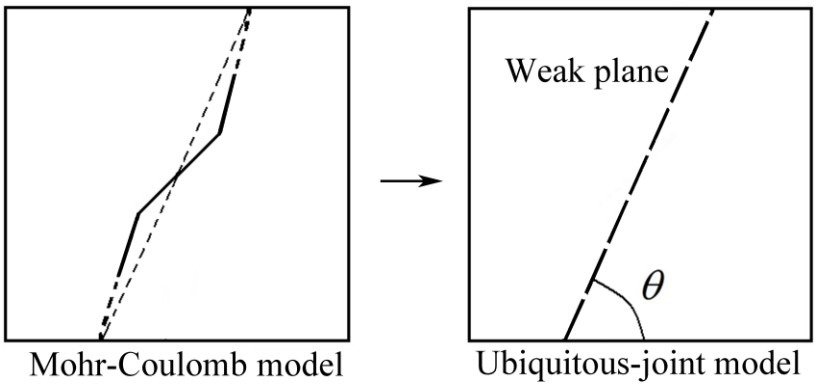

(a) $K_I \geq K_{IC}$

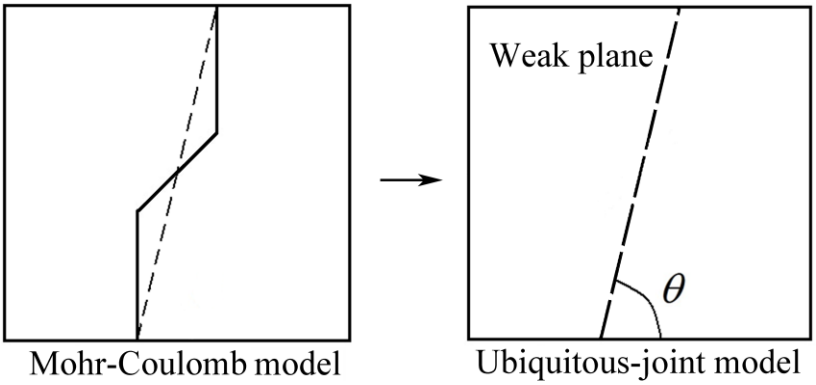

(b) Crack reaching the zone dimension

Figure 4-66 Model scheme for wing crack combined ubiquitous-joint model (the solid line in the zone is the actual crack)

4.6.2 Fixed orientation combined ubiquitous-joint model

Based on the calculation schemes of fixed orientation model introduced in Section 4.4, and incorporating the combined ubiquitous-joint constitutive model scheme described in Subsection 4.6.1, tests have been made on multi-zone models under both tensile and compressive loads. The geometry, parameters and magnitudes of the loads are the same as in the fixed orientation models (Section 4.4) for the convenience of comparison. The same initial crack characteristics as for Model A (Subsection 4.4.3) were used.

As can been seen from the macroscopic failure processes of the model under tensile load of 12 MPa and under constant compressive load of 18 MPa (Fig. 4-67 and Fig. 4-68), the fixed orientation combined ubiquitous-joint model has the same first zone failure location and first failure time as the corresponding fixed orientation model (Fig. 4-29 and Fig. 4-34) due to the same constitutive model applied before any zone fails. The lifetime of the fixed orientation combined ubiquitous-joint model under tension load is 0.4316 seconds if the initial crack orientation follow uniform distribution, and 0.4874 seconeds for normal distribution (Fig. 4-67), slightly longer than the corresponding case in fixed orientation model (0.36 seconds and 0.4826 seconds, respectively, consulting Fig. 4-27 or Table 4-15). Under compressive

load, if the initial crack orientation follows uniform distribution, the lifetime is about 9 years 237 days (Fig. 4-68), longer than the corresponding case in fixed orientation model (7 years 230 days, consulting Fig. 4-34 or Table 4-17), while for the case with normal distribution of orientation, the lifetime is about 11 years 54 days (Fig. 4-68), slightly lower than the corresponding case in fixed orientation model (11 years 68 days, consulting Fig. 4-34 or Table 4-17).

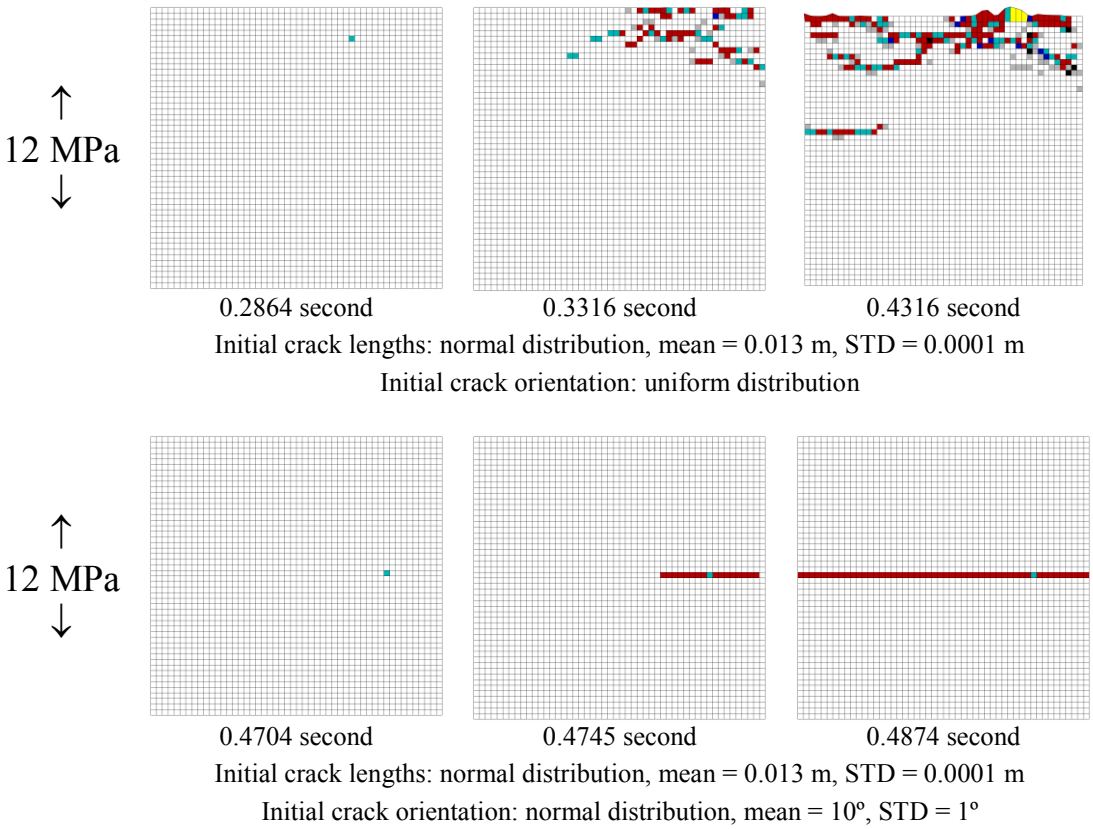

Figure 4-67 Uniaxial tensile test of model A (zones in red: slip along ubiquitous joint; zones in green: tensile failure on ubiquitous joint; zones in yellow: zone failed in tension; zones in black: failed in past (elastic); zones in gray: ubiquitous joint failed in the past)

As for the macroscopic fracture, the combined ubiquitous-joint model has shown similar fracture pattern for the fixed orientation model (consulting Fig. 4-27 and Fig. 4-34). Under tensile load, the macroscopic fracture was formed perpendicular to the applied load, while under compressive load, shear band has been formed with an inclination of 60º to the applied load. It is noticed that the shear band is inclined to an opposite direction compared with the fixed orientation model (lower Fig. 4-68 compared with middle Fig. 4-34). If the initial crack lengths follow uniform distribution, the fracture patterns seem to be more scattered in combined ubiquitous-joint model than in fixed orientation model under both tensile load and compressive load.

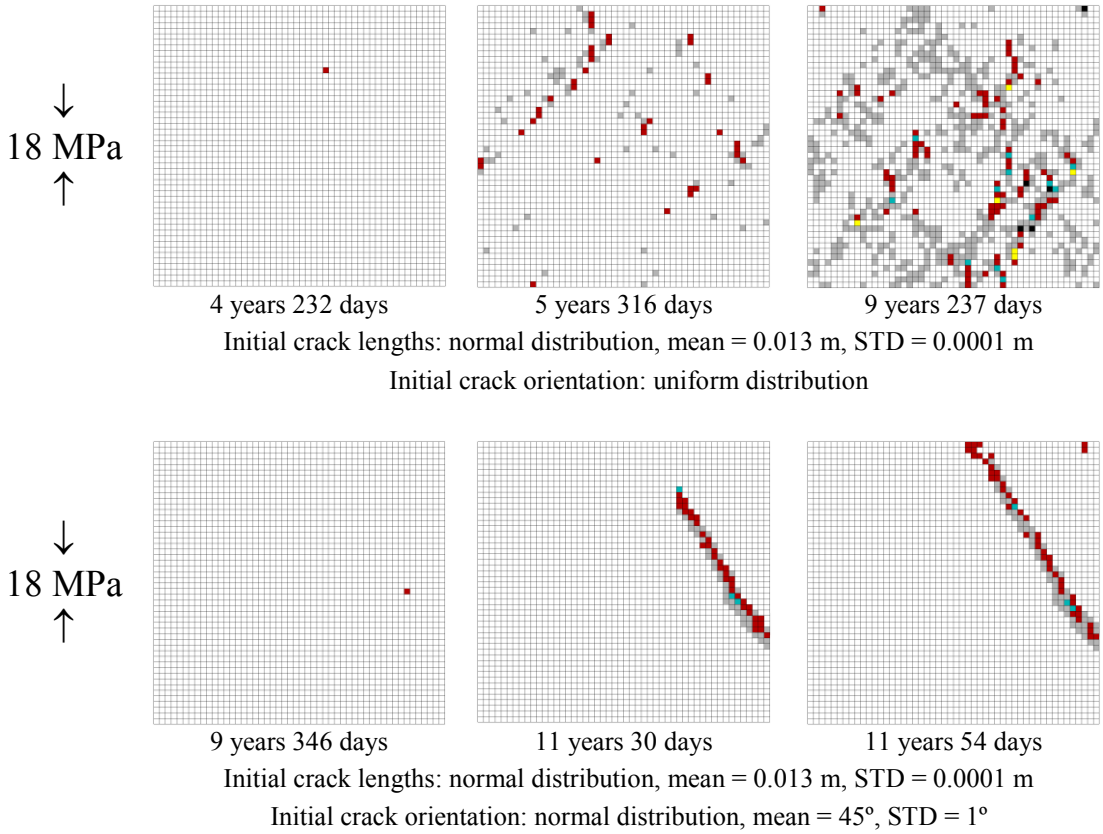

Figure 4-68 Uniaxial compressive test of model A (zones in red: slip along ubiquitous joint; zones in green: tensile failure on ubiquitous joint; zones in yellow: zone failed in tension; zones in black: failed in past (elastic); zones in gray: ubiquitous joint failed in the past)

4.6.3 Wing crack combined ubiquitous-joint model

The wing crack combined ubiquitous-joint model is studied under different loading configurations. The multi-zone models with the same initial crack conditions and loadings as in the wing crack models described in Subsection 4.5.6 have been used here, where the initial crack lengths follow the normal distribution with a mean length of 0.035 m and standard deviation of 0.0001 m. The initial crack orientation follows uniform and normal distributions with a mean value of 45º from the horizontal direction and a standard deviation of 1º.

It is seen in Fig. 4-69 that, under a constant tensile load of 5.5 MPa the macroscopic fracture in combined ubiquitous-joint model shows a similar pattern as the wing crack model in both initial crack configurations (Fig. 4-54). Macroscopic fracture was formed perpendicular to the applied load, and a more uneven pattern of the fracture is observed if the initial crack orientation follows the uniform distribution. Similar to the wing crack model with uniformly distributed initial crack orientation, the penetration of the macroscopic fracture is also not observed (after 17 days 21 hours), while with normally distributed initial crack orientation, the lifetime is about 7 hours 36 minutes 37 seconds (Fig. 4-69), slightly longer than in wing crack model (7 hours 36 minutes

1 second, consulting Fig. 4-55 or Table 4-24). Under a compressive load of 22 MPa, shear band was formed at an inclination of about 70º to the direction of the applied compressive load if the initial crack orientation follows uniform distribution (upper Fig. 4-70). If the initial crack orientation follows normal distribution, straight macroscopic fractures were formed following the direction of the applied compressive load (lower Fig. 4-70). Both fracture patterns are similar to the wing crack model (Fig. 4-58). The lifetime of combined ubiquitous-joint model is slightly longer than that of the wing crack model for both cases: for uniformly and normally distributed orientation, the model failed after about 91 years 340 days and 94 years 102 days (Fig. 4-70), respectively, both are longer than the corresponding wing crack models (91 years 34 days and 94 years 97 days, consulting Fig. 4-58 or Table 4-26).

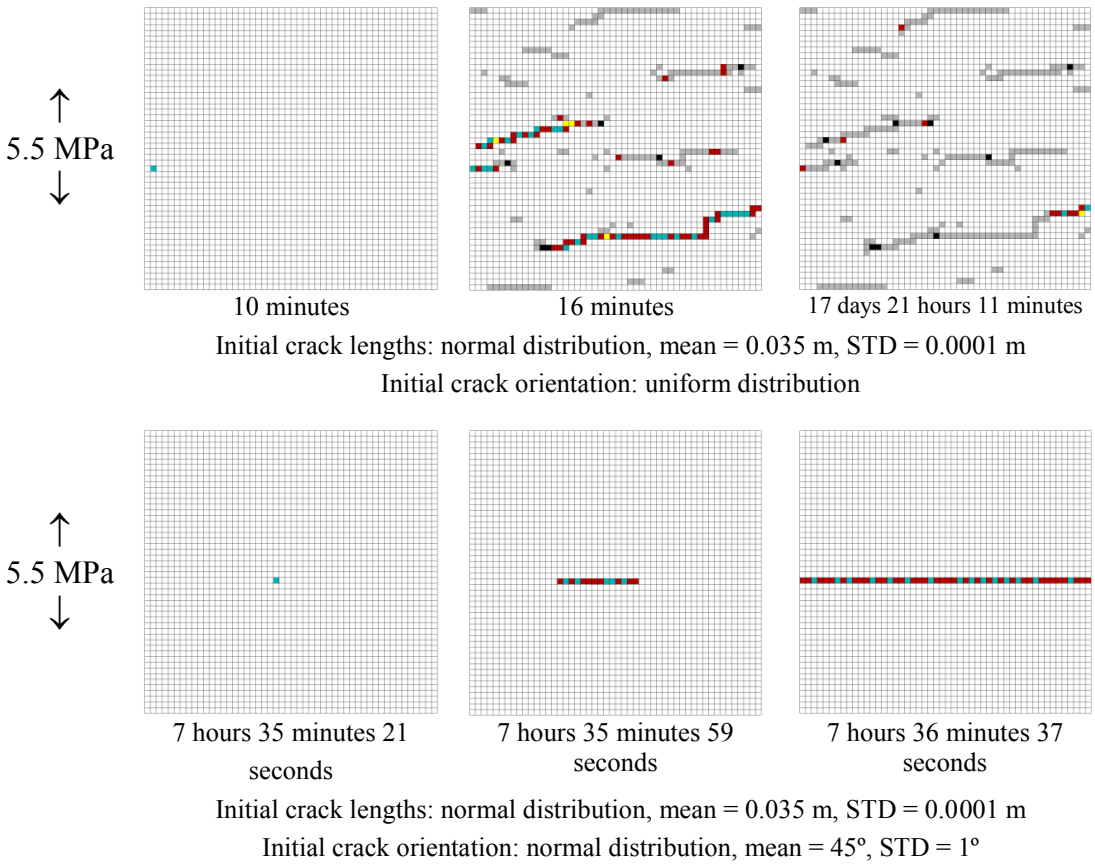

Figure 4-69 Uniaxial tensile test of the wing crack combined ubiquitous-joint model (zones in red: slip along ubiquitous joint; zones in green: tensile failure on ubiquitous joint; zones in yellow: zone failed in tension; zones in black: failed in past (elastic); zones in gray: ubiquitous joint failed in the past)

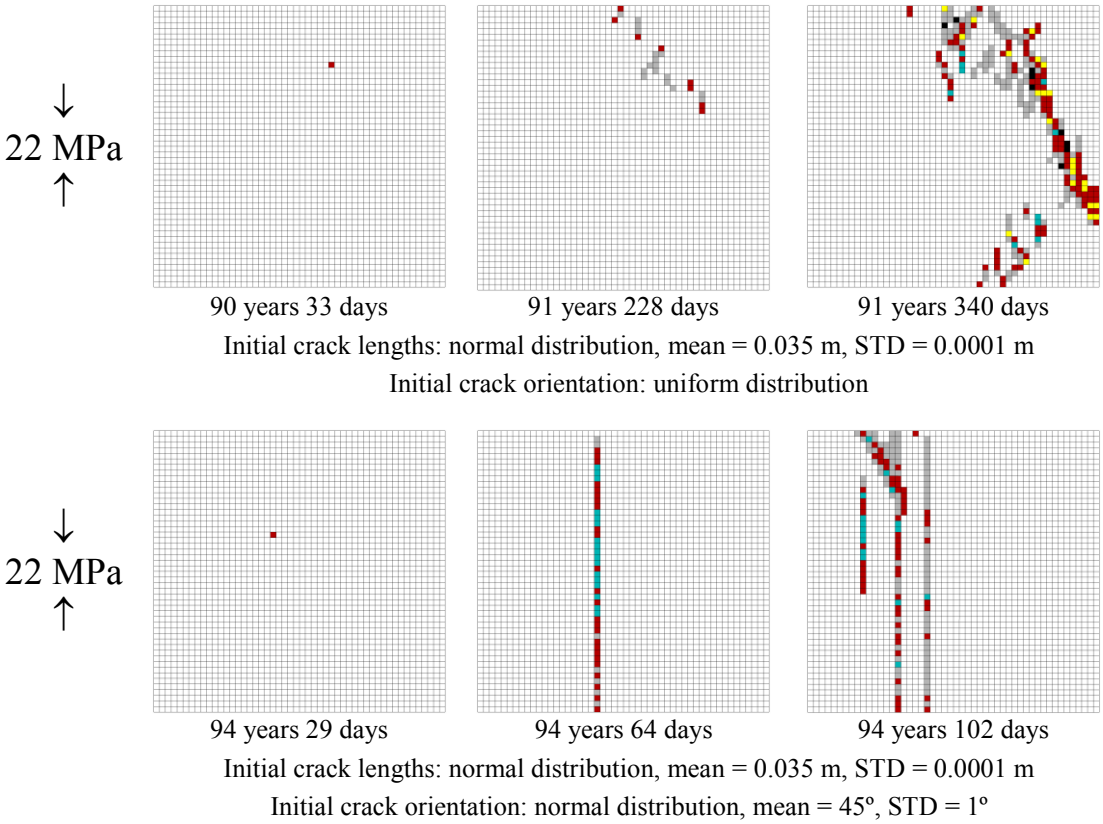

Figure 4-70 Uniaxial compressive test of the wing crack combined ubiquitous-joint model (zones in red: slip along ubiquitous joint; zones in green: tensile failure on ubiquitous joint; zones in yellow: zone failed in tension; zones in black: failed in past (elastic); zones in gray: ubiquitous joint failed in the past)

Under the major vertical principal compressive stress of 22 MPa and the minor horizontal principal stress of 0.5 MPa, shear band was formed with an inclination of 70º to the major principal stress if the initial crack orientation follows uniform distribution (upper Fig. 4-71), similar to the wing crack model. While if the initial crack orientation follows normal distribution, macroscopic fracture was formed with the same direction as the major principal stress (lower Fig. 4-71). The combined ubiquitous-joints model fails after about 393 year 340 days for uniformly distributed initial crack orientation, which is shorter than for the corresponding wing crack model (about 399 years 299 days, consulting Fig. 4-62 or Table 4-28). It takes about 399 years 186 days for normally distributed initial crack orientation (Fig. 4-71) and slightly longer for the corresponding wing crack model (399 years 129 days, consulting Fig. 4-62 or Table 4-28) to fail.

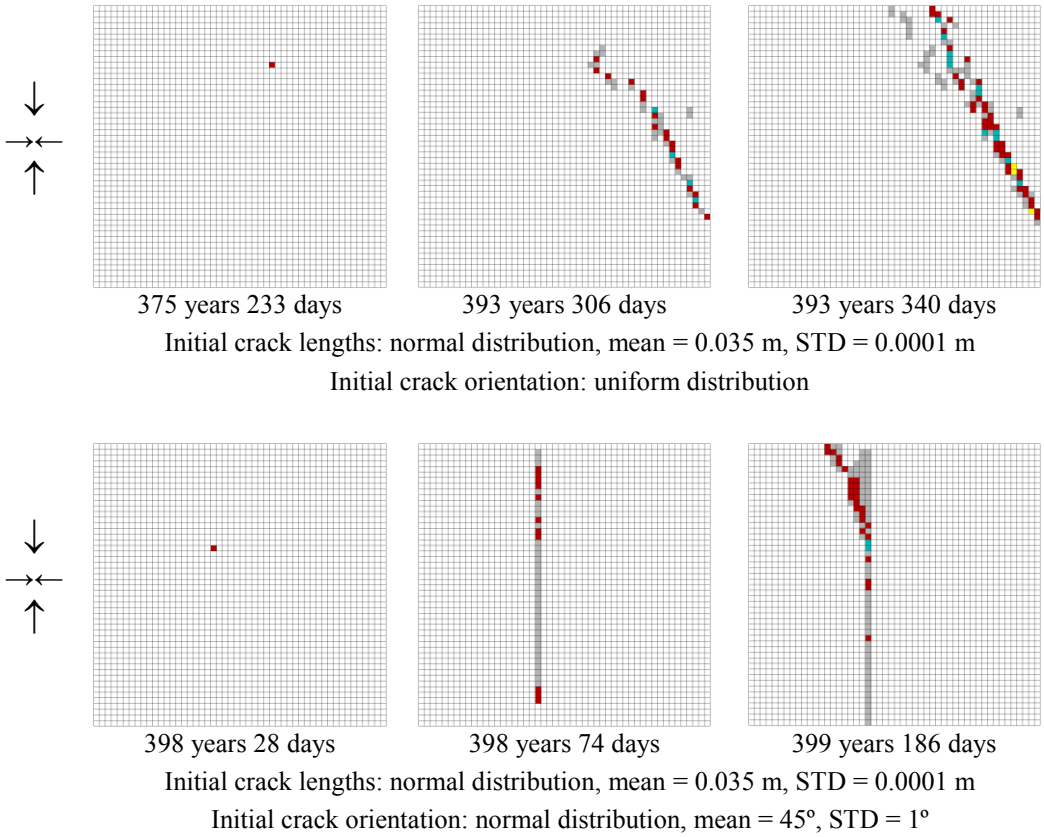

Figure 4-71 Biaxial compressive test of the wing crack combined ubiquitous-joint model (major compressive load of 22 MPa applied vertically; minor compressive load of 0.5 MPa applied horizontally; zones in red: slip along ubiquitous joint; zones in green: tensile failure on ubiquitous joint; zones in yellow: zone failed in tension; zones in gray: ubiquitous joint failed in the past)

4.6.4 Conclusions

A combined ubiquitous-joint model has been proposed based on the fixed orientation model and wing crack model described in the last two sections, incorporating the ubiquitous-joint constitutive model provided by FLAC (Itasca Consulting Group 2005). The simulation scheme for the combined ubiquitous-joint model was also introduced and applied to the multi-zone numerical models under different loading conditions. Macroscopic fracture pattern and lifetime have been studied. It is concluded that in general, the macroscopic fracture pattern of the combined ubiquitous-joint model is similar to that of the corresponding fixed orientation model or wing crack model. The lifetime results have shown only slight differences: in most cases, the combined ubiquitous-joint model has a longer lifetime than the corresponding fixed orientation model or wing crack model. It is believed that this phenomenon is correct even though two cases were observed where the combined ubiquitous-joint model has a shorter lifetime (fixed orientation combined ubiquitous-joint model under compressive load, initial crack orientation follows normal distribution (lower Fig. 4-68); wing crack combined ubiquitous-joint model under biaxial compressive loads, initial crack orientation following uniform distribution

(upper Fig. 4-71)). The irregularity of these two cases can be explained by differences in the macroscopic fracture pattern.

4.7 Comparison between different model concepts

The comparison of the different numerical models revealed that the basic model predicted the most conservative lifetime results (shortest lifetime), while the wing crack model and wing crack combined ubiquitous-joint model predicted the longest lifetimes. The factors influencing the lifetime predictions are similar in different models. It is understood that bigger loads or longer initial crack lengths would cause a shorter lifetime in both fixed orientation and wing crack models. The influence of initial crack orientation on lifetime is also similar for both models: if the model is under tensile load, the lifetime is longer the more the crack axis is perpendicular to the applied load, while if the model is under compressive load, the lifetimes showed a U-shaped curve with ascending crack orientation, with the shortest lifetime found at slightly different crack orientation. Influence of crack orientation on lifetime can not be studied on basic model since it is not defined, but the influence of the load on the lifetime is clearly the same as the other models. As the combined ubiquitous-joint model is based on the former models, the influence of these factors on the lifetime is also the same.

The macroscopic fracture has shown similar pattern for different models under tensile load. That means, the macroscopic fracture was formed perpendicular to the applied tensile load. While under the compressive load, the macroscopic fracture has shown much difference: in basic model, shear band was formed about 45º to the direction of the applied load, which coincides with the maximal shear stress direction; in the fixed orientation model and fixed orientation combined ubiquitous-joint model, shear band was formed about 30º to the direction of the applied load (60º to the horizontal direction), which confirms Mohr-Coulomb theory; in the wing crack model and wing crack combined ubiquitous-joint model, the macroscopic fracture has the trend of following the direction of the applied compressive load, which agrees with the characteristic of the wing crack propagation (propagation in a pure Mode I case). It is also a common feature in all the models including initial crack orientation that, the macroscopic tensile fracture has an uneven pattern and the shear band was formed by a more scatter group of failed zones if the initial crack orientation follows uniform distribution instead of normal distribution.

5 Application of the numerical models

In this chapter, possible applications have been investigated by using the 5 distinct numerical models introduced in the former chapters. The applications focus on the following topics:

- propagation and coalescence of cracks / weak planes
- long-term behavior of underground openings
- long-term stability of pillars

5.1 Existing weak plane problems

In this section, propagation and coalescence of microscopic cracks in models with existing initial macroscopic fracture (weak plane) has been studied. Different model schemes have been applied to the simulation for comparison. The lifetime results are obtained and the macroscopic fracture patterns are investigated.

5.1.1 Single weak plane simulation

A square shaped numerical model was built with the size of 4×4 m^2, and was divided by a 100 by 100 element mesh, each zone with the size of 0.04×0.04 m^2. The initial microscopic crack lengths follow normal distribution with a mean length of 0.02 m and standard deviation of 0.005 m. The initial crack orientation follows normal distribution. For the fixed orientation model, fixed orientation combined ubiquitous-joint model, wing crack model and wing crack combined ubiquitous-joint model, both the mean angle of 45º and 135º have been applied, and standard deviation was 1º. A 'weak plane' was created at the middle of the model by some failed zones to which residual strength values were assigned. This 'weak plane' has an inclination of 45º from the horizontal direction. A compressive load with the same magnitude of 12 MPa was applied uniaxially for each model for the convenience of comparison. The geometry of the model is seen in Fig. 5-1, and the simulation results are shown in Fig. 5-2.

It is seen that under same loading condition, the basic model had the shortest lifetime (about 2 and a half hours). It took the fixed orientation model and the fixed orientation combined ubiquitous-joint model more than 16 years and 28 years to fail, respectively. The wing crack model and the wing crack combined ubiquitous-joint model had the longest lifetime with 1.3391e19 seconds and 4.0919e20 seconds, respectively (Fig. 5-2). The macroscopic fracture pattern is characterized by failed zones forming a shear band with inclination of about 45º from the tip of the macroscopic fracture and penetrates the basic model. In the fixed orientation model, shear bands were also formed from the tip of the macroscopic fracture with a curved shape and with inclination of about 60º to the horizontal direction. In the fixed orientation combined ubiquitous-joint model, the inclination of the shear band is about 60º. In the wing

crack model, failed zones have also formed tensile fractures in addition to the shear bands. The tensile fractures follow the direction of the applied compressive load. In the wing crack combined ubiquitous-joint model, tensile fractures are observed having an inclination of 20º ~ 25º from the direction of the applied load. The failed zones have formed longer tensile fractures at the tip of the original macroscopic fracture than in the middle of the macroscopic fracture. It is also noticed that, changing the mean angle of the initial microcrack orientation does not influence the fracture pattern for the fixed orientation and wing crack models (Fig. 5-2 (b) and (d)). While in the corresponding model with anisotropy, the fracture pattern changes with the different mean initial microcrack orientation. For the fixed orientation combined ubiquitous-joint model, although the inclination of the shear band is the same (about 60º), the shear band was 'thicker' in case of mean initial microcracks' orientation being 45º instead of 135º (Fig. 5-2 (c)). For the wing crack combined ubiquitous-joint model, the fractures are inclined to the left of the applied load for the case where the mean initial microcrack orientation is 45º and inclined to the right of the applied load for the case where the mean initial microcrack orientation is 135º (Fig. 5-2 (e)).

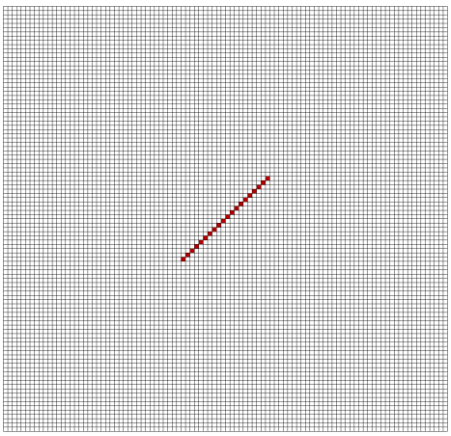

Figure 5-1 Weak plane inside the model (Zones in red: failed zones forming the weak plane with inclination of 45º to the horizontal direction)

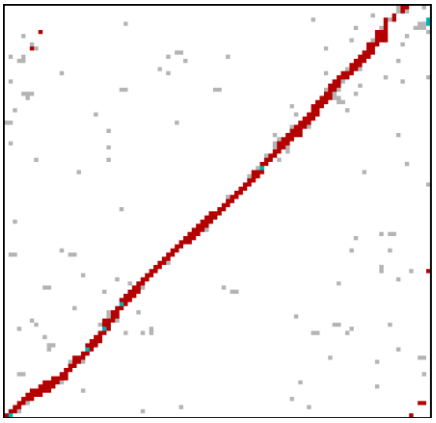

9,003 (s)
(2 hours 30 minutes)
(a) Basic model

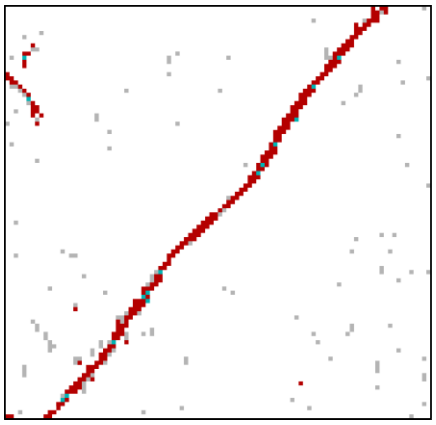

5.1323e8 (s)
(16 years 100 days)
Initial crack orientation: normal distribution;
mean = 45º, STD = 1º

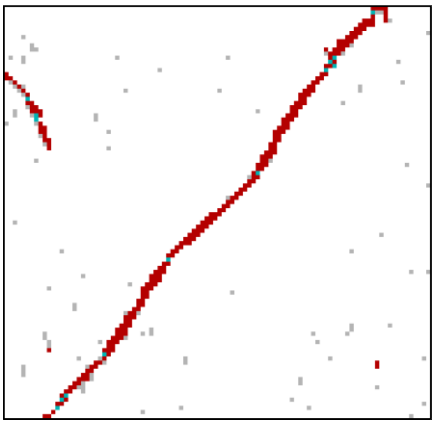

9.4618e8 (s)
(30 years 1 day)
Initial crack orientation: normal distribution;
mean = 135º, STD = 1º

(b) Fixed orientation model

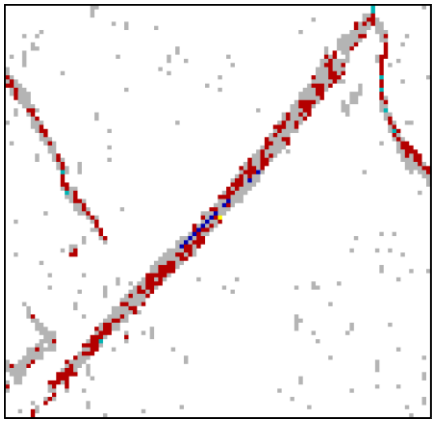

9.0961e8 (s)
(28 years 307 days)
Initial crack orientation: normal distribution;
mean = 45º, STD = 1º

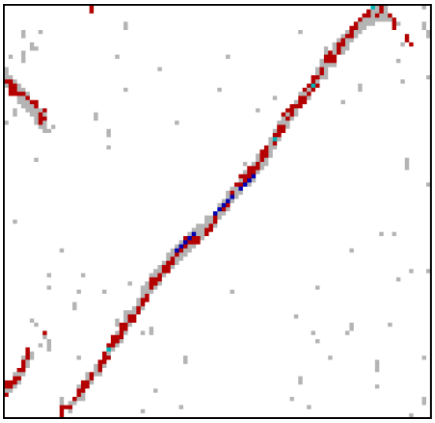

1.2436e9 (s)
(39 years 158 days)
Initial crack orientation: normal distribution;
mean = 135º, STD = 1º

(c) Fixed orientation combined ubiquitous-joint model

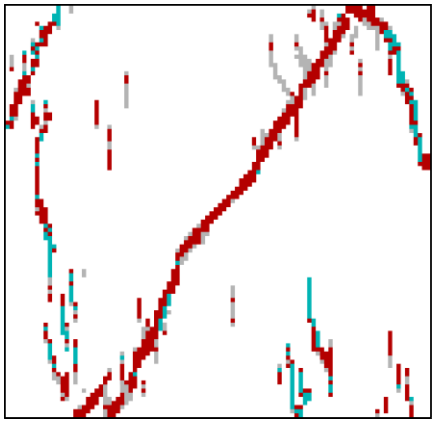

1.3391e19 (s)
(exceeds 1,000 years)
Initial crack orientation: normal distribution;
mean = 45º, STD = 1º

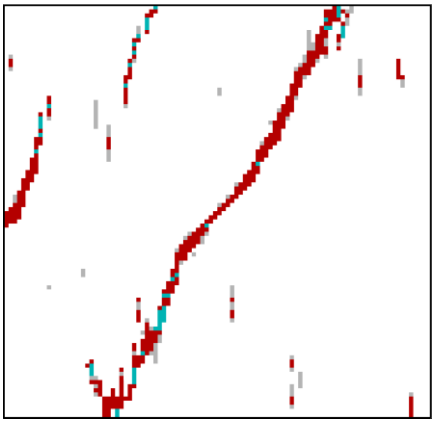

7.1485e18 (s)
(exceeds 1,000 years)
Initial crack orientation: normal distribution;
mean = 135º, STD = 1º

(d) Wing crack model

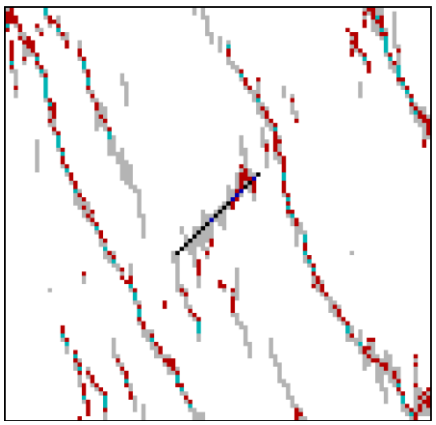

4.0919e20 (s)
(exceeds 1,000 years)
Initial crack orientation: normal distribution;
mean = 45º, STD = 1º

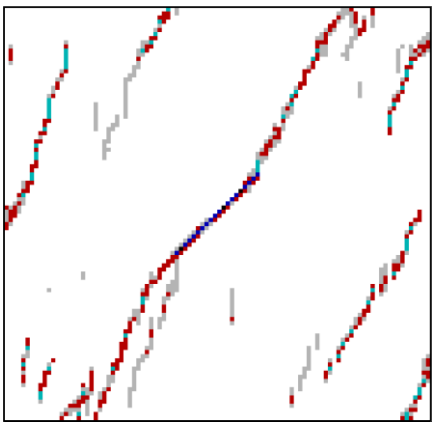

3.4813e19 (s)
(exceeds 1,000 years)
Initial crack orientation: normal distribution;
mean = 135º, STD = 1º

(e) Wing crack combined ubiquitous-joint model

Figure 5-2 Failure of the model with different modeling schemes under compressive load of 12 MPa (initial crack lengths: normal distribution, mean = 0.02 m, STD = 0.005 m) (Zones in red: shear failure of the zone/slip along ubiquitous joint; zones in green: tensile failure of the zone/tensile failure on ubiquitous joint; zones in gray: zone failed in the past/ubiquitous joint failed in the past)

5.1.2 Two weak planes simulation

With the same model size and microcrack characteristics, and under the same uniaxial compressive load of 12 MPa, simulations have been made with two existing weak planes. The 'weak planes' have an inclination of 45º but are placed at different positions as shown in Fig. 5-3.

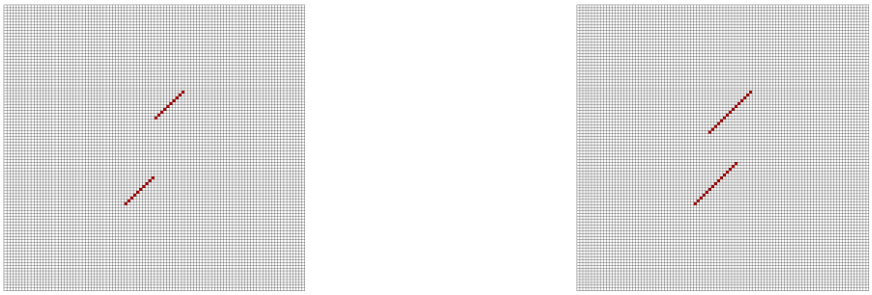

(a) Position 1 (b) Position 2

Figure 5-3 Weak planes inside the model (Inclination: 45º)

It is seen from Fig. 5-4 to Fig. 5-8 that with the same geometry, initial crack characteristics and loading condition, the lifetime for the basic model is the shortest, and the lifetime for the fixed orientation model and fixed orientation combined ubiquitous-joint model is longer, while the wing crack model and wing crack combined ubiquitous-joint model have the longest lifetime. The macroscopic fractures also showed distinct features. For the basic model, the shear bands have been formed from the tips of the existing macroscopic fractures. For the case where the weak planes were arranged according to Position 1, the shear band (inclination of about 45º to horizontal direction) from the upper plane finally reached the model boundary, while the formation of a massive shear band from the lower fracture has somehow stopped (Fig. 5-4 (a)). For the case where the weak planes were arranged according to Position 2, shear bands were formed from the tips of both existing fractures, and the shear bands were parallel with each other (5-4 (b)).

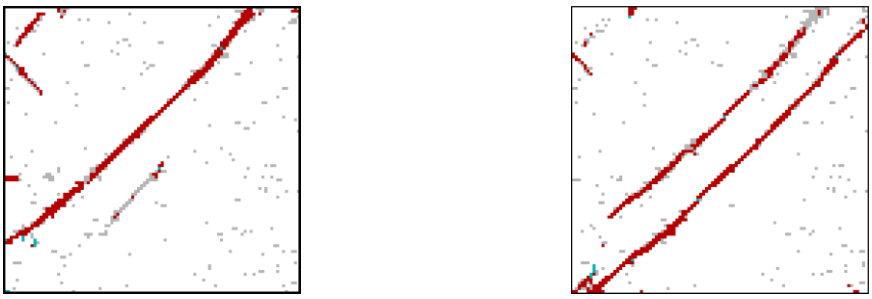

1.4537e4 (s)
(4 hours 2 minutes)
(a) Position 1

1.3059e4 (s)
(3 hours 37 minutes)
(b) Position 2

Figure 5-4 Failure of basic model under compressive load of 12 MPa (Zones in red: shear failure of the zone; zones in green: tensile failure of the zone; zones in gray: zone failed in the past)

For the fixed orientation model, shear bands were formed from the 'outside' tips of the existing macroscopic fractures and reached the boundary of the model (inclination of about 60º to horizontal direction), while the fractures formed from the 'inside' tips curved towards each other and show a trend of connecting each other (Fig. 5-5). As the orientation of the initial microcracks follows a normal distribution, the

macroscopic fracture patterns are similar for the case with a mean orientation of 45º and 135º.

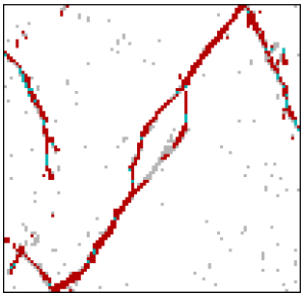

8.6581e8 (s)
(27 years 165 days)
(a) Position 1

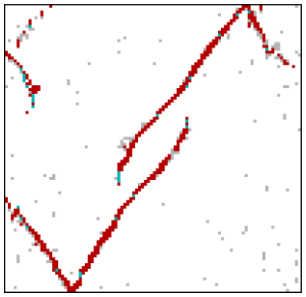

6.0871e8 (s)
(19 years 110 days)
(b) Position 2

Initial crack orientation: normal distribution, mean = 45º, STD = 1º

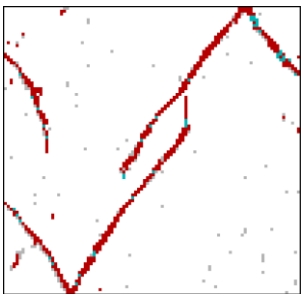

1.3136e9 (s)
(41 years 239 days)
(c) Position 1

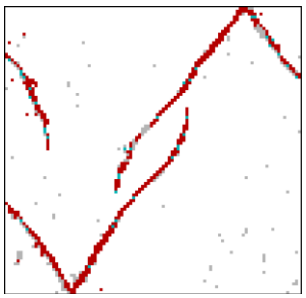

1.0719e9 (s)
(33 years 361 days)
(d) Position 2

Initial crack orientation: normal distribution, mean = 135º, STD = 1º

Figure 5-5 Failure of fixed orientation model under compressive load of 12 MPa (Zones in red: shear failure of the zone; zones in green: tensile failure of the zone; zones in gray: zone failed in the past)

Anisotropy has shown its influences in the fixed orientation combined ubiquitous-joint model. As is seen in Fig. 5-6, the shear bands formed from the tips of the macroscopic fractures were parallel to each other if the mean orientation of the initial microcracks is 45º (Fig. 5-6 (a), (b)), while the fractures formed from the 'inside' tips of the existing macroscopic fractures curved towards each other if the mean orientation is 135º (Fig. 5-6 (c), (d)). It is also interesting to notice that if the mean orientation of the initial microcracks is 45º, the shear bands formed from the tips of the macroscopic fractures (inclination close to 45º) are much 'thicker' than those formed in other parts of the model (Fig. 5-6 (a), (b)), while it is opposite if the mean orientation of the initial microcracks is 135º (Fig. 5-6 (c), (d)).

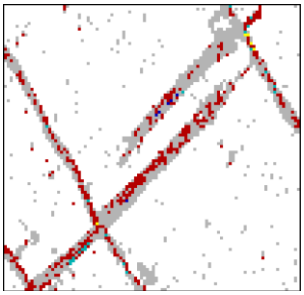

9.3463e10 (s)
(2,963 years 247 days)
(a) Position 1

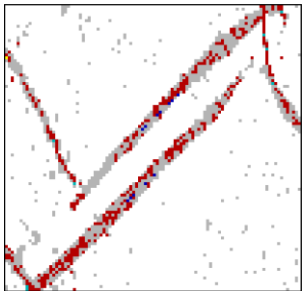

9.9946e9 (s)
(316 years 338 days)
(b) Position 2

Initial crack orientation: normal distribution, mean = 45º, STD = 1º

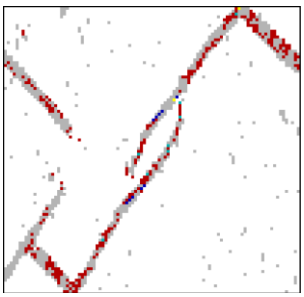

5.3221e9 (s)
(168 years 278 days)
(c) Position 1

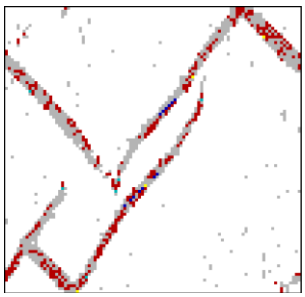

7.6826e10 (s)
(2436 years 53 days)
(d) Position 2

Initial crack orientation: normal distribution, mean = 135º, STD = 1º

Figure 5-6 Failure of fixed orientation combined ubiquitous-joint model under compressive load of 12 MPa (Zones in red: slip along ubiquitous joint; zones in green: tensile failure on ubiquitous joint; zones in yellow: zone failed in tension; zones in gray: ubiquitous joint failed in the past)

In the wing crack model, for the case where the weak planes were arranged according to Position 1, tensile fractures are formed from the 'inside' tips of the existing macroscopic fractures and connection of these two tips is observed (Fig. 5-7 (a), (c)). For the case where the weak planes were arranged according to Position 2, tensile fractures formed from the 'inside' tips of the existing macroscopic fractures propagated farther and reached each other (Fig. 5-7 (b), (d)). Macroscopic tensile fractures were formed in the direction of the applied compressive load. The fracture patterns are similar for mean initial microcrack orientation of 45º and 135º.

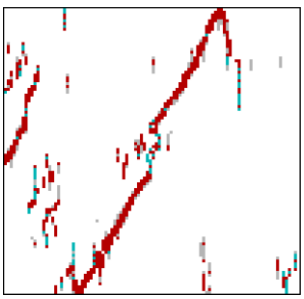

1.0083e19 (s)
(exceeds 1,000 years)
(a) Position 1

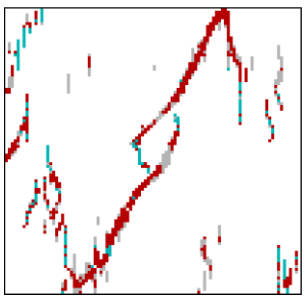

1.3739e19 (s)
(exceeds 1,000 years)
(b) Position 2

Initial crack orientation: normal distribution, mean=45º, STD=1º

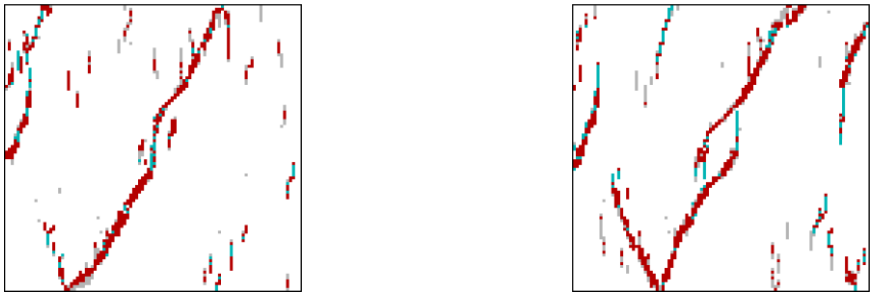

1.4756e19 (s)
(exceeds 1,000 years)
(c) Position 1

2.0268e19 (s)
(exceeds 1,000 years)
(d) Position 2

Initial crack orientation: normal distribution, mean = 135º, STD = 1º

Figure 5-7 Failure of wing crack model under compressive load of 12 MPa (Zones in red: shear failure of the zone; zones in green: tensile failure of the zone; zones in gray: zone failed in the past)

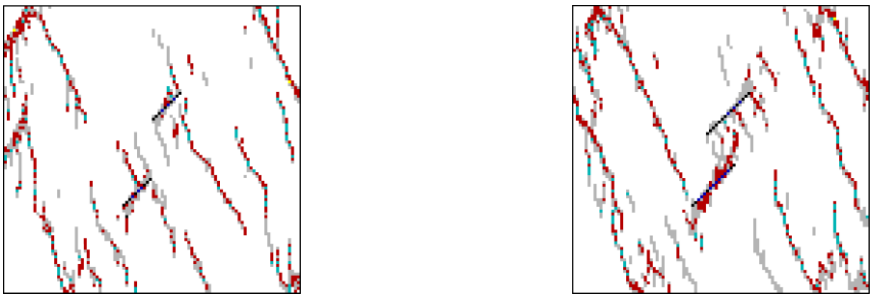

7.2179e19 (s)
(exceeds 1,000 years)
(a) Position 1

1.6599e22 (s)
(exceeds 1,000 years)
(b) Position 2

Initial crack orientation: normal distribution, mean = 45º, STD = 1º

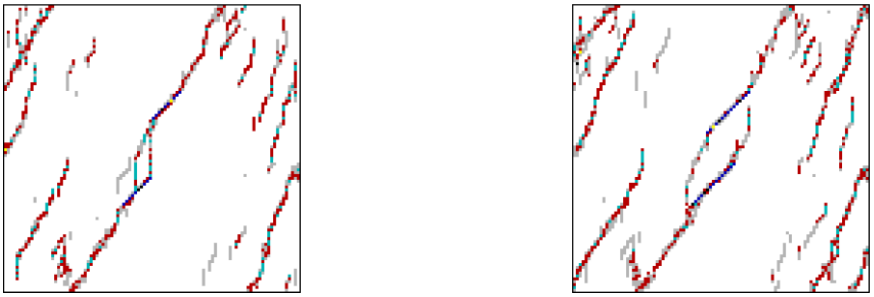

2.4431e20 (s)
(exceeds 1,000 years)
(c) Position 1

2.2030e21 (s)
(exceeds 1,000 years)
(d) Position 2

Initial crack orientation: normal distribution, mean = 135º, STD = 1º

Figure 5-8 Failure of wing crack combined ubiquitous-joint model under compressive load of 12 MPa (zones in red: slip along ubiquitous joint; zones in green: tensile failure on ubiquitous joint; zones in yellow: zone failed in tension; zones in black: failed in past (elastic); zones in gray: ubiquitous joint failed in the past)

The effects of the anisotropy are also clear in wing crack combined ubiquitous-joint model. It is seen in Fig. 5-8 (a) (b) that with a mean initial microcrack orientation of 45º, the tensile fractures are inclined to the left of the applied load, so that fractures

formed from the tips of the existing fractures do not connect (Fig. 5-8 (a)). While for the case where the mean orientation of the initial microcracks is 135º, the tensile fractures are inclined to the right of the applied load. In this case the fractures formed from the tips of the existing fractures connect to each other for both position arrangements (Fig. 5-8 (c) (d)).

5.1.3 Conclusions

Numerical models with existing macroscopic fracture(s) have been investigated. Single existing weak plane and two existing weak planes (different positions) have been modeled. The lifetime and macroscopic fracture pattern have been studied. The most conservative lifetime result was obtained by the basic model, while the wing crack combined ubiquitous-joint model has predicted the longest lifetime. Following the ascending order of the predicted lifetime, the model schemes are: basic model, fixed orientation model, fixed orientation combined ubiquitous-joint model, wing crack model and wing crack combined ubiquitous-joint model. As for the macroscopic fracture, in both cases (single and two weak planes), shear band was formed (about 45º) from the tips of the weak model in basic model, fixed orientation model and fixed orientation combined ubiquitous-joint model. Macroscopic tensile fractures were formed following the direction of applied load in wing crack model. Inclined macroscopic fractures were formed in wing crack combined ubiquitous-joint model, where if the mean initial crack orientation is 45º, the macroscopic fracture is inclined to the left of the direction of the applied load; if the mean initial crack orientation is 135º, the macroscopic fracture is inclined to the right of the direction of the applied load . Especially, if two weak planes exist, the macroscopic fractures propagate inclining towards each other and finally joint each other except the basic model, where the shear band develops with its own inclination. In addition, it is also found that anisotropy (including the ubiquitous-joint model) can influence the inclination of the macroscopic fracture, thus preventing the connecting of the fractures (Fig. 5-8 (a) and Fig. 5-6 (a), (b)).

5.2 Underground opening problems

The safety of underground openings, such as tunnels, underground storages, natural openings and underground pipe networks has always been an important issue in civil engineering. The proposed model schemes have been applied to such geometries and numerical models, respectively, in a simplified manner. With the proposed numerical modeling schemes, the service life of such structures can be predicted through crack propagation simulation. This section focus on using different numerical model schemes to study underground opening problems. Discussions and suggestions are made for the applicability of different models.

5.2.1 Numerical implementation and initial simulation results

The numerical model has a size of 2 × 2 m^2 and was divided by a 50 by 50 element mesh, same as in the former chapters. The simulation of underground excavation or opening situation is realized by creating a hollow area inside the numerical model. Fig. 5-9 shows an example of a square shaped opening formed by "null zones" (Itasca Consulting Group 2005) at the middle of the numerical model. Each zone of the model contains an initial crack with normal distribution (mean length of 0.02 m and standard deviation of 0.005 m). For the fixed orientation model, fixed orientation combined ubiquitous-joint model, wing crack model and wing crack combined ubiquitous-joint model, the initial crack orientation follows normal distribution with mean angle of 45º and standard deviation of 1º. Biaxial compressive loading has been applied to the numerical model to represent the underground stress field, where a constant compressive load of 8 MPa is applied vertically and a constant compressive load of 2 MPa is applied horizontally. It is seen from the stress distributions shown in Fig. 5-10 that the maximum compressive stresses concentrate at the corners of the opening. Tensile stresses develop along the top and the bottom of the opening.

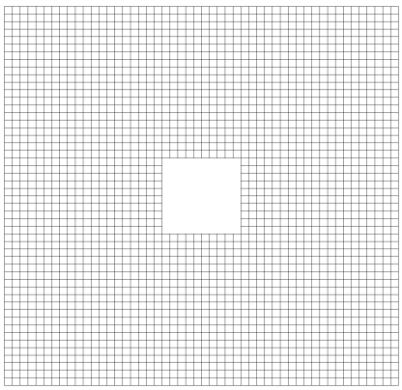

Figure 5-9 Geometry of numerical models for underground opening problems (Model size: 2 × 2 m^2; opening size: 0.4 × 0.4 m^2)

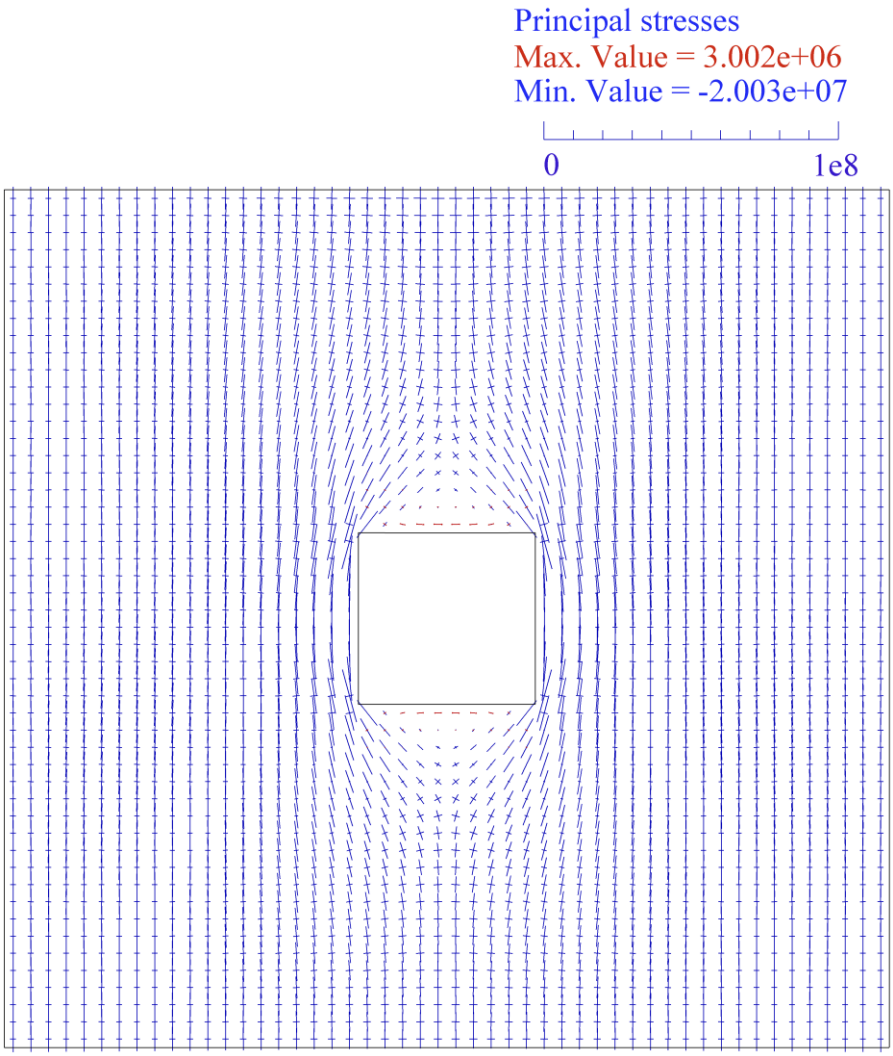

Figure 5-10 Initial principal stress vectors of the numerical model (red vector: tensile stress; blue vector: compressive stress)

As is seen from the failure stages of the numerical models (Fig. 5-11), shear bands are formed in each model. The macroscopic fractures formed by the coalescence microscopic cracks also show some differences for different models. The first failure zone appeared at the corners of the opening in the basic model, fixed orientation model and fixed orientation combined ubiquitous-joint model, and shear bands were formed initiating from here with an inclination of 45º to 65º to the applied major compressive load (Fig. 5-11 (a), (b) and (c)). Most of the failed zones forming the shear band failed in shear. In wing crack model and wing crack combined ubiquitous-joint model, the first failure zone appeared at the top of the opening, where tensile stresses appear (see Fig. 5-10), and macroscopic fracture has been formed initiating from here and from the bottom side of the opening (Fig. 5-11 (d), (e)). Some macroscopic tensile fractures following the direction of the applied major compressive load (vertical), developed but were finally arrested. In addition, shear bands with an inclination of about 60º to the applied major compressive stress

developed along the side walls of the opening and penetrate the models (Fig. 5-11 (d), (e)). The predicted lifetimes have shown great difference for different model schemes. It is seen in Fig. 5-11 that under the same loads, the basic model failed after 6 minutes and the first failed zone is found after only 2 seconds. The fixed orientation model failed after 362 days and the fixed orientation combined ubiquitous-joint model failed after 6,265 years and the first failed zone is found after 11 days for both of these two cases. The lifetime is 4e23 seconds for the wing crack model and 9e26 seconds for the wing crack combined ubiquitous-joint model. The first failed zone is found after 1e16 seconds for these 2 models.

To give a more detailed view of the microcrack pattern at failure, a zoomed in area with microcracks presented in each model (except the basic model) is shown in Fig. 5-12 to Fig. 5-15. It is seen that for most of the failed zones, the microcrack inside has reached the zone boundary, which confirmed failure in the subcritical crack propagation phase. In the wing crack model and wing crack combined ubiquitous-joint model, the wing cracks in each zone follow the direction of the major compressive stress in the zone (Fig. 5-14 and Fig.5-15).

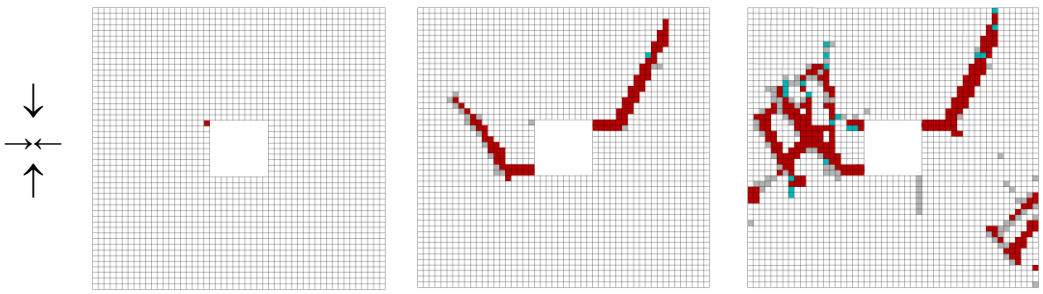

2.5 seconds | 2 minutes 41 seconds | 6 minutes 4 seconds

(a) Basic model

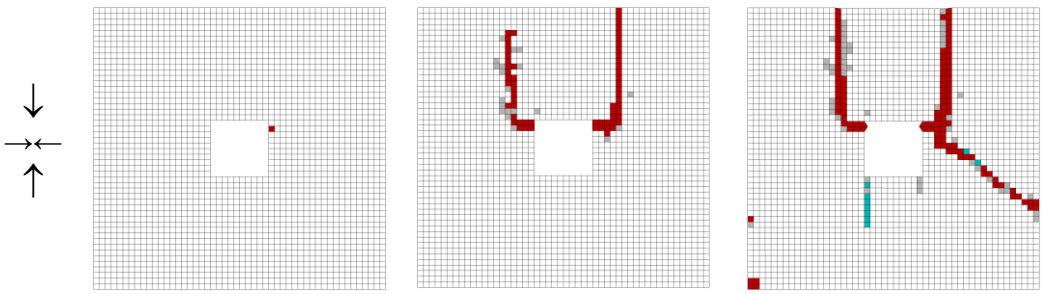

11 days 19 hours | 230 days 3 hours | 362 days 37 minutes

(b) Fixed orientation model

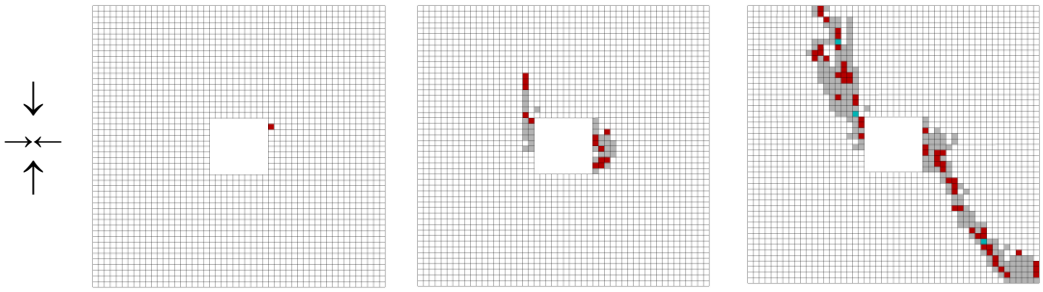

11 days 19 hours | 288 years 201 days | 6,265 years 167 days

(c) Fixed orientation combined ubiquitous-joint model

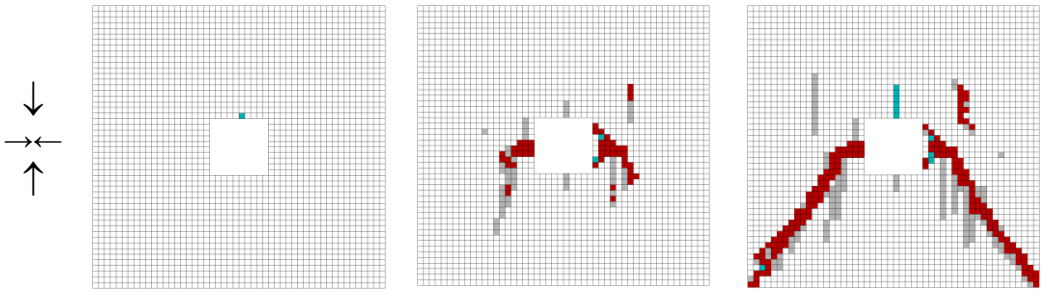

1.2311e16 (s) | 3.4319e23 (s) (exceeds 10,000 years) | 4.1748e23 (s)

(d) Wing crack model

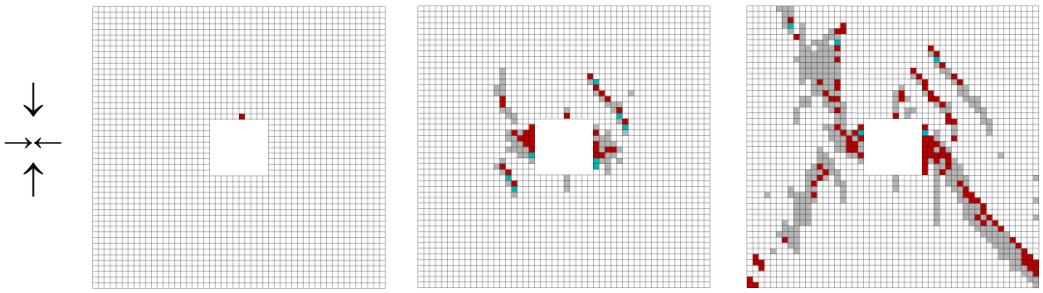

1.2311e16 (s) | 2.3906e26 (s) (exceeds 10,000 years) | 9.3315e26 (s)

(e) Wing crack combined ubiquitous-joint model

Figure 5-11 Failure of the numerical models under biaxial loading conditions (compressive load: 8 MPa (vertical), 2 MPa (horizontal); zones in red: shear failure of the zone/slip along ubiquitous joint; zones in green: tensile failure of the zone/tensile failure on ubiquitous joint; zones in gray: zone failed in the past/ubiquitous joint failed in the past)

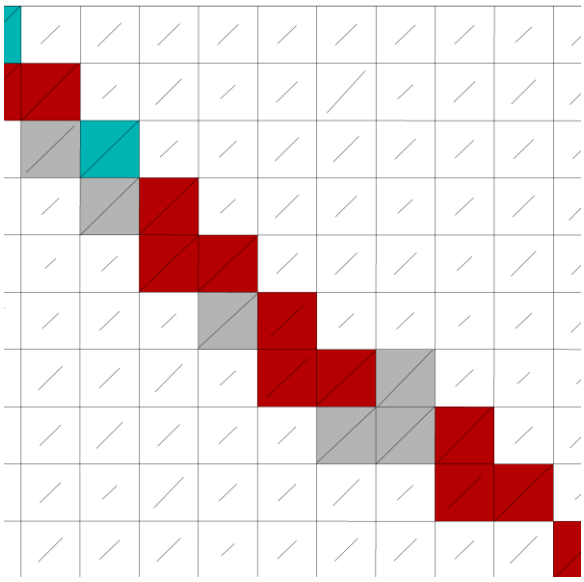

Figure 5-12 A zoomed in area in fixed orientation model at failure (corresponding to Fig. 5-11 (b); zones in red: shear failure of the zone; zones in green: tensile failure of the zone; zones in gray: zone failed in the past)

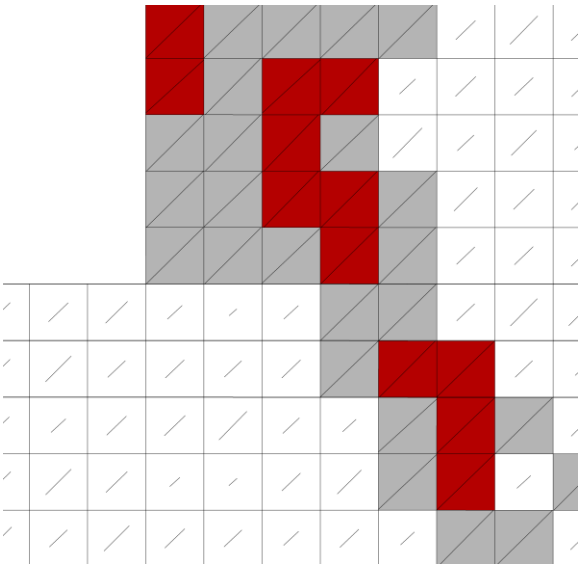

Figure 5-13 A zoomed in area in fixed orientation combined ubiquitous-joint model at failure (corresponding to Fig. 5-11 (c); zones in red: slip along ubiquitous joint; zones in gray: ubiquitous joint failed in the past)

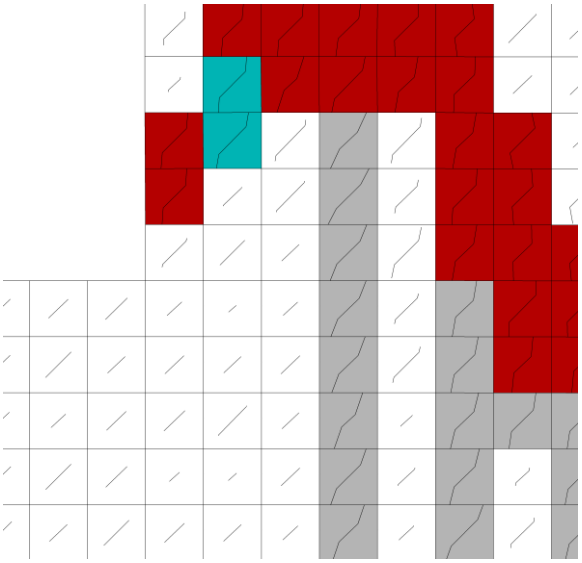

Figure 5-14 A zoomed in area in wing crack model at failure (corresponding to Fig. 5-11 (d); zones in red: shear failure of the zone; zones in green: tensile failure of the zone; zones in gray: zone failed in the past)

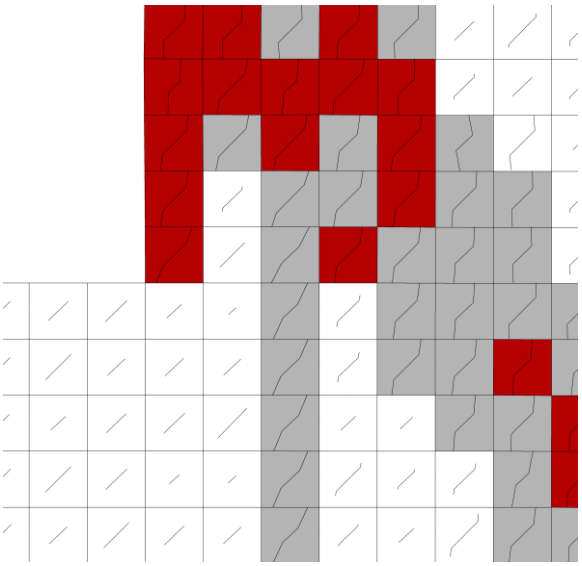

Figure 5-15 A zoomed in area in wing crack combined ubiquitous-joint model at failure (corresponding to Fig. 5-11 (e); zones in red: slip along ubiquitous joint; zones in gray: ubiquitous joint failed in the past)

5.2.2 Simulation of underground openings with different shape

Different shapes (cross sections) of the opening have been studied in models of larger scale (Fig. 5-16). The size of the new model is $10 \times 10\ m^2$ with 62500 zones (500×500 zones). Length of each zone is still 0.04 m. The size of the opening is $2 \times 2\ m^2$ for the quadratic opening (Fig. 5-16 (a)), $2 + \pi/2\ m^2$ for the opening with an arched roof and flat floor (Fig. 5-16 (b)), and $\pi\ m^2$ for the circular opening (radius of 1 m) (Fig. 5-16 (c)). The numerical simulation is performed under the same biaxial loading condition for different modeling schemes: a constant compressive load of

8 MPa is applied vertically and a constant compressive load of 2 MPa is applied horizontally. Initial crack lengths follow normal distribution with the mean value of 0.02 m and standard deviation of 0.005 m. The crack orientation follows normal distribution with mean value of 45º and standard deviation of 1º.

A zoomed in area of the models is shown in Fig. 5-17, 5-18 and 5-19, respectively, to show the stress condition at the periphery of the openings. It is seen in Fig. 5-17 that the compressive stresses concentrate at the corners of the opening, and these maximum principal stresses have certain inclination from the vertically applied major compressive stress. Compressive stresses act along the side walls of the opening with same direction as the vertically applied major compressive stress. Tensile stresses occur symmetrically along the roof and floor of the opening. The tensile stress becomes bigger at a position closer to the middle of the roof or floor of the opening. For the arch-shaped opening (Fig. 5-18), the stress distributions are similar to the square opening along the side walls and floor. But along the arched roof, the directions of major stresses are the same as the directions of the tangent lines of the arch. For the circular opening (Fig. 5-19), the compressive stresses are the biggest at the left and right boundary and the tensile stresses are found at the roof and floor of the opening. The directions of the major stresses follow the surface of the opening.

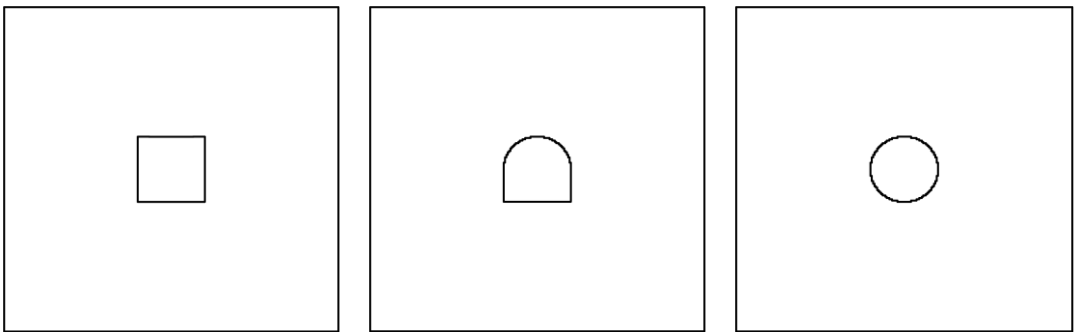

(a) (b) (c)

Figure 5-16 Geometry of the numerical models

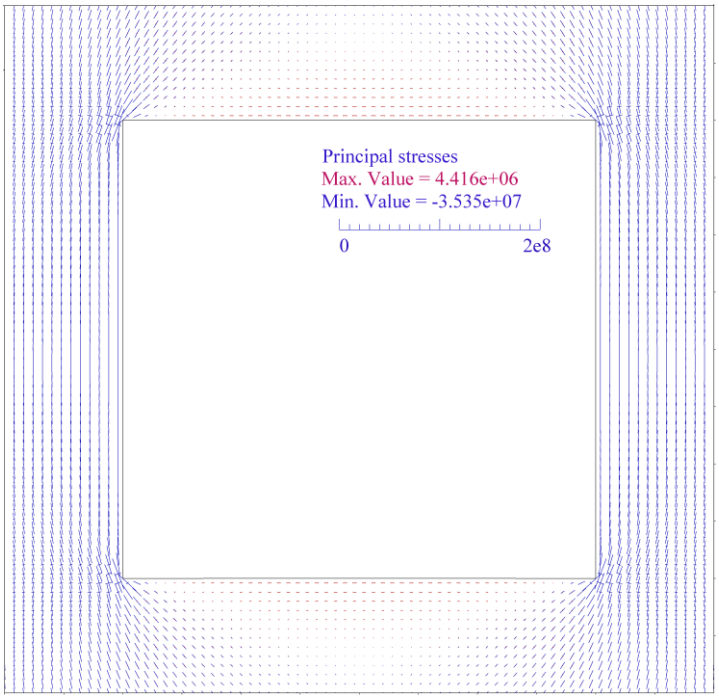

Figure 5-17 Stress condition at the periphery of the square opening (compressive load: 8 MPa (vertical), 2 MPa (horizontal); red vector: tensile stress; blue vector: compressive stress, unit: Pa)

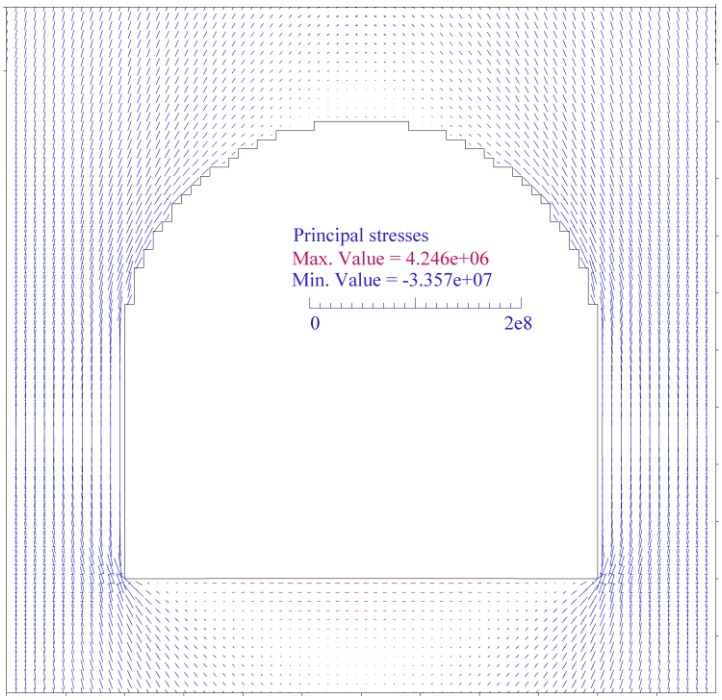

Figure 5-18 Stress condition at the periphery of the arched opening (compressive load: 8 MPa (vertical), 2 MPa (horizontal); red vector: tensile stress; blue vector: compressive stress, unit: Pa)

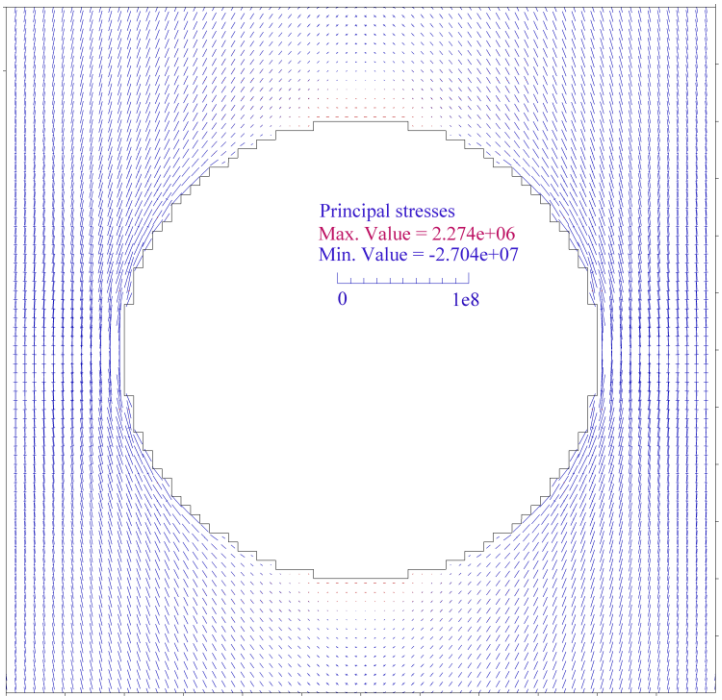

Figure 5-19 Stress condition at the periphery of the circular opening (compressive load: 8 MPa (vertical), 2 MPa (horizontal); red vector: tensile stress; blue vector: compressive stress, unit: Pa)

(1) Basic model

The failure stages of the basic model under biaxial loads are seen in Fig. 5-20. It is seen that for the model with the square opening, the zones failed first at the 4 corners, where the compressive stresses concentrate and the largest deviatonic stress is observed. Shear bands (55º) were formed from the corners and connected at both the left and right side wall. More zones failed after that and continued forming the shear bands (55º ~ 70º inclined to the horizontal direction) extending towards the boundary of the model (Fig. 5-20 (a)). The macroscopic fracture pattern around the arched opening is similar to the square opening, except that the zones first failed are located at the 2 bottom corners and at the transition from the side walls to the arched roof. The positions where the shear bands connect are also closer to the side walls (Fig. 5-20 (b)). For the circular opening, the zones failed first at the left and right boundary of the opening, where the compressive stresses concentrate, and later on shear bands are formed, which finally reach the boundary of the model (Fig. 5-20 (c)). It is also seen that the predicted lifetime differ greatly with different opening shapes: it takes more than 3 years for the macroscopic fractures to reach the boundary of the model with square opening, more than 33 years for the model with the arched roof and more than 78 years for the model with the circular opening.

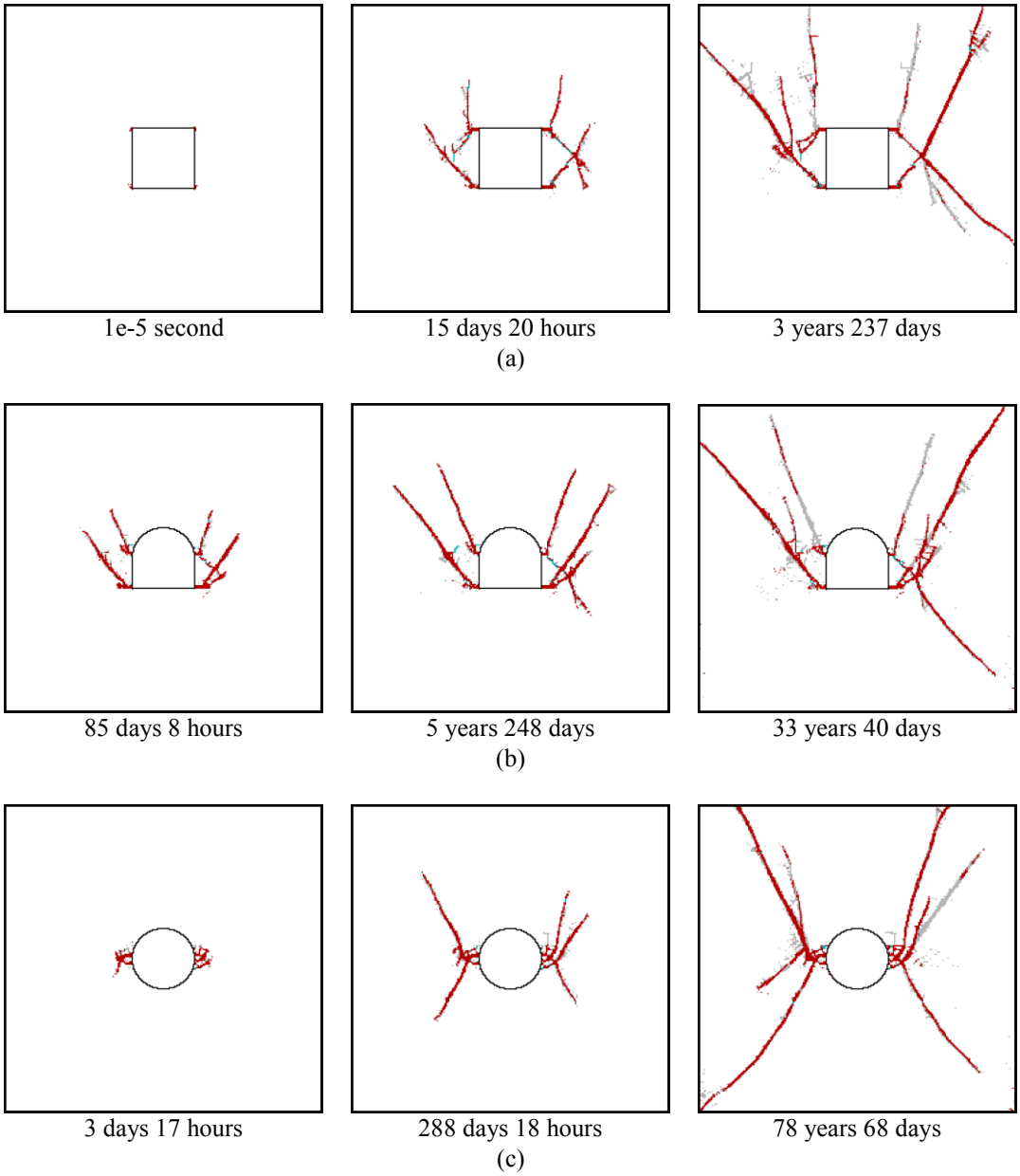

Figure 5-20 Failure process of the basic models (compressive load: 8 MPa (vertical), 2 MPa (horizontal); initial crack lengths: normal distribution, mean = 0.02 m, STD = 0.005 m; initial crack orientation: normal distribution, mean = 45º, STD = 1º)

(2) Fixed orientation model

The failure stages of the fixed orientation model are shown in Fig. 5-21. Compared to the basic model, the zones failed first at similar positions, which means at the periphery of the opening. Later on shear bands were also formed from these initiating failure positions inclined 65º ~ 70º to the horizontal direction. Additional straight macroscopic fractures along the direction of the major compressive load have also been found for all opening shapes. For the square-shaped opening, the straight fractures started from the region near the corners of the opening, also from the shear bands (Fig. 5-21 (a) and Fig. 5-23). For the arched opening, the straight fractures

started from the transition between side walls and arched roof (Fig. 5-21 (b) and Fig. 5-24). For the circular opening, the straight fractures start close to the left and right side of the opening (Fig. 5-21 (c) and Fig. 5-25).

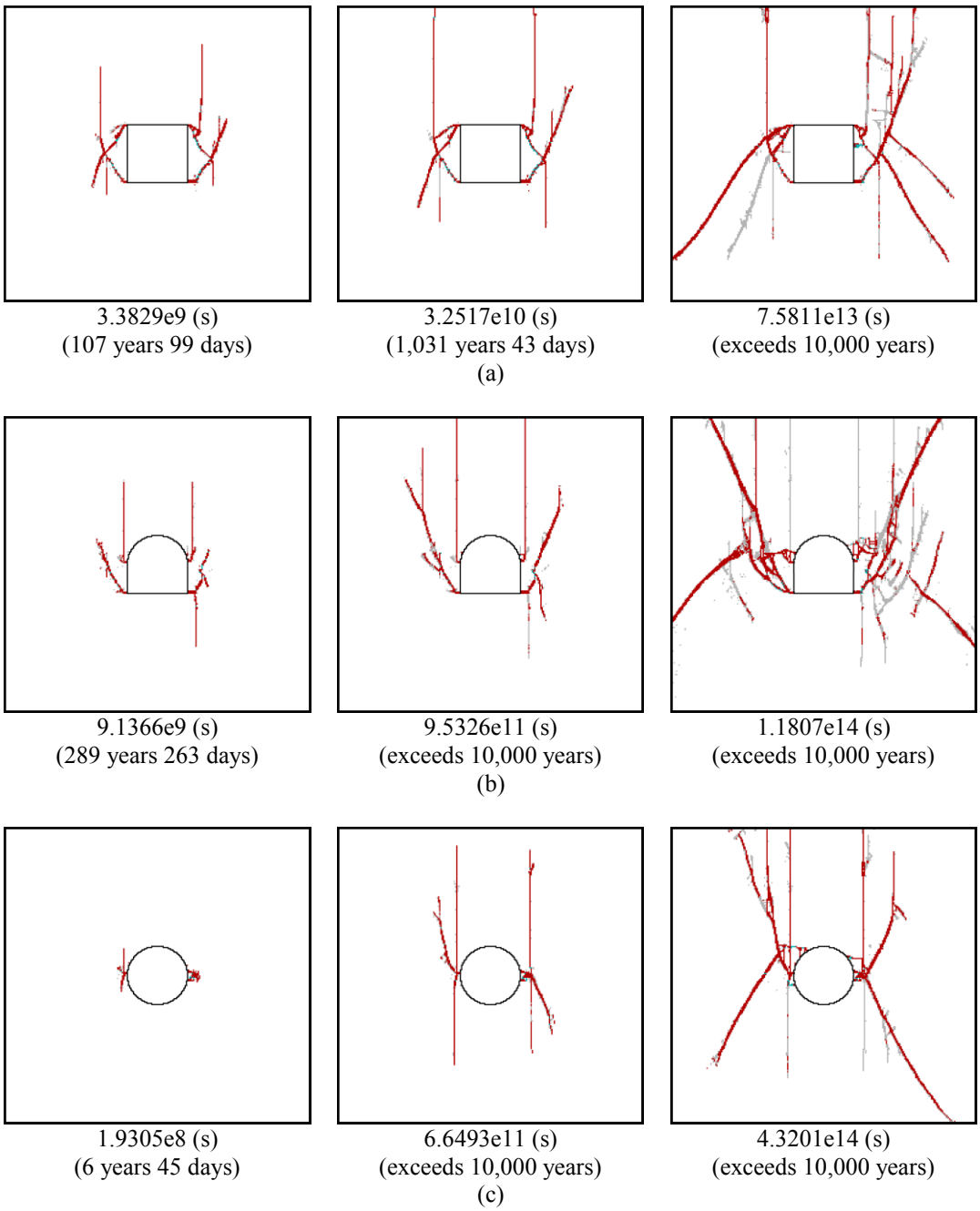

Figure 5-21 Failing process of the fixed orientation models (compressive load: 8 MPa (vertical), 2 MPa (horizontal); initial crack lengths: normal distribution, mean = 0.02 m, STD = 0.005 m; initial crack orientation: normal distribution, mean = 45º, STD = 1º; zones in red: shear failure of the zone; zones in green: tensile failure of the zone; zones in gray: zone failed in the past)

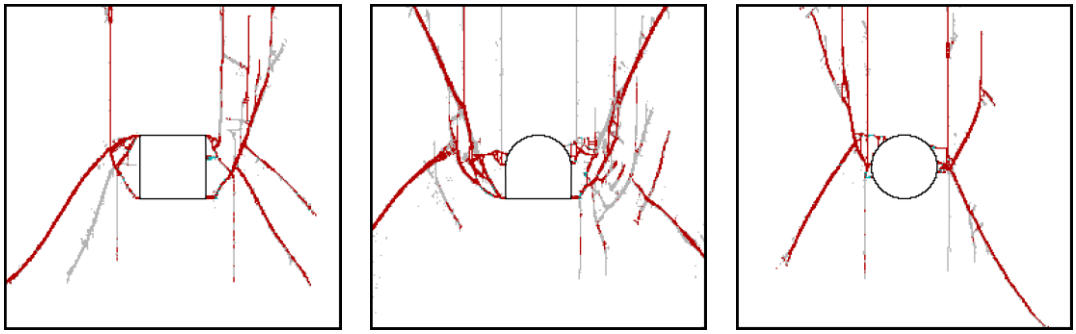

(a) (b) (c)

Figure 5-22 Final fracture pattern for fixed orientation models (compressive load: 8 MPa (vertical); 2 MPa (horizontal); initial crack lengths: normal distribution, mean = 0.02 m, STD = 0.005 m; initial crack orientation: normal distribution, mean = 45º, STD = 1º)

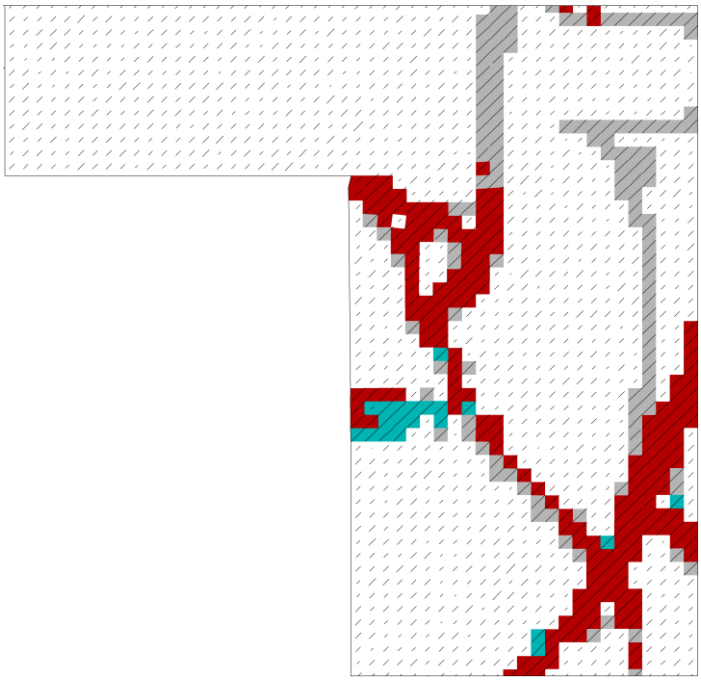

Figure 5-23 Microcracks around the up right corner of the square opening at failure (corresponding to Fig. 5-21 (a); initial crack lengths: normal distribution, mean = 0.02 m, STD = 0.005 m; initial crack orientation: normal distribution, mean = 45º, STD = 1º; zones in red: shear failure of the zone; zones in green: tensile failure of the zone; zones in gray: zone failed in the past)

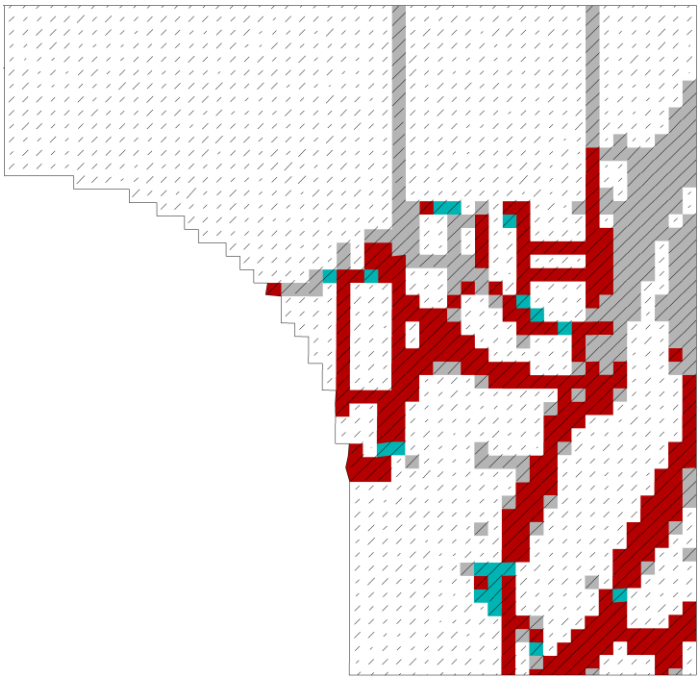

Figure 5-24 Microcracks around the right side of the arched opening at failure (corresponding to Fig. 5-21 (b); initial crack lengths: normal distribution, mean = 0.02 m, STD = 0.005 m; initial crack orientation: normal distribution, mean = 45º, STD = 1º; zones in red: shear failure of the zone; zones in green: tensile failure of the zone; zones in gray: zone failed in the past)

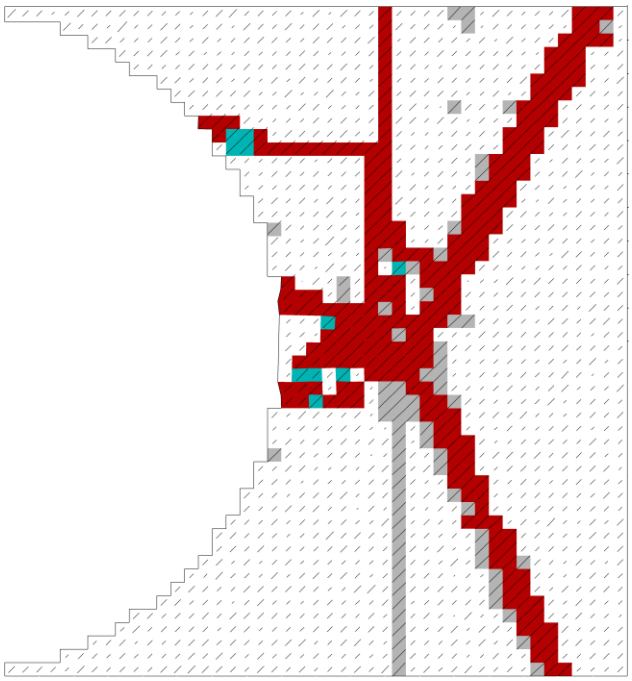

Figure 5-25 Microcracks around the right side of the circular opening at failure (corresponding to Fig. 5-21 (c); initial crack lengths: normal distribution, mean = 0.02 m, STD = 0.005 m; initial crack orientation: normal distribution, mean = 45º, STD = 1º; zones in red: shear failure of the zone; zones in green: tensile failure of the zone; zones in gray: zone failed in the past)

The predicted lifetime also shows great difference for different shapes of openings. The model with the square opening, arched opening and circular opening failed at

7.5811e13 seconds, 1.1807e14 seconds and 4.3201e14 seconds, respectively. The final fracture pattern for models with different opening shapes are shown in Fig. 5-22. A more detailed view on the area near the openings revealed that, in most of the failed zones the cracks have reached the zone boundaries, which indicated the zones failed in the subcritical crack growth phase (Fig. 5-23, Fig. 5-24 and Fig. 5-25).

(3) Fixed orientation combined ubiquitous-joint model

With anisotropy included in the fixed orientation model, the simulation results have shown difference with respect to both the lifetime and fracture patterns. The lifetime for the model with the square opening, arched opening and circular opening is 9.613e14 seconds, 7.2478e15 seconds and 5.4358e16 seconds, respectively, all longer than the corresponding case in the fixed orientation model. Shear bands have formed (with an inclination of about 70º to the horizontal direction) for each opening shape, but with less macroscopic fractures as compared to the fixed orientation model. The macroscopic fracture shows asymmetric features: if shear bands start from the left side of the openings they reach the upper boundary of the model, if shear bands start from the right side they reach the lower boundary of the model (Fig. 5-26). Also, straight macroscopic fractures following the direction of the applied major vertical compressive load have been formed at the left side of the openings but were arrested inside boundaries of the models (Fig. 5-26, Fig. 5-28, Fig. 5-29 and Fig. 5-30). Fig. 5-27 compares the final fracture pattern for openings of different shape. A more detailed view on the openings is shown in Fig. 5-28, Fig. 5-29 and Fig. 5-30, respectively. It is also observed that in most of the failed zones forming the macroscopic fractures the zones failed by the crack reaching the zone boundary (subcritical crack grow phase).

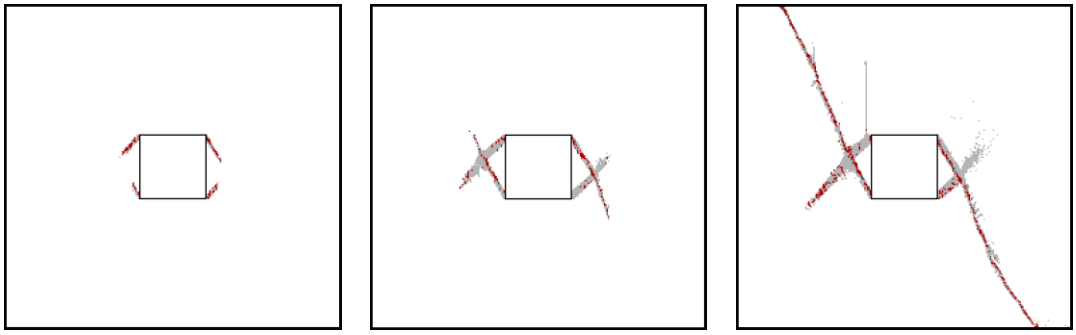

1.8699e8 (s) (5 years 339 days) | 2.1944e12 (s) (exceeds 10,000 years) | 9.6130e14 (s) (exceeds 10,000 years)

(a)

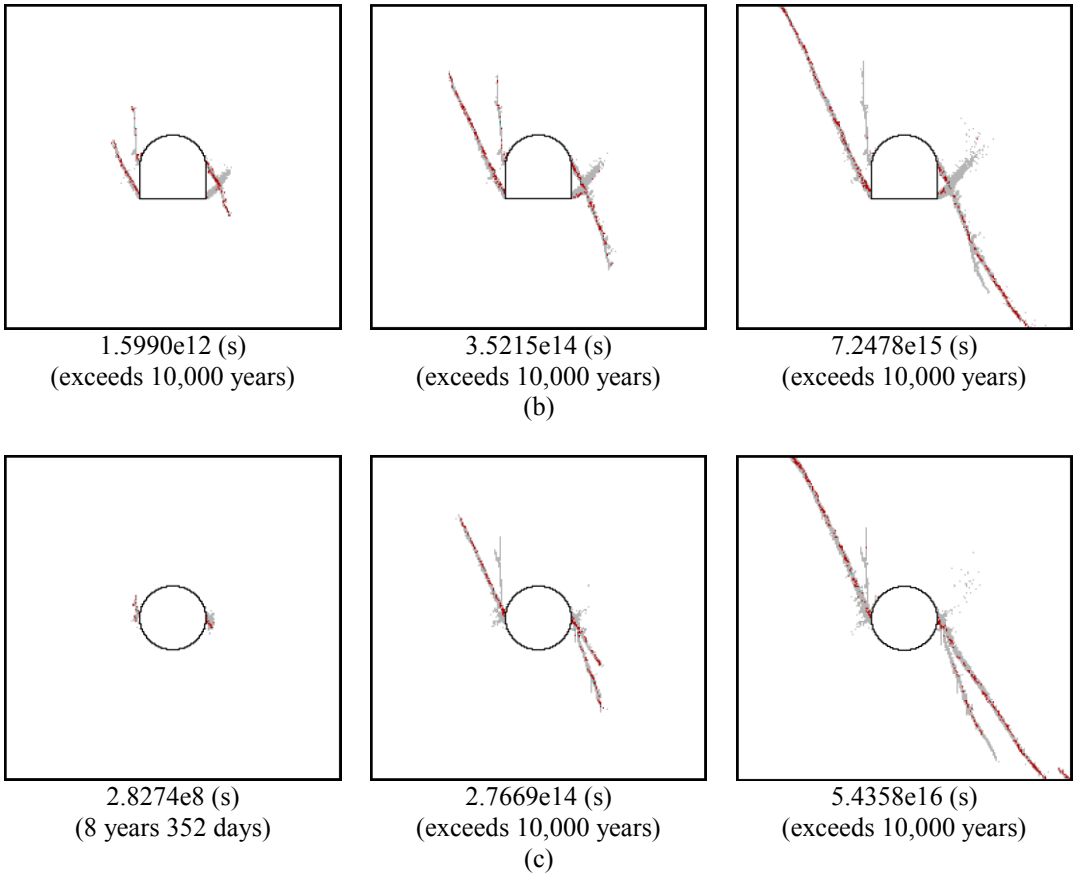

Figure 5-26 Failure process of the fixed orientation combined ubiquitous-joint models (compressive load: 8 MPa (vertical), 2 MPa (horizontal); initial crack lengths: normal distribution, mean = 0.02 m, STD = 0.005 m; initial crack orientation: normal distribution, mean = 45º, STD = 1º; zones in red: slip along ubiquitous joint; zones in green: tensile failure on ubiquitous joint; zones in gray: ubiquitous joint failed in the past)

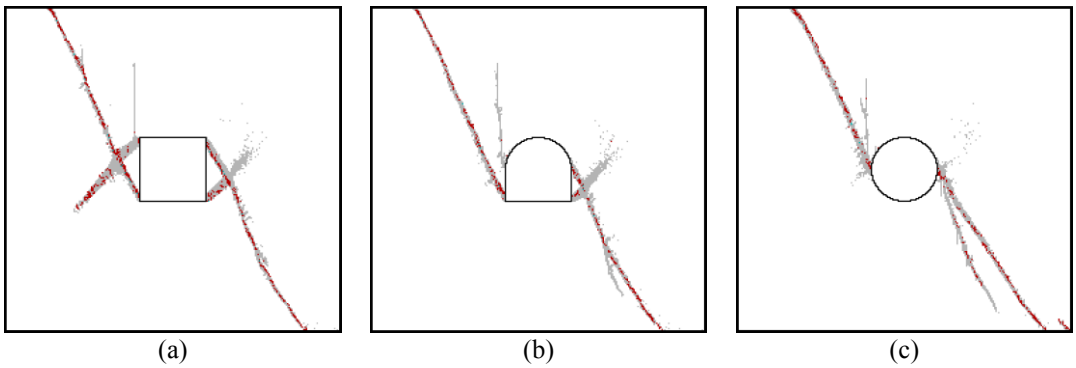

Figure 5-27 Final fracture pattern for fixed orientation combined ubiquitous-joint models (compressive load: 8 MPa (vertical), (horizontal): 2 MPa; initial crack lengths: normal distribution, mean = 0.02 m, STD = 0.005 m; initial crack orientation: normal distribution, mean = 45º, STD = 1º)

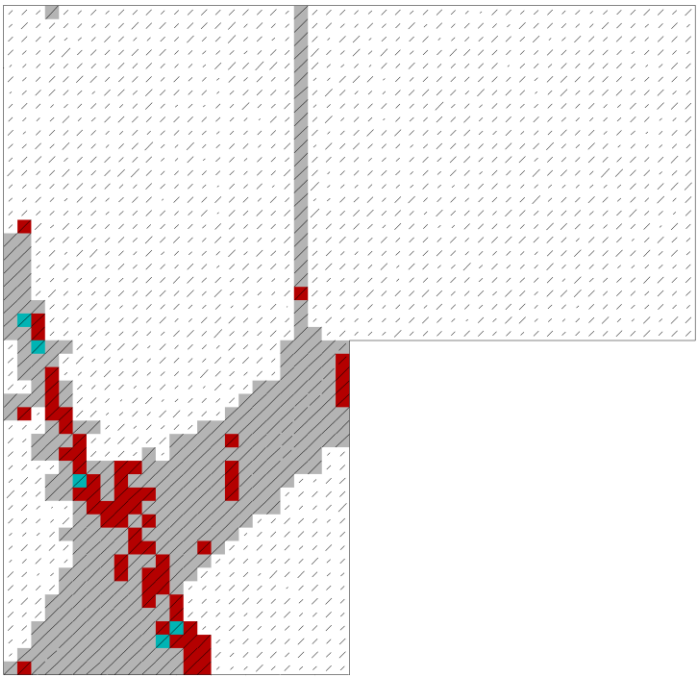

Figure 5-28 Microcracks around the up left corner of the square opening at failure (corresponding to Fig. 5-26 (a); initial crack lengths: normal distribution, mean = 0.02 m, STD = 0.005 m; initial crack orientation: normal distribution, mean = 45º, STD = 1º; zones in red: slip along ubiquitous joint; zones in green: tensile failure on ubiquitous joint/zone failed in tension; zones in gray: ubiquitous joint failed in the past)

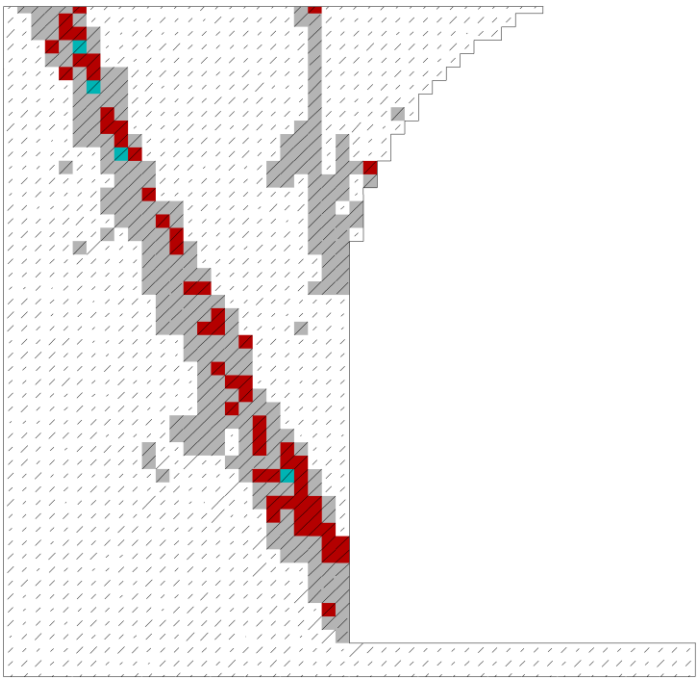

Figure 5-29 Microcracks around the left side of the arched opening at failure (corresponding to Fig. 5-26 (b); initial crack lengths: normal distribution, mean = 0.02 m, STD = 0.005 m; initial crack orientation: normal distribution, mean = 45º, STD = 1º; zones in red: slip along ubiquitous joint; zones in green: tensile failure on ubiquitous joint/zone failed in tension; zones in gray: ubiquitous joint failed in the past)

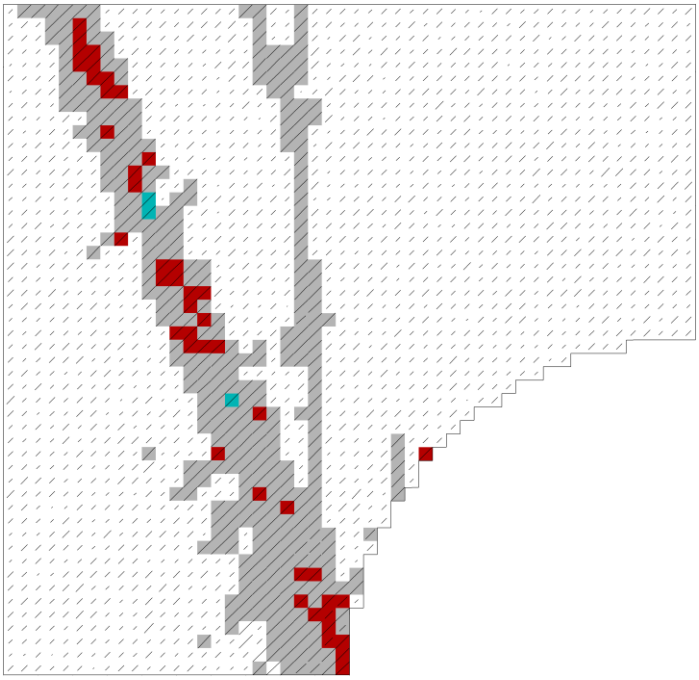

Figure 5-30 Microcracks around the left side of the circular opening at failure (corresponding to Fig. 5-26 (c); initial crack lengths: normal distribution, mean = 0.02 m, STD = 0.005 m; initial crack orientation: normal distribution, mean = 45º, STD = 1º; zones in red: slip along ubiquitous joint; zones in green: tensile failure on ubiquitous joint/zone failed in tension; zones in gray: ubiquitous joint failed in the past)

(4) Wing crack model

The lifetime for the wing crack model is much longer time than that for the models mentioned before. The lifetime for the model with the square opening, arched opening and circular opening are 1.0444e26 seconds, 9.9069e26 seconds and 1.0227e29 seconds, respectively (Fig. 5-31). The macroscopic fractures also showed distinct features. As shown in Fig. 17, Fig. 18 and Fig.19, macroscopic tensile fractures have been found at the middle of the roof and floor of the square opening, at the floor of the arched opening and at the roof of the circular opening (all of them are located in the area of tensile stress concentrations). These macroscopic tensile fractures develop in the same direction as the applied major compressive load, and were later arrested and do not reach the model boundary. The shear band (inclined about 70º to the horizontal direction) formed from the side walls of the openings have a 'feather' liked structure (Fig. 5-31). Especially, macroscopic fractures circling the opening have been found in the model with the circular opening (Fig. 5-31 (c) and Fig. 5-32 (c)). The wing cracks inside the failed zones forming these macroscopic fractures have the trend of follow the direction of the tangent line of the boundary of the opening (Fig. 5-35). A more detailed view close to the openings is shown in Fig. 5-33, Fig. 5-34 and Fig. 5-35, respectively.

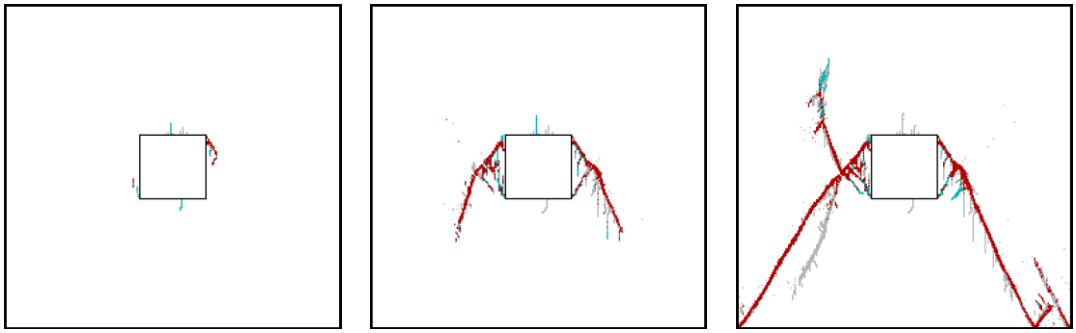

1.5207e17 (s) 5.3997e24 (s) (exceeds 10,000 years) 1.0444e26 (s)

(a)

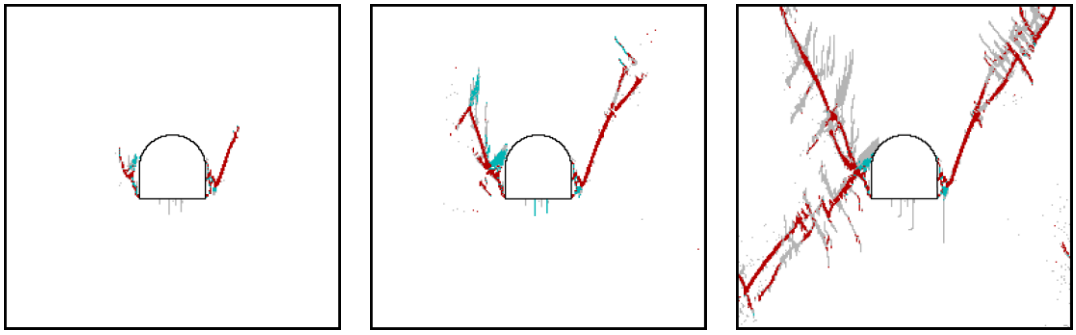

5.8440e22 (s) 3.0776e26 (s) (exceeds 10,000 years) 9.9069e26 (s)

(b)

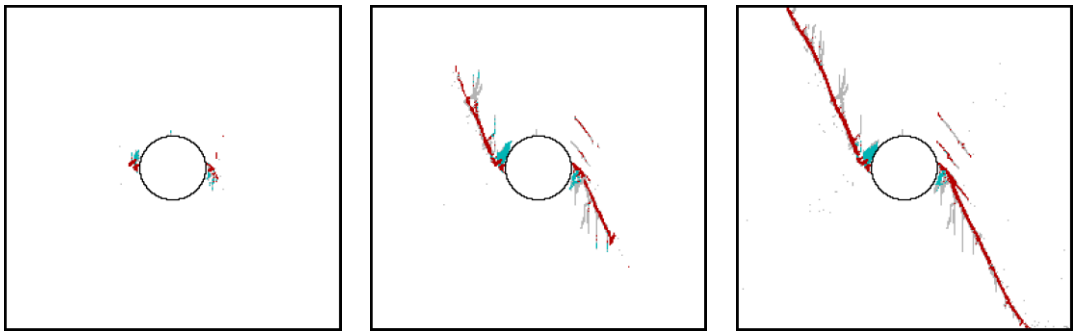

1.4976e24 (s) 4.0248e26 (s) (exceeds 10,000 years) 1.0227e29 (s)

(c)

Figure 5-31 Failure process of the wing crack models (compressive load: 8 MPa (vertical), 2 MPa (horizontal); initial crack lengths: normal distribution, mean = 0.02 m, STD = 0.005 m; initial crack orientation: normal distribution, mean = 45º, STD = 1º; zones in red: shear failure of the zone; zones in green: tensile failure of the zone; zones in gray: zone failed in the past)

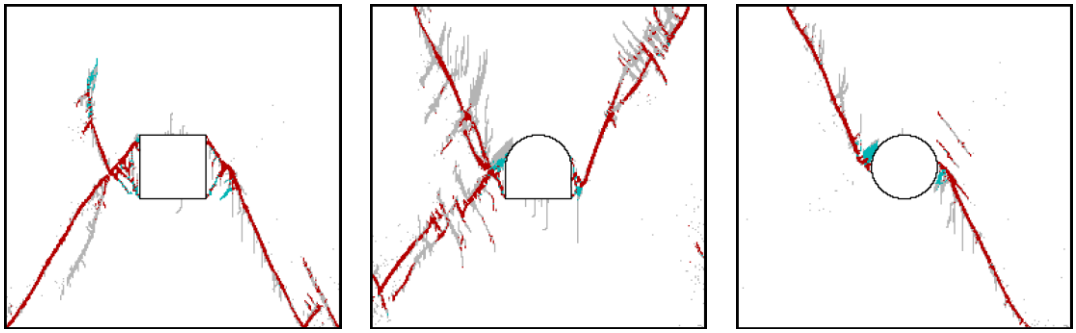

(a) (b) (c)

Figure 5-32 Final fracture pattern for the wing crack models (compressive load: 8 MPa (vertical), 2 MPa (horizontal); initial crack lengths: normal distribution, mean = 0.02 m, STD = 0.005 m; initial crack orientation: normal distribution, mean = 45º, STD = 1º)

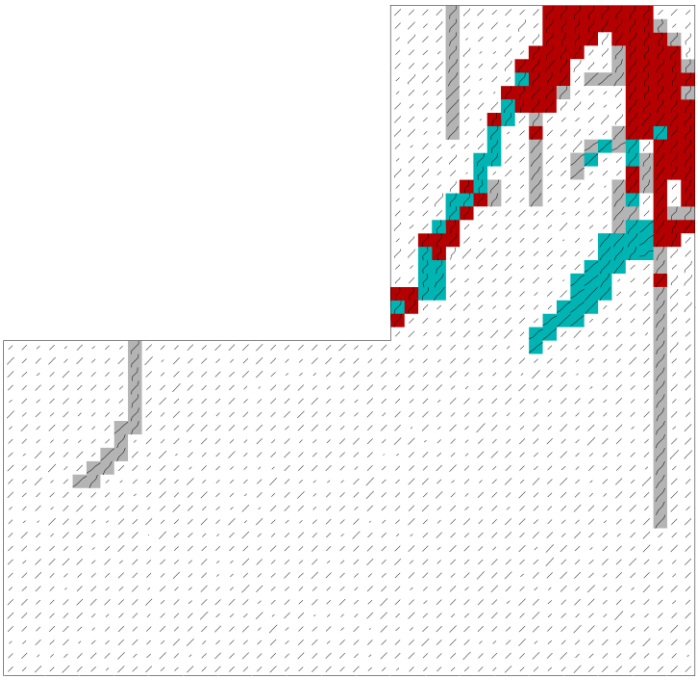

Figure 5-33 Microcracks around the lower right corner of the square opening at failure (corresponding to Fig. 5-31 (a); initial crack lengths: normal distribution, mean = 0.02 m, STD = 0.005 m; initial crack orientation: normal distribution, mean = 45º, STD = 1º; zones in red: shear failure of the zone; zones in green: tensile failure of the zone; zones in gray: zone failed in the past)

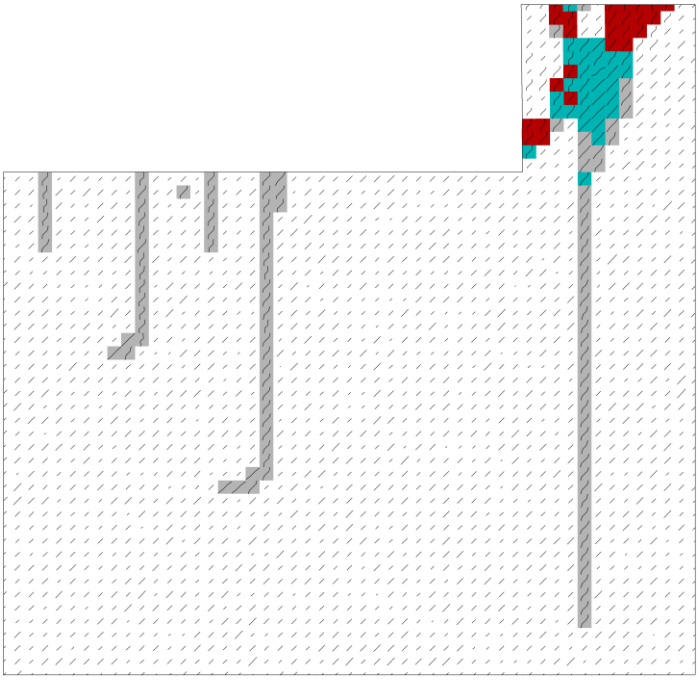

Figure 5-34 Microcracks around the floor of the arched opening at failure (corresponding to Fig. 5-31 (b); initial crack lengths: normal distribution, mean = 0.02 m, STD = 0.005 m; initial crack orientation: normal distribution, mean = 45º, STD = 1º; zones in red: shear failure of the zone; zones in green: tensile failure of the zone; zones in gray: zone failed in the past)

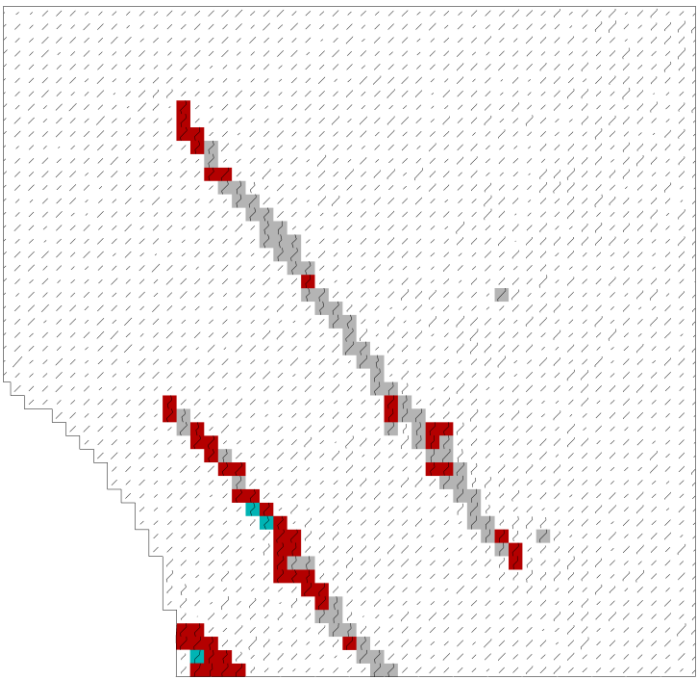

Figure 5-35 Microcracks around the up right side of the circular opening at failure (corresponding to Fig. 5-31 (c); initial crack lengths: normal distribution, mean = 0.02 m, STD = 0.005 m; initial crack orientation: normal distribution, mean = 45º, STD = 1º; zones in red: shear failure of the zone; zones in green: tensile failure of the zone; zones in gray: zone failed in the past)

(5) Wing crack combined ubiquitous-joint model

The lifetimes for the wing crack combined ubiquitous-joint model with square opening, arched opening and circular opening are 6.1862e32 seconds, 8.666e32 seconds and 9.1208e32 seconds (Fig. 5-36), respectively, longer than the corresponding cases in wing crack model. For the model with a square opening, the failed zones first appeared at the corners and middle of the roof and floor boundaries of the opening. For the model with an arched opening, the failed zone first appeared around the bottom corners of the opening and at the transition between the arched roof and the side walls. For the model with a circular opening, the failed zones first appeared at the left and right sides of the opening. Shear bands (inclined about 60º to the horizontal direction) were later on formed starting from the sides of the openings and reaching the boundary of the model. Macroscopic tensile fractures also were formed from the middle of the roof and floor of the openings, but were arrested already shortly away from the boundary (Fig. 5-36). A detailed view about the final fracture pattern is seen in Fig. 5-38, Fig. 5-39 and Fig. 5-40. The final fracture pattern for models with different opening shapes are shown in Fig. 5-37.

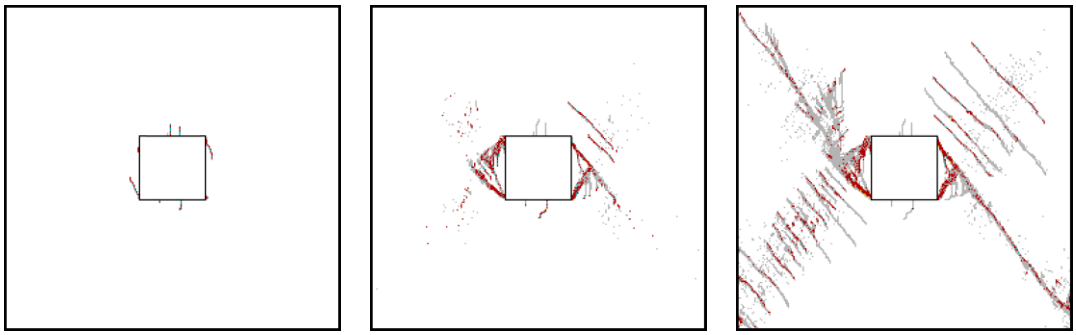

2.7063e17 (s) 4.7502e28 (s) (exceeds 10,000 years) 6.1862e32 (s)

(a)

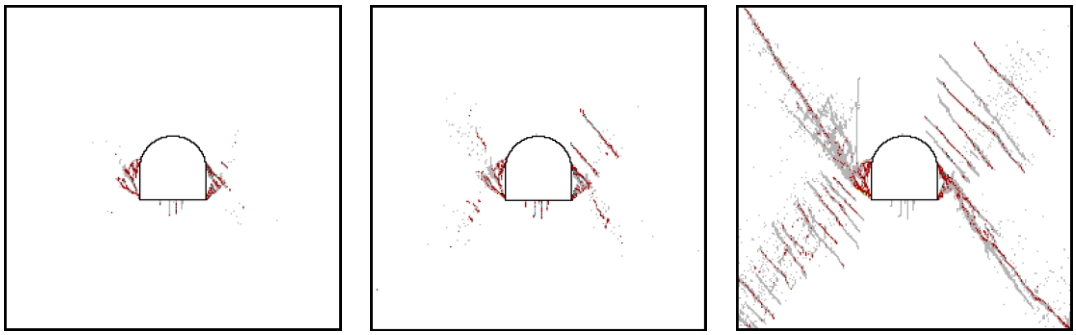

4.6035e26 (s) 2.5801e28 (s) (exceeds 10,000 years) 8.6660e32 (s)

(b)

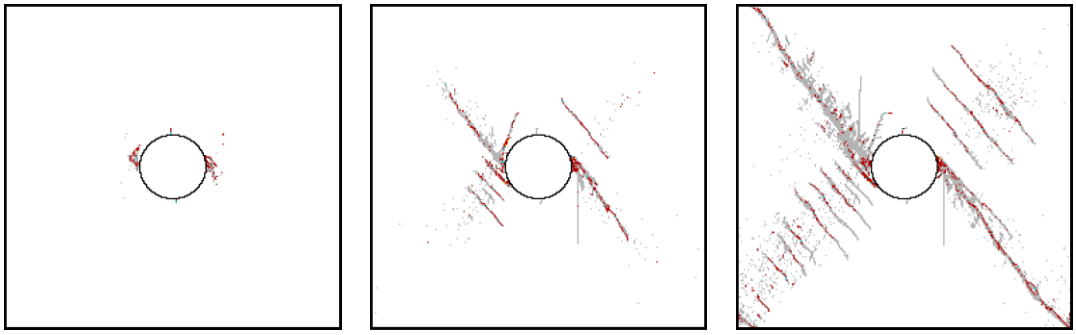

2.0607e25 (s) 1.2790e30 (s) (exceeds 10,000 years) 9.1208e32 (s)

(c)

Figure 5-36 Failure process of the wing crack combined ubiquitous-joint models (compressive load: 8 MPa (vertical); 2 MPa (horizontal); initial crack lengths: normal distribution, mean = 0.02, STD = 0.005; initial crack orientation: normal distribution, mean = 45º, STD = 1º; zones in red: slip along ubiquitous joint; zones in green: tensile failure on ubiquitous joint; zones in gray: ubiquitous joint failed in the past)

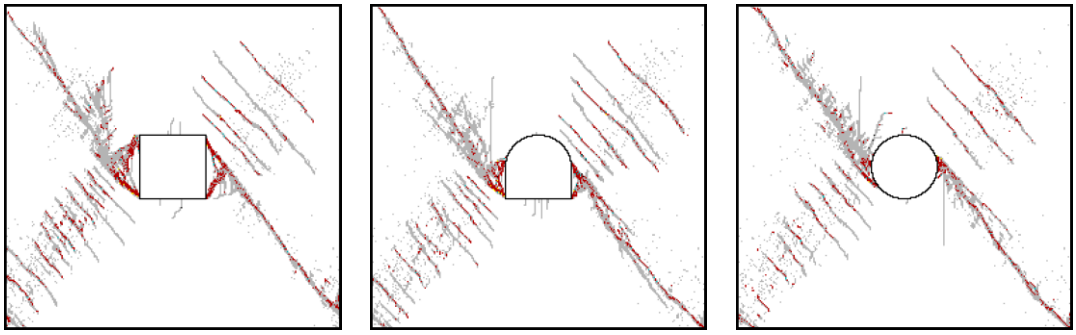

(a) (b) (c)

Figure 5-37 Final failure pattern of the wing crack combined ubiquitous-joint models at failure (compressive load: 8 MPa (vertical), 2 MPa (horizontal); initial crack lengths: normal distribution, mean = 0.02, STD = 0.005; initial crack orientation: normal distribution, mean = 45º, STD = 1º)

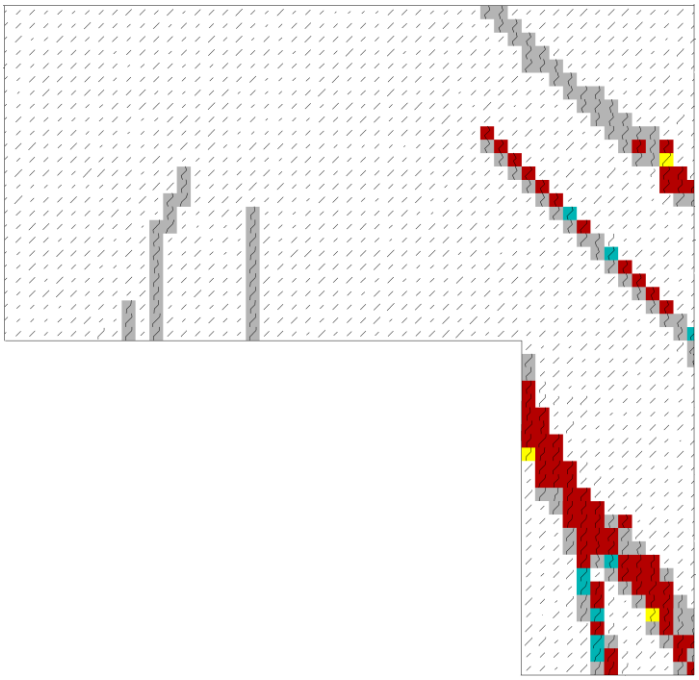

Figure 5-38 Microcracks around the up right corner of the square opening at failure (corresponding to Fig. 5-36 (a); initial crack lengths: normal distribution, mean = 0.02 m, STD = 0.005 m; initial crack orientation: normal distribution, mean = 45º, STD = 1º; zones in red: slip along ubiquitous joint; zones in green: tensile failure on ubiquitous joint; zones in yellow: zone failed in tension; zones in gray: ubiquitous joint failed in the past)

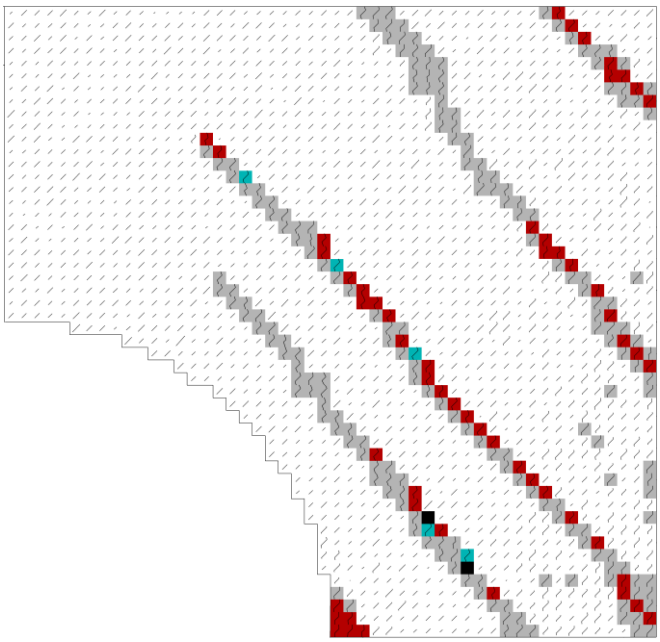

Figure 5-39 Microcracks around the up right side of the arched opening at failure (corresponding to Fig. 5-36 (b); initial crack lengths: normal distribution, mean = 0.02 m, STD = 0.005 m; initial crack orientation: normal distribution, mean = 45º, STD = 1º; zones in red: slip along ubiquitous joint; zones in green: tensile failure on ubiquitous joint; zones in black: failed in past (elastic); zones in gray: ubiquitous joint failed in the past)

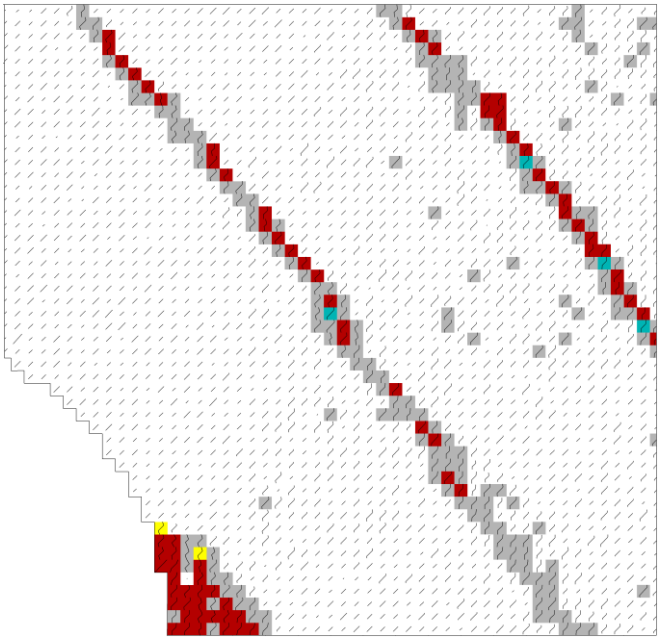

Figure 5-40 Microcracks around the up right side of the circular opening at failure (corresponding to Fig. 5-36 (c); initial crack lengths: normal distribution, mean = 0.02 m, STD = 0.005 m; initial crack orientation: normal distribution, mean = 45º, STD = 1º; zones in red: slip along ubiquitous joint; zones in green: tensile failure on ubiquitous joint; zones in yellow: zone failed in tension; zones in gray: ubiquitous joint failed in the past)

5.2.3 Conclusions

Underground opening problem was simulated using the five distinct model schemes proposed in the former chapters. Models with different scales have been investigated. Also, different shapes of openings have been modeled for comparison. Lifetime and micro- and macroscopic fractures were studied. It is observed in each model scheme that with the similar sizes of the opening, the model with the square opening has the shortest lifetime. The lifetime of the model with the arched opening is longer and the model with the circular opening has the longest lifetime. In addition, by comparing the lifetimes between the different model schemes, it is concluded that the basic model gives the most conservative lifetime, while the wing crack combined ubiquitous joint model has predicted the longest lifetime. It is seen that following the ascending order of the predicted lifetime, the model schemes are: basic model, fixed orientation model, fixed orientation combined ubiquitous-joint model, wing crack model and wing crack combined ubiquitous-joint model. Shear bands have been observed in each model scheme. Especially, macroscopic tensile fractures have been formed from the roof and floor of the openings in the wing crack model and wing crack combined ubiquitous-joint model. In addition, the area where the microcracks have grown significantly longer coincides with the macroscopic fractures in each model. This phenomenon agrees with the laboratory observation that the macroscopic fractures were formed by the propagation and coalescence of the microcracks.

5.3 Underground pillar problems

5.3.1 Numerical simulation

Different numerical model schemes have been used to study the fracture pattern and lifetime of underground pillars under load. The height of the assumed pillar is 5 meters. Only half of the pillar is modeled because of the symmetrical geometry, as is shown in Fig. 5-41. The numerical model contains 23,750 zones, with a length of each zone of 0.04 m. The crack length inside each zone follows normal distribution with a mean value of 0.02 m and standard deviation of 0.005 m. For the fixed orientation model, fixed orientation combined ubiquitous-joint model, wing crack model and wing crack combined ubiquitous-joint model the initial crack orientation follows uniform distribution and normal distribution for comparison. As shown in Fig. 5-42, under a compressive load (8 MPa), compressive stress concentrates at the corner of the pillar and the tensile stresses along the roof of the chamber are observed.

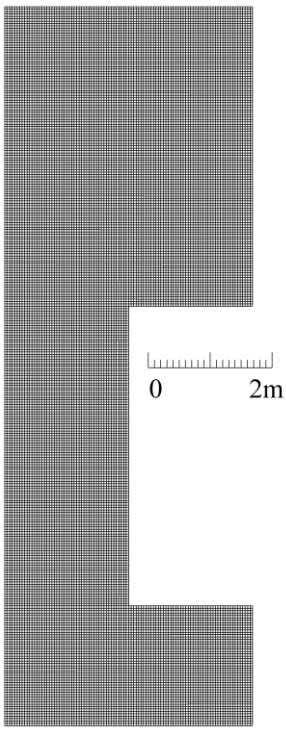

Figure 5-41 Geometry of numerical models for underground pillar (Model height: 12 m; pillar height 5 m; zone size: 0.04 × 0.04 m^2)

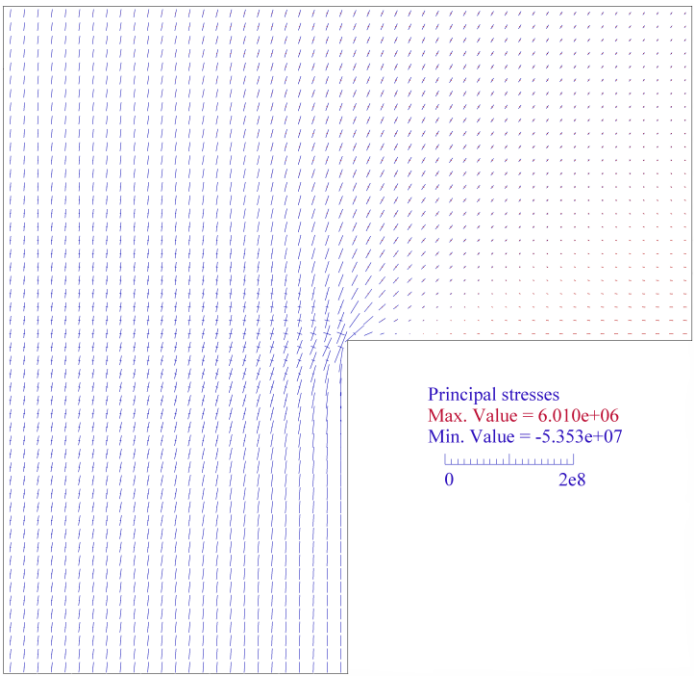

Figure 5-42 Initial principal stress vectors at the joint of the pillar top and the ceiling (under uniaxial compressive load of 8 MPa)

The failure stages for the basic model scheme, fixed orientation model scheme and fixed orientation combined ubiquitous-joint model scheme under the uniaxial compressive load of 8 MPa are shown in Fig. 5-43, Fig. 5-44 and Fig. 5-45, respectively. It is seen that under the uniaxial compressive load of the same magnitude (8 MPa), the basic model fails after about 18 seconds (Fig. 5-43), while the fixed orientation model failed after about 610 years if the initial crack orientation follows uniform distribution and after about 2 days if the initial crack orientation follow normal distribution with mean orientation of 45º and standard deviation of 1º (Fig. 5-44). The lifetime for the fixed orientation combined ubiquitous joint model is about 5.6065e11 seconds and 2.6057e5, respectively (Fig. 5-45). Under a bigger compressive load (12 MPa), the lifetime of the wing crack model is about 8.0574e14 seconds if the initial crack orientation follows uniform distribution, and 2.0657e15 seconds if the initial crack orientation follows normal distribution with mean orientation of 45º and standard deviation of 1º (Fig. 5-46); for the two orientation distributions in wing crack combined ubiquitous-joint model, the lifetime is about 2.0797e13 and 1.1355e16 seconds, respectively (Fig. 5-47).

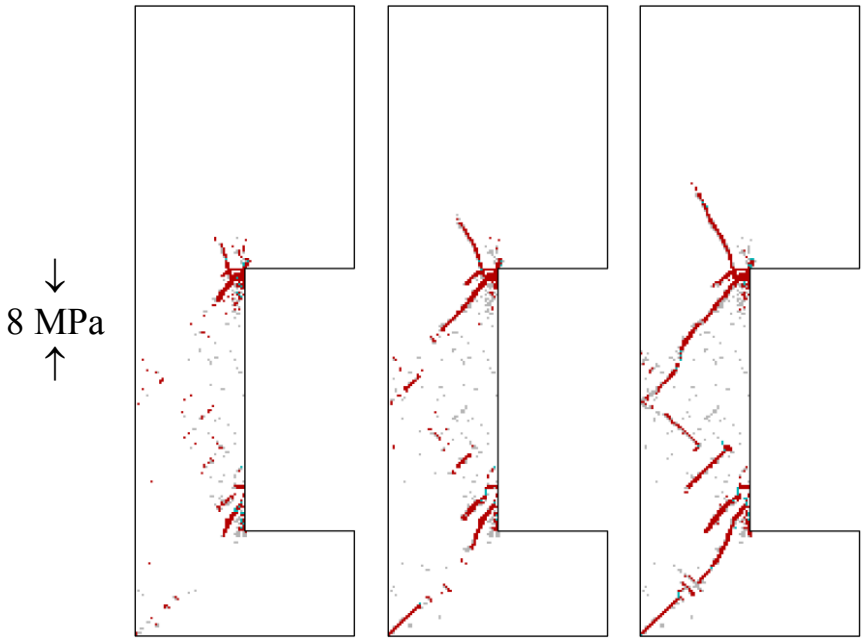

1.2 second 4.3 seconds 18.7 seconds

Initial crack lengths: normal distribution, mean = 0.02 m, STD = 0.005 m

Figure 5-43 Failure process of the basic model (Zones in red: shear failure of the zone; zones in green: tensile failure of the zone; zones in gray: zone failed in the past)

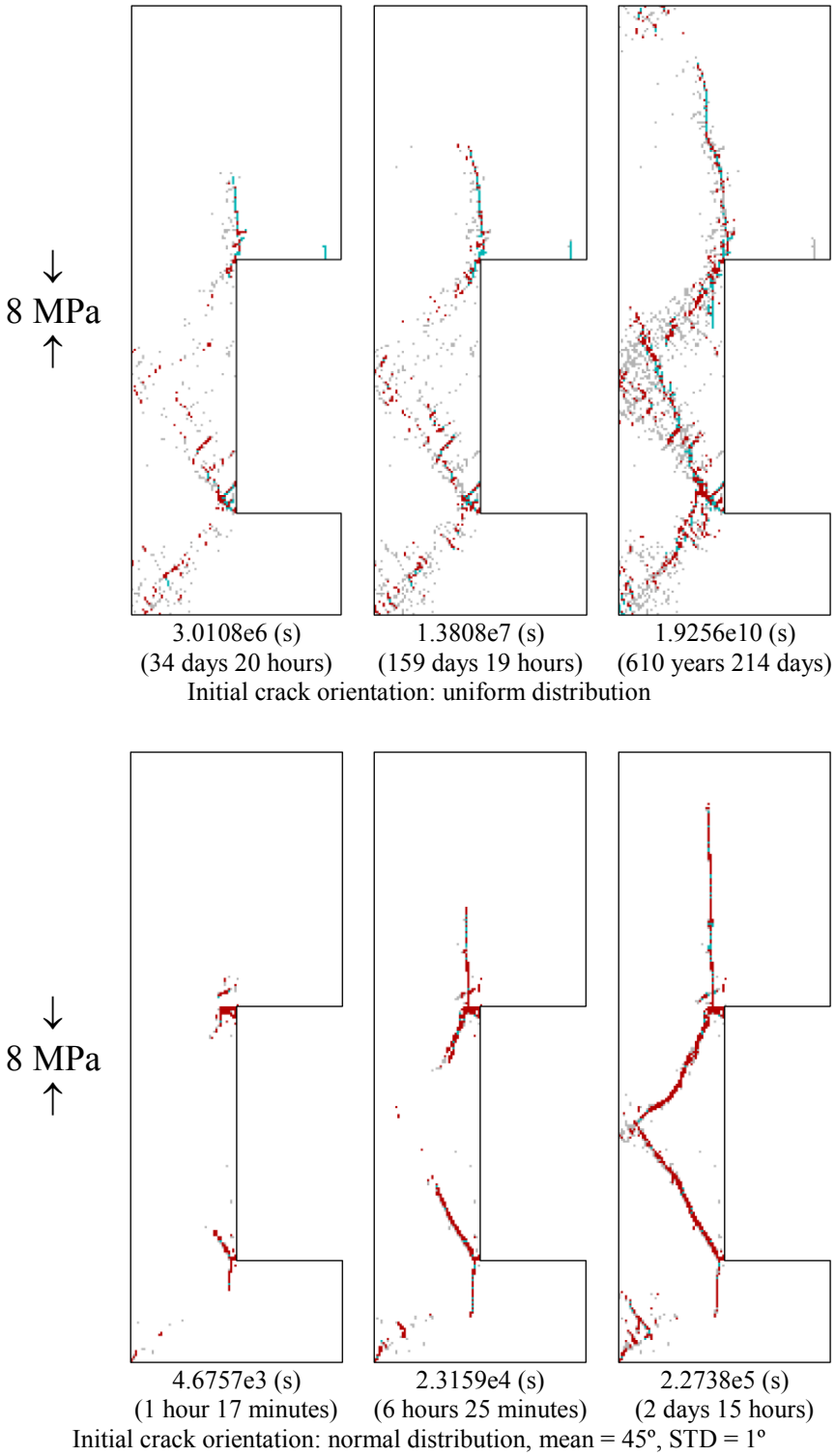

Figure 5-44 Failure process of the fixed orientation model (Zones in red: shear failure of the zone; zones in green: tensile failure of the zone; zones in gray: zone failed in the past; initial crack lengths: normal distribution, mean = 0.02 m, STD = 0.005 m)

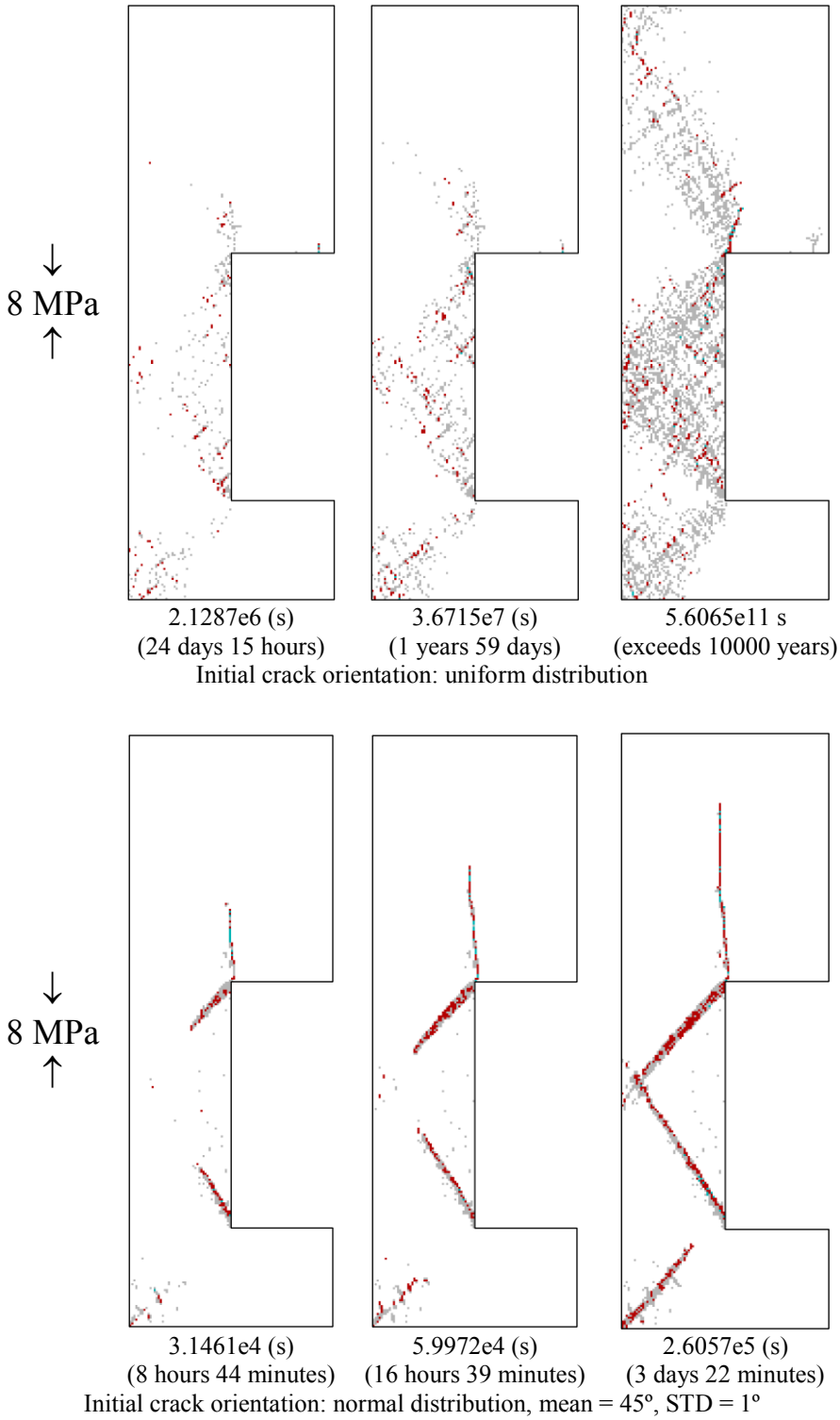

Figure 5-45 Failure process of the fixed orientation combined ubiquitous-joint model (Zones in red: slip along ubiquitous joint; zones in green: tensile failure on ubiquitous joint; zones in gray: ubiquitous joint failed in the past; initial crack lengths: normal distribution, mean = 0.02 m, STD = 0.005 m)

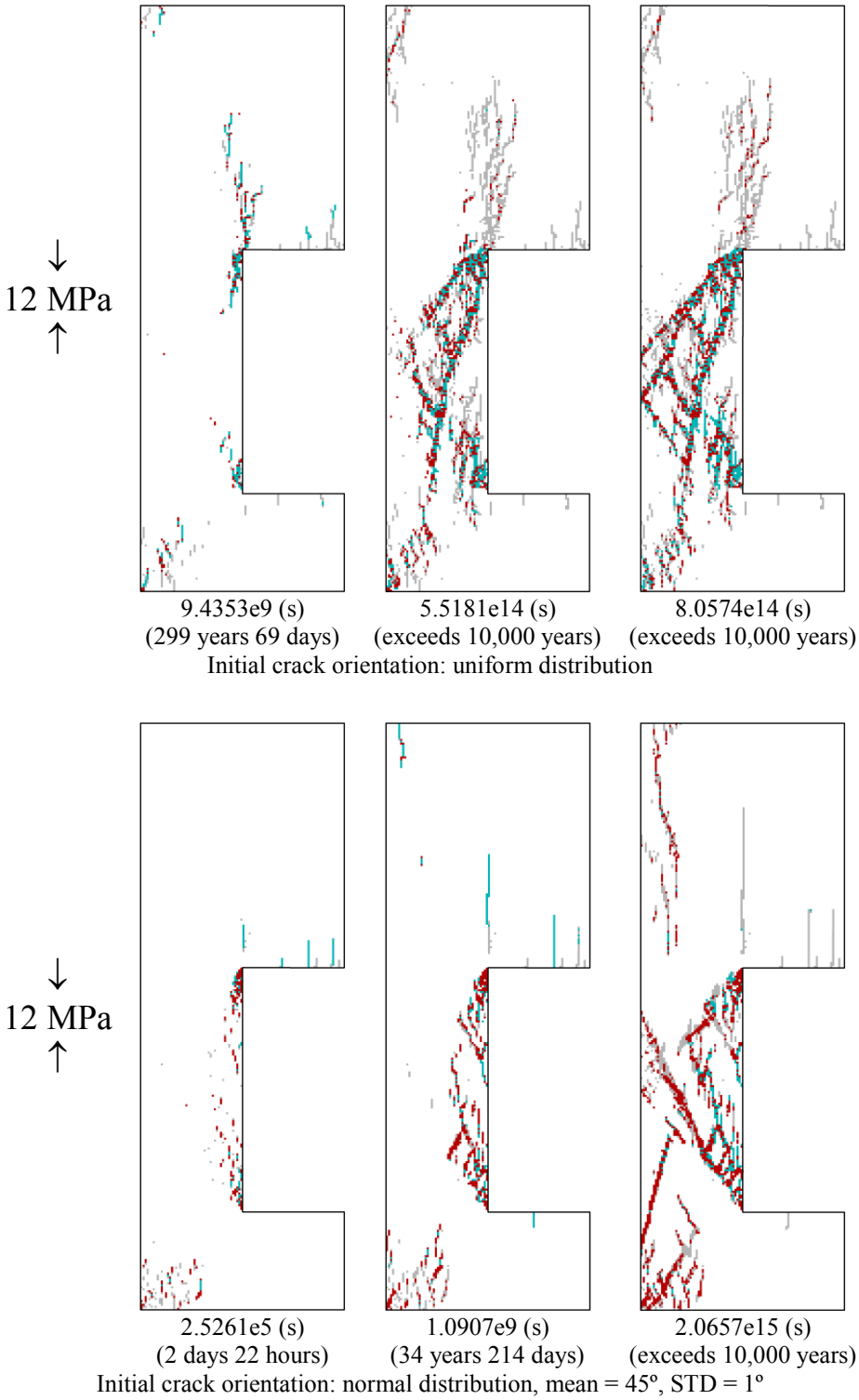

Figure 5-46 Failure process of the wing crack model (Zones in red: shear failure of the zone; zones in green: tensile failure of the zone; zones in gray: zone failed in the past; initial crack lengths: normal distribution, mean = 0.02 m, STD = 0.005 m)

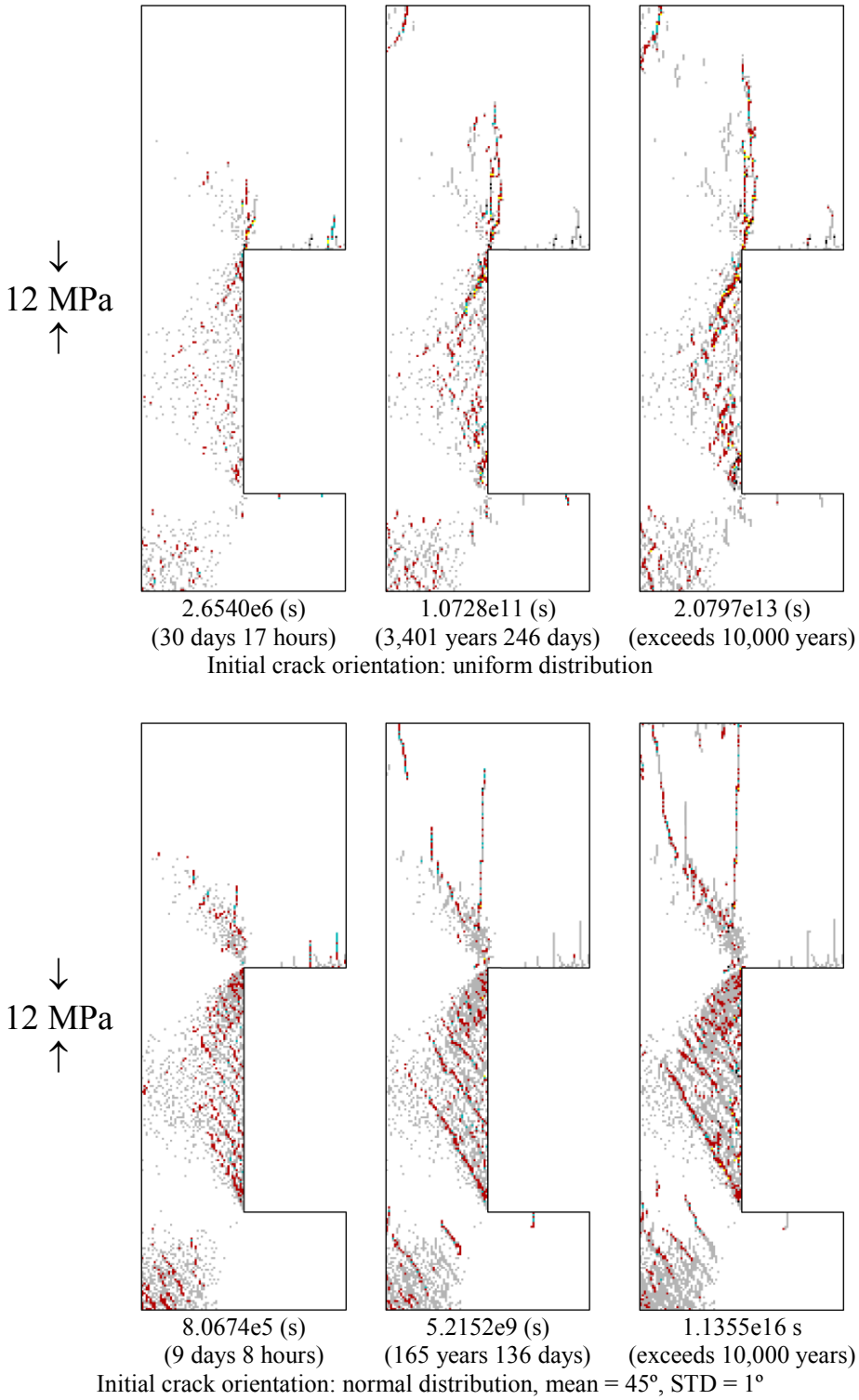

Figure 5-47 Failure process of the wing crack combined ubiquitous-joint model (Zones in red: slip along ubiquitous joint; zones in green: tensile failure on ubiquitous joint; zones in yellow: zone failed in tension; zones in black: failed in past (elastic); zones in gray: ubiquitous joint failed in the past; initial crack lengths: normal distribution, mean = 0.02 m, STD = 0.005 m)

Shear bands are observed in each of the models. In the basic model, the shear band has been formed inclining about 45º to the horizontal direction (Fig. 5-43). In the

fixed orientation model and fixed orientation combined ubiquitous-joint model, the inclination of the shear band is 60º ~ 70º to the horizontal direction (Fig. 5-44 and Fig. 5-45). In the wing crack model and wing crack combined ubiquitous-joint model, the inclination of the shear band is 65º ~ 80º to the horizontal direction (Fig. 5-46 and Fig. 5-47). Especially, at the corners of the pillar and the hanging wall except the basic model, macroscopic fracture are observed following the same direction as the applied load. In addition, tensile macroscopic fracturing has also been observed at the hanging walls (Fig. 5-46 to Fig. 5-47). It is also observed that if the initial crack orientation follows uniform distribution, the failed zones forming the shear band are more scattered than if the orientation follows normal distribution. The macroscopic fracture in the model with uniformly distributed initial cracks has a more uneven pattern.

5.3.2 Conclusions

Lifetime and fracture patterns of a pillar under compressive load have been investigated in this section. It can be concluded that, the basic model has the most conservative lifetime, while the wing crack combined ubiquitous-joint model has predicted the longest lifetime. It is also concluded that the lifetime is influenced by the initial crack orientation. In the fixed orientation model and fixed orientation combined ubiquitous-joint model, the lifetime is much longer if the initial crack orientation follows uniform distribution than if they follow normal distribution, while in the wing crack model and wing crack combined ubiquitous-joint model, the lifetime is shorter. Shear bands were observed in each model with distinct inclinations. The shear band was formed by more scattered failed zones if the initial crack orientation follows uniform distribution than normal distribution. Macroscopic fracture with the same direction as the applied compressive load has also been formed from the corner of the pillar and from roof of the opening. In addition, more shear bands have been observed in the pillar in wing crack model and wing crack combined ubiquitous-joint model (Fig. 5-46 and Fig. 5-47), compared to more singular shear bands observed in other models (Fig. 5-43 to Fig. 5-45).

5.4 Comparison between numerical results and observations in situ

So far the numerical simulation results were compared with analytical solutions of very simple constellations and lab test results in terms of general failure pattern. The question arises, if this procedure would also predict realistic fracture (failure) pattern for large-scale geotechnical constructions in rock masses like tunnels, pillars etc. Therefore, a few preliminary studies were performed to investigate if numerical predicted failure pattern correspond to typical failure pattern in-situ.

Exemplary, the numerical simulation results are compared to observations of underground tunnel and pillar fracture patterns considering shape of geotechnical

construction and stress ratios and orientations. Fig. 5-48 (b) shows the excavation disturbed zone around a tunnel (Bossart et al. 2002, Blümling and Konietzky 2003). The extensional failures in the sidewalls of the tunnel are represented by the circular macroscopic fractures observed in wing crack combined ubiquitous-joint model (Fig. 5-48 (a)). Damage zones around excavated circular cavities of different scale are shown in Fig. 5-49. It is seen that the damage locations agree with those of the numerical simulation, where the mean orientation direction of initial cracks correspond to the bedding direction of the rock around the cavities. Macroscopic fracture pattern similar to typical V-shaped notches are observed in the numerical model (Fig. 5-50 (a)). The numerical simulation is also compared to an in situ observation at a Mine-by Experiment tunnel (Read 2004, Chandler 2004), as seen in Fig. 5-50 (b). Macroscopic fracture is also observed in agreement with classical fracture pattern as seen in Fig. 5-51. It is seen in Fig. 5-51 (b) that if the sidewalls of the opening are not stable, sliding faces with the inclination of 45º - φ/2 from the vertical direction are formed from the floor of the opening. Macroscopic fractures are observed in fixed orientation model with the inclination in agreement with the classical fracture pattern (Fig. 5-51 (a)). Vertical macroscopic fractures are also observed in Fig. 5-51 (a) in agreement with the vertical sliding faces shown in Fig. 5-51 (c). For the case where a pressure arch can not be formed naturally, or the pressure arch has not enough load bearing capability, inclined sliding faces can be formed from the floor of the opening, with the inclination of 45º - φ/2 from the vertical direction as shown in Fig. 5-51(e) (Xu 1993). Similar fracture pattern is also observed in fixed orientation model, where the inclination of the macroscopic fracture is also in agreement with the classical result (Fig. 5-51 (d)).

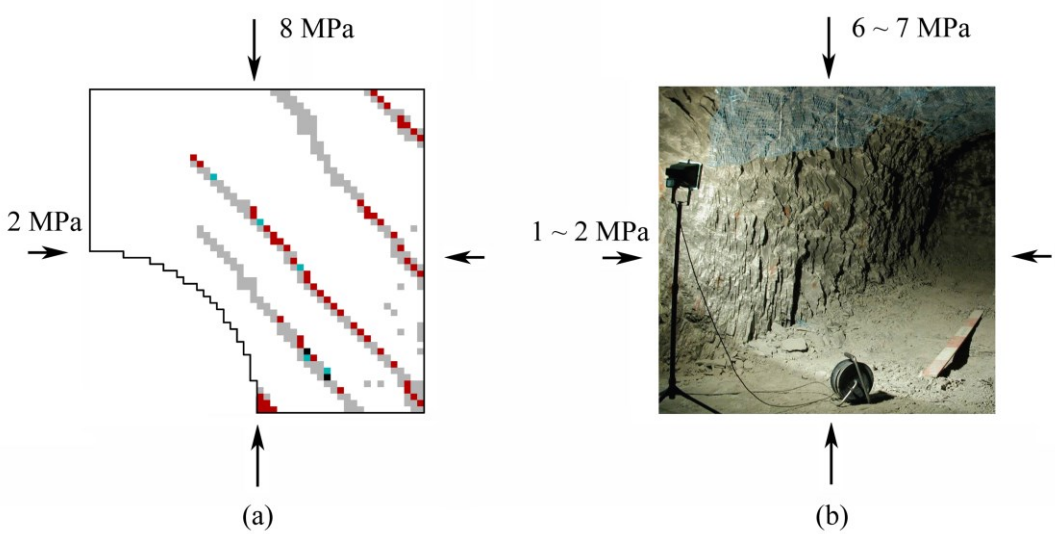

Figure 5-48 The excavation disturbed zone around a tunnel (a) the fracture features around the sidewalls in wing crack combined ubiquitous-joint model with initial crack orientation following normal distribution (b) at an intersection of two tunnels at Mont Terri (modified from Blümling and Konietzky 2003, photo B. Niederberger)

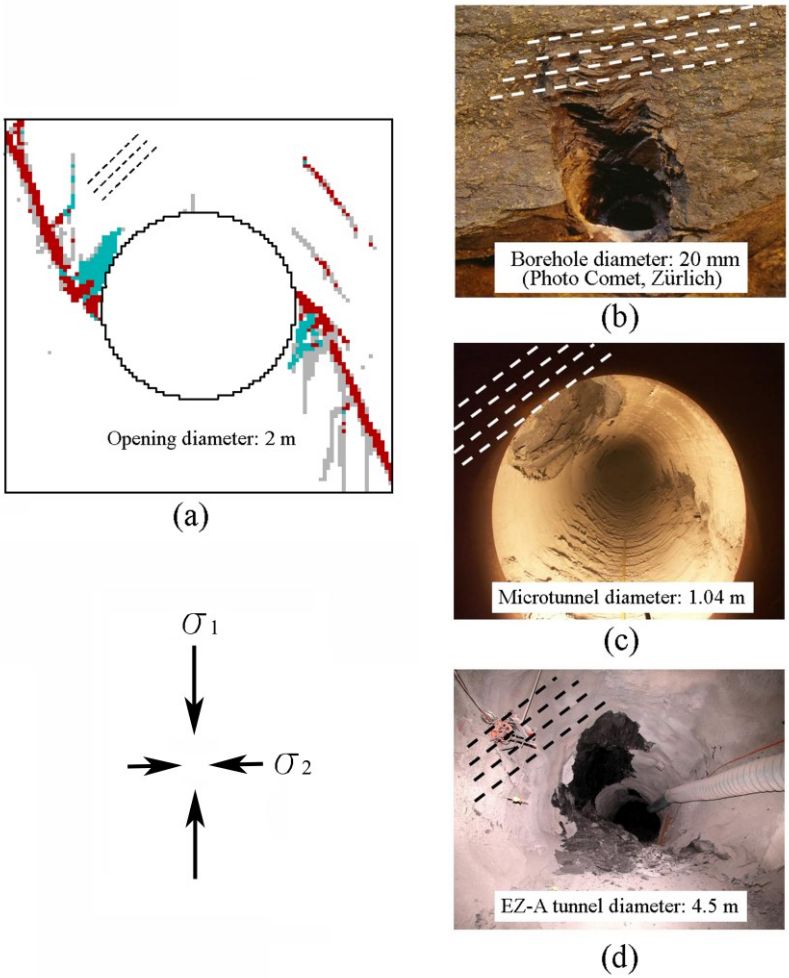

Figure 5-49 Damage zones around underground cavities on different scales (a) macroscopic fracture in wing crack model, σ_1 = 8 MPa, σ_2 = 2 MPa (b) slim horizontal borehole (c) gas path through host rock and along seal sections/ HG-A microtunnel (d) overbreak in the EZ-A tunnel of the Mont Terri Underground Research Laboratory, σ_1 = 6.5 MPa, σ_1 / σ_2 = 1.5 ~ 2 (Marschall et al. 2008) (dashed line: (a) mean initial crack orientation; (b), (c) and (d): bedding direction)

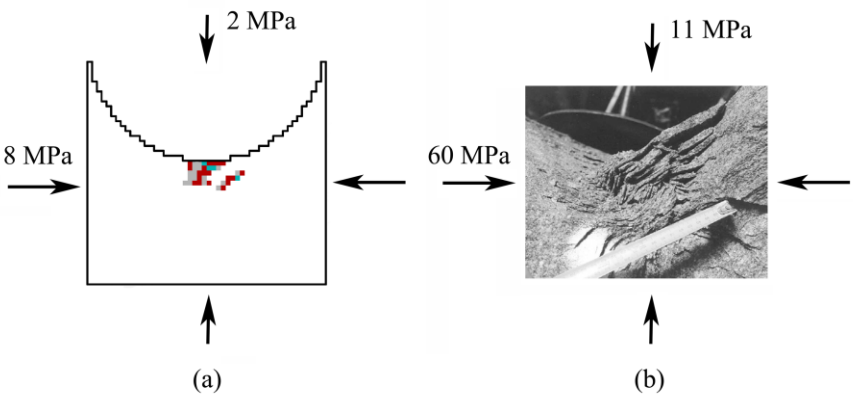

Figure 5-50 Tip of the V-shaped notch of the underground opening (a) macroscopic fracture pattern at the sidewalls at the early stage of the damage process of the opening in wing crack combined ubiquitous-joint model with initial crack orientation following normal distribution (b) V-shaped notch tip of a Mine-by Experiment Tunnel at the Underground Research Laboratory in Canada (Chandler 2004)

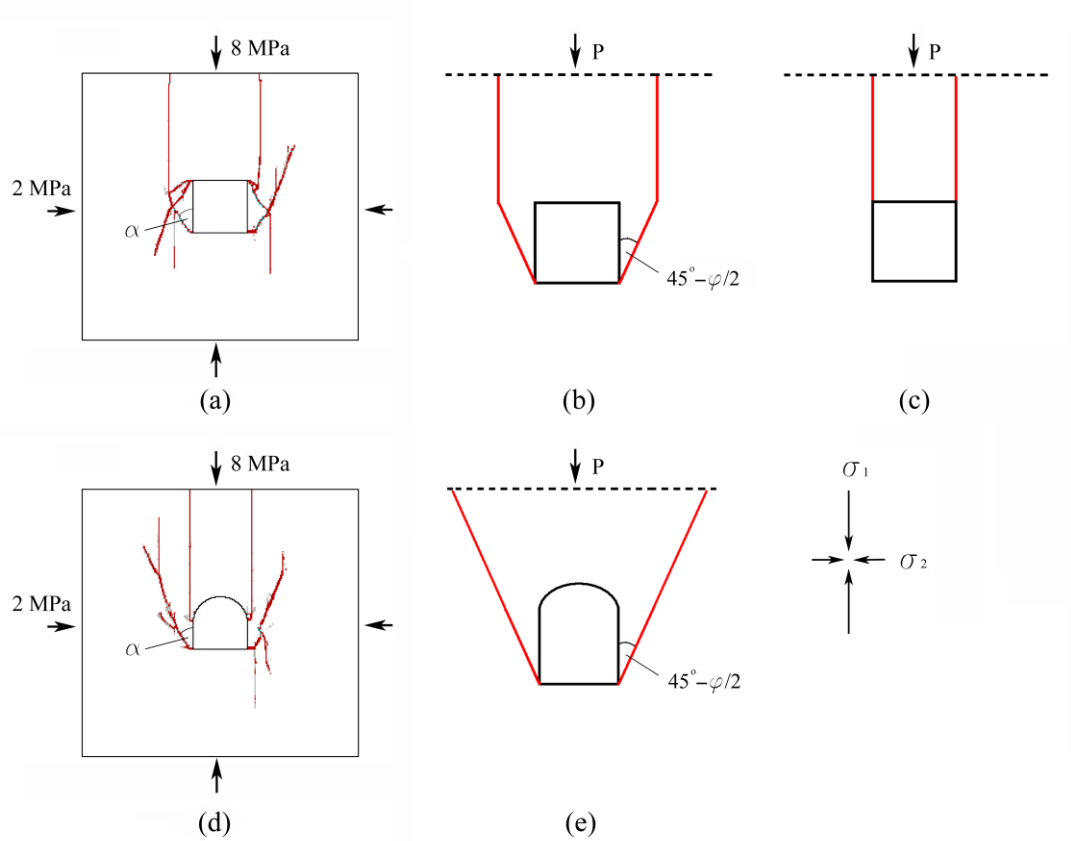

Figure 5-51 Macroscopic fracture pattern of underground opening (a), (d) fixed orientation model, α = 45º - φ/2 = 30º, φ = 30º (b), (c), (e) classical fracture pattern of underground opening ((b): sidewalls are not stable; (c) sidewalls are stable; (e) pressure arch is not formed naturally) (modified from Xu 1993) (P: initial vertical pressure on the rock, dashed line: presumable ground, red line: sliding face)

A commonly seen hourglass shaped pillar caused by spalling at the rib structure is shown in Fig. 5-52 (c). This failure pattern is better represented by the simulation of wing crack model scheme (Fig. 5-52 (b)) and wing crack combined ubiquitous-joint model scheme, where failed zones formed macroscopic fractures more parallel to the surface of the pillar and facilitate the spalling process. However, fixed orientation model (Fig. 5-52 (a)) and fixed orientation combined ubiquitous-joint model where singular macroscopic fracture was formed may not be used to describe this type of failure process.

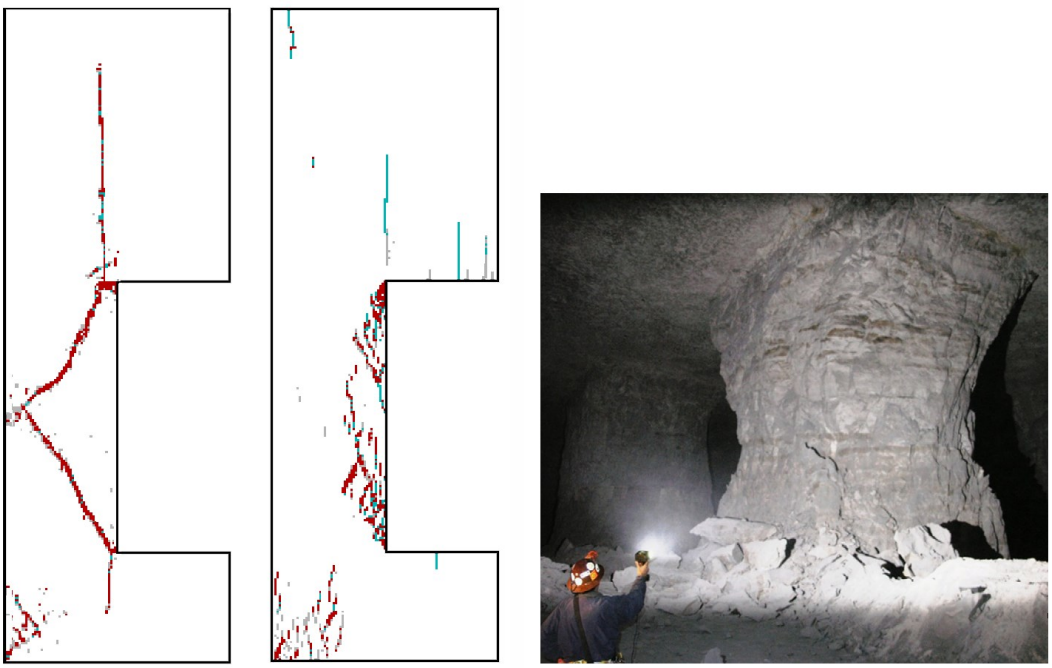

(a) (b) (c)

Figure 5-52 Spalling at the rib of the pillar (a) fracture pattern of pillar in fixed orientation model (b) fracture pattern of pillar in wing crack model (c) hourglass formation of a pillar because of spalling (Esterhuizen et al. 2011)

On the basis of these studies the preliminary conclusion can be drawn, that several typical fracture (failure) pattern, observed in nature, are quite well reproduced by the proposed simulation schemes. Nevertheless, the different schemes also produce to some extent also different failure mechanisms. Therefore, further studies, beyond the scope of this work, are necessary to clarify which scheme is appropriate to be applied in-situ.

6 Summaries and conclusions

In this thesis, lifetime prediction schemes for rocks have been proposed and were realized using numerical simulations. The developed simulation strategy is based on the assumption, that macroscopic fractures are created by coalescence of micro-cracks and the growth of micro-cracks is governed by the grain structure. Therefore growth and arrest of micro-crack growth is controlled by characteristics of grains (size, distribution, strength etc.). Based on linear elastic fracture mechanics, numerical models have been built. The subcritical crack growth of the microcracks inside the mode has also been modeled. The fracture growth is controlled by Charles equation. Different numerical models have been built and tested with the corresponding lifetime prediction schemes. The factors influencing the lifetime have been investigated through both single zone model and multi-zone model. Numerical predicted lifetime has been obtained and compared with analytical solutions. Macroscopic fracture patterns of the numerical models have been studied. The failure modes of the zone under different loads and initial crack characteristics have been investigated. Finally, the proposed numerical models have been used to simulate underground openings and weak plane problems.

The following conclusions can be drawn:

(1) Using a smaller time step, the numerical result for the lifetime comes closer to the analytical solution. However, a longer computing time is caused in this case. It is also observed that changes in time step value do not have much influence in predictions of the first zone failure time. In view of this, a scheme with changeable time steps is proposed and applied to the model. A comparatively bigger time step value is first used in the calculation before any zone fails to save computing time and the time step is reduced if the mechanical unbalanced force ratio suddenly rises, which indicates that zones have failed and stress-redistributions occur. The developed scheme with changeable time steps is efficient and guarantees an acceptable precision.

(2) Based on the basic model (Konietzky et al. 2009), four new numerical model schemes have been proposed, namely: fixed orientation model, wing crack model, fixed orientation combined ubiquitous-joint model and wing crack combined ubiquitous-joint model. These models (including basic model) have been studied under different loading conditions using a single zone, and the numerical predicted lifetime and important parameters relating to the lifetime (stress intensity factor and critical crack lengths) have shown excellent agreement with the analytical solutions in all cases. Also, the correct failure mode of the zone in the single zone studies (or first failure zone in the multi zone studies) has been predicted by the numerical simulation in each case.

(3) Factors influencing the lifetime for in fixed orientation models and wing crack models were investigated. Some common features have been observed: The lifetime is shorter if the applied load becomes bigger, or the initial crack is longer in both uniaxial tensile and compressive loading. Under uniaxial tensile load, the lifetime is longer the more the crack axis is perpendicular to the applied tensile load (the same holds for the mean orientation in multi zone models), while under compressive load, the lifetimes have a U-shaped curve with ascending crack orientation (the same holds for the mean orientation in multi zone models). It is also observed that under the same amplitude of load, the time to failure under tension is much shorter than under compression.

(4) Macroscopic fractures have been studied for all the numerical models. Under tensile load, macroscopic fractures were formed perpendicular to the applied load in all numerical models. Under compressive load, shear bands were formed with the inclination of about 45º to the loading direction in the basic model, and 30º in the fixed orientation model and in the fixed orientation combined ubiquitous-joint model, which confirms Mohr-Coulomb theory, while in the wing crack model and wing crack combined ubiquitous-joint model, the macroscopic fractures follow the direction of the applied compressive load (or the direction of the major compressive load under biaxial compressive stress). Both of the above failure modes, inclined shear bands and tensile fractures are also observed at the macroscopic scale in uniaxial compressive lab tests.

(5) The wing crack propagation scheme has been programmed where the wing cracks extend in the direction of the maximum circumferential stress. A superposition method for calculating the stress intensity factor has been incorporated into the program. Numerical results of the superposition method were validated by comparison with exact analytical solutions.

(6) The influence of the orientation of the initial microcracks on the macroscopic fractures has been investigated for all models. If the orientation of the initial microcracks follows uniform distribution, compared with the case of normal distribution, under tensile load the tensile macroscopic fracture has shown a more uneven pattern. Under compressive load, the shear band is formed by groups of more scattered distributed failed zones. In addition, the shear band is found more scattered and the lifetime is shorter with bigger standard deviation (5º) compared to a smaller standard deviation (1º) (fixed orientation model).

(7) Under tensile loads, the zones forming the macroscopic tensile fractures are more likely to fail by $K_I \geq K_{IC}$, which explains the comparatively short lifetime. This

phenomenon is also supported by laboratory observation which shows abrupt failure for rock under tensile load. In compressive tests, zones forming the shear bands often fail by crack lengths reaching the zone boundaries, which indicates that such zones failed in the subcritical crack propagation phase.

(8) The numerical models have shown much higher resistance against fracturing in shear than in tension, like observed in nature. Especially, the wing crack model has shown great resistance against fracturing under biaxial loading. Even with small additional lateral compressive loading, the lifetime is increased significantly.

(9) Underground opening problems have been simulated using the developed modeling schemes. It is observed that with the similar size (cross section area) of the opening, the model with the square opening has the shortest lifetime. The lifetime of the model with the arched opening is longer and the model with the circular opening has the longest lifetime. Shear bands have been observed in each of the models. In addition, macroscopic tensile fractures have been formed from the roof and floor of the opening in the wing crack model and wing crack combined ubiquitous-joint model.

(10) The propagation and coalescence of microcracks in models with existing weak plane(s) have been studied. Shear bands are formed in the basic model, fixed orientation model and fixed orientation combined ubiquitous-joint model. Macroscopic tensile fractures are formed following the direction of applied load in wing crack model. Inclined macroscopic fractures were formed in wing crack combined ubiquitous-joint model. In this case, the inclination of the macroscopic fractures was found greatly influenced by the mean initial crack orientation of the initial cracks.

(11) It is concluded that with the same rock parameters, same initial crack conditions and under the same loading condition, the lifetime of basic model is the most conservative, while the wing crack combined ubiquitous-joint model predicts the longest lifetime. Arranged by the ascending order of the predicted lifetime: basic model, fixed orientation model, fixed orientation combined ubiquitous-joint model, wing crack model and wing crack combined ubiquitous-joint model.

This study has been an attempt to predict the lifetime of rock under load from the microcrack propagation point of view. An extensive programming work has been performed to implement several crack propagation schemes into a numerical code. Reasonable results have been obtained from the numerical simulations. However, further improvements can be made: study on the influence of different mesh size and shape on the lifetime and macroscopic fractures; extending the model schemes into 3 dimensional models, where also the out-of-plane shear fracture (Mode III) is

considered; extending and implementation of the lifetime prediction schemes into the Discrete Element Modeling technique, where discrete fracturing could be simulated; detailed quantitative verification of the proposed modeling schemes by comparing with lab tests and in situ observations.

7 Major contributions of this thesis

The main contributions can be summarized as follows:

- Development, programming and verification of five different approaches (improvement of the basic model developed by Konietzky et al. 2009) to simulate micro-mechanical fracture growth within a numerical cellular automata.
- Explicit consideration of initial micro fracture length and orientation.
- Development and verification of an automatic algorithm to adjust the calculation time step (optimization of calculation time).
- Extension of the Wing-crack-model to include tensile failure.
- Application of the developed models to simplified geomechanical problems.
- Investigation of the influence of micro-crack characteristics and stress state on the formation of macroscopic fracture pattern.

References

Alehossein H, Boland JN (2004) Strength, toughness, damage and fatigue of rock. SIF2004 Structural Integrity and Fracture

Amitrano D, Helmstetter A (2006) Brittle creep, damage, and time to failure in rocks. J Geophys Res 111:B11201:1–B11201:17

Anderson OL, Grew PC (1977) Stress corrosion theory of crack propagation with applications to geophysics. Rev Geophys Space Phys 15(1):77–104

Anderson TL (1995) (2005) Fracture Mechanics. CRC Press LLC, USA

Aubertin M, Li L, Simon R (2000) A multiaxial stress criterion for short- and long-term strength of isotropic rock media. Int J Rock Mech Min Sci 37:1169–1193

Ashby MF, Hallam SD (1986) The failure of brittle solids containing small cracks under compressive stress states. Acta Metall 34(3):497–510

Ashby MF, Sammis CG (1990) The damage mechanics of brittle solids in compression. Pure Appl Geophys 133(3):489–521

Atkinson BK (1979) A fracture mechanics study of subcritical tensile cracking of quartz in wet environments. Pure Appl Geophys PAGEOPH 117(5):1011–1024

Atkinson BK (1982) “Subcritical crack propagation in rocks: theory, experimental results and applications” J Struct Geol 4:41–56

Atkinson BK (1984) “Subcritical crack growth in geological materials” J Geophys Res 89(B6):4077–4114

Atkinson BK (1987) Fracture Mechanics of Rock. Academic Press INC LTD, London

Atkinson BK, Meredith PG (1987) The theory of subcritical crack growth with applications to minerals and rocks, in Fracture mechanics of rock. Academic Press, London

Ayatollahi MR, Aliha MRM (2007) Fracture toughness study for a brittle rock subjected to mixed mode I/II loading. Int J Rock Mech Min Sci 44:617–624

Ayatollahi MR, Aliha MRM (2009) Mixed-mode fracture in soda-lime glass analyzed

by using the generalized MTS criterion. Int J Solids Struct 46:311–321

Ayatollahi MR, Sedighiani K (2010) Crack tip plastic zone under Mode I, Mode II and mixed mode (I + II) conditions. Struct Eng Mech 36:575–598

Ayatollahi MR, Sedighiani K (2012) Mode I fracture initiation in limestone by strain energy density criterion. Theor Appl Fract mec 57:14–18

Backers T, Stephansson O, Rybacki E (2002) Rock fracture toughness testing in Mode II – Punch-through shear test. Int J Rock Mech Min Sci 39:755–769

Backers T, Stephansson O (2012) ISRM suggested method for the determination of Mode II fracture toughness. Rock Mech Rock Eng 45:1011–1022

Baud P, Reuschlé T, Charlez P. (1996) An Improved Wing Crack Model for the Deformation and Failure of Rock in Compression. Int J Rock Mech Min Sci 33(5):539–542

Bhat HS, Sammis CG, Rosakis AJ (2011) The micromechanics of westerley granite at large compressive loads. Pure Appl Geophys 168:2181–2198

Blümling P, Konietzky H (2003) Development of an excavation disturbed zone in claystone (Opalinus Clay). In Natau, Fecker & Pimentel (Eds.). Swets & Zeitlinger, Lisse

Bobet A, Einstein HH (1998) Fracture coalescence in rock-type materials under uniaxial and biaxial compression. Int J Rock Mech Min Sci 35(7):863–888

Bossart P, Meier PM, Moeri A, Trick T, Mayor JC (2002) Geological and hydraulic characterization of the excavation disturbed zone in the Opalinus Clay of the Mont Terri Rock Laboratory. Eng Geol 66:19–38

Cao P, Li JT, Yuan HP (2006) Testing study of subcritical crack growth rate and fracture toughness in different rocks. T Nonferr Metal Soc 16:709–713

Cartwright DJ, Rooke DP (1974) Approximate stress intensity factors compounded from known solutions. Eng Fract Mech 6(3):563–571

Challamel N, Lanos C, Casandjian C (2006) Stability analysis of quasi-brittle materials – creep under multiaxial loading. Mech Time-Depend Mater 10:35–50

Chandler N (2004) Developing tools for excavation design at Canada's Underground Research Laboratory. Int J Rock Mech Min Sci 41(8):1229–1249

Chang SH, Lee CI, Jeon S (2002) Measurement of rock fracture toughness under modes I and II and mixed-mode conditions by using disc-type specimens. Eng Geol 66:79–97

Chao YJ, Liu S, Broviak BJ (2001) Brittle fracture: variation of fracture toughness with constraint and crack curving under mode I conditions. Exp Mech 41:232–241

Charles RJ (1958) Static fatigue of glass. J Appl Phys 29:1549-1560

Chen WZ, Zhu WS, Shao JF (2004) Damage coupled time-dependent model of a jointed rock mass and application to large underground cavern excavation. Int J Rock Mech Min Sci 41(4):669–677

Chen ZT, Wang D (1994) A note on the fracture criteria for mixed-mode crack problems of materials with different yield strengths in tension and compression. Int J Fracture 69:R11–R14

Ciccotti M (2009) Stress-corrosion mechanisms in silicate glasses. J Phys D Appl Phys 42:1–18

Costin LS (1983) A microcrack model for the deformation and failure of brittle rock. J Geophys Res 88(B11):9485–9492

Costin LS (1985) Damage mechanics in the post-failure regime. Mech Mater 4(2):149–160

Cotterell B. and Rice J. R. (1980) Slightly curved or kinked cracks. Int J Fracture 16(2):155–169

Cristescu ND, Hunsche U (1998) Time effects in rock mechanics. Wiley Series in Materials, Modelling and Computation, John Wiley & Sons, Chichester, New York, Weinheim, Brisbane, Singapore, Toronto

Damjanac B, Fairhurst C (2010) Evidence for a long-term strength threshold in crystalline rock. Rock Mech Rock Eng 43:513–531

Das S. and Scholz C. H. (1981) Theory of time-dependent rupture in the earth. J Geophys Res 86(B7):6039–6051

Davenport JCW, Smith DJ (1993) A study of superimposed modes I, II and III on PMMA. Fatigue Fract Eng M 16:1125–1133

Dienes JK (1978) A statistical theory of fragmentation, In: Proc 19th US Symp Rock Mech Rena, Nev.. pp. 51–55

Dill SJ, Bennison SJ, Dauskardt RH (1997) Subcritical crack-growth behavior of borosilicate glass under cyclic loads: evidence of a mechanical fatigue effect. J Am Ceram Soc 80(3):773–776

Eberhardt EB (1998) Brittle rock fracture and progressive damage in uniaxial compression. Dissertation, University of Saskatchewan, Department of Geological Sciences

Erdogan F, Sih GC (1963) On the crack extension in plate under plane loading and transverse shear. J Basic Eng-T ASME 85(4):519–527

Esterhuizen GS, Dolinar DR, Ellenberger JL (2011) Pillar strength in underground stone mines in the United States. Int J Rock Mech Min Sci 48:42–50

Feng XT, Chen S, Li S (2001) Effects of water chemistry on microcracking and compressive strength of granite. Int J Rock Mech Min Sci 38(4):557–568

Fortin J, Stanchits S, Vinciguerra S, Guéguen Y (2011) Influence of thermal and mechanical cracks on permeability and elastic wave velocities in a basalt from Mt. Etna volcano subjected to elevated pressure. Tectonophysics 503:60–74

Fowell RJ (1995) Suggested methods for determining mode I fracture toughness using cracked chevron notched Brazilian disc specimens. Int J Rock Mech Min Sci 32(1):57–64

Freiman SW (1984) Effects of chemical environments on slow crack growth in glasses and ceramics. J Geophys Res 89(B6):4072–4076

Fujii Y, Kiyama T, Ishijima Y, Kodama J (1999) Circumferential strain behavior during creep tests of brittle rocks. Int J Rock Mech Min Sci 36(3):323–337

Golshania A, Odaa M, Okuia Y, Takemurab T, Munkhtogooa E (2007) Numerical simulation of the excavation damaged zone around an opening in brittle rock. Int J Rock Mech Min Sci 44:835–845

Griffith AA (1921) The phenomena of rupture and flow in solids. Phil Trans Royal Soc London; SeriesA, 221:163–198

Gross D. and Seelig T. (2006) Fracture Mechanics: with an introduction to micromechanics. Springer-Verlag Berlin Heidelberg

Guedes RM (2006) Lifetime predictions of polymer matrix composites under constant or monotonic load. Composites: Part A 37:703–715

Guinea GV, Planas J, Elices M (2000) KI evaluation by the displacement extrapolation technique. Eng Fract Mech 66(3):243–255

Hadley K (1976) Comparison of calculated and observed crack densities and seismic velocities in Westerly granite. J Geophys Res 81:3484–3494

Hakami H, Stephansson O (1990) Shear fracture energy of Stripa granite – results of controlled triaxial testing. Eng Fract Mech 35:855–865

Hellan K (1985) Introduction to fracture mechanics. McGraw – Hill Book Co, Singapore

Horii H, Nemat-Nasser S (1983) Estimate of stress intensity factors for interacting cracks. In Yuceoglu U, Sierakowski RL, Glasgow DA (Eds.) Advances in aerospace structures, materials and dynamics. ASME, New York

Horii H, Nemat-Nasser S (1985) Compression-induced microcrack growth in brittle solids: axial splitting and shear failure. J Geophys Res 90(B4):3105–3125

Horii H, Nemat-Nasser S (1986) Brittle failure in compression: splitting, faulting and brittle-ductile transition. Phil Trans R Soc Lend A. 319:337–374

Huang J, Wang S (1985) An experimental investigation concerning the comprehensive fracture toughness of some brittle rocks. Int J Rock Mech Min Sci 22(2):99–104

Hutchinson JW (1968) “Singular Behavior at the End of a Tensile Crack Tip in a Hardening Material” J Mech Phys Solids 16:13–31

Ignatovich SR (1996) Method for prediction of the accrued lifetime of structural materials up to formation of a crack of the limiting length. Strength Mater 28:376–380

Inglis CE (1913) Stresses in a plate due to the presence of cracks and sharp corners. Transactions of the institute of naval architects 55:219–230

Ingraffea AR (1981) Mixed-mode fracture initiation in Indiana limestone and Westerly granite. In: Einstein HH (editor) Rock mechanics from research to application. Proceedings of the 22nd US Symposium on Rock Mechanics. Cambridge: Mass. MIT. pp. 199–204

Irwin, GR (1948) "Fracture dynamics," in: Proceedings of the ASM Symposium on Fracturing of Metals, Cleveland (OH) (1948), pp. 147–166
(Irwin, GR, “Fracture Dynamics.” Fracturing of Metals, American Society for Metals, Cleveland, OH, 1948, pp. 147–166)

Irwin GR (1956) Onset of fast crack propagation in high strength steel and aluminum alloys. Sagamore research conference proceedings 2:289–305

Irwin GR (1957), Analysis of stresses and strains near the end of a crack traversing a plate, J Appl Mech 24:361–364

Irwin GR (1961) Plastic zone near a crack and fracture toughness. Sagamore research conference proceedings Vol. 4

Isaksson P, Ståhle P (2002) Prediction of shear crack growth direction under compressive loading and plane strain conditions. Int J Fracture 113:175–194

Itasca Consulting Group (2005) FLAC, second ed. Minneapolis, Minnesota, USA

Jeong HK, Kang SS and Obara Y (2007) Influence of surrounding environments and strain rates on the strength of rocks subjected to uniaxial compression. Int J Rock Mech Min Sci 44(3):321–331

Jiang Q, Cui J, Chen J (2012) Time-dependent damage investigation of rock mass in an in situ experimental tunnel. Materials 5:1389–1403

Kemeny J (1991) A model for non-linear rock deformation under compression due to sub-critical crack growth. Int J Rock Mech Min Sci 28(6):459–467

Kemeny J (2003) The time-dependent reduction of sliding cohesion due to rock bridges along discontinuities: a fracture mechanics approach. Rock Mech Rock Eng 36(1):27–38

Kemeny J (2005) Time-dependent drift degradation due to the progressive failure of rock bridges along discontinuities. Int J Rock Mech Min Sci 42:35–46

Khan K, Al-Shayea NA (2000) Effect of specimen geometry and testing method on mixed Mode I – II fracture toughness of a limestone rock from Saudi Arabia. Rock Mech Rock Eng 33:179–206

Ko TY, Kemeny J (2006) Determination of Mode II stress intensity factor using short beam compression test. In: 4th Asian Rock Mechanics Symposium, Singapore

Kong XM, Schluter N, Dahl W (1995) Effect of triaxial stress on mixed-mode fracture, Eng Fract Mech 52:379–388

Konietzky H., Heftenberger A. and Feige M. (2009) "Life-time prediction for rocks under static compressive and tensile loads: a new simulation approach" Acta Geotech 4:73–78

Kranz RL (1983) Microcracks in rocks: a review. Tectonophysics 100:449–480

Kumar B, Chitsiriphanit S, Sun CT (2011) Significance of K-dominance zone size and nonsingular stress field in brittle fracture. Eng Fract Mech 78:2042–2051

Lam YC (1989) Mixed mode fatigue crack growth and the strain energy density factor. Theor Appl Fract Mec 12:67–72

Lau JSO, Chandler NA (2004) Innovative laboratory testing. Int J Rock Mech Min Sci 41:1427–1445

Lauterbach B, Gross D (1998) Crack growth in brittle solids under compression. Mech Mater 29:81–92

Le JL, Bažant ZP, Bazant MZ (2009) Subcritical crack growth law and its consequences for lifetime statistics and size effect of quasibrittle structures. J Phys D Appl Phys 42:1–8

Lei X, Satoh T, Nishizawa O (2006) Experimental study on stress-induced pre-failure damage in rocks and its applications to earthquake source-process research based on AE. Proc. National Seminar on Non-Destructive Evaluation Dec. 7 - 9, 2006, Hyderabad pp. 263–270

Li H (1988) Rock fracture mechanics. Chongqing University Press, Chongqing, China

Li JT, Cao P, Gu DS, Wu C (2008) Crack growth time dependence analysis of granite under compressive-shear stresses state. Journal of Coal Science and Engineering (China) 14(1):34–37

Lim IL, Johnston IW, Choi SK (1993) Stress Intensity Factors for Semicircular Specimens under 3-Point Bending. Eng Fract Mech 44(3):363–382

Liu S, Chao YJ (2003) Variation of fracture toughness with constraint. Int J Fracture 124:113–117

Liu XM (2003) Stable or unstable crack growths in thin rock plate under compression for predicting buckling rockburst. Chinese J Rock Mech Eng 22(12):2011–2018

Malan DF (1999) Time-dependent behaviour of deep level tabular excavations in hard rock. Rock Mech Rock Eng 32(2):123–155

Malan DF (2002) Manuel Rocha Medal Recipient simulating the time-dependent behaviour of excavations in hard rock. Rock Mech Rock Eng 35(4):225–254

Maranini E, Yamaguchi T (2001) A non-associated viscoplastic model for the behaviour of granite in triaxial compression. Mech Mater 33(5):283–293

Martin RJ, III (1972) Time-dependent crack growth in quartz and its application to the creep of rocks. J Geophys Res 77(8):1406-1419

Mayr SI, Stanchits S, Langenbruch C, Dresen G, Shapiro SA (2011) Acoustic emission induced by pore-pressure changes in sandstone samples. Geophysics 76(3):MA21–MA32

Masuda K (2001) Effects of water on rock strength in a brittle regime. J Structural Geol 23(11):1653–1657

Mindess S. (1977) “The J-Integral as a Fracture Criterion For Fiber Reinforced Concrete” Cement Concrete Res 7:731–742

Mishnaevsky LL Jr (1996) Determination for the time-to-fracture of solids. Int J Fracture 79:341–350

Miura K, Okui Y, Horii H (2003) Micromechanics-based prediction of creep failure of hard rock for long-term safety of high-level radioactive waste disposal system. Mech Mater 35:587–601

Morais AB (2007) Calculation of stress intensity factors by the force method. Eng Fract Mech 74(5):739–750

Nara Y, Imai Y, Kaneko K (2004) Dependence of subcritical crack growth on rock fabric and environment. Shigen-to-Sozai 120:431–439

Nara Y, Kaneko K (2004) Dependence of subcritical crack growth in rocks on water vapor pressure. In Stephansson O, Hudson JA, Jing LR (Eds.) Coupled thermo-hydro-mechanical-chemical processes in geo-systems. Elsevier B.V., Amsterdam, The Netherlands, pp 529–534

Nara Y, Kaneko K (2005) Study of subcritical crack growth in andesite using the Double Torsion test. Int J Rock Mech Min Sci 42:521–530

Nara Y, Kaneko K (2006) Sub-critical crack growth in anisotropic rock. Int J Rock Mech Min Sci 43:437–453

Nara Y, Koike K, Yoneda T, Kaneko K (2006) Relation between subcritical crack growth behavior and crack paths in granite. Int J Rock Mech Mining Sci 43:1256–1261

Nara Y, Ohno Y, Imai Y, Kaneko K (2004) Anisotropy and grain-size dependency of crack growth due to stress corrosion in granite. Shigen-to-Sozai 120:25–31

Napier J, Backers T (2006) Comparison of numerical and physical models for understanding shear fracture processes. Pure Appl Geophys 163: 1153–1174

Nemat-Nasser S and Horii H (1982) Compression-induced nonplanar crack extension with application to splitting, exfoliation, and rockburst. J Geophys Res 87(B8):6805-6821

Nemat-Nasser S, Horii H (1983) Rock failure in compression. Proceedings Ninth Workshop Geothermal Reservoir Engineering Stanford University, Stanford, California, December 1983 pp. 381–385

Orowan E (1949) Fracture and strength of solids. Rep Prog Phys 12:185–232

Ouchterlony F (1988) Suggested methods for determining the fracture toughness of rock. Int J Rock Mech Min Sci 25(2):71–96

Pang HLJ (1995) Mixed mode fracture analysis and toughness of adhesive joints. Eng Fract Mech 51(4):575–583

Rao QH, Sun ZQ, Stephansson O, Li CL, Stillborg B (2003) Shear fracture (Mode II) of brittle rock. Int J Rock Mech Min Sci 40:355–375

Read RS (2004) 20 years of excavation response studies at AECL's Underground Research Laboratory. Int J Rock Mech Min Sci 41:1251–1275

Rice JR (1968) "A Path Independent Integral and the Approximate Analysis of Strain Concentration by Notches and Cracks." J Appl Mech 35:379–386

Rice JR, Rosengren GF (1968) "Plane Strain Deformation near a Crack Tip in a Power-Law Hardening Material" J Mech Phys Solids 16:1–12

Rinne M (2008) Fracture mechanics and subcritical crack growth approach to model time-dependent failure in brittle rock. Dissertation, Helsinki University of Technology

Ritter JE, Huseinovic A, Chakravarthy SS, Lardner TJ (2000) Subcritical crack growth in soda–lime glass under mixed-mode loading. J Am Ceram Soc 83(8):2109–2111

Rybicki EF, Kanninen MF (1977) Finite-element calculation of stress intensity factors by a modified crack closure integral. Eng Fract Mech 9(4):931–938

Sahouryeh E, Dyskin AV, Germanovich LN (2002) Crack growth under biaxial compression. Eng Fract Mech 69:2187–2198

Scholz CH (1972) Static fatigue of quartz. J Geophys Res 77(11):2104-2114

Shao JF, Hoxha D, Bart M, Homand F, Duveau G, Souley M, Hoteit N (1999) Modelling of induced anisotropic damage in granites. Int J of Rock Mech Min Sci 36(8):1001–1012

Shen B, Stephansson O (1993) Numerical analysis of mixed mode I and mode II fracture propagation. Int J Rock Mech Min Sci 30(7):861–867

Shen B, Stephansson O (1994) Modification of the G-criterion for crack propagation subjected to compression. Eng Fract Mech 47(2):177–189

Shih CF (1981) Relationships between J-integral and the crack opening displacement for stationary and extending cracks. J Mech Phys Solids 29(4):305–326

Shin K, Okubo S, Fukui K, Hashiba K (2005) Variation in strength and creep life of six Japanese rocks. Int J Rock Mech Min Sci 42(2):251–260

Sih GC (1973) Some basic problems in fracture mechanics and new concepts. Eng Fract Mech 5:365–377

Sih GC (1974) Strain-energy-density factor applied to mixed mode crack problems. Int J Fracture 10:305–321

Sih GC, Liebowitz H (1968) Mathematical theories of brittle fracture. In Fracture, 2, Mathematical Fundamentals (Edited by Liebowitz, H.), pp. 67-190. Academic Press, New York

Sun J, Hu YY (1997) Time-dependent effects on the tensile strength of saturated granite at Three Gorges Project in China. Int J Rock Mech Min Sci 34:3–4

Sun CT, Qian HY (2009) Brittle fracture beyond the stress intensity factor. J Mech Mater Struct 4:743–753

Swanson PL (1985) Subcritical crack fracture propagation in rocks: an examination using the methods of fracture mechanics and nondestructive testing. Dissertation, University of Colorado

Szczepanik Z, Milne D, Kostakis K, Eberhardt E (2003) Long term laboratory strength tests in hard rock. ISRM 2003 – Technology roadmap for rock mechanics.

South African Institute of Mining and Metallurgy, 1179-1184

Tapponier P, Brace WF (1976) Development of stress-induced microcracks in Westerly granite. Int J Rock Mech Min Sci 13:103–112

Theocaris PS, Andrianopoulos NP (1982) The Mises elastic-plastic boundary as the core region in fracture criteria. Eng Fract Mech 16:425–432

Theocaris PS, Andrianopoulos NP (1982) The T-criterion applied to ductile fracture. Int J Fracture 20:125–130

Ukadgaonker VG, Awasare PJ (1995) A new criterion for fracture initiation. Eng Fract Mech 51:265–274

Watkins J, Liu KLW (1985) A finite element study of the short beam test specimen under mode II loading. International journal cement composites lightweight concrete 7(1):39–47

Waza T , Kurita K, Mizutani H (1980) The effect of water on the subcritical crack growth in silicate rocks. Tectonophysics 67:25–34

Wiederhorn SM (1967) Influence of water vapor on crack propagation in soda-lime glass. Journal of the American Ceramic Society 50(8):407–414

Wiederhorn SM, Bloz LH (1970) Stress corrosion and static fatigue of glass. J Am Ceram Soc 53(10):543–548

Wilson WK (1971) Numerical method for determining stress intensity factors of an interior crack in a finite plate. J Basic Eng-T ASME 93:685–689

Wong RHC, Chau KT, Wang P (1996) Microcracking and grain size effect in Yuen Long marbles. Int J Rock Mech Min Sci 33:479–485

Wong TF (1985) Geometric probability approach to the characterization and analysis of microcracking in rocks. Mech Mater 4:261–276

Wong TF, Wong RHC, Chau KT, Tang CA (2006) Microcrack statistics, Weibull distribution and micromechanical modeling of compressive failure in rock. Mech Mater 38:664–681

Xu ZY (1993) Rock mechanics. Water Resources and Electric Power Press, Beijing

Yang SQ, Jing HW, Wang SY (2012) Experimental investigation on the strength, deformability, failure behavior and acoustic emission locations of red sandstone under triaxial compression. Rock Mech Rock Eng 45:583–606

Yoon J, Jeon S (2003) An experimental study on Mode II fracture toughness determination of rock. J Korean Soc Rock Mech 13(1):64–75

Yoon JS, Zang A, Stephansson O (2012) Simulating fracture and friction of Aue granite under confined asymmetric compressive test using clumped particle model. International J Rock Mech Min Sci 49:68–83

Yoshida H, Horii H (1992) A micromechanics-based model for creep behavior of rock. Appl Mech Rev 45(8):294–303

Yuan HP, Cao P, Xu WZ (2006) Mechanism study on subcritical crack growth of flabby and intricate ore rock. T Nonferr Metal Soc 16:723–727

Zhao YL and Wang WJ (2011) Wing crack propagation model under high hydraulic pressure in compressive-shear stress state. Journal of Coal Science & Engineering (CHINA) 17(1):34–38

Zhou XP, Yang HQ (2012) Multiscale numerical modeling of propagation and coalescence of multiple cracks in rock masses. Int J Rock Mech Min Sci 55:15–27

Zhu Z, Wang LG, Mohanty B, Huang CY (2006) Stress intensity factor for a cracked specimen under compression. Eng Fract Mech 73:482–489

Zhu Z, Xie H, Ji S (1997) The mixed boundary problems for a mixed mode crack in a finite plate. Eng Fract Mech 56(5):647–655

Zietlow WK, Laubuz JF (1998) Measurement of the Intrinsic Process Zone in Rock Using Acoustic Emission. Int J Rock Mech Min Sci 35(3):291–299